On the nature of different Fe sites in Fe-containing micro and mesoporous materials and their catalytic role in the abatement of nitrogen oxides from exhaust gases

D i s s e r t a t i o n

zur Erlangung des akademischen Grades

D o c t o r r e r u m n a t u r a l i u m

(Dr. rer. nat.)

im Fach Chemie

eingereicht an der

Mathematisch-Naturwissenschaftlichen Fakultät I

der Humboldt-Universität zu Berlin

von

M. Santhosh Kumar, M.Sc.

geboren am 10.10.1975 in Secunderabad, Indien

Präsident der Humboldt-Universität zu Berlin
Prof. Dr. Jürgen Mlynek

Dekan der Mathematisch-Naturwissenschaftlichen Fakultät I
Prof. Thomas Buckhout, Ph.D

Gutachter/innen:

1. PROF. DR. R. STÖSSER
2. HABIL. DR. A. BRÜCKNER

Tag der mündlichen Prüfung: 22.09.2005

ZUSAMMENFASSUNG

Einführung und Zielsetzung

Die Entfernung von Stickoxiden aus Abgasen mobiler und stationärer Emissionsquellen gehört seit Jahren zu den wichtigsten Forschungsthemen in der Umweltkatalyse. Der Dreiwegekatalysator für Ottomotoren und die selektive katalytische Reduktion (SCR) von Stickoxiden mit NH_3 in Abgasströmen von Kraftwerken sind seit langem kommerziell etablierte Technologien. In den vergangenen Jahren sind verstärkt Forschungsarbeiten zur SCR von Stickoxiden im Sauerstoffüberschuss durchgeführt worden, da diese eine elegante Lösung für die Abgasreinigung bei Diesel- und Magermix-Ottomotoren darstellt. Neben Kohlenwasserstoffen (HC) ist auch NH_3 als Reduktionsmittel untersucht worden, da die NH_3-SCR einerseits als Teilprozess der HC-SCR verstanden werden kann und andererseits zumindest für schwere Dieselfahrzeuge auf der Basis von Harnstoff als Reduktionsmittel entwickelt worden ist (SINOX-Technologie, Siemens). Eisen-dotierte Zeolith-Katalysatoren, insbesondere solche mit MFI-Struktur sind als besonders Erfolg versprechend identifiziert worden, zeigten jedoch z. T. stark differierende SCR-Aktivitäten. Als Ursache kommt die Koexistenz von Fe-Spezies unterschiedlicher Natur in Betracht, deren katalytische Wirkung bisher widersprüchlich diskutiert bzw. kaum verstanden wurde. Mit dieser Arbeit wurden deshalb folgende Ziele verfolgt:

1) Aufklärung des Einflusses verschiedener Präparationsmethoden sowie des Si/Al-Verhältnisses auf Struktur und Redoxeigenschaften von Fe-Spezies in Fe-MFI-Zeolithen.
2) Aufklärung des Einflusses der Porenstruktur auf Natur und Redoxverhalten der Fe-Spezies. Dies wurde durch Vergleich von mikroporösem Fe-Silikalith und mesoporösem Fe-SBA-15 erreicht.
3) Aufklärung der Rolle verschiedener Fe-Spezies in der SCR von NO mit NH_3 und Isobutan sowie in der direkten Zersetzung bzw. der SCR von N_2O mit CO durch Anwendung verschiedener in situ-Methoden unter reaktionsnahen Bedingungen.
4) Korrelation der erhaltenen Ergebnisse mit den Resultaten katalytischer Tests zur Ableitung von Struktur-Wirkungs-Beziehungen.

Experimentelles

Diese Arbeit ist Bestandteil eines DFG-Verbund-Projektes (Förderkennzeichen: BR 1380/7-1, BR 1380/7-2). Die katalytische Testung sowie die Präparation der mikroporösen Fe-Zeolithe erfolgte in den Arbeitskreisen der Kooperationspartner Prof. W. Grünert (Ruhr-Universität Bochum) sowie Prof. J. Pérez-Ramírez (Yara-Technology Center Porsgrun (Norwegen) und ICREA (Tarragona, Spanien)). Dabei kamen folgende Methoden zum Einsatz:

a) Chemical Vapour Deposition (CVD) von wasserfreiem $FeCl_3$ in H-ZSM-5
b) Festkörperionenaustausch (Solid State Ion Exchange, SSIE) von $FeCl_3 \cdot 6\ H_2O$ in H-ZSM-5

c) konventioneller Ionenaustausch (Liquid Ion Exchange, LIE) mit $Fe(NO_3)_3$-Lösung in NH_4-ZSM-5 und Improved Liquid Ion Exchange (ILIE) in H-ZSM-5 unter Verwendung von Eisenpulver in verdünnter HCl
d) eine mechanochemische Route (MR) der Vermischung von $FeCl_3 \cdot 6\ H_2O$ mit H-ZSM-5 gefolgt von kurzzeitigem Waschen
e) isomorpher Einbau von Fe auf Gitterplätzen von ZSM-5, Silikalith und Zeolith Beta durch Hydrothermalsynthese mit anschließender Extraktion durch Wasserdampfbehandlung (ex-HS)

Mesoporöses Fe-SBA-15 wurde im Rahmen dieser Arbeit am ACA durch Imprägnieren hergestellt.

Struktur und Verteilung der Fe-Spezies nach verschiedenen Schritten des Präparationsprozesses sowie nach dem Einsatz in der SCR wurden mittels EPR- und UV/VIS-Spektroskopie in diffuser Reflexion untersucht. Insbesondere konnten die Vorteile der Kombination beider Methoden im Vergleich zu anderen in der Literatur verwendeten Techniken (z. B. EXAFS, Mössbauer-Spektroskopie, TPR) eindrucksvoll demonstriert werden, da mittels EPR vorzugsweise verschiedene isolierte Fe^{3+}-Spezies detektiert werden können, während intensive charge-transfer (CT)-Banden im UV/VIS-Bereich Auskunft über deren Koordinationsgeometrie, die Größe von Fe_xO_y-Clustern sowie den relativen Anteil der dieser Spezies in der Probe geben.

Die Redoxeigenschaften sowie das Verhalten der verschiedenen Fe-Spezies bei höheren Temperaturen in Gegenwart von Komponenten der SCR-Reaktionsgasmischungen wurde mittels in situ-EPR und in situ-UV/VIS-DRS unter Verwendung spezieller Reaktionszellen verfolgt. Darüber hinaus wurden an ausgewählten Proben in situ-FT-IR-Untersuchungen durchgeführt, um Oberflächenintermediate zu identifizieren. Diese Methode kam auch bei der Analyse azider Zentren mittels Pyridinadsorption zum Einsatz.

Ergebnisse und Schlussfolgerungen

Einfluss der Präparationsmethoden auf Struktur, Verteilung und Redoxverhalten der Fe-Spezies

Mittels EPR wurden praktisch in allen Katalysatoren mindestens zwei Arten isolierter Fe^{+3}-Spezies nachgewiesen (Signale bei $g' \approx 4.3$ und 6). Das Signal einer weiteren isolierten Fe^{+3}-Spezies ($g' \approx 2$) wird in Proben mit Fe_xO_y-Clustern vom Signal letzterer überlagert. In den UV/VIS-Spektren werden isolierte Fe^{3+}-Spezies in tetraedrischer und höherer Koordination durch CT-Banden um 240 bzw. 290 nm reflektiert, während die CT-Banden von Fe_xO_y-Clustern oberhalb 300 nm auftreten und mit zunehmender Clustergröße zu höheren Wellenlängen verschoben werden. Auf der Basis dieser Untersuchungen wurde gefunden, dass die Methoden MR und ILIE mit Fe-Gehalten <0.5 M.-% vorzugsweise zu Katalysatoren mit isolierten Fe-Spezies führen und die Bildung oxidischer Cluster weitgehend unterdrückt wird. Dies gilt auch für die Synthese von Fe-Silikalith mittels ex-HS, während in den Al-haltigen Katalysatoren Fe-ZSM-5 und Fe-Beta die Bildung von Fe_xO_y-Clustern mit ex-HS nicht verhindert werden kann. Signifikante Mengen isolierter Fe-Zentren entstehen auch durch CVD und SSIE, mit denen

deutlich größere Fe-Gehalte bis 5 M.-% in H-ZSM-5 eingebracht werden können. Allerdings bilden sich mit diesen Methoden auch beträchtliche Mengen oligonuklearer Fe_xO_y-Cluster und, insbesondere bei SSIE, auch größere Fe_2O_3-Partikel. Am wenigsten förderlich für die Erzeugung hoher Fe-Dispersitäten ist die LIE-Methode. Hingegen kann mittels ILIE durch geeignete Wahl des Fe-Gehalts der Agglomerisatiosgrad gezielt gesteuert werden.

Am Beispiel von zwei CVD-Proben auf der Basis von H-ZSM-5 mit unterschiedlichem Si/Al-Verhältnis (14 und 40) wurde der Einfluss des Wasch- und Calciniervorgangs, des Si/Al-Verhältnisses in der H-ZSM-5-Matrix (14 und 40) sowie des Einsatzes in der Isobutan-SCR von NO untersucht. Es zeigte sich, dass die Bildung oxidischer Cluster durch intensives Waschen und geringe Aufheizraten bei der Calcinierung teilweise vermindert werden kann. In der Probe mit Si/Al ≈ 40, die eine vergleichsweise hohe Konzentration an Silanol-Defekten enthält, wird das Clusterwachstum während der Calcinierung durch Fixierung des Fe an den Defekten vermindert. Allerdings wurden mit dieser Matrix deutlich geringere Fe-Gehalte erreicht. Der Einsatz der Katalysatoren in der SCR führt zur verstärkten Bildung größerer Partikel durch Wachstum oligonuklearer Cluster.

UV/VIS-Untersuchungen des Redoxverhaltens der verschiedenen Fe-Spezies haben gezeigt, dass in weitgehend clusterfreien Katalysatoren von den isolierten Fe-Spezies in den Poren solche in tetraedrischer Koordination mit vergleichbarer Geschwindigkeit reduziert und reoxidiert werden, während die Reduktion höher koordinierter Fe^{3+}-Spezies etwas schneller, ihre Reoxidation hingegen langsamer verläuft als die tetraedrisch koordinierter Fe-Zentren. Fe_xO_y-Cluster werden im Vergleich zu isolierten Fe^{3+}-Spezies deutlich langsamer reduziert und schneller reoxidiert. Interessanterweise gleicht das Redoxverhalten isolierter Fe^{3+}-Spezies in clusterhaltigen Katalysatoren dem der Fe_xO_y-Cluster, da während der Calcinierung bevorzugt die leicht reduzierbaren Fe-Spezies zu Clustern agglomerieren während die reduktionsstabilen isoliert bleiben. Im Gegensatz zu Fe^{3+}-Spezies in den Poren konnte für solche, die während der Hydrothermalsynthese auf Gitterplätzen der Zeolith-Struktur eingebaut werden, unter gleichen Bedingungen keine Reduzierbarkeit festgestellt werden.

Struktur-Reaktivitäts-Beziehungen in der SCR von NO mit Isobutan und NH_3

Ein Vergleich des katalytischen Verhaltens verschieden präparierter Fe-ZSM-5-Katalysatoren mit dem aus UV/VIS-Untersuchungen abgeleiteten relativen Anteil isolierter und clusterförmiger Fe-Spezies hat gezeigt, dass Aktivität und Selektivität im unteren Temperaturbereich der Isobutan-SCR hauptsächlich durch isolierte Fe-Spezies und kleine, oligonukleare Fe_xO_y-Cluster in den Poren getragen wird, während große Oxidpartikel, zumindest in der Isobutan-SCR, inaktiv sind. Mit steigender Temperatur wirken die Fe_xO_y-Cluster aufgrund ihrer schnellen Reoxidierbarkeit zunehmend unselektiv und führen zur Totaloxidation des Reduktionsmittels. Die besten Katalysatoren für die Isobutan-SCR sind deshalb solche mit vorzugsweise isolierten Fe-Zentren (MR- und ILIE-Proben mit geringem

Fe-Gehalt). Die unerwünschte Totaloxidation ist bei der NH_3-SCR deutlich weniger ausgeprägt, weshalb hier die Aktivität mit dem Anteil zugänglicher Fe-Spezies zunimmt.

Anhand der Ergebnisse spektroskopischer in situ-Untersuchungen kann eine weitere Differenzierung zwischen den an der Reaktion mitwirkenden Fe-Spezies vorgenommen werden. So wurde mittels in-situ-FT-IR gefunden, dass NO vorzugsweise an oxidierten Fe^{3+}-Spezies über Nitrat-Intermediate aktiviert wird, während reduziertes Fe^{2+} dazu kaum in der Lage ist. Dies deutet darauf hin, dass Fe^{3+}-Ionen, die unter SCR-Bedingungen irreversibel reduziert werden (EPR-Signal bei g' ≈ 6), möglicherweise nur Spektator-Spezies sind, während die katalytische Aktivität durch oxidiertes Fe^{3+} (EPR-Signal bei g' ≈ 2 und z. T. bei 4.3) getragen wird. Die beobachtete höhere Aktivität der Katalysatoren in der NH_3-SCR wird auf die im Vergleich zur Isobutan-SCR deutlich geringere Reduktion der Fe-Spezies im Gleichgewicht zurückgeführt.

Struktur-Reaktivitäts-Beziehungen in der SCR und direkten Zersetzung von N_2O

In Analogie zur SCR von NO wird auch die SCR von N_2O mit CO durch isolierte und oligonukleare Fe-Spezies katalysiert, offensichtlich aber nach unterschiedlichen Mechanismen. Isolierte, tetraedrische Fe^{3+}-Spezies werden durch CO kaum reduziert. Es wird angenommen, dass letzteres im adsorbierten Zustand mit N_2O unter Bildung von CO_2 und N_2 reagiert. Hingegen werden oktaedrische Fe^{3+}-Spezies und Fe_xO_y-Cluster durch CO reduziert und durch N_2O unter Bildung von N_2 reoxidiert. Im Gegensatz zur SCR von N_2O sind Katalysatoren mit überwiegend isolierten Fe-Zentren für die direkte N_2O-Zersetzung deutlich weniger aktiv, da die Rekombination von an isolierten Fe-Zentren adsorbiertem O zu O_2 gehindert ist.

Einfluss von Acidität und Porenstruktur auf die Reaktivität der Katalysatoren

Katalysatoren mit MFI-Struktur, vergleichbarem Fe-Gehalt und überwiegend isolierten Fe-Spezies, jedoch stark verschiedener Acidität (Fe-ZSM-5 hergestellt durch ILIE und Fe-Silikalith hergestellt durch ex-HS) zeigten ähnliche katalytische Aktivität in der Zersetzung und SCR von N_2O mit CO, was darauf hindeutet, dass beide Reaktionen keine aziden Zentren erfordern. Im Unterschied dazu ist der deutlich azidere Fe-ZSM-5-Katalysator in der SCR von NO wesentlich aktiver. Dies veranschaulicht die Bedeutung azider Zentren für diese Reaktion.

In dieser Arbeit ist es gelungen, einen mesoporösen Fe-SBA-15-Katalysator mit vergleichbarer Menge von praktisch ausschließlich isolierten Fe^{3+}-Spezies identischer Struktur und vergleichbarer (sehr geringer) Acidität herzustellen. Dadurch ist erstmals eine explizite Bewertung des Poreneinflusses möglich. Im Gegensatz zu Fe-Silikalith ist Fe-SBA-15 sowohl in der SCR von NO als auch in der SCR von N_2O deutlich weniger aktiv. Dies zeigt, dass eine hohe Dispersität von Fe-Zentren ein notwendiges, aber kein hinreichendes Kriterium für hohe SCR-Aktivität ist. Optimale Porendimensionen sind ebenfalls erforderlich, um einen ausreichenden Kontakt zwischen aktiven Zentren und Reaktant-Molekülen zu ermöglichen. Dies ist in den Mesoporen von Fe-SBA-15 offensichtlich nicht gegeben.

SUMMARY

Introduction and Objectives

The abatement of nitrogen oxides including NO, NO_2 and N_2O is essential before being discharged from their sources such as lean-burn Otto engines, chemical plants etc. Since, they contribute to ozone layer depletion, greenhouse gas effect, acid rain and smog. Hence, emission regulations for nitrogen oxides are becoming more and more stringent all over the world. The available catalytic technologies (e.g., Selective Catalytic Reduction (SCR), direct catalytic decomposition etc.) reduce nitrogen oxides from lean conditions to a great extent. However, catalysts which have been in use so far for these technologies are inadequate and vary in their reduction efficiency in different sources. Differently, Fe-zeolites, in particular Fe-MFI shows high activity, selectivity and durability for reducing nitrogen oxides under lean conditions from various sources. However, this type of catalytic system is not yet developed for practical applications. This mainly is due to the fact that the structure of the Fe sites in Fe-MFI zeolites and their catalytic role are not yet clearly known. Also, the structure of the adsorbed NO_x species is not unambiguous. Thus, the understanding of the structure of Fe sites in differently prepared Fe-MFI and their catalytic role in the abatement of nitrogen oxides is crucial for optimization of this catalytic system to be considered for practical applications.

Hence, the goal of this work is to elucidate the structure of iron oxo sites formed by different preparation routes using EPR and UV/VIS-DR spectroscopy, which can distinguish between isolated Fe species of different structure on the one hand and between Fe_xO_y clusters of different nuclearity on the other hand. The influence of the pore structure (micro and meso) of the support on the nature and distribution of the Fe species has been studied. The redox properties of different Fe species and their catalytic role in the SCR of NO, N_2O and N_2O decomposition have been investigated by in situ-UV/VIS-DRS and -EPR. In situ FT-IR spectroscopy has been used to give more insights into the structure of adsorbed NO_x species and the structure of possible reaction intermediates in the SCR of NO.

Experimental

Differently prepared (Chemical Vapor Deposition (CVD), Solid-State Ion Exchange (SSIE), Mechanochemical Route (MR), Conventional Liquid Ion Exchange (LIE), Improved Liquid Ion Exchange (ILIE) and Hydrothermal synthesis followed by steam activation) Fe-MFI and Fe-beta samples have been provided by the cooperation partners, Prof. Dr. W. Grünert and Prof. Dr. Javier-Perez Ramirez. Fe-SBA-15 was prepared by impregnation method within this thesis work at ACA Berlin. The samples have been tested for SCR of NO with NH_3 and isobutane as well as for direct decomposition of N_2O and SCR of N_2O with CO at the laboratories of the cooperation partners.

The nature and distribution of Fe species in Fe-catalysts were investigated by UV/VIS-DRS and EPR after synthesis, calcination, steaming and use in catalysis as well as in situ during calcination. Iron redox properties of different isolated Fe^{3+} species and $Fe^{3+}{}_xO_y$ clusters have been studied by UV/VIS-DRS to evaluate the impact of different Fe species on the reactions.

The surface acidity was investigated by pyridine adsorption monitored by FT-IR. The interaction of NO with oxidized and reduced Fe species was also studied by FT-IR. The behavior of different Fe species in Fe-catalysts under true reaction conditions was investigated by in situ UV/VIS-DRS, in situ EPR and in situ FT-IR to derive structure activity relationships.

Results and Discussion

Structure, distribution and redox behaviour of Fe sites and surface acidity of the Fe-catalysts

From EPR results it was found that almost all samples contain at least two kinds of strongly distorted isolated Fe^{+3} ions, probably in tetrahedral and higher coordination as reflected by EPR signals at g' ≈ 4.3 and g' ≈ 6. A third kind of isolated Fe^{+3} ions in less distorted environment contributes to the EPR signal at g' ≈ 2. However, iron oxide clusters also contribute to this signal which was distinguished by temperature dependent signal behavior. In UV/VIS-DRS isolated Fe^{3+} sites of different coordination geometry (tetrahedral and octahedral) rather than distortion of the site is reflected by two charge transfer (CT) bands below 300 nm. CT bands above 300 arise from iron oxide clusters of different sizes.

The influence of the mode of Fe insertion: The results of UV/VIS-DRS and EPR clearly show that the distribution of iron species, as isolated iron ions, oligomeric iron oxo species and iron oxide particles, is a function of the sample genesis. Thus, it was found that all preparations lead to the coexistence of different iron species. However, MR, ILIE at low Fe content and hydrothermal synthesis at low Al content followed by steam activation are the most effective techniques to prepare highly dispersed Fe species as isolated iron ions. Similarly, SBA-15 favours the formation of highly dispersed, almost exclusively isolated Fe species upon incipient wetness preparation. No doubt CVD and SSIE are also effective to produce considerable amount of isolated Fe sites but cluster formation cannot be avoided. Contrarily, conventional LIE produces preferably large iron oxide clusters besides small amount of isolated Fe sites.

The nature and distribution of iron species depending on the washing (1 or 10 l of water per 5 g catalyst) and calcination (heating rate 0.5 or 5 K/min) procedure, Al content of the parent zeolite matrix (Si/Al ≈ 14 or 40) and use in the SCR reaction were studied for samples prepared by CVD. The high washing intensity (10 l) and low heating rate (0.5 K/min) during calcination suppress the formation of large iron oxide clusters slightly. Low Al content in the H-ZSM-5 support (Si/Al ≈ 40) favors iron aggregation, however after calcination the cluster size is somewhat restricted by being trapped in the silanol nests compared to the Al rich support (Si/Al ≈ 14). By comparing the calcined samples before and after use in SCR of NO with isobutane it is evident that during catalysis structural changes do take place and form large clusters from small ones.

In situ UV/VIS-DRS shows that the framework Fe^{3+} species either in the MFI or in the beta are well shielded in the zeolite framework and are not reduced upon reductive treatment with 20 vol.% H_2/Ar at 773 K for 1 h.

Studies of the time dependence of reduction and reoxidation at 673 K by UV/VIS-DRS show that in cluster free samples, extraframework isolated Fe^{+3} ions in tetrahedral and octahedral coordination possess different redox properties. The former species are slightly slowly reduced and fastly reoxidized while the latter species are relatively fastly reduced but only slowly reoxidized. In contrast, iron oxide clusters are hardly reduced and very fastly reoxidized in cluster containing samples. Interestingly, Fe^{3+} sites that remain isolated in samples dominated by Fe_xO_y clusters, change their redox behaviour and become highly reduction resistant in comparison to those in samples without oxide clusters.

Brønsted acidity of the samples decreases with increasing Si/Al ratio as evidenced by FT-IR studies of adsorbed pyridine over catalysts with different Si/Al ratio (Si/Al≈14 *vs.* 40). It was also found that iron oxide clusters provide additional Lewis acidity.

Studies on the behavior of Fe sites in the presence of feed components by in situ techniques

Under typical NH_3 and isobutane-SCR conditions, the different isolated iron ions show a different sensitivity versus reduction/reoxidation. Accordingly, in cluster free samples isolated Fe^{3+} ions are partially reduced under steady-state SCR conditions, however, to different extents. Octahedral Fe^{3+} reflected by EPR signals around g' ≈ 6 and a UV/VIS band around 290 nm are the most sensitive to reduction followed by tetrahedral Fe^{3+} (g' ≈ 4.3, 240 nm) while Fe^{3+} ions evidenced by the EPR signal at g' ≈ 2, for which the coordination geometry cannot be easily specified, are hardly reduced. With increasing Fe content, the amount of these hardly reducible isolated Fe^{3+} sites increases as evidenced by a comparison of the UV/VIS intensity below 300 nm under steady-state conditions. In situ FT-IR results revealed a preferred reaction of NO with oxidized Fe^{3+} species. Thus, it is possible that among the isolated Fe species, it might be just the hardly reducible Fe^{3+} ions which play an active role in the SCR reaction. This is also supported by the fact that in used Fe-ZSM-5 catalysts the g' ≈ 6 signal disappeared completely, however, no deactivation was observed during the SCR reaction. Since the amount of hardly reducible isolated Fe increases with rising Fe content, it is not surprising that the activity of the Fe-samples has been observed to increase, too. In situ FT-IR studies show that isobutane-SCR of NO reaction over Fe-ZSM-5 mainly proceeds via nitriles, cyanates and/or isocyanates. Interestingly, the formation of nitriles, cyanates and/or isocyanates seem to proceed preferentially on isolated Fe sites, the amount of which increases from sample A(ILIE)0.2 to A(ILIE)1.2. Therefore, it can be regarded as another reason for the superior catalytic performance of isolated Fe sites in the isobutane-SCR.

However, attempts to correlate the rate of the SCR reaction with the number of Fe sites in the Fe-catalysts show the involvement of isolated Fe ions and oligonuclear Fe_xO_y clusters in both SCR reactions. Additionally, it was found that in NH_3-SCR probably even Fe ions accessible on the surface of oxide particles also participate. In situ UV/VIS studies including those of the redox kinetics have shown that Fe_xO_y clusters are much faster reoxidized than isolated Fe sites and, thus, can immediately enter in another redox cycle. It is therefore plausible to assume that they contribute to the selective catalytic process at lower reaction temperature, too. At higher temperature these agglomerates, due to their higher oxidation potential in

comparison to isolated Fe^{3+} species, give rise to unselective total oxidation of the reductant, thus, limiting the temperature window of selective NO reduction. This effect is much more pronounced for isobutane-SCR since Fe_xO_y clusters oxidize the isobutane to CO_x already at temperatures as low as 623 K, whereas in NH_3-SCR they are selective up to temperatures of about 700 K. This is also evident from carbonyl-containing species detected by in situ FT-IR preferentially on cluster containing A(ILIE)1.2 but not on cluster free A(ILIE)0.2. These species are regarded as intermediates in the total oxidation of isobutane. As a result of this unselective oxidation behaviour of the Fe_xO_y agglomerates, the NO conversion drops dramatically above 600 K in case of isobutane. Hence, the catalyst performing best in this reaction (A(ILIE)0.3) is almost void of clusters. With the NH_3 reductant, the unselective attack occurs at much higher temperature and to a much lower extent. Thus, the limitation of the selective temperature region is of little practical importance. Hence, the best catalyst for NH_3-SCR was the one with the highest number of accessible Fe sites (A(ILIE)1.2).

The acidity of the zeolite is essential for both NH_3 and isobutane-SCR as evidenced by the catalytic performance of cluster free *ex*-Fe-silicalite and A(ILIE)0.3 and cluster containing B(CVD,W1,C5) with Si/Al ≈ 40 and A(ILIE)1.2 with Si/Al ≈ 14. By comparing the catalytic performance of *ex*-Fe-silicalite (microporous) and (Fe-SBA-I)0.95 (mesoporous) it is evident that the microporous structure of the Fe-catalysts is favorable for the SCR of NO than the mesoporous materials.

Decomposition and SCR of N_2O with CO: By correlation of the decomposition and reduction of N_2O activities with different iron species detected by UV/VIS-DRS it was found that in direct N_2O decomposition oligomers are preferred over isolated Fe^{3+} ions in view of the easier oxygen recombination (rate determining step in the process) of two iron centers that are close together. Hence, the best catalyst for the decomposition of N_2O was the one with high amounts of oligomers, A'(CVD,W1,C2).

For SCR of N_2O by CO, isolated Fe^{3+} are the active iron centers. The importance of the mononuclear iron sites in the reduction of N_2O by CO was strongly evidenced by the high specific activity of A(ILIE)0.2 and *ex*-Fe-silicalite, with a remarkable uniform distribution of isolated iron ions. Furthermore, a correlation between the N_2O conversion and the fraction of isolated Fe^{3+} ions in the catalysts was found. In situ UV/VIS-DRS and EPR studies further evidenced the participation of mononuclear iron ions in the SCR of N_2O with CO, however, they also support the involvement of oligomeric species. The interaction of N_2O and CO and the reaction mechanism is iron site dependent. Over tetrahedral isolated iron sites, which are coordinatively unsaturated and, thus, can extend their coordination sphere, the reduction of N_2O with CO occurs via coordinated CO species on Fe^{3+} ions, not involving change of oxidation state. In contrast, octahedrally coordinated isolated Fe^{3+} sites convert N_2O in the presence of CO by involving a Fe^{3+}/Fe^{2+} redox process. The reaction over oligomers proceeds, too, via a redox Fe^{3+}/Fe^{2+} process and involves the intermediate formation of O^- radicals.

The acidity of the zeolite has no affect on both the decomposition and SCR of N_2O reactions as evidenced by the catalytic performance of *ex*-Fe-silicalite (Si/Al ≈ ∞) and A(ILIE)0.2 (Si/Al ≈ 14). In contrast, pore structure of the Fe-catalyst strongly influences the catalytic activity as shown by *ex*-Fe-silicalite and (Fe-SBA-I)0.95. Additionally, *ex*-Fe-ZSM-5

and *ex*-Fe-beta with similar pore structure show similar activity in both SCR and decomposition of N_2O. Thus, it was found that microporous structure such as MFI is more favorable than mesoporous material.

Conclusions

The UV/VIS and EPR spectroscopic investigation of Fe-micro and mesoporous materials showed that the preparation method, framework composition of the support and pretreatment conditions determine the nature and distribution of Fe species in the final catalyst. In situ-UV/VIS, -EPR and -FT-IR studies under typical SCR of NO, N_2O and N_2O decomposition show relationships between the nature of active Fe sites and the catalytic performance. Thus, from this study the following structure activity relationships can be drawn:

- SCR of NO with isobutane and NH_3: isolated Fe sites are efficient active sites for both the reactions. However, oligomeric species also contribute to the reactions at lower temperatures. Due to their higher oxidation potential, at high temperatures they cause undesired total oxidation of the reductant being much more severe in the case of isobutane than NH_3. Thus, oligomers drastically deteriorate the activity in isobutane-SCR while they play a constructive role, to some extent, in NH_3-SCR.
- The strong Brønsted and Lewis acidity is required for both the SCR reactions.
- SCR and direct decomposition of N_2O: for SCR of N_2O isolated Fe sites are more effective, while for decomposition highly dispersed oligomeric moieties are preferred.
- Acidity of Fe-catalysts is not mandatory for both SCR and decomposition of N_2O.
- Studies on the microporous *ex*-Fe-silicalite and mesoporous (Fe-SBAI)0.95 show that the latter supports are only suitable for high Fe dispersion but their pore structure is not suitable for catalytic activity (SCR of NO, N_2O and N_2O decomposition). Thus, the confinement of the iron species in the microporous material is essential to facilitate intimate contact between active Fe sites and reactants.

TABLE OF CONTENTS

1.	**Introduction and Objectives**	**1**
2.	**State of the art**	**4**
2.1	Catalytic abatement of nitrogen oxides from exhaust gases	4
2.1.1	Removal of NO	6
2.1.2	Removal of N_2O	8
2.2	Synthesis strategies and activity of Fe-zeolites	10
2.2.1	Liquid ion exchange (LIE)	10
2.2.2	Sublimation of $FeCl_3$ into the pores (CVD)	13
2.2.3	Solid state ion exchange (SSIE)	14
2.2.4	Other preparation techniques	14
2.3	Structure-reactivity relationships in Fe-zeolites	15
2.3.1	Structure-reactivity relationships in the SCR of NO	16
2.3.2	Structure-reactivity relationships in the decomposition and SCR of N_2O	17
2.4	Physico-chemical techniques for the characterization of Fe-containing zeolites	18
2.4.1	EPR spectroscopy and spectra evaluation	19
2.4.2	UV/VIS-Diffuse Reflectance Spectroscopy (DRS) and spectra evaluation	21
2.4.3	Fourier Transformed Infra Red (FT-IR) spectroscopy	23
2.4.4	Other spectroscopic techniques	25
3.	**Experimental**	**29**
3.1	Synthesis of Fe-containing zeolites	29
3.1.1	Microporous Fe-MFI and Fe-beta zeolites	29
3.1.2	Mesoporous Fe-SBA-15	31
3.2	Characterisation of the catalysts	32
3.2.1	EPR spectroscopy	32
3.2.2	UV/VIS-DR spectroscopy	34
3.2.3	FT-IR spectroscopy	35
3.3	Catalytic tests	36
4.	**Results**	**38**
4.1	Structure, distribution and redox behaviour of Fe species and surface acidity of the Fe-zeolites	38
4.1.1	UV/VIS-DRS studies	38
4.1.2	EPR studies	53
4.2	Analysis of acidic properties of Fe-zeolites by FT-IR investigation of adsorbed pyridine	68
4.3	Studies on the behaviour of Fe species in the presence of feed components by in situ techniques	

4.3.1 EPR, UV/VIS/DRS and FT-IR spectroscopic studies during interaction of NH_3, NO and SCR of NO with NH_3 74
4.3.2 EPR, UV/VIS/DRS and FT-IR spectroscopic studies during SCR of NO with isobutane 87
4.3.3 EPR and UV/VIS-DRS spectroscopic studies during decomposition and SCR of NO with CO 96
4.4 Catalytic behaviour 104
4.4.1 SCR of NO with NH_3 and isobutane 105
4.4.2 Decomposition and SCR of N_2O with CO 109

5. Discussion 114
5.1 Influence of synthesis conditions and SCR reaction on the nature of Fe species 114
5.1.1 Mode of Fe incorporation 114
5.1.2 Washing intensity 118
5.1.3 Calcination procedure 118
5.1.4 Al content and defect density of the parent zeolite matrix 119
5.1.5 Use in the SCR reaction 119
5.2 Structure-reactivity relationships in Fe-containing zeolites 120
5.2.1 Low temperature interaction of NH_3 and NO with Fe-ZSM-5 zeolites 120
5.2.2 SCR of NO with NH_3 and isobutane 122
5.2.3 Decomposition and SCR of N_2O with CO 127

6. Conclusions 133

7. References 138

1. Introduction and Objectives

Nitrogen oxides, NO_x (NO and NO_2) and N_2O, are noxious air pollutants in the atmosphere, contributing to ozone layer depletion, greenhouse effect, smog and acid rain [1-30]. The chief sources of NO_x are automobiles, lean-burn diesel engines, fossil and fuel-fired power plants, etc [1-6], while N_2O is mainly released from industrial processes such as nitric acid and caprolactam production, etc [7,8]. Therefore, many efforts have been made world wide to reduce NO_x and N_2O emissions from mobile and stationary sources.

For stationary sources, the selective catalytic reduction of NO_x with NH_3 (NH_3-SCR) over vanadia-based catalysts is commercially applied since a long time [3,26-30]. However, the respective V_2O_5/TiO_2 and V_2O_5-WO_3/TiO_2 catalysts used for this process work optimally only in a narrow temperature range (573–673 K), while they are not active enough at lower temperature and at higher temperature they oxidize the reduction agent NH_3 and deactivate irreversibly. Therefore, much effort has been dedicated in recent years to develop catalysts that are suitable, too, for the low and high temperature range to gain more flexibility for the application of SCR devices in exhaust gas flows, whereby hydrocarbons have been frequently used as reducing agents (HC-SCR). For mobile sources, this has the advantage that no NH_3 source has to be maintained on board.

For the abatement of N_2O from tail gases, direct catalytic decomposition of N_2O into N_2 and O_2 is an attractive and cost effective catalytic technology. Alternatively, SCR of N_2O is also an effective method for N_2O abatement. However, catalysts proposed in the literature so far (e.g. supported transition (Cu, Co, Ni) and noble (Rh, Ru, Pd) metal based catalysts) were frequently not active and stable enough under realistic conditions, i.e. in the presence of other components such as O_2, NO_x, and H_2O in the flue gases [8].

Zeolites containing extra-framework Fe species, in particular those of the MFI type, revealed to be highly promising catalysts for the catalytic abatement of both NO_x [31-36] and N_2O [37-54]. Nevertheless, marked differences in their catalytic activity have been observed which are most likely due to the highly heterogeneous structure of Fe sites in these materials. This is mainly due to the fact that in most cases, depending on the preparation method and the Fe content, a variety of coexisting Fe species is created, ranging from isolated Fe ions via dimers and small oligonuclear Fe_xO_y clusters inside the pores to large Fe_2O_3 particles on the external surface. The inhomogeneous distribution of Fe species is a major problem for a doubtless identification of active sites. Detailed knowledge about the structure of Fe sites and their function in the catalytic NO_x and N_2O abatement process could open new ways for the development of highly active and stable catalysts.

The objective of this work comprises three main aspects:

1) Identification of the structure and redox properties of extra-framework Fe sites in differently prepared Fe-containing microporous materials (Fe-MFI) in dependence on peculiarities of the synthesis procedure and the composition (Si/Al ratio) of the MFI matrix.

2) Elucidation of the influence of the pore network structure on the nature and redox properties of the Fe sites. For this purpose Fe-silicalite and Fe-SBA-15 have been compared
3) In situ studies of selected catalysts with known Fe site structure in the presence of reactants used in the SCR of NO with NH_3 and isobutane, as well as in the direct decomposition and SCR of N_2O by CO, at elevated temperatures to distinguish the role of different Fe species in the reaction mechanism
4) Correlation of the obtained results with the results of catalytic tests (performed in the laboratories of our cooperation partners) to derive structure-reactivity relationships for the abatement of NO_x and N_2O.

Considerable research has been performed in recent years by several groups using a multitude of characterization techniques, among them XAS, TPR, voltammetry, Mössbauer and FT-IR spectroscopy. However, it turned out that a reliable identification of the different Fe species coexisting in these materials and, in particular, their relative quantities, is not straightforward because the sensitivity of the techniques for the various types of Fe species differs. Thus, it was found that EXAFS, being one of the most frequently used techniques, is highly sensitive for isolated Fe sites while it underestimates the presence of the Fe_xO_y clusters [43,55]. Moreover, the doubtless identification of particular species such as iron dimers [56,57] seems questionable in systems with different coexisting Fe species since EXAFS gives average values for coordination numbers and bond distances. In contrast, Mössbauer and TPR measurements indicated a much larger degree of clustering than was found by EXAFS [43,55].

Therefore, EPR and UV/VIS spectroscopy have been selected in this work to reach objective 1). EPR spectroscopy is a powerful tool to identify isolated Fe^{3+} species of different coordination geometry by the position of their signals [55,58-63] as well as Fe_xO_y cluster species of different degree of aggregation by analysis of the mutual magnetic interactions of the Fe sites [55,64,65]. UV/VIS spectroscopy, on the other hand, is especially sensitive to charge-transfer (CT) bands of Fe^{3+}, the wavelength of which depends on the coordination number and the degree of aggregation [55,60,66]. By combining investigations with both techniques, progress in discriminating between different coexisting Fe species in the same matrix was expected.

The remarkable activity of Fe-MFI zeolites is motivating the research community to study the role of different Fe species in SCR of NO, N_2O and N_2O decomposition for further development of this catalyst. To this end, some efforts have been dedicated using in situ spectroscopic techniques under true reaction conditions. However, most of the studies were done by in situ FT-IR spectroscopy to derive reaction mechanism rather than active sites. A very few studies dealing with changes in oxidation and coordination state of Fe species under SCR of NO are reported. However, the findings are not consistent. Despite severe drawbacks of EXAFS, it being very sensitive to isolated Fe sites and giving only average values for coordination numbers and bond distances (see also above), Koningsberger et al. have used this technique in situ to study the changes in the oxidation and coordination states of Fe species under isobutane-SCR of NO [35]. Based on these studies, the authors attributed the SCR

activity of Fe-ZSM-5 merely to Fe-O-Fe dimers. In contrast, Kucherov et al. concluded from in situ EPR studies, performed during propene-SCR of NO, that coordinatively unsaturated isolated Fe sites reflected by EPR signals at g' ≈ 5.6 and 6.5 are the only active Fe sites in Fe-ZSM-5 [59]. However, the authors did not discuss the role of other Fe sites reflected by EPR signals at g' ≈ 4.3 and 2.

Moreover, only little is known whether the different coordination state of Fe species in Fe-ZSM-5 give rise to alterations of the reduction and reoxidation behaviour which should be a crucial property in view of their participation in the catalytic redox cycle. Thus, it is an open question whether differently coordinated isolated Fe sites and iron oxide clusters of different nuclearity (including dimers) are participating equally in the catalytic cycle. Therefore, in the present study an effort is made to give more insights into the nature of active Fe sites for SCR of NO, N_2O and N_2O decomposition by in situ EPR, in situ UV/VIS-DR and in situ FT-IR spectroscopy. In situ EPR and in situ UV/VIS-DRS techniques are especially suitable since they provide simultaneous information on the oxidation and coordination state of Fe spices.

This thesis is part of a joint research project sponsored by Deutsche Forschungsgemeinschaft which was performed in cooperation with Prof. W. Grünert (Ruhr-University Bochum) and Prof. J. Pérez-Ramírez (Catalan Institution for Research and Advanced Studies, Tarragona). Parts of the work (synthesis of most catalysts, catalytic tests) have not been performed within this thesis but in the laboratories of our cooperation partners. This is denoted in the respective sections below. Based on the integrated evaluation of the characterization results obtained in this thesis including a comparative discussion of catalytic tests performed by the project partners, general features on the structure of Fe sites and their role in the catalytic reactions could be derived.

2. State of the Art

2.1 Catalytic abatement of nitrogen oxides from exhaust gases

Nitrogen oxides such as NO, NO_2 (NO_x) and N_2O are noxious air pollutants in the atmosphere [1-30] produced by both natural and anthropogenic sources. However, the latter contribute approximately 75% of the total amount of NO_x and N_2O emitted into the atmosphere. The major anthropogenic sources can be classified as:

1) Mobile sources such as spark ignition automobiles, lean-burn diesel engines, locomotives etc.
2) Stationary sources such as fossil and fuel-fired power plants, waste incinerators, industrial ovens, chemical processes such as nitric acid plants etc.

NO_x released into the atmosphere contributes to ozone depletion and smog and reacts with O_2 and moisture to form nitric acid that leads to acid rain [1,2,4-6].

N_2O is a greenhouse gas [7,8], since it strongly absorbs infrared radiation in the atmosphere. Moreover, it has a much higher Global Warming Potential (GWP) than other greenhouse gases such as CO_2 and CH_4 [7,8].

Legislations for the emission of nitrogen oxides, unburned hydrocarbons and particulates from mobile and stationary sources are becoming more stringent all over the world. Thus, the abatement of NO_x and N_2O from exhaust gases is essential to reach those legislation standards and also for a clean and healthy global environment. Catalytic methods for the reduction of nitrogen oxides offer a rational solution to the problem. The best available catalytic technologies for the reduction of NO_x and N_2O emission can be divided into three categories [1,8,9]: (1) selective catalytic reduction, (2) direct decomposition and (3) non-selective catalytic reduction.

For NO_x, this is achieved by Selective Catalytic Reduction (SCR) using NH_3 or hydrocarbons as reducing agents in the case of stationary or mobile emission sources respectively, while N_2O can be removed from exhaust gases by both SCR and direct decomposition. A number of catalysts have been tested so far [5,10,11-25] which can be classified into three groups: supported metal oxides, noble metals and zeolites containing transition metal ions [21,22]. Among the various metal oxide catalysts [5,11-17], V_2O_5 supported on anatase TiO_2 and promoted with either WO_3 or MoO_3 is commercially used for stationary emission sources since many years [3,26-30], though this system is not without problems [4]. Thus, despite a rather high resistance of this catalyst to SO_2 poisoning, deactivation does take place at high concentrations of SO_2 and ash in the flue gas. Moreover, this catalyst has high activity for oxidation of SO_2 to SO_3 which can react with slipped NH_3 at high temperatures giving rise to ammonium salts that cause fouling and corrosion problems in the downstream equipment. To avoid these problems, the SCR unit should be placed downstream, in the tail-end, but there, the flue gas temperature drops below 423 K. This is too low for the SCR reaction and requires reheating to the typical SCR operating temperatures, which makes the overall operation very expensive. Furthermore, these catalysts are not suitable for lean-burn diesel and gasoline engines since they are not active at low temperatures and at high temperatures they promote unselective total oxidation of reducing agents. Hence, there is a strong need for the development of an efficient, economic and eco-friendly SCR catalyst that

should be active over a wide temperature range, be resistant towards SO_2 and water, have a long life with relatively low cost and should not be a problem for the disposal of the used catalyst.

Therefore, many efforts have been devoted to develop inexpensive low temperature SCR catalysts and a variety of catalysts have been proposed in the literature, among them mixed Fe-Mn oxides [23], supported MnO_x-CeO_2 [24], and recently supported Mn_xO_y-TiO_2 (anatase) [4]. These catalysts have shown potential low temperature NH_3-SCR activity and do not have the deficiencies that are associated with the commercial vanadia based and noble metal oxide catalysts [4,23,24]. Hence, they could be potential candidates for low temperature NH_3-SCR catalysts for stationary sources in the future.

Another group of catalysts are noble metal oxides such as Pt supported on Al_2O_3 which exhibits the best low temperature SCR activity in comparison to other metals. Though they are more resistant against H_2O and SO_2 poisoning [25], they have other drawbacks such as high prices, formation of substantial quantities of N_2O and a narrow temperature window for NO reduction [25].

Zeolites containing transition metal ions are the third type of catalysts [2,10,31-36,67-73]. Many reasons were suggested in the literature for the superior performance of zeolites, in particular ZSM-5 zeolite as a support for SCR of NO_x and N_2O decomposition. These include the fact that the highly dispersed transition metal oxo-cations in the zeolite channels are accessible, possess a high degree of coordination of unsaturation and are in the appropriate oxidation state [74-78].

In the series of metal ion exchanged zeolites Cu- and Co-zeolites were extensively studied. In particular, the Cu-ZSM-5 system is very well studied for both NH_3- and hydrocarbon-SCR of NO because of its promising catalytic activity [67-71]. Unfortunately, it is not resistant to deactivation by H_2O and SO_2 [73,79-81]. Co-zeolites are active only at higher temperatures, being not suitable for practical applications and are sensitive (mainly at lower temperatures) to H_2O and SO_2 [10]. Fe-containing zeolites have got a great deal of attention due to their high activity in a wide temperature window and their stability even in the presence of H_2O and SO_2 [2,31,37,73].

A great variety of catalysts including metals, pure and mixed oxides and zeolitic systems have been reported for the decomposition or SCR of N_2O [38-43]. Abatement of N_2O emissions in chemical plants (eg. Nitric acid plants) is a challenging task since exhaust gases contain other components such as O_2, NO, CO_2, SO_2 and H_2O which can reduce the catalyst performance or even cause deactivation [40,41]. Fe-zeolites have attracted much attention for the abatement of N_2O emissions, too, from chemical plants because of its insensitivity to O_2, NO, CO_2, SO_2 and H_2O [42,43,82]. Moreover, NO and SO_2 enhance the catalysts performance in direct N_2O decomposition, while O_2 and CO_2 do not [41]. Differently, H_2O considerably inhibits the decomposition of N_2O but only in the absence of other extra gas components (O_2, NO, CO_2 and/or SO_2) [41]. Hence, a variety of Fe-containing zeolites including Fe-ZSM-5 [44,45,48,53], Ferrierite (FER) [44,46,47,53], Mordenite (MOR) [44,45,46,48,53], beta [44,46,48,50], Faujasite (FAU) [48,49], Y [40,44,45,53], Chabazite (CHA) [46], Cliniptilolite (HEU) [46], ZSM-11 [47], SBA-15 [51], SAPO-34 [54], HMS and MCM-41 [45,52] have been studied in both SCR of NO_x or N_2O and direct decomposition of N_2O [44-54].

However, in summary, it turns out that Fe-MFI zeolites belong to the best catalysts known for the abatement of both NO_x and N_2O. Understanding the corresponding reaction mechanism on this catalytic system can provide vital information for the development of this system and consequently, the corresponding abatement process. Considerable research has been devoted to the reaction mechanism of removal of NO_x and N_2O decomposition. Therefore, catalytic abatement of nitrogen oxides from exhaust gases is discussed with respect to the process for the removal of NO and N_2O over Fe-MFI zeolites with mechanistic insights.

2.1.1 Removal of NO

Selective catalytic reduction (SCR) of NO_x

The major anthropogenic sources for NO_x are power plants, stationary engines, lean-burn Otto engines, industrial boilers, process heaters, gas turbines, combustion of fuels, chemical industries etc. Emission gases from almost all of these sources contain an excess of O_2 and depending on the source, moisture and SO_2 can also be present. Under these conditions SCR of NO_x with a reducing agent is the best available technology for NO_x abatement. Typically, NH_3 has been used as a reducing agent in the SCR of NO_x due to its high selectivity towards reaction with NO in the presence of excess O_2 and the promoting effect of O_2 on the rate of this reaction. The stoichiometric NH_3-SCR of NO reaction can be written as:

$$4NO + 4NH_3 + O_2 \rightarrow 4N_2 + 6H_2O \quad (2.1)$$

This technology has been successfully used for stationary sources in industrially developed countries. The most commonly used catalytic system is V_2O_5/TiO_2-WO_3 or MoO_3. However, this catalytic system is not adequate and is associated with some problems as mentioned above (page 5). Promisingly, these can be greatly suppressed using Fe-ZSM-5 as a SCR catalyst [37,46,83].

The reaction mechanism of the SCR of NO with NH_3 has been extensively investigated over Fe or H-zeolites [37,46,84,85]. The schematic representation of this reaction mechanism is as follows.

1. Quick adsorption of gaseous NH_3 molecules on the Brønsted acid sites to form NH_4^+ ions with two or three hydrogen atoms bonded to the AlO_4 tetrahedra of ZSM-5 zeolite

$$2NH_{3\,(g)} + 2H^+ \rightarrow 2NH_4^+{}_{(ad)} \quad (2.2)$$

2. Simultaneously, NO is oxidized to NO_2 on Fe^{+3} sites in the presence of oxygen

$$NO_{(g)} + 1/2O_{2(ad)} + Fe^{+3}\ \text{sites} \rightarrow NO_{2(ad)} \quad (2.3)$$

3. One NO_2 molecule diffuses to two adjacent NH_4^+ ions to form an active complex

$$NO_{2(ad)} + 2NH_4^{+}{}_{(ad)} \rightarrow NO_2(NH_4^{+})_{2(ad)} \quad (2.4)$$

4. The active complex subsequently reacts with one molecule of NO to form N_2 and H_2O and regenerates two Brønsted acid sites:

$$NO_2(NH_4^{+})_{2(ad)} + NO_{(g)} \rightarrow 2N_{2(g)} + 3H_2O_{(g)} + 2H^{+} \quad (2.5)$$

In this process the oxidation of NO to NO_2 on Fe^{+3} sites was considered as the rate determining step [37].

However, NH_3-SCR technology is not successfully used for mobile applications such as lean burn Otto and gasoline engines due to the variety of the transient conditions, NH_3 slip and the complications of maintaining an on-board NH_3 source. Hence, an alternative hydrocarbon (HC)-SCR of NO_x was proposed for this purpose [1,67].

Hydrocarbon-SCR of NO

For this process there is no need to carry around an additional reductant just to reduce the NO_x from mobile engines since one could readily use the fuel (LPG or gasoline) to reduce NO_x emissions also. Fe-ZSM-5 appeared to be more efficient for this reaction than any other catalysts tested so far [31,36]. Although there are complicated sequences of the reaction, it can be simply described by the following equation:

$$NO + \text{hydrocarbon} + O_2 \rightarrow N_2 + CO_2 + H_2O \quad (2.6)$$

Considerable research has been done on the reaction mechanism of the SCR of NO with hydrocarbons over different zeolites and different reaction mechanisms involving different intermediates have been proposed [86-90]. Hence, the complicated multistep HC-SCR of NO reaction mechanism is simplified and generalized (for all hydrocarbons) as shown schematically below. Fe^{+3} ions play a major role in the HC-SCR of NO reaction. Though the structure is still at the debate stage, they are proposed as active iron centers for the oxidation of NO to NO_2 and NO_3^{-} (Eq. (2.7) and (2.8)) [86-89,91].

$$NO_{(g)} + 1/2O_{2(ad)} \xrightarrow{Fe^{+3}} NO_{2(ad)} \quad (2.7)$$

$$NO_{(g)} + O_{2(ad)} \xrightarrow{Fe^{+3}} NO_3^{-}{}_{(ad)} \quad (2.8)$$

These NO_2/NO_3^{-} species reacts with hydrocarbons to form N-containing deposits, the structure of which is ambiguous [86-89] and undergoes some subsequent rearrangements. These N-containing deposits are designated as active complex in the reaction.

$$NO_{x(ad)} + C_mH_{n(ad)} \rightarrow NO_xC_mH_{n(ad)} \quad (2.9)$$

NO_2 reacts with N-containing deposits to produce N_2, CO_x and H_2O.

$$NO_xC_mH_{n(ad)} + NO_{2(g)} \rightarrow N_2 + yCO_p + zH_2O \quad (2.10)$$

Non-selective catalytic reduction of NO_x

Non-selective catalytic reduction of NO_x is an interesting technology from the practical point of view since, in this process the combustion gases such as CO and unburned hydrocarbons can be used as reducing agents for the abatement of NO_x. Consequently, harmful emission gases (CO, NO_x and hydrocarbons) will be cleaned off before being discharged into the atmosphere hence, this process is called as three way catalysis and the catalyst is called as three way catalyst (TWC) [1,9].

Using Pt, Pd and Rh based catalysts this technology has been successfully implemented in the combustion automobile applications for the abatement of NO_x. However, under O_2 rich conditions this process is not effective, since O_2 competes with NO_x to react with combustible gases. Consequently this technology is not suitable for lean-burn applications such as diesel engines. For the latter applications hydrocarbon-SCR of NO_x with Fe-ZSM-5 could be the best process.

Direct catalytic decomposition of NO

Direct catalytic decomposition of NO into its elements is an attractive and economical approach to reduce NO emissions since it does not demand the use of a reductant and avoids undesired emissions and slip of reductants. Unfortunately, none of the catalysts proposed in the literature shows a good activity and stability in direct NO decomposition under true reaction conditions.

2.1.2 Removal of N_2O

Direct catalytic decomposition of N_2O

The steamed Fe-ZSM-5 attracted much attention in recent years due to its significant activity, stability and durability in the direct N_2O decomposition under realistic conditions, that means, in the presence of O_2, NO, H_2O and with high space velocities. Moreover, the potential of steamed Fe-ZSM-5 for direct N_2O decomposition was confirmed in the simulated tail-gas at a pilot-scale [8]. Hence, reaction mechanism of N_2O decomposition over different Fe-zeolites has been extensively studied [39,58,92-97] to comprehend the unique properties of Fe-zeolites. It is commonly accepted that the activation of N_2O on active iron site, which is a Fe-oxo species (monomer or binuclear or oligonuclear), is the first step in the decomposition of N_2O. This leads to the formation of highly active oxygen species, which is the so-called α-oxygen (Eq. (11)) [98-100].

$$N_2O + \square_{\text{active site}} \rightarrow N_2 + O_\alpha^* \quad (2.11)$$

The α-oxygen can react with either N_2O or with an other α-oxygen to form molecular O_2 and

subsequently regenerates the active site for the propagation of N_2O decomposition as shown by (Eq. (2.12) and (2.13)).

$$N_2O + O_\alpha^* \rightarrow N_2 + O_2 + \square_{\text{active site}} \quad (2.12)$$

$$O_\alpha^* + O_\alpha^* \rightarrow O_2 + 2\square_{\text{active site}} \quad (2.13)$$

However, regeneration of active iron sites by forming molecular O_2 is still not clear but it is widely accepted that O_2 desorption is a rate-determining step in this reaction [39-41,58,95]. The unique performance of this catalytic system could be an efficient technology in the near future for the abatement of N_2O in different sources.

Selective catalytic reduction (SCR) of N_2O

SCR of N_2O with different reducing agents such as CO, NH_3, hydrocarbons etc. was investigated. As compared to the direct decomposition, the presence of a reductant in the feed not only enhances the N_2O conversion but also shifts the conversion onset to lower temperatures. But studies dealing with the reaction mechanism are almost neglected. Reaction mechanism seems to be dependent on the reducing agent and the active iron sites [48,82,93-96,101,102]. In a study using labeled $^{15}NH_3$ for SCR of $^{14}N_2O$, differently labeled molecular nitrogens $^{14}N_2$, $^{15}N_2$ and $^{14}N\ ^{15}N$ were found in the products [64]. Hence, the authors suggested three reactions for the formation of different nitrogen isotopes, though they are not clear.

1. $^{14}N_2O$ decomposes on the active iron site

$$^{14}N_2O + \square_{\text{active site}} \rightarrow {}^{14}N_2 + O_\alpha^* \quad (2.14)$$

2. Adsorbed oxygen reacts with $^{15}NH_3$ to regenerate the active site and forms $^{15}N_2$ and H_2O.

$$3O_\alpha^* + 2{}^{15}NH_3 \rightarrow {}^{15}N_2 + 3H_2O + \square_{\text{active site}} \quad (2.15)$$

3. $^{14}N_2O$ and $^{15}NH_3$ react together at the same active site, after ^{14}N-^{14}N splitting of $^{14}N_2O$, forming ^{14}N-^{15}N.

$$\square_{\text{active site}} + 2{}^{15}NH_3 + {}^{14}N_2O + 2O_\alpha^* \rightarrow 2{}^{14}N\text{-}{}^{15}N + 3H_2O \quad (2.16)$$

Pophal et al. studied the propene-SCR of N_2O on Fe-MFI zeolite but they did not study the reaction mechanism [101]. However, based on the FT-IR studies they proposed protonated propene might play an important role in the SCR of N_2O.

In propane SCR of N_2O, propane reacts with the atomic oxygen, which is deposited by N_2O and reduces the active iron site. Subsequently, this site is reoxidized by N_2O [96].

Delahay et al. reported SCR of N_2O with CO on Fe-beta zeolite [102]. They suggested that CO reacts with a binuclear Fe oxo cation to form CO_2 and reduces the iron site. The reduced binuclear iron oxo site is reoxidized by N_2O.

$$CO + Fe\text{-}O\text{-}Fe \rightarrow CO_2 + Fe\text{-}\square\text{-}Fe \quad (2.17)$$

$$Fe\text{-}\square\text{-}Fe + N_2O \rightarrow N_2 + Fe\text{-}O\text{-}Fe \quad (2.18)$$

2.2 Synthesis strategies and activity of Fe-zeolites

It is commonly accepted that the preparation method determines the activity in the SCR of NO_x and N_2O as well as N_2O decomposition. Hence, different techniques were aimed to prepare Fe-zeolites with extraframework Fe species [2,31,32,37,45,53,103]. So far, a vast number of publications dealing with NH_3 and hydrocarbon SCR of NO_x, N_2O and decomposition of N_2O over Fe-MFI zeolites appeared. In contrast, limited research has been done on Fe-exchanged Mordenite, Ferrierite, beta, Y, LTL, Chabazite, Cliniptilolite, ZSM-11, ZSM-12, SBA-15, Al-HMS and MCM-41 catalysts. These studies revealed that Fe-MFI is more active and stable for these reactions than the other Fe-zeolites. However, the literature data are not directly comparable, since the applied experimental conditions were different in different research groups. Hence, only those reports which were performed under similar conditions are considered and studies under realistic conditions as in chemical plants are shortly mentioned. Furthermore, the Si/Al ratio, the ion exchange level of the Fe-zeolites, the pretreatment conditions, reducing agent, space velocity and the pore geometry of the zeolites can also influence the catalytic activity [34,44-46,53,55,58,103-105]. In this section, Fe-zeolites are discussed with respect to the preparation method and their activity in the removal of NO_x and N_2O.

2.2.1 Liquid ion exchange (LIE)

Traditional aqueous ion exchange aiming at the replacement of H^+, Na^+ or NH_4^+ cations of the zeolite matrix by Fe^{3+} or Fe^{2+} ions has been used to prepare extraframework iron containing Fe-zeolites. Sato and Iwamoto et al. investigated the influence of the zeolite framework on C_2H_4-SCR of NO reaction in the presence of O_2 under dry conditions [53]. However, it should be mentioned that they are the first authors who proposed the hydrocarbon SCR of NO_x and investigated the effect of zeolite framework on the reaction. For this study, Fe-exchanged MOR, FER, MFI, Y, LTL were prepared by conventional ion exchange from their Na form and tested under dry conditions. The Fe-MOR with an ion exchange level of 97% (Fe/Al ≈ 0.33) was found to be the most active catalyst among the Fe-zeolites with a maximum NO conversion of 20% at 523 K. On the basis of NO conversion at 473 K these catalysts were ranked as:

Fe-MOR 97≈Fe-MOR 54 > Fe-FER 49 ≈ Fe-MFI 94 > Fe-Y 89 > Fe-LTL 53

The number in the sample labeling denotes the percentage of ion exchange level with respect to the exchange of protons with Fe^{3+} i.e., Fe/Al = 0.33 (ion exchange level ≈ 100%). The activity order of different Fe-zeolites may not be merely due to their structure as claimed by the authors, since the ion exchange levels and the Si/Al ratio of the Fe-zeolites are different [53].

R. Q. Long and R. T. Yang prepared a series of Fe-exchanged zeolites including Fe-ZSM-5, Fe-MOR, Fe-FER, Fe-beta, Fe-Y, Fe-CHA, Fe-HEU, Fe- Al-HMS and Fe-MCM-41 by conventional ion exchange and tested them in NH_3-SCR of NO [2,45,46,52]. They always used the same feed composition and Gas Hourly Space Velocity (GHSV) for dry and wet conditions.

The NO reduction rate was negligible in the absence of O_2 and increases rapidly when the latter is introduced in the NH_3-SCR feed. This indicates the requirement of O_2 for the stoichiometric reaction (Eq. (2.1)). Under dry conditions, on 58% ion exchanged Fe-ZSM-5 (Fe% ≈ 1.59) nearly ≈ 100 % NO conversion was achieved in a broad temperature window from 673 to 823 K, higher than any other catalyst tested under these conditions (Table 2.1). When a small amount of Ce was introduced in Fe-ZSM-5 the activity further increased [2]. Therefore, the 58% Fe exchanged Fe-ZSM-5 (Fe% ≈ 1.59) and Ce-Fe-ZSM-5 (Fe% ≈ 1.14) catalysts were tested under realistic conditions with H_2O and SO_2 present in the feed [2,46]. The NO conversion only slightly decreased below 623 K but significantly increased and widened the temperature window at higher temperatures. Increase in activity was explained by increase in surface acidity, mainly Brønsted acidity of the catalysts. Especially, Ce-Fe-ZSM-5 was more stable during 60 h on stream under these conditions than the other two catalysts hence, the authors concluded that the Ce may be playing a stabilization role in Fe-ZSM-5 catalyst [2].

Under the same dry reaction conditions as for Fe-ZSM-5 (Fe% ≈ 1.59) and Ce-Fe-ZSM-5 (Fe% ≈ 1.14), the ≈ 60% iron exchanged Fe-MOR (Fe% ≈ 2.41) and 81% iron exchanged Fe-HEU (Fe% ≈ 3.5) also exhibited high activity. Differently, the other Fe-zeolites such as, Fe-Y, Fe-FER, Fe-beta, Fe-CHA, and Fe-MCM-41 were found to be less active than Fe-ZSM-5, Fe-MOR and Fe-HEU catalysts [1,45,46]. Furthermore, under similar conditions, the latter three catalysts have shown much higher SCR activity than a commercial V_2O_5+WO_3/TiO_2 catalyst. The different behaviour of different Fe-zeolites in NH_3-SCR reaction was explained by their unique structures. Mesoporous materials like Y, MCM-41 and HMS with large pore diameter are favorable for the diffusion rates but are less active in the NH_3-SCR reaction. Hence, the authors suggest that the SCR reaction could be free of diffusion limitation.

However, with conventional ion exchange, Fe/Al ratios only lower than 1 was achieved frequently. This is due to the fact that one Fe^{+3} ion must compensate three Brønsted acid sites to balance spatially separated negative charges of the zeolite matrix. Hence, only a small amount of Fe^{+3} ions could exchange with protons. The additional Fe^{+3} ions most likely form iron oxo- or hydroxo cations that can undergo complex chemical transformation during subsequent washing and calcination which lead to highly heterogeneous materials. Despite these problems considerable achievements with special techniques were reported [105,106].

Pioneer work reported by Feng and Hall aimed at the replacement of Na^+ by monovalent cations into a zeolite matrix rather than di and trivalent cations in order to achieve maximum iron exchange levels. In this regard they proposed a peculiar aqueous ion exchange method using FeC_2O_4 solution in an inert atmosphere in order to prevent oxidation of Fe^{+2} to Fe^{+3}. The authors achieved the objective by hydrolysis of Fe^{+2} to $Fe(OH)^+$ ions by FeC_2O_4 in H_2O and showed, that the existence of such $Fe(OH)^+$ ions is strongly pH sensitive. By this procedure an ion exchange level of 183% was achieved [73,81]. This catalyst showed superior performance in

comparison to under-exchanged (≈ 22% ion exchanged) Fe-ZSM-5 and unusual stability even in the presence of 20% H_2O and 150 ppm SO_2 during 2500 h on stream in realistic conditions (Table 1). Unfortunately, these results could not be reproduced by the authors or by other groups [31,105,107]. The main reason for the non-reproducibility of the obtained results could be due to the difficulty of an accurate control of pH inside the zeolite pores.

Certainly, this work generated enormous research in the preparation of over-exchanged Fe-zeolites for SCR of NO_x. Long and Yang reported an improved aqueous ion exchange method. In this method Fe^{+2} ions, which were generated in situ by reacting diluted HCl with iron powder, were exchanged with H^+ of H-ZSM-5. The ion exchange was performed in an inert atmosphere in order to prevent oxidation of Fe^{+2} to Fe^{+3}. An ion exchange level of 130% was achieved. At lower temperatures this catalyst (Fe-ZSM-5-130 with 3.58% Fe) showed superior performance in NH_3-SCR in comparison to a 58% ion exchanged Fe-ZSM-5-58 (Fe% ≈ 1.59), which was prepared by conventional ion exchange methods [45]. However, at higher temperatures both catalysts show similar activity (Table 2.1).

Table 2.1. Summary of the performance of differently prepared Fe-ZSM-5 and different Fe-zeolites prepared by CVD are compared in NH_3 and isobutane SCR of NO

Fe-Catalyst*	**Preparation method**	**Feed composition**	**GHSV h^{-1}**	**X%$_{max}$ (NO)**	**Y%$_{max}$ (N_2)**	**T (K) at %$_{max}$ (NO) or Y%(N_2)**	**Ref**
1.59%Fe-ZSM5	Conventional ion exchange	1000 ppm NO, 1000ppm NH_3, 2%O_2	4.6 X 10^5	72.5	-	623	[2,45]
				99	-	673	
3.58%FeZSM5	Improved Liquid Ion Exchange (ILIE)			85.4	-	623	[45]
				99	-	673	
Fe-ZSM-5-183	FeC_2O_4 exchange	2000 ppm NO, 2000 ppm i-C_4H_{10}, 3%O_2	42,000	100	-	723	[73]
Fe-ZSM-5-22				40	-	773	
Fe-ZSM-5	Chemical Vapor Deposition (CVD)	2000 ppm NO, 2000 ppm i-C_4H_{10}, 3%O_2	42,000	-	76	623	[31]
5% Fe-ZSM-5				-	76		[44]
3.5% Fe-beta				-	64		
7.1% Fe-FER				-	18		
10.3% Fe-MOR				-	9		
2.7% Fe-Y				-	11		
5.4% Fe-ZSM-5		1000 ppm NO, 1000 ppm i-C_4H_{10}, 2%O2	30,000	73	-	603	[36]
0.5% Fe-ZSM-5	Mechanochem-ical Route (MR)	1000 ppm NO, 1000 ppm i-C_4H_{10}, 2%O2	30,000	81	-	673	[32]

* The labeling of Fe-catalysts indicates the Fe Wt.% and the type of zeolite. The absence of Fe Wt.% in some samples indicates its unavailability.

2.2.2 Sublimation of $FeCl_3$ into the pores of the zeolite matrix (CVD)

Inspired by Feng and Hall's work, Chen and Sachtler prepared an over-exchanged Fe-ZSM-5 catalyst by chemical vapor deposition (CVD) of $FeCl_3$ into the pores of H-ZSM-5 in an inert atmosphere [31]. Fourier Transformed Infra Red (FT-IR) spectroscopy was used to study the effect of sublimation of $FeCl_3$ into the pores of the zeolite. They found that the Brønsted OH groups (3610 cm^{-1}) and silanol groups (3750 cm^{-1}) were completely consumed after sublimation. However, after subsequent washing and calcination steps, peaks at 3610 cm^{-1} weakly and 3750 cm^{-1} completely reappeared. Hence, the authors proposed that $[Fe_2Cl_4]^{2+}$ ions replace two protons located within suitable distances according to the following reaction:

$$Fe_2Cl_6 + 2H^+ \rightarrow [Fe_2Cl_4]^{2+} + 2HCl \qquad (2.19)$$

With this technique the authors achieved Fe/Al = 1 (ion exchange level ≈ 300%) [31] and the catalyst showed a high activity and stability for isobutane-SCR of NO under wet conditions during 100 h on stream at 623 K (Table 2.1).

These authors prepared a variety of Fe-zeolites (MFI, beta, MOR, FER, Y) by this method and studied the influence of their pore geometry and the reductant on the SCR of NO [44]. The five Fe-zeolites were tested under identical conditions in both isobutane and propane SCR of NO under dry conditions (Table 2.1). Therefore, the catalytic performance of these catalysts have been compared and tabulated in Table 2.1.

In both isobutane and propane SCR, Fe-MFI and Fe-beta exhibited higher activity than the other catalysts tested in this study (Table 2.1). The presence of 10% H_2O in the SCR feed does not deteriorate the SCR activity of Fe-MFI but does deplete the activity of other Fe-zeolites studied for this work [44]. This indicates that MFI pore structure is more suitable for this reaction than any other zeolite pore structure, which can be clearly seen, too, from Table 2.1.

The CVD preparation technique attracted much attention in recent years by many research groups because of the high activity, stability and reproducibility, not only for the reduction of NO with isobutane [31,35,36,108] and NH_3 [2,33,34] but also for the direct decomposition [42,43] or reduction of N_2O with CO and propane [42,58,109].

Grünert et al. investigated the effect of Si/Al ratio of the parent H-ZSM-5 support, washing intensity and calcination ramp of Fe-ZSM-5 catalyst on the activity of SCR of NO [36,55]. Fe-ZSM-5 catalysts were prepared by a method similar to the one of Chen et al. using different H-ZSM-5 supports with different ratios of Si/Al, 14 and 44, with different washing procedures and with different heating rates during calcination. The high Si/Al (44) containing catalyst showed lower activity than the low Si/Al (14) containing Fe-ZSM-5 catalyst in isobutane-SCR of NO. The low Si/Al (14) of the parent H-ZSM-5, high washing intensity (10 l H_2O for 5 g of catalyst) and low heating rate during calcination process suppresses the formation of Fe_xO_y clusters.

Prins and Marturano et al. have shown that the distribution of iron species in Fe-ZSM-5 (prepared by CVD) is strongly dependent on the source of the parent ZSM-5 and hydrolysis processes of the zeolite after preparation [56]. Recently, Battiston et al. proposed that calcination is a crucial step in the final distribution of iron species in sublimed Fe-ZSM-5

sample [57]. Furthermore, van Santen and Zhu et al. reported that the pressure of $FeCl_3$ vapor in the sublimation procedure plays a role in the formation of iron oxide clusters [92].

However, different characterization techniques, including FT-IR, H_2-TPR, EXAFS, XANES, Mössbauer, EPR and UV/VIS spectroscopy revealed that samples prepared by CVD contain different iron species varying from isolated iron ions to oligomers and large iron oxide particles [36,55,108]. Heterogeneous distribution of iron species in Fe-ZSM-5 makes the catalyst complicated to comprehend the active iron centers in SCR of NO_x. Consequently, based on their characterization studies on Fe-ZSM-5, which exhibited comparable SCR activities, different research groups proposed different active iron species for this reaction [36,55-57, 86,91,105, 110,111], which will be separately discussed in section 2.3.

2.2.3 Solid-state ion exchange (SSIE)

This technique is based on the mechanical mixing of appropriate amounts of H-ZSM-5 support and Fe precursor ($FeCl_3$. $6H_2O$ or $FeCl_2$. $4H_2O$) and subsequent heating (usually above the sublimation temperature of the Fe source) in an inert gas flow in an oven for a desired time followed by washing with H_2O [36,103,106]. The method of Fe insertion into the zeolite pores is more or less similar to CVD but the required experimental setup is simple for SSIE.

Bell and Lobree et al. studied the effect of Fe/Al ratio on the nature and distribution of iron species in ZSM-5 zeolite matrix and reported that Fe/Al ratios below ≈ 0.6 favour the formation of isolated iron ions [103].

Long and Yang et al. studied the effect of preparation method on the NH_3-SCR reaction over Fe-ZSM-5 and reported that the sample prepared by SSIE is more active than the CVD method [106].

Grünert et al. also studied the effect of preparation method on the NH_3-SCR reaction and the findings were different from that of Long and Yang et al. The authors found that the sample prepared by CVD method is more active than the SSIE method [36]. However, different characterization techniques revealed that the SSIE method leads to a highly heterogeneous distribution of iron species with extensive formation of clusters in Fe-ZSM-5. [36,55].

2.2.4 Other preparation techniques

For unambiguous assignment of active iron sites in SCR of NO_x and N_2O, it was essential to prepare a catalyst with a defined distribution of iron species. In this connection, recently Grünert et al. reported a novel mechano chemical route (MR) to prepare Fe-ZSM-5 catalyst [32]. This technique comprises of intense grinding of appropriate amounts of H-ZSM-5 support with $FeCl_3$. $6H_2O$, followed by 2-3 short-time washing steps (0.5 l H_2O per 2 g catalyst). Despite the much lower Fe content, this catalyst is more active in SCR of NO than the sample prepared by the CVD technique of Sachtler et al. indicating the importance of the mononuclear iron sites in the reaction (Table 2.1).

Another method for obtaining highly active Fe-MFI zeolites is hydrothermal synthesis followed by steam treatment. Here, Fe ions are added to the synthesis mixture and are incorporated in the zeolite lattice during crystallization. Subsequent steaming causes dislodgement of framework Fe to extraframework Fe species. J. Pérez-Ramírez et al. studied

the steam activated Fe-silicalite and Fe-ZSM-5 with similar Fe content (≈ 0.68%) prepared by hydrothermal synthesis which exhibit different nature and distribution of iron species and thus resulted in different catalytic activity in SCR and decomposition of N_2O [96]. Steam activated *ex*-Fe-silicalite with uniform distribution of isolated iron ions exhibited higher specific activity in the reduction of N_2O with C_3H_8 and CO than the steam-activated *ex*-Fe-ZSM-5 catalyst with heterogeneous distribution of iron species. Nevertheless, *ex*-Fe-ZSM-5 showed remarkable performance in the decomposition of N_2O in simulated tail gases (realistic conditions) as compared to ion exchanged and sublimed Fe-ZSM-5 [8,42,111].

On comparing the different preparation techniques, it appears that traditional aqueous ion exchange method aiming at the replacement of H^+ or Na^+ cations of zeolite matrix by ferric ions leads to highly heterogeneous distribution of iron species in the zeolite with poor activity in the HC-SCR of NO_x or reduction of N_2O and N_2O decomposition [32,42,53,82,96]. That's why, Feng and Hall introduced a novel idea to exchange H^+, Na^+ or NH_4^+ ions with monovalent metal cations to prepare over exchanged Fe-MFI zeolites. However, this technique is strongly pH sensitive which lead to the problem of reproducibility. Hence, this technique was almost disregarded. In contrast, sublimation method is much less sensitive to the origin of the zeolite i.e., the pH inside the zeolite pores. An advantage of this preparation method is the ease to achieve high ion exchange levels of Fe/Al up to ≈ 1 and more reproducibility. Though this technique leads to highly heterogeneous distribution of iron species in the zeolite, the obtained material is undoubtedly more active in various reactions. Improved liquid ion exchange method also leads to highly active materials for SCR of NO_x with reproducible results. On the other hand, hydrothermal synthesis of Fe-MFI and steam activation allows the preparation of zeolites with framework and extraframework iron in a more reproducible manner.

Considering the pore size of different zeolite matrices, it appears that the activity of NH_3- and HC-SCR of NO decreases with increasing pore size of the zeolite though the accessibility of iron sites to reactants increases [44-46,52]. In NH_3-SCR of NO the Fe-ZSM-5 and Fe-MOR zeolites show higher activity in both dry and wet conditions than the other Fe-zeolites. While, in HC-SCR of NO, Fe-ZSM-5 and Fe-beta zeolites exhibit superior performance than the other studied Fe-zeolites and Fe-ZSM-5 was more stable in wet conditions. Interestingly, the best candidate in both SCR of NO reactions is Fe-ZSM-5. Furthermore, Fe-ZSM-5 shows superior performance in both direct catalytic decomposition and SCR of N_2O reaction in dry and realistic conditions. Hence, the possible synergistic effect of the Brønsted acid sites (mainly on the SCR of NO_x) and intrinsic activity of the ZSM-5 pore structure for SCR of NO_x and N_2O and N_2O decomposition make ZSM-5 a potential candidate for the support [112,113].

2.3 Structure-reactivity relationships in Fe-zeolites

As mentioned in the previous sections, the activity, stability and durability of Fe-MFI zeolites in SCR of NO_x and N_2O or N_2O decomposition have motivated researchers to investigate the origin of the catalytic activity of this system. Most of the research on the

nature of active iron sites was carried out for HC-SCR of NO_x or N_2O decomposition while only few studies dealt with the NH_3-SCR of NO_x. The majority of these studies was performed by applying physico-chemical techniques ex situ, in the absence of reactants, and the results were discussed in relation to separately measured catalytic data. This can lead to ambiguous conclusions on the nature of active iron sites. Very few in situ studies during interaction of feed components with iron species in the zeolite have been reported. In this section, studies dealing with the evaluation of the nature of active iron sites are discussed separately for SCR of NO_x and decomposition or SCR of N_2O.

2.3.1 Structure-reactivity relationships in the SCR of NO

Among the various types of Fe species that can exist in Fe-containing zeolites, binuclear Fe-O-Fe species have been discussed with emphasis by several groups. The idea of binuclear iron oxide complex was first proposed by Garten et al. for Fe-Y zeolite [114] and Hall et al. confirmed these results over Fe-Y and Fe-MOR zeolites [40,115]. After that Panov et al. reported that N_2O decomposition occurs on the bivalent iron dimers which produces α-oxygen with high oxidation potential [98-100]. Taking account of these reports and based on the TPR, EPR and IR results, Chen and Sachtler proposed an oxygen bridged binuclear iron complex such as $[(HO)Fe\text{-}O\text{-}Fe(OH)]^{+2}$ as active iron species for SCR of NO_x with hydrocarbons [31]. In fact, merely based on the CO-TPR data they proposed this binuclear iron complex [31] and later supported this argument by EPR spectroscopy. They assigned a signal at $g' \approx 2.03$ to such a dimer species which was observed at room temperature. In relation to the temperature, the identification of an iron dimer by EPR line at $g' \approx 2.03$ is highly questionable (see also section 4.1.2).

Marturano and Prins et al. studied the structure of iron species in Fe-ZSM-5 which was prepared by CVD technique using IR, Al MAS NMR and EXAFS spectroscopy [56]. Mainly based on the EXAFS data they suggested that the iron is mostly in the form of intrazeolite diferric (hydr)oxo-bridged binuclear clusters similar to those in MMO. Recently, Battiston et al. strongly supported the idea of binuclear iron oxide complex (Fe-O-Fe) as active iron species [35,116]. On the basis of in situ-EXAFS and XANES studies, these authors suggested that the binuclear iron species are the dominating species in sublimed overexchanged Fe-ZSM-5 and are proposed to be the active iron species in isobutane-SCR of NO reaction. However, when a variety of iron species coexists, only average coordination values can be derived from this technique. Discrimination of dimers is difficult and, as Grünert et al. have shown [64], the presence of clusters can be underestimated hence, the obtained results are ambiguous.

Recently, Grünert et al. studied sublimed overexchanged Fe-ZSM-5 catalysts by FT-IR, XRD, XPS, TPR, EXAFS, XANES and Mössbauer spectroscopy. Their findings were different from that of the above authors and suggested that the sublimed Fe-ZSM-5 contains a multitude of iron species including isolated Fe ions, oligomers (including dimers), iron oxide clusters and Fe_2O_3 particles [36,55]. Hence, they concluded that assignment of SCR of NO activity merely to binuclear iron species as ascribed by some authors might be doubtful. Considering the fact that different forms of iron species are coexisting in Fe-ZSM-5 zeolites, they suggested that isolated and oligomeric iron species including dimers are the active sites in both NH_3- and isobutane-

SCR of NO, whereby mononuclear iron species appeared to be more efficient than oligomers. However, they also suggested that the cluster species are unselective at higher temperatures [32,36,55].

Previously, Joyner et al. have observed different forms of iron in the ion exchanged Fe-ZSM-5 zeolites and based on their EXAFS results they proposed Fe_4O_4 nanoclusters as the active iron species in propane-SCR of NO [105].

Kucherov et al. assigned, based on in situ EPR studies, the catalytic activity of Fe-ZSM-5 and Fe-SAPO-34 catalysts in propene-SCR of NO_x to distorted tetrahedral isolated Fe^{+3} ions [59]. Similarly, Sobalik and Wichterlova et al. ascribed the activity of Fe-FER zeolite in propane-SCR of NO merely to isolated iron sites [91]. Long and Yang concluded by EPR studies of differently prepared Fe-ZSM-5 zeolites, that isolated Fe^{+3} ions in tetrahedral coordination are the only active iron species in NH_3-SCR of NO reaction [106].

By comparing all the results and discussion presented above, the high degree of debate and controversy on the nature of the active sites is readily evident. The only agreement seems to be that large Fe_2O_3 particles are not active sites for SCR of NO and must be avoided [36,86]. Moreover, there are only few studies dealing with the role of acidity in the SCR of NO, which may be an important property. However, Long and Yang reported that the higher the Brønsted acidity of the Fe-zeolite higher is the activity in the NH_3-SCR of NO [46].

2.3.2 Structure-reactivity relationships in the decomposition and SCR of N_2O

Significant research has been done to evaluate the nature of active iron sites in N_2O decomposition and in N_2O-SCR. For N_2O decomposition, catalytic activity is often ascribed to binuclear iron sites of different structures [58,56,93].

Panov et al. have suggested that a dinuclear iron complex with two α-sites is the active site for N_2O decomposition that produces α-oxygens with high oxidation potential which can oxidize a wide range of organic molecules even at room temperature [98,99,117,118]. Sachtler et al. investigated the active iron sites in sublimed Fe-ZSM-5 zeolites in N_2O decomposition [93]. They formulated that the binuclear iron sites, similar to the active iron sites in SCR of NO, and larger clusters are more active for N_2O decomposition than the mononuclear sites. Lioubov et al. reported a binuclear iron center similar to a diamond core structure of the MMO as the active site in N_2O decomposition [94].

Centi and Vizzana have studied the activity, stability and nature of active sites of differently prepared Fe-ZSM-5 zeolites in SCR of N_2O with propane under true industrial emission like conditions [82]. Samples prepared from liquid ion exchange method showed a large amount of iron oxide clusters and Fe_2O_3 particles while sublimed Fe-ZSM-5 showed mainly isolated Fe^{+3} ions and iron-oxo nanoclusters but not particles. The liquid ion-exchanged sample exhibited higher oxidation activity of propane and of SO_2 to SO_3 and the latter formed surface iron sulphate species that lead to the deactivation of the catalyst. In contrast, sublimed Fe-ZSM-5 showed a low oxidation activity and higher resistance to deactivation by SO_2 during 600 h on stream. Hence, the authors concluded that the isolated Fe^{+3} ions and iron-oxo nanoclusters are the active iron sites for this reaction.

Delahay et al. studied a series of ion-exchanged Fe-beta zeolites for SCR of N_2O with NH_3 in the presence of O_2 [95]. On the basis of their studies they proposed that the mononuclear iron oxo cations are the active sites for SCR of N_2O with NH_3.

Similarly, J. Pérez-Ramírez et al. studied the active site structure in N_2O conversions over different Fe-MFI zeolites [96]. They have reported that steamed Fe-silicalite, which has exclusively isolated Fe^{+3} ions, was more active than a steamed Fe-ZSM-5 zeolite with pronounced cluster formation in SCR of N_2O with different reducing agents. Interestingly, the steamed Fe-silicalite was less active in direct N_2O decomposition than the steamed Fe-ZSM-5. Furthermore, they found different activation energies for the same reaction over these two catalysts. Hence, the authors concluded that in the reduction of N_2O with a reductant the isolated Fe^{+3} ions are preferred over oligomers while the latter species are more active in direct N_2O decomposition due to the easier oxygen recombination of two iron centres that are close together.

van Santen and Zhu et al. studied the effect of high temperature calcination and steaming on sublimed Fe-ZSM-5 catalyst for N_2O decomposition [92]. The authors observed disappearance of Brønsted acid sites in FT-IR spectra and high catalytic activity after high temperature calcination (973 K). Hence, it was concluded that upon high temperature calcination, iron oxide clusters react with Brønsted acid sites and form isolated cationic iron sites such as $[FeO]^+$. Taking account of this observation they ascribed catalytic activity to cationic isolated iron sites and iron oxo nanoclusters.

In summary, despite considerable research on the nature of active iron sites in Fe-MFI zeolites for SCR of NO_x/N_2O and N_2O decomposition, ambiguities and discrepancies still exist as described above. This could be due to the complexity of the Fe-MFI zeolites with respect to the iron constitution and the different sensitivity of the applied spectroscopic techniques to different iron species. It has been suggested on the basis of multitechnique studies that the Fe-ZSM-5 contains a multitude of iron species. In contrast, some authors concluded from their limited characterization studies the involvement of only one kind of iron species such as dimers in the reaction which seems to be highly unlikely. But it is rather likely that there is an involvement of different iron species in the reaction as suggested by other authors [36,82,96, 105]. It is also not yet clear whether the same active iron species that are involved in the NO-SCR are involved in the N_2O reduction. Hence, this thesis was performed to clarify these contradictions and to give more insights into the structures of iron oxo sites formed by different preparation techniques and their role in the SCR of NO_x/N_2O and N_2O decomposition by in situ spectroscopic studies.

2.4 Physico-chemical techniques for the characterization of Fe-containing zeolites

In the literature, Fe-MFI zeolites are comprehensively characterized for the structure of iron sites such as valence and coordination state of iron ions by using EPR [55,58,59,62-64,66, 93,104,106,119,120-130,131], UV/VIS-DRS [60-62,66,82,130,132-138], X-ray absorption spectroscopy (XANES and EXAFS) [35,36,56,57,62,64,66,86,93,105,108,111,116],

Mössbauer spectroscopy [36,104,118,139] and XPS [36,83,104] and structural properties and surface acidity were investigated by Solid-state NMR [56,104,108,139,140], IR or FT-IR [36,104,141-143] and NH_3-TPD measurements [103,141,144,145]. The Fe-MFI zeolites were also investigated under reaction conditions by in situ-EPR [59], in situ-X-ray absorption spectroscopy [35,57,105,116] and in situ-FT-IR spectroscopy [37,46,83-91] to identify the nature of active iron species and active reaction intermediates in SCR of NO_x and N_2O as well as in N_2O decomposition.

In the following section, opportunities and limitations of the main characterization techniques used for Fe-containing zeolites are critically reviewed. Emphasis is dedicated to EPR, UV/VIS-DRS and FT-IR spectroscopy since these methods have been preferentially applied in this thesis. Special attention is paid to in situ spectroscopic studies, performed at elevated temperature and in the presence of reactants.

2.4.1 EPR spectroscopy of iron species

EPR spectroscopy has been extensively used to identify the state of iron species in molecular sieves, since it is an efficient tool to identify isolated Fe^{3+} species of different coordination geometry [55,58,59,62-64,66,83,104,106,119-130] and Fe_xO_y clusters of different degrees of aggregation by analysis of the mutual magnetic interactions of the Fe sites [55]. Moreover, EPR spectroscopy has been also applied in situ under true SCR conditions. These studies were aimed at the identification of active iron species in SCR of NO by propane over Fe-MFI [59].

EPR is a unique technique to characterize geometrical and electronic peculiarities of different isolated Fe^{+3} ions in very low iron concentrations (which is often not possible by other techniques e.g. Mössbauer). Moreover, it provides information not only on the structure and valance state of isolated Fe^{+3} ions but also on electronic interactions between Fe^{+3} ions as well as with reactants. Based on the temperature dependence of the signal intensity one can derive information on the magnetic behavior such as para, ferri or antiferromagnetic interactions of the iron ions in zeolites.

The main advantage of EPR is that this technique can be used under true reaction conditions, i.e., at elevated temperatures and under reactant gas flow. Hence, the obtained results can be considered as authentic to draw conclusions on structure-activity relationships and, consequently, on the nature of active iron species in the SCR of NO or N_2O by different reducing agents and in direct N_2O decomposition.

In general, Fe^{+3} ions in zeolites are in high-spin electronic configuration since the possible ligands are oxygen, OH or H_2O molecules which are weak field ligands. This results in a total spin of 5/2 and, thus, in a S ground state. The number and position of observable electronic transitions for Fe^{+3} ions depends strongly on the local crystal field symmetry, i.e zero field splitting (ZFS) parameters. The ZFS parameters (D and E) are expressed by second order terms in the spin-Hamiltonian:

$$H = g \cdot \beta \cdot H_o \cdot S + D\,[S_z^2 - (1/3)\,S(S+1)] + E\,[S_x^2 - S_y^2] + \text{higher order terms} \qquad (2.20)$$

where g is the g-tensor, β is the Bohr magneton, H_o is the magnetic field vector, S is the electron spin operator, S_x, S_y and S_z are the spin matrices. The higher order terms come from the cubic field splitting constants and are usually much smaller than the ZFS parameters (D and E). The ZFS parameters are a measure of the deviation of the Fe^{+3} ion crystal field symmetry from cubic symmetry. For Fe^{+3} ions in cubic symmetry D = 0 and E = 0. In this case, the energy levels corresponding to the different values of the spin quantum number m_s are degenerate in the absence of an external magnetic field. Under the influence of an external magnetic field, this degeneracy is removed and the energy levels split with equal distance. Then, the allowed five EPR transitions with $\Delta m_s = \pm 1$ take place at the same resonant field value resulting in an isotropic EPR signal at g' ≈ 2 as shown in Fig. 1a. When distortion takes place from the ideal octahedral or tetrahedral symmetry to axial or rhombic symmetry respectively, the ZFS parameters for axial and rhombic distortion are D ≠ 0, E = 0 and D > E ≠ 0 respectively. In these cases, the orbital degeneracy is partly removed even in the absence of an external magnetic field giving rise to three so-called Kramer's doublets (m_s = ±5/2, ±3/2, ±1/2) as shown in Fig. 1b. When the zero field splitting between the Kramer's doublets is large in comparison to the microwave energy (strong rhombic or axial distortion), the only allowed EPR transitions occur between m_s = –1/2 and +1/2. In the case of maximum rhombic distortion for D >> hν, E/D ≈ 1/3, a single line at g' ≈ 4.3 is observed from the –1/2 → +1/2 transition together with a weak and broad feature at g' ≈ 9 which is due to a forbidden transition [120]. For D >> hν, E = 0 (strong axial distortion), a signal at g' ≈ 6 is observed [120].

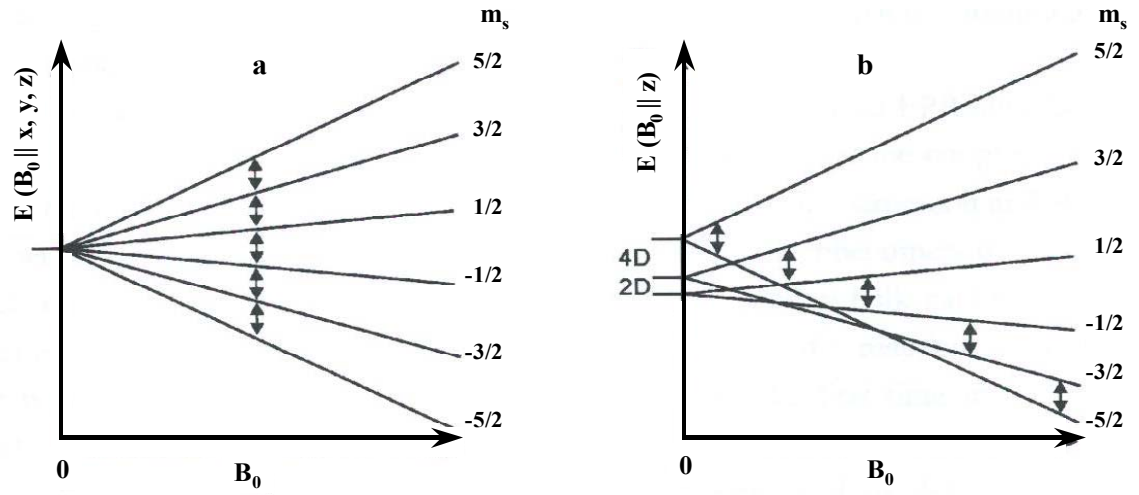

Fig. 2.1. Schematic representation of energy level splitting for isolated Fe^{3+} ions in high symmetry (a) and axial distortion (b), adopted from [129].

For magnetically interacting Fe^{3+} ions, when the mutual distance between Fe^{3+} ions in a matrix is short enough, spin-spin dipolar and/or exchange interactions can average out the ZFS, resulting in a more or less isotropic signal in the range of g' ≈ 2. In general, the line width of those signals is much larger than that of g' ≈ 2 signals arising from isolated highly symmetric Fe^{3+} ions for which narrow lines are to be expected. Information, whether a signal at g' ≈ 2

arises from isolated or interacting Fe^{3+} species can be derived from the temperature dependence of the signal intensity.

For pure paramagnetic behavior (no magnetic interactions between Fe^{3+} ions) the EPR signal intensity follows Curie's law and is inversely proportional to temperature. Deviations from this proportionality can provide information about the strength and type of magnetic interactions between Fe^{3+} ions in a sample. Thus, it has been shown that for antiferromagnetic compounds, long range antiferromagnetic ordering of the spins collapses above the Neel temperature and an EPR signal appears [131].

It has been shown that in Fe-containing zeolites frequently three types of EPR signals are observed at g'-values of 6, 4.3 and 2. For illustration, the EPR spectrum of an Fe-ZSM-5 prepared by solid state ion exchange is shown in Fig. 2. The signal at g' ≈ 4.3 has been equivocally assigned to Fe^{+3} ions in tetrahedral coordination, either in framework [121-123] or extraframework positions [63,124,125], while the signal at g' ≈ 6 is frequently assigned to isolated Fe^{3+} species with higher coordination numbers [126,127]. However, it must be noted that just from the position of an EPR signal no conclusion on the number of coordinating ligands can be derived. The EPR signal at g' ≈ 2 has been typically assigned to iron oxide clusters. However, as mentioned above, isolated Fe^{3+} ions in positions of high symmetry (ZFS parameters D = E = 0) also contribute to an isotropic signal at g' ≈ 2 [123,128]. Moreover, it has been demonstrated, that small changes of D and E can induce dramatic changes in the number and position of observable Fe^{3+} signals [123,129]. Accordingly, R. Stösser et al. have shown that slight changes in the Fe site symmetry cause shift in the position of the EPR signal [146].

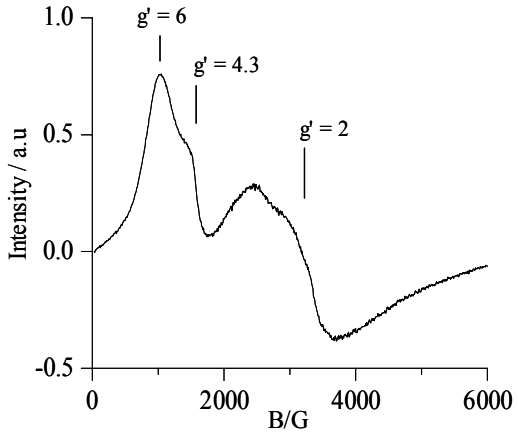

Fig. 2.2. X-band EPR spectrum at 293 K of an Fe-ZSM-5 prepared by solid-state ion exchange (Fe content: 5.2 wt.%).

2.4.2 UV/VIS-DRS spectroscopy of iron species

UV/VIS-DRS is an important technique which is partly complimentary to EPR. It is also able to distinguish between isolated Fe species of different structure and Fe_xO_y clusters of different nuclearity (which is sometimes not possible by other techniques e.g. EXAFS). It has been widely used to study Fe-zeolites [82,104,60,61,62,66,130,132-138]. In principle, two different types of electron transitions can be detected, mainly d-d and charge-transfer (CT)

transitions. The d-d transitions of Fe^{+3} ions are symmetry and spin forbidden. Hence, often d-d transitions are weak and/or not observed. On the other hand, CT bands are allowed transitions and are usually intense. The wavelength of Fe^{+3} CT bands depends on the coordination number and on the degree of aggregation [58,82,66,147]. As an illustration example, the UV/VIS-DR spectrum of an Fe-ZSM-5 with 5.2% Fe is shown in Fig. 2.3.

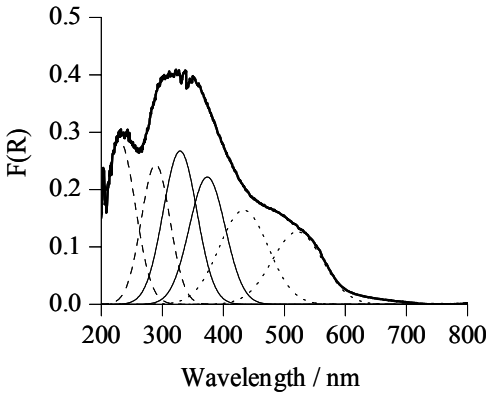

Fig. 2.3. Experimental UV/VIS diffuse reflectance spectrum and deconvoluted sub-bands of an Fe-ZSM-5 prepared by solid-state ion exchange (Fe content: 5.2 wt.%).

Usually, UV/VIS-DR spectra of iron species in solids contain several broad bands which overlap each other. This makes spectral analysis difficult, hence, for facilitating spectral assignment, spectra deconvolution has to be used [138]. In Fig. 3 the UV/VIS-DR spectrum of the sample exhibits strong absorption in the whole ultraviolet and visible region, which arises from $Fe^{+3} \leftarrow O$ CT transitions. After deconvolution, six bands are resolved. This deconvolution was based on the following considerations. In general, Fe^{+3} ions give two CT bands associated to $t_1 \rightarrow t_2$ and $t_1 \rightarrow e$ transitions [132]. For isolated Fe^{+3} ions these two CT transitions fall in the high energy range of the spectrum (< 300 nm) [55,58,66,134,135]. Octahedral Fe^{+3} ions in small oligomeric iron-oxo clusters give bands between 300-400 nm and bands above 400 nm are characteristic for large iron oxide particles [82,135]. Assuming that the absorption coefficient is roughly equal in the maxima of the sub-bands, the percentage of each type of species can be derived from the area of the sub-bands. However, these values have to be regarded as an estimate due to the intrinsic uncertainty of the deconvolution procedure. Despite this fact the quantification provides a valuable indication of the relative amounts of various iron species structure among the zeolites investigated.

UV/VIS spectra of solids are recorded in diffuse reflectance mode. In general, in an UV/VIS-DRS spectrum the ratio of the light reflected from the sample and from an ideal non-absorbing reference standard is measured as a function of wavelength (λ). This can be expressed by Schuster-Kubelka-Munk equation:

$$F(R_\infty) = (1- R_\infty)^2 / 2R_\infty = K/S \qquad (2.21)$$

where (R_∞) is the ratio of the reflectivity of an infinitely thick layer of the sample and the one of a standard, K is the apparent absorption coefficient and S is the apparent scattering coefficient. Indeed, this equation is valid only under defined conditions. These are: sample should be an infinitely thick layer, diffuse monochromatic irradiation of the powder sample, isotropic light scattering, uniformly distributed TMI in low concentration (low absorption) and the absence of fluorescence.

The main advantage of the UV/VIS-DRS technique is that it provides information on d-d and CT transitions of iron species in the zeolite matrix, which strongly depend on the oxidation and coordination environment. Hence, this information can be used as a fingerprint for the identification of oxidation and coordination state of iron species in zeolites. Furthermore, for low absorbance [F (R) < 0.5] the Schuster-Kubelka-Munk function can be used for quantitative analysis [138].

To my knowledge, until now there are no reports on in situ applications of this technique during SCR of NO_x and N_2O over Fe-MFI zeolites. For the first time in situ UV/VIS studies for SCR of NO_x and N_2O were reported from this thesis [58].

2.4.3 FT-IR spectroscopy

FT-IR spectroscopy is an important and versatile technique to probe hydroxyl stretching and framework vibrations as well as surface acidity of micro and mesoporous materials. A great advantage of IR spectroscopy is that the construction of IR transparent windows withstands high temperatures and pressures. Hence, this technique is being widely used for in situ studies during catalysis (in the presence of reactants) to probe adsorbed species, active intermediates and the acid base-base properties of the catalyst surface.

Brønsted and Lewis acidity of Fe-zeolites are probed by FT-IR analysis of adsorbed probe molecules such as pyridine or NH_3 [148]. Besides, formation of NO_x species, intermediates or active adsorbed species/deposits during NH_3- or isobutane-SCR of NO can be studied.

FT-IR spectroscopy belongs to the most frequently used technique for investigating the structural properties of MFI zeolites. Thus, it has been extensively used to probe both the hydroxyl stretching and framework vibrations. In general, bands around 3740 cm^{-1} are observed from terminal Si-OH groups, while a band around 3630 cm^{-1} is observed for Brønsted acidic bridging Si-O(H)-Al groups [104,141]. Usually, the number of Brønsted sites increases with the Al/Si ratio, since each Al atom replacing a Si framework atom creates a Brønsted site. Based on this information one can readily see the lattice arrangement of the zeolite. Grünert et al. found more silanol groups and less Brønsted OH groups in high Si/Al ratio (44) containing H-ZSM-5 zeolite than in H-ZSM-5 with low Si/Al ratio (14), indicating the presence of lattice defects in the former sample [36]. Infrared spectroscopy in the framework vibration range between 400-1200 cm^{-1} was also used to probe the framework substitution of iron ions. The band position of both symmetric and asymmetric Si-O-Fe stretching vibrations is shifted to lower wavenumbers as compared to Si-O-Si bands [141-143].

The role of acidity of Fe-MFI zeolites in the SCR of NO_x is not completely understood and is still subject to debate [46,95,96,105]. FT-IR spectroscopy has been widely applied to

investigate the surface acidity of Fe-MFI zeolites by adsorption of pyridine or NH_3 [46,83,148]. This technique distinguishes between Lewis and Brønsted acidic sites and allows to discriminate between acidic sites of different strengths. For this purpose pyridine was considered to be a better probe molecule than NH_3 [148]. In FT-IR studies of pyridine adsorption, Brønsted acid centres are detected by a band around 1540 cm^{-1}, which originates from pyridinium ions ($C_5H_5NH^+$) created via protonation of pyridine molecules by surface acidic hydroxyl groups [148]. On the other hand, Lewis acidic centres are characterised by bands around 1600 cm^{-1} and 1460-1445 cm^{-1}, originating from pyridine coordinatively linked to a Lewis acidic sites. The band position around 1600 cm^{-1} reflects the strength of the Lewis acidity [148]. However, bands of hydrogen-bonded and physisorbed pyridine are expected in the similar range of Lewis acidic centres i.e., bands around 1440-1447 and 1580-1600 for hydrogen-bonded pyridine and 1439 and 1580 cm^{-1} for physisorbed pyridine [148,149,150]. Therefore, it is difficult to distinguish between differently adsorbed pyridine at normal conditions. However, exploiting the thermal stability of these pyridine species one can unambiguously determine the Lewis bonded pyridine by recording FT-IR spectra at sufficiently high temperatures [149]. Finally, the assignment of the band around 1620 cm^{-1} is ambiguously discussed in the literature. Buzzoni et al. ascribed it to Brønsted acidic sites in zeolites [150], while Busca et al. attributed it to Al Lewis acid sites of γ-Al_2O_3 and amorphous Al_2O_3/SiO_2 [148].

In addition to the analysis of surface OH groups and acidity, IR spectroscopy has been extensively used in situ (in the presence of feed components) to probe the nature of adsorbed species and the reaction mechanism of the SCR of NO_x and N_2O [37,46,83-91]. Generally, adsorption of NO and co-adsorption of NO/O_2 leads to the formation of adsorbed NO_x ($x \geq 2$). In the presence of NH_3 or hydrocarbons, the formation of different adsorbed species/deposits can be detected. In general, adsorption of NO or NO/O_2 on Fe-ZSM-5 leads to the formation of bands at around 1577, 1627, 1743, 1880, 2140 and 2198 cm^{-1}. However, the assignment of some bands is ambiguously discussed. Table 2.2 gives an overview of the assignment of the different FT-IR bands that are reported in the literature. The 2198, 2140 and 1743 cm^{-1} bands are commonly assigned to $[NO^+][N_2O_4]$, NO^+ (occupying cation exchange sites in the zeolite matrix) and N_2O_4 respectively [86-89,151]. But the ambiguity is concerning the 1577, 1627 and 1880 cm^{-1} bands (Table 2.2). For instance, Chen and Sachtler et al. observed 1625 and 1570 cm^{-1} bands [87], the 1625 cm^{-1} band assigned to nitro group coordinating to an iron ion and the 1570 cm^{-1} band is attributed to nitrate group. Similarly, Lobree and Bell et al. also observed bands at 1620 and 1577 cm^{-1} and assigned these bands to NO_2 and NO_3 species respectively [88]. Different from the above author's assignment, Hadjiivanov et al. assigned [89] the 1620 cm^{-1} band to bridging nitrates and the band at 1575 cm^{-1} to bidentate nitrate (Table 2.2). On the other hand the same 1880 cm^{-1} band was assigned to NO adsorbed on isolated Fe^{+3} ions [152], isolated Fe^{+2} ions [87,88] and iron oxide clusters [105] (Table 2.2). Hence, in this work an attempt was made to clarify these contradictions and to give more insights into the structures of adsorbed species formed by the adsorption of NO, NO/O_2, NH_3 and isobutane/NO/O_2 by in situ FT-IR spectroscopic studies.

Table 2.2. Summary of the assignment of the different FT-IR bands

Band position (Wavenumber cm^{-1})	Assignment	Reference
2195	$[NO^+][N_2O_4]$	[86-89]
2133	(NO^+)	[87-89]
1880	Fe^{2+}-NO, Fe^{3+}-NO (γ)	[152]
	Fe^{2+}-NO (γ)	[88]
	Fe^{2+}-NO, Fe^{3+}-NO	[86]
	Fe^{2+}-NO	[89]
	$Fe^{2+}{}_2O_4$-NO (α)	[96]
1743	N_2O_4	[86,88,89]
1635	NO_2	[86,88]
1627	NO_2	[86,88]
1650-1600	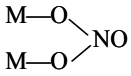	[89,153]
1605	NO_2	[87]
	NO_3	[88]
1575	NO_3	[86,88]
	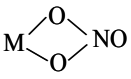	[89,153]
1465	O–N=O	[153]

Long and Yang studied the reaction mechanism of NH_3-SCR of NO over Fe-ZSM-5 catalysts [37,46,83]. Upon subsequent adsorption of NH_3, NO, NO/O_2 and the complete NH_3-SCR mixture they observed changes in the band positions and the appearance of new bands. On the basis of these findings they proposed a reaction mechanism, which is similar to that discussed in detail in the section 2.1.1. In this study the authors suggested that NO is first oxidized by Fe^{3+} ions to NO_2 which subsequently reacts with NH_4^+ ions to form active $NO_2(NH_4^+)_2$ complex. The active complex further reacts with NO to form N_2 and H_2O.

Sachtler et al. studied the reaction mechanism of HC-SCR of NO_x over a Fe-ZSM-5 sample prepared by sublimation [86,87]. They proposed that Fe^{3+} sites are active centers to oxidize NO to NO_2 and NO_3 (NO_x, $x > 2$). These NO_x species react with hydrocarbons to form N-containing active intermediates, the structure of which is not yet conclusively known. However, this intermediate is reactive towards NO/O_2 feed to form N_2 (section 2.1.1).

2.4.4. Other spectroscopic techniques

Solid-state NMR spectroscopy

Solid-state MAS ^{29}Si-NMR and ^{27}Al-NMR spectroscopy were implemented to probe the structural ordering of Fe^{+3} and Si^{+4} in Fe-silicalite and the coordination state of Si^{+4} and Al^{+3}

in Fe-ZSM-5 zeolites after hydrothermal synthesis and steam activation [56,104,108,139,140]. Depending on Fe^{+3} and Si^{+4} interactions one can readily distinguish between long and short range local ordering, since the nucleus Si^{+4} feels the dipolar coupling with the paramagnetic Fe^{+3} sites which strongly depends on the spatial organization of the material. Accordingly, the presence of iron in the framework broadened the Si resonance and causes a shift of the signal linear with the iron concentration. This indicates a uniform distribution of iron species and a high degree of spatial ordering in Fe-ZSM-5 zeolite [104]. Depending on the tetrahedral or octahedral coordination of the ^{27}Al-sites, peaks at different chemical shifts arise. Hence, ^{27}Al-NMR spectroscopy was utilized to investigate the changes of aluminum coordination in the zeolites upon calcination and steam treatment. This information gives a hint on the position of Al in the zeolite such as in the framework or in the extraframework position.

Mössbauer spectroscopy

Mössbauer spectroscopy is used to study the nature and distribution of iron species in iron rich Fe-MFI zeolites, since it can detect the iron in almost all forms i.e., different oxidation states (Fe^{+3} and Fe^{+2}), different coordination states (octahedral and tetrahedral) and different aggregation [36,104,118,139]. This ability distinguishes Mössbauer spectroscopy from other spectroscopic techniques. On the basis of isomer shift and quadrupole splitting parameters, the above mentioned different forms of iron species can be distinguished. On the other hand, the paramagnetic hyperfine structure in the presence of an external magnetic field provides information about the iron aggregation. However, small iron-oxo clusters such as oligomers require temperatures as low as < 1 K to get paramagnetic hyperfine structure resolved as compared to large aggregates. Large iron oxide clusters have different Debye temperatures as compared to isolated or oligomers [36]. Hence, this could lead to a biased spectral analysis. Accordingly, Grünert et al. have found that this technique overestimates large clusters and makes coexisting isolated Fe sites difficult to detect [36]. Furthermore, the low natural abundance of ^{57}Fe isotope limits the technique to only iron rich samples and thus, samples with low Fe content are difficult to analyze.

X-ray Photoelectron Spectroscopy

Oxidation states of iron species in Fe-MFI zeolites are often investigated by X-ray Photoelectron Spectroscopy (XPS) [36,104,83]. This technique is surface sensitive and gives information about the external surface region of the material. Thus, it was found that Fe species which are present inside the zeolite pores could not be seen by this technique. In this technique, the binding energies of photoelectrons, liberated from the electronic core shells of Fe-atoms by X-rays are scanned. Depending on the valence state of surface Fe species, the $Fe2p_{3/2}$ peaks appear at different binding energies. The binding energies of the $Fe2p_{3/2}$ usually reported around ≈ 711 eV and ≈ 708 eV were attributed to Fe^{+3} and Fe^{+2} ions respectively [36,104,83].

X-ray absorption spectroscopy

X-ray absorption spectroscopy has been extensively used to investigate the coordination, oxidation state as well as atomic bonding parameters such as bond lengths and coordination

numbers of iron ions in Fe-MFI zeolites [35,36,56,57,62,64,65,86,93,105,108,111,116]. In particular, the near edge region of X-ray absorption (XANES) has been proven to be a valuable technique to gain qualitative information on coordination and oxidation state of iron ions. Thus, a well defined pre-edge peak, which arises from the 1s → 3d transition, at around 7110.5 eV was attributed to Fe^{+3} ions in tetrahedral or distorted octahedral coordination. The region behind the edge was used to analyse the degree of agglomeration of iron species.

This technique has been used in situ under conditions of isobutane SCR of NO at 623 K to monitor changes in both coordination and oxidation state of iron species and to derive information on active sites in Fe-ZSM-5 prepared by sublimation [35]. In this study, the sample was treated subsequently with He, O_2, isobutane, NO, NO/O_2 and isobutane/NO/O_2. On the basis of the changes in the intensity of the pre-edge peak and the position of the Fe k edge peak, Koningsberger et al. studied the oxidation and coordination state of iron species in Fe-ZSM-5 zeolite [35]. Accordingly, XANES spectra of the catalyst after He, O_2 and isobutane SCR of NO treatments were compared. The authors found that the spectrum after O_2 treatment was similar to that of the spectrum after isobutane SCR of NO. Hence, they concluded that the mean oxidation state of iron under isobutane-SCR conditions is +3. These results were further supported by EXAFS and are discussed below.

EXAFS has been utilized to elucidate the coordination numbers, bond lengths, inter-atomic distances and degree of agglomeration of FeO_x species. Thus, it has been used in situ under isobutane-SCR conditions [35]. As mentioned above, after subsequent feed treatments Koningsberger et al. studied the changes in the Fe-O and Fe-Fe coordination sphere [35]. Mainly they discussed changes in the Fe-O_1 coordination sphere in the *R* range of 1.0 to 2.0 Å, which was attributed to Fe-O-Fe dimers. The changes in the intensity of Fe-O_1 shell after He, O_2, isobutane, NO and NO/O_2 treatments were ascribed to the redox behavior of these dimers. Spectra of the catalyst after O_2 treatment and isobutane-SCR reaction were compared and found to have similar spectra feature. Hence, they concluded that the mean oxidation state of iron is +3 in Fe-ZSM-5 catalyst under typical conditions of isobutane-SCR of NO.

However, EXAFS can only give average coordination values of different iron species present in the sample and thus it is difficult to distinguish between different Fe sites (e.g. isolated ions, oligomers including dimers and large clusters) when they are coexisting in the same sample. Recently, Grünert et al. found that this technique is not sensitive enough to the poorly ordered intra-zeolitic iron oxide clusters [64]. Hence, using this technique, one cannot achieve unambiguous information about the degree of agglomeration of iron species, which is often encountered in Fe-molecular sieves. In summary, X-ray absorption spectroscopy is most sensitive for highly dispersed iron species but not for clusters hence, clusters could be underestimated.

Temperature-programmed desorption of NH_3

Temperature-programmed desorption of NH_3 (NH_3-TPD) was also applied to evaluate the intrinsic acidity of the catalysts [103,141,144,145]. The strength of the acidic sites in Fe-MFI zeolites can be qualitatively estimated by the desorption temperature of NH_3: the stronger the acidic sites, the stronger NH_3 is bound and, thus, the higher is the temperature needed for

its desorption. However, in contrast to FT-IR of pyridine/NH_3 adsorption, it is not possible to distinguish between Lewis and Brønsted acidity by NH_3-TPD directly.

In summary, after critical review of the different characterization techniques it appears that, certainly, every technique has its own unique character to analyse Fe-zeolites but most of them are not able to distinguish between isolated Fe^{3+} species of different structure and iron oxide clusters of different nuclearity when they coexist in the same sample. For instance, Mössbauer spectroscopy is suitable for iron rich samples. However, it can also be used if samples are ^{57}Fe enriched. In the presence of clusters, it is difficult to detect isolated Fe species and the large iron oxide clusters can be over estimated. X-ray photoelectron spectroscopy (XPS) is surface sensitive and it cannot detect Fe species that are present inside the pores. On the other hand, X-ray absorption spectroscopy (XAS) is sensitive only for highly dispersed Fe species but not for poorly ordered intra-zeolitic iron oxide clusters which are frequently present in the Fe-zeolites. By using NH_3-TPD, intrinsic acidity of the zeolite can be measured but this technique cannot distinguish between Lewis and Brønsted acidity of the zeolite.

However, from this critical review it also appears that EPR and UV/VIS-DRS are able to detect Fe^{3+} species in a variety of forms and at any concentration in the Fe-zeolite. First of all, EPR is a sensitive technique to identify isolated Fe^{3+} species of different coordination geometry by the position of their signals and Fe_xO_y clusters of different degree of aggregation by analysis of the mutual magnetic interactions of the Fe sites. The position of the charge-transfer (CT) bands of Fe^{3+} species in UV/VIS-DRS strongly depends on the coordination number and the degree of aggregation. Therefore, these two techniques are powerful tools to distinguish between isolated Fe^{3+} sites of different structures on the one hand and Fe_xO_y clusters of different nuclearity on the other hand.

FT-IR spectroscopy, on the other hand, is suitable to study the strength of the acidity and to distinguish between Lewis and Brønsted acidity of the zeolite by the position of the bands, which are characteristic for the interaction of the probe molecule (e.g., pyridine) with Lewis and Brønsted acid centres. Finally, considering all these special benefits of EPR, UV/VIS-DRS and FT-IR spectroscopy for characterizing complex materials like Fe-zeolites, these three techniques have been used for this thesis work to give more insights into the structure of Fe-oxo species formed by different preparation techniques and acidic properties of different Fe-zeolites with different framework composition as well as after different pre-treatments. Furthermore, these techniques have been used under in situ conditions (in the presence of reactants) to throw some light on the nature of active iron sites and adsorbed species.

3. Experimental

3.1 Synthesis of Fe-containing zeolites

In this section, the different preparation procedures are described and the code used to label catalysts with respect to their preparation is explained. Mesoporous Fe-containing silica has been prepared within the work of this thesis. Fe-MFI and Fe-beta catalysts have not been prepared within this thesis work but were provided by the cooperation partners Prof. Dr. W. Grünert (Ruhr Universität Bochum, Germany) and Prof. Dr. Pérez-Ramírez (Yara-Technology Center Porsgrun, Norway/ICREA, Tarragona, Spain). Nevertheless, the main features of their preparation procedures are shortly described in this section since they lead to different Fe speciations as revealed by the spectroscopic techniques used in this thesis.

3.1.1 Microporous Fe-MFI and Fe-beta zeolites

Fe-ZSM-5 catalysts were prepared by six different methods (a-f). Samples provided by Prof. Dr. W. Grünert were prepared by methods a-c and e using two different H-ZSM-5 supports which were obtained from commercial Na-ZSM-5 with different Si/Al ratio (≈ 14 and ≈ 40, the latter with high density of structure defects, e.g. silanol nests, labeled A and B, respectively) by treating with 0.1 M HCl. The first one (A) was used for all six preparations, the second one (B) was used only for the CVD method for comparative purposes.

Samples provided by Prof. Dr. Pérez-Ramírez were prepared by methods a (chemical vapor deposition), d (liquid ion exchange) and f (hydrothermal synthesis followed by steam activation). Two different commercial H-ZSM-5 (Si/Al ≈14) and NH_4-ZSM-5 (Si/Al ≈37) supports (Degussa and Zeolyst) were used for CVD and liquid ion exchange methods respectively.

a. Chemical Vapour Deposition (CVD)

This preparation method was proposed by H.-Y. Chen and W. M. H. Sachtler [31]. Samples provided by Prof. Dr. W. Grünert were prepared according to the following procedure. Fe ions were introduced into the dried parent H-ZSM-5 matrices (A and B) by evaporating anhydrous $FeCl_3$ in an inert atmosphere into the pores of the zeolite followed by washing with 1 l or 10 l water per 5 g catalyst (W1 and W10, respectively) and calcination in air. The standard calcination procedure [36,55] was as follows: samples were heated in air from 293 K to 423 K at 2 K/min and kept isothermally at this temperature for 15 min, further heated to 873 K with a heating rate of 5 K/min and kept isothermally at this temperature for 2 h. Besides, a heating rate of 0.5 K/min was also used to elucidate the influence of different heating rates on the properties of the catalysts. Details on the preparation procedure and pretreatment conditions of these zeolites can be found elsewhere [36,55].

Throughout this thesis sample labels reflecting the preparation history are used. The label is composed of symbols for the type of ZSM-5, Fe introduction route, washing intensity and heating rate during calcination. Thus, A(CVD,W1,C0.5) means a material in which Fe was introduced via CVD into ZSM-5 of type A, washed with 1 l water per 5 g catalyst and

calcined with a heating rate of 0.5 K/min. Missing symbols mean that the respective step has been omitted (i.e., A(CVD,W1) is A(CVD,W1,Cx) before calcination with a ramp of x K/min). The Fe content of the samples has been determined in the group of Prof. Dr. W. Grünert by ICP analysis. It amounted to 5.4 wt.-% for A(CVD, W1), 5.0 wt.-% for A(CVD,W10) and 2.6 wt.-% for B(CVD,W1) (Table 3.1).

A sample provided by Prof. Dr. Pérez-Ramírez was also prepared by the same CVD procedure as proposed by H.-Y. Chen and W. M. H. Sachtler [31]. Fe ions were introduced into a dried parent H-ZSM-5(A) (Si/Al ≈14) by using anhydrous $FeCl_3$ followed by washing and calcination in static air at 823 K for 5 h [58]. The resulting catalyst is labeled as A'(CVD,W1,C2). The chemical composition of the catalysts was determined by ICP and is presented in Table 3.1.

b. Solid State Ion Exchange (SSIE)

Solid state ion exchange was performed by mixing 7 g of H-ZSM-5(A) and 3.5 g of $FeCl_3 \cdot 6\ H_2O$. The mixture was placed into a porcelain boat and heated in nitrogen flow (50 ml/min) at 573 K for 1 h followed by washing with 1 l of double deionized water and calcined according to the standard calcination procedure [36,55]. The same washing and calcination procedures are also used for samples in subsections c, d and e. Henceforth, these two steps are omitted from the sample labeling for the sake of clarity. The Fe content of the sample determined by ICP analysis amounted to 5.2 wt.-% for A(SSIE). The resulting sample is labeled as A(SSIE)5.2 (Table 3.1). For some experiments uncalcined sample was used and is mentioned so.

c. Mechanochemical Route (MR)

This method comprises intense grinding of the parent H-ZSM-5(A) with $FeCl_3 \cdot 6\ H_2O$, followed by 2-3 short-time washing steps (0.5 l water per 2 g catalyst). Calcination was performed according to the standard procedure in air at 873 K for 2 h [33,55]. The Fe content of the sample determined by ICP analyses amounted to 0.5 wt.-% for A(MR). The sample is labeled as A(MR)0.5 (Table 3.1). For some experiments uncalcined sample was used and is mentioned so.

d. Conventional liquid ion exchange method

A sample provided by Prof. Dr. Pérez-Ramírez was prepared by conventional aqueous ion exchange. Diluted solutions (0.30 mM) of $Fe(NO_3)_3 . 9H_2O$ and NH_4-ZSM-5 (Zeolyst with Si/Al ≈37) were vigorously stirred at 293 K for 15 h without control of the pH. The ion-exchanged zeolite was then filtered, washed thoroughly, dried and finally calcined in static air at 823 K for 5 h. The Fe-content of the catalyst determined by ICP is 1.4 wt% (Table 3.1). This catalyst is labeled as Fe-ZSM-5(LIE)1.4 [58].

e. Improved Liquid Ion Exchange (ILIE)

R. Q. Long and R. T. Yang proposed this preparation method [106]. Ion exchange was performed in Ar flow in order to prevent oxidation of Fe^{+2} to Fe^{+3} during exchange, by using

different amounts of iron powder in 200 ml of 0.1 M HCl and 2 g of H-ZSM-5(A) support stirred at 293 K for 5 days. The ion exchanged zeolites were then filtered, washed with deionized water, dried and finally calcined according to the standard procedure in air at 823 K with a heating rate of 5 K/min. The iron percentage was determined by ICP. The resulting five catalysts are labeled as: A(ILIE)0.2 (that means a sample prepared by improved liquid ion exchange and containing 0.2 wt.-% iron (Table 3.1)), A(ILIE)0.3, A(ILIE)0.6, A(ILIE)0.7 and A(ILIE)1.2 [115].

f. Hydrothermal synthesis of FeMFI and Fe-beta catalysts

As synthesized, calcined and steamed Fe-silicalite, Fe-ZSM-5 and Fe-beta samples provided by Prof. Dr. Pérez-Ramírez were prepared by isomorphous substitution of iron in the zeolite framework. The preparation procedure is described in detail elsewhere [41,58,154,155]. Briefly, for Fe-silicalite, a solution of Tetraethylorthosilicate, tetrapropyl ammonium hydroxide and NaOH was dropwise added to an iron nitrate solution while for Fe-ZSM-5, aluminum nitrate was additionally added as Al source. The gel was then treated in a static air at 448 K for 5 days in a stainless steel autoclave lined with Teflon. The solid was filtered and washed with deionized water. The as-synthesized sample was calcined in air at 823 K and converted into the H-form by exchange with ammonium nitrate solution followed by calcination at 823 K for 5 h.

For Fe-beta the preparation procedure was modified using TEAOH as templating agent and HF was added as a mineraliser agent. The gel was heated in a Teflon-lined steel autoclave at 423 K for 10 days under static conditions. The solid was washed, dried at 353 K, and calcined at 853 K for 3 h.

Finally, the calcined Fe-zeolites were activated in flowing steam at ambient pressure (water partial pressure of 300 mbar and 30 ml STP min^{-1} of N_2 flow) at 873 K during 5 h. A ramp of 2 K min^{-1} was used during heating up and cooling down the sample in N_2. The resulting catalysts were labeled as: *c*-Fe-silicalite, *c*-Fe-ZSM-5, *c*-Fe- beta, *ex*-Fe-silicalite *ex*-Fe-ZSM-5 and *ex*-Fe- beta that mean samples calcined (*c*) and steam activated (*ex*) respectively. The chemical composition of the catalysts was determined by ICP and is presented in Table 3.1.

3.1.2 Mesoporous Fe-SBA-15

g. Impregnation by incipient wetness

The parent siliceous SBA-15 material was provided by Dr. H. Kosslick (ACA Berlin) and was prepared by an optimized synthesis procedure, details of which are described in [156]. The BET surface area and the average pore diameter of the Si-SBA-15 support were determined to be 558 m^2/g and 7-8 nm respectively.

Iron was introduced into the parent SBA-15 by impregnation. 0.1092 g of iron acetylacetonate, $Fe(acac)_3$ (purity > 97 %, Fluka Chemicals), was dissolved in 10 ml of acetone. The resulting solution was added dropwise to 1.6517 g of the SBA-15 support, which had been pretreated in air at 673 K for 30 min to remove adsorbed moisture. The resulting sample was dried at 293 K and subsequently calcined in airflow at 823 K for 2 h with a heating rate of 5

K/min. The washing step was omitted for this sample. The Fe% of the catalyst was determined by ICP to be 0.95 Fe Wt.% (Table 3.1). The resulting catalyst was labeled as: (Fe-SBA-I)0.95, that means iron deposited in SBA-15 support via impregnation method and contains 0.95 wt.% iron. The structure of SBA-15 consists of a well-ordered hexagonal array of linear cylindrical channels (d = 7.5 nm) [157,158].

Table 3.1. Chemical composition of the catalysts as determined by ICP-OES [55,58,64,159]

Catalyst	Fe(wt%)	Si/Al	Catalyst	Si/Al	Fe(wt%)
A(CVD,W1)	5.4	14	A(ILIE)0.2	14	0.2
A(CVD,W1,C0.5)	5.4	14	A(ILIE)0.3	14	0.3
A(CVD,W1,C5)	5.4	14	A(ILIE)0.6	14	0.6
A(CVD,W10)	5.0	14	A(ILIE)0.7	14	0.7
A'(CVD,W1,C2)	5.0	14	A(ILIE)1.2	14	1.2
B(CVD,W1)	2.6	44	Fe-ZSM-5(LIE)1.4	37	1.4
B(CVD,W1,C5)	2.6	44	*c*-Fe-silicalite	∞	0.68
A(SSIE)5.2 uncalcined	5.2	14	*ex*-Fe-silicalite	∞	0.68
A(SSIE)5.2	5.2	14	*c*-Fe-ZSM-5	31	0.67
A(MR)0.5 uncalcined	0.5	14	*ex*-Fe-ZSM-5	31	0.67
A(MR)0.5	0.5	14	*c*-Fe-beta	31.5	0.61
(Fe-SBA-I)0.95	∞	0.95	*ex*-Fe-beta	31.8	0.63

3.2 Characterisation of the catalysts

3.2.1 EPR spectroscopy

EPR spectra in the X-band ($\nu \approx 9.5$ GHz) were recorded with the cw-spectrometer ELEXSYS 500-10/12 (Bruker) using a microwave power of 6.3 mW, a modulation frequency of 100 kHz and a modulation amplitude of 0.5 mT. The magnetic field was measured with respect to the standard 2,2-diphenyl-1-picrylhydrazyl hydrate (DPPH). For temperature-dependent measurements in the range from 90 to 293 K, a commercial variable temperature control unit (Bruker) and a conventional EPR sample tube was used, while in situ EPR measurements during calcination in the range $293 < T/K < 773$ and in situ measurements in the presence of reactants were performed in a home-made EPR flow reactor (Fig. 3.1) which was placed into the rectangular X-band cavity of the spectrometer [147]. Temperature programmer (Eurotherm) and a gas dosing system with mass flow controllers (Bronkhorst) were attached to the system for controlling temperature and gas flows. In situ EPR experiments with NH_3, isobutane, CO, NO and N_2O were performed at 623 K since at this temperature all catalysts have shown substantial activity in steady-state catalytic experiments. For all experiments 50 mg of granular catalyst with a particle size of 125-200 μm was used.

Low temperature NH_3 interaction experiments with A(MR)0.5 and A(CVD,W1,C5) were performed at 293 K according to the following sequence: (a) pretreatment in air (10 ml/min) at 773 K for 1 h and cooling to 293 K, (b) changing the flow from air to 1% NH_3/He

(10 ml/min) for 1 h followed by flushing with N_2 at the same temperature for 15 min. Spectra were recorded after each treatment.

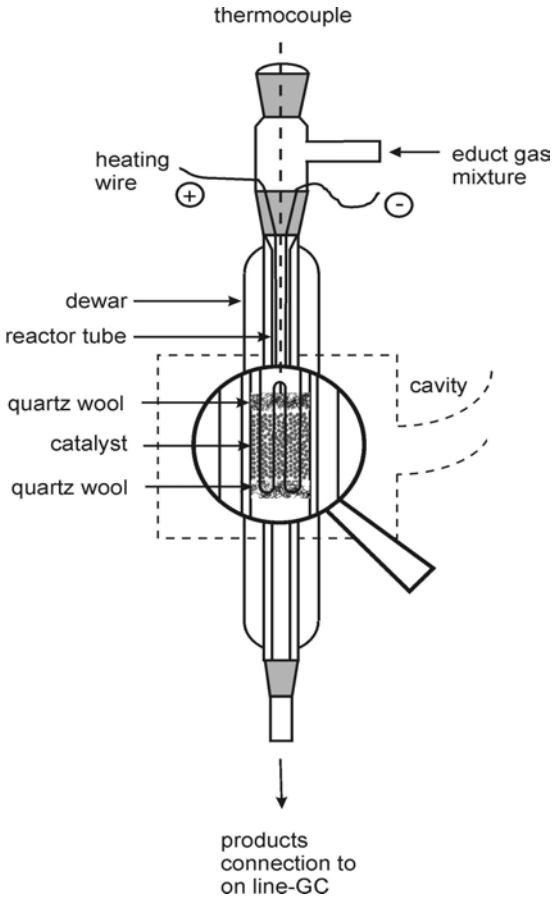

Fig. 3.1. Home-made EPR flow reactor for in situ measurements [147].

For NH_3 or isobutane-SCR, the catalysts were treated according to the following sequence: (a) pretreatment in air (20 ml min^{-1}) at 773 K for 1 h and cooling to 623 K (denoted as the reaction temperature), (b) changing the flow from air subsequently to total feed, i.e., 0.1% NO, 0.1% reducing agent and 2% O_2/He (reducing agent: NH_3 or isobutane, respectively) (GHSV for NH_3 and isobutane-SCR was 30,000 h^{-1}) for 1 h, (c) switching to air (20 ml min^{-1}) for 1 h and for 15 min at 773 K to ensure complete reoxidation of iron species having been reduced in step (b), followed by cooling to 623 K again, (d) changing flow from air to 0.1% NH_3/He (34.7 ml/min) or 0.1% isobutane/He (34.7 ml/min) for 1 h, and (f) switching to 0.1% NO/He (34.7 ml/min) for 1 h.

To study the influence of temperature on the redox behaviour of different isolated Fe sites, subsequent interactions of 0.1% NH_3/He and 0.1% NO/He with Fe-ZSM-5 were also performed at 773 K in the following sequence: (a) pretreatment in air (20 ml min^{-1}) at 773 K for 1 h, (b) changing the flow from air to 0.1% NH_3/He (34.7 ml/min) for 1 h, and (f) switching to 0.1% NO/He (34.7 ml/min) for 1 h.

In situ experiments with N_2O and CO were performed according to the following sequence: (a) heating in air (15 ml/min) at 773 K for 1 h and cooling to 623 K (denoted as the reaction temperature), (b) changing the flow from air to 2 vol.% N_2O/He (12.5 ml/min) for

1 h, (c) switching to 2 vol.% CO/He (12.5 ml/min) for 1 h, and finally (d) switching back to 2 vol.% N_2O/He (12.5 ml/min) at reaction temperature.

Additional in situ EPR experiments over A'(CVD,W1,C2) were performed at atmospheric pressure at 623 K with mixtures of 1 vol.% N_2O + 1 vol.% CO in He (25 ml/min) and 0.66 vol.% N_2O + 1.34 vol.% CO in He (18.7 ml/min). For on-line analysis of N_2 formed during N_2O-CO reaction, the outlet of the EPR flow reactor was connected to a GC 17AAF capillary gas chromatograph (Shimadzu) equipped with a 30 m × 0.32 mm molecular sieve 5A column (CP-7534, Chrompack) and a thermal conductivity detector.

3.2.2 UV/VIS-DRS measurements

UV/VIS-DRS measurements were performed with a Cary 400 spectrometer (Varian) equipped with a diffuse reflectance accessory (praying mantis, Harrick, Fig. 3.2). To reduce light absorption, catalysts were diluted with α-Al_2O_3 (calcined at 1473 K for 4 hours), also used as white reference sample, in a ratio of 1:3, 1:5 or 1:10. The UV/VIS-DR spectra were collected in reflectance mode and evaluated after converting them into the Kubelka-Munk-Function (F(R)).

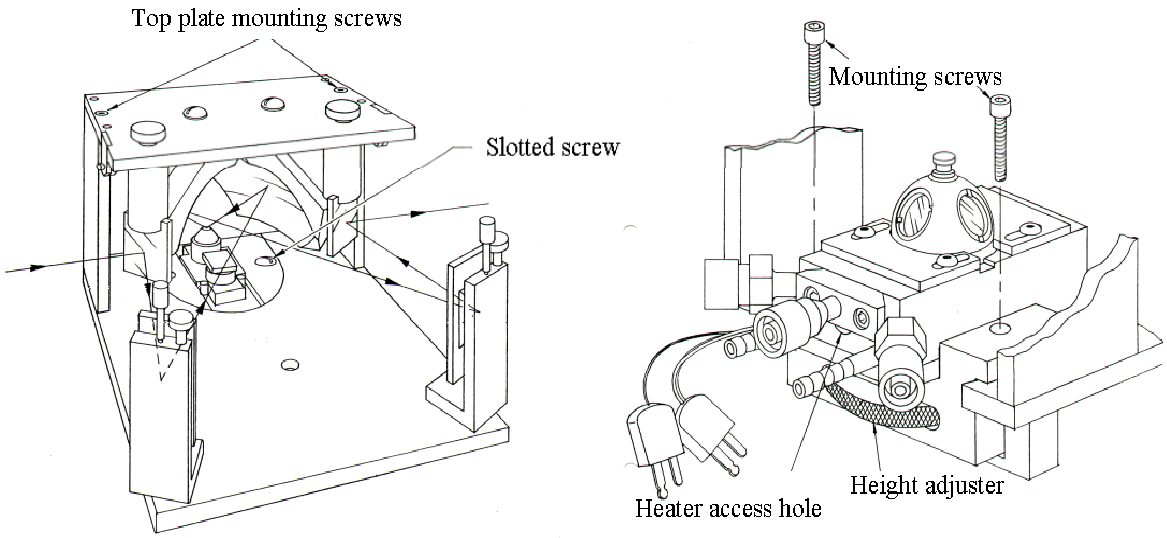

Fig. 3.2. In situ DRS cell: left praying mantis (Harrick) diffuse reflection attachment and right stainless steel reaction chamber.

UV/VIS-DR spectra were deconvoluted into subbands with Gaussian line shape by means of GRAMS/32 software (Galactic), which uses a least-square fitting algorithm. In practice, the peak fitting was run until satisfactory statistical results were obtained, i.e. until the solution was converged. This occurs when reduced χ^2 (Chi squared) has reached a minimum and five successive iterations have not significantly improved the fit. A fitting is considered to be converged if χ^2 value is lower than 3. The spectra were interpreted by comparing positions of the peaks, obtained from deconvolution, with the literature data.

In situ measurements at elevated temperatures and in flowing gas mixtures were carried

out in a heatable reaction chamber (Harrick) (Fig. 3.2) equipped with a temperature programmer (Eurotherm) and a gas dosing system with mass flow controllers (Bronkhorst).

For elucidating the influence of calcination conditions on the nature of the Fe sites, the effect of calcination on selected catalysts was studied by performing in situ calcination in air using the standard calcination procedure (section 3.1.1.a).

The reduction/reoxidation behavior of selected catalysts was analyzed by treatment in a flow of 20 vol.% H_2 in N_2 (10 ml/min) and air (10 ml/min) respectively at 773 K at ambient pressure for 1 h. After the respective treatment, the catalysts were cooled to 293 K in the same mixture and the spectrum was recorded.

Kinetic studies of the reduction/reoxidation were performed with A(ILIE)0.3 and A(ILIE)1.2 at 673 K. The time dependence of the absorbance (at 238 and 290 nm for isolated Fe^{+3} ions and 350 nm for iron oxide clusters) was measured in reducing and oxidizing atmospheres. The obtained redox kinetic curves were evaluated according to a pseudo-first order rate law using the following equation:

$$Abs_t = Abs_{t=\infty} + (Abs_{t=0} - Abs_{t=\infty})\, e^{-kt} \qquad (3.1)$$

Here, $Abs_{t=0}$, Abs_t and $Abs_{t=\infty}$ are the absorbance values at a given wavelength at the start of the experiment, at time t and after reaching steady state respectively.

The reduction and reoxidation treatments were performed according to the following sequence: (a) pretreatment in air (10 ml/min) at 773 K for 1 h and cooling to 673 K, (b) changing the flow from air to 1% NH_3/He (10 ml/min) for 2 h, and (c) switching to air (10 ml/min) for 2 h. After treatments (a) and (b) the pipeline was flushed with N_2 for 5 min. Spectra were recorded after each treatment.

In situ measurements with NH_3, isobutane, CO, NO and N_2O were performed according to the same sequence and with the same gas composition and flow rate as described for in situ EPR experiments.

3.2.3 FT-IR spectroscopy

The surface acidity of the Fe-zeolites was studied by FT-IR spectroscopic analysis of adsorbed pyridine. Spectra were recorded using a Bruker IFS 66 spectrometer equipped with a heatable and evacuable reaction cell with CaF_2 windows, connected to a gas dosing and evacuation system. The zeolite powder was pressed into self-supporting wafers with a diameter of 20 mm and a weight of 50 mg. Prior to pyridine adsorption, the samples were pretreated in flowing air (30 ml/min) at 673 K for 1 h followed by cooling to 373 K. Then, pyridine was adsorbed at 373 K for 1 h by bubbling an argon flow (60 ml/min) through a pyridine-containing saturator (at 293 K). Physisorbed pyridine was removed by evacuation for 30 min at 373 K and infrared spectra were recorded at the same temperature with 2 cm^{-1} resolution and 100 scans.

NO adsorption experiments on pre-oxidized and pre-reduced surfaces of H-ZSM-5(A), A(CVD,W1,C5), A(MR)0.5, A(ILIE)0.3 and A(ILIE)1.2 were performed according to the following sequence: samples were oxidatively pretreated in air flow (30 ml/min) at 673 K for

1 h followed by cooling to 293 K and initial spectra were recorded for oxidized surfaces. NO adsorption was performed at 293 K with 1% NO/He (40 ml/min) for 1 h followed by evacuation at the same temperature for 30 min. Spectra were recorded before and after evacuation.

Subsequently, the samples were heated in air at 673 K for 1 h. At this temperature, the flow was changed from air to 2 or 10% NH_3/He (40 ml/min) for 1 h followed by evacuation at the same temperature for 30 min. Afterwards samples were cooled to 293 K and evacuated for 30 min and initial spectra were recorded for reduced surfaces. NO interaction with prereduced zeolites was studied by switching to 1% NO/He (40 ml/min) at 293 K for 1 h followed by evacuation at the same temperature for 30 min and spectra were recorded before and after evacuation with 2 cm^{-1} resolution and 100 scans.

In situ FT-IR experiments over H-ZSM-5(A), A(ILIE)0.2 and A(ILIE)1.2 with isobutane and NO were performed at 623 K. The catalysts were treated according to the following sequence: (a) pretreatment in air (30 ml/min) at 673 K for 1 h and cooling to 623 K, (b) changing the flow from air subsequently to total feed, i.e., 1% NO/He (30 ml/min), 1% isobutane/He (30 ml/min) and air (30 ml/min) for 1 h. Spectra were recorded after different time intervals after which samples were evacuated and spectra were recorded again. Subsequently, samples were heated again in air (30 ml/min) at 623 K for 1 h and spectra were recorded at the same temperature.

3.3 Catalytic tests

Activity measurements of catalysts in the SCR of NO either with NH_3 or isobutane and SCR of N_2O with CO or direct N_2O decomposition were performed at the laboratories of Prof. Dr. W. Grünert and Prof. Dr. Pérez-Ramírez respectively. However, since the results of these tests are discussed in this thesis in relation to the nature of the Fe sites in the tested zeolites, the main features of these tests are shortly described below.

3.3.1 SCR of NO either with NH_3 or isobutane

The selective reduction of NO with isobutane or NH_3 was studied in a catalytic micro-flow reactor with a product analysis scheme that combined calibrated mass spectrometry, gas chromatography and non-dispersive IR photometry (NH_3). Feed gases containing 1000 ppm NO, 1000 ppm reductant (isobutane or NH_3), 2 % O_2 in He were charged onto the catalyst at GHSV of 30,000 and 42,000 h^{-1} for isobutane-SCR and 750,000 h^{-1} for NH_3-SCR. Generally, the catalytic runs were started with a thermal activation and stabilization treatment of the catalysts in flowing He at 823 K (isobutane) or at 873 K (NH_3). The activities were measured from the higher to the lower reaction temperatures. Under experimental conditions, the only reaction product of NO observed in the limits of experimental accuracy was N_2, i.e. the NO conversions given are equal to N_2 yields [32,36,55,64].

3.3.2 SCR of N_2O with CO or direct N_2O decomposition

Activity measurements were carried out in a parallel-flow reactor system, similar to that described in [160], using 50 mg of catalyst (125-200 μm) and space velocities $W/F(N_2O)_o$ of $3 \cdot 10^5$ and $9 \cdot 10^5$ g s mol^{-1} at atmospheric pressure, where $W/F(N_2O)_o$ is the ratio between the catalyst mass and the molar flow of N_2O at the reactor inlet. Feed mixtures containing N_2O (1.5 mbar) and CO (0-1.5 mbar) in He were applied and conversions of both components were measured in the range between 475-1100 K. The product gases were analyzed by online gas chromatography. During the experiments, the mass balances of N, C, and O closed at > 98%. N_2O and CO conversions were calculated from the amount of N_2 and CO_2 formed, respectively [58,161,162].

4. Results

In this section, ex situ and in situ-UV/VIS-DR, EPR and FT-IR spectroscopic results obtained for the different catalysts are described in relation to their preparation procedure, as well as in dependence on their interaction with different reactants. Although catalytic tests have not been performed within this thesis, but in the laboratories of the cooperation partners Prof. Dr. W. Grünert and Dr. Javier Pérez-Ramírez, their main results are also shortly described in this section since their knowledge is essential for the discussion of structure-reactivity relationships (section 5.2)

4.1 Structure, distribution and redox behaviour of Fe species and surface acidity of the Fe-zeolites

First of all, results of the characterization of the zeolites by UV/VIS-DR, EPR and FT-IR spectroscopy are described in relation to their preparation procedure. These measurements were performed to investigate the effect of the genesis of the samples on the nature and distribution of iron species. For samples prepared by CVD, the influence of washing intensity, heating rate during calcination, Si/Al ratio of the zeolite matrix and use in the SCR reaction on the nature and distribution of iron species in Fe-ZSM-5 zeolites has been explicitly studied. Redox properties of iron species play a crucial role in the catalytic reactions, hence, redox kinetics of isolated Fe^{+3} ions and iron oxide clusters were studied by in situ UV/VIS-DRS. Surface acidity of the zeolites was analyzed by adsorption of pyridine using FT-IR spectroscopy.

4.1.1 UV/VIS-DRS studies

Assignment of UV/VIS-DRS signals

A typical UV/VIS spectrum of an Fe-containing zeolite is shown in Fig. 3 (section 2.4.2). It is characterized by a broad absorption which is deconvoluted into subbands to facilitate the assignment of different iron species. In principle, two ligand-to-metal charge-transfer (CT) transitions, $t_1 \rightarrow t_2$ and $t_1 \rightarrow e$, are to be expected for a Fe^{3+} ion [132]. For isolated Fe^{3+} ions they fall in the high energy range of the spectrum, usually below 300 nm, whereby their particular position depends on the number of ligands. Thus, CT bands of isomorphously incorporated tetrahedrally coordinated Fe^{3+} ions have been observed at 215 and 241 nm in Fe-silicalite [66] while a band at 278 nm is detected for isolated octahedral Fe^{3+} sites in Al_2O_3 [135]. Although a clear discrimination of CT bands of isolated Fe^{3+} ions in tetrahedral and higher coordination is not straightforward due to their similar wavelength range, these values suggest that CT bands of Fe^{3+} ions are red-shifted with increasing number of coordinating oxygen ligands. The same trend has been observed accordingly also for V^{5+} species [163]. Based on these considerations, subbands below 250 nm are assigned to isolated tetrahedral Fe^{3+} while those between 250 and 300 nm are attributed to isolated Fe^{3+} with a higher number of coordinating ligands.

CT bands between 300 and 400 nm are assigned to octahedral Fe^{3+} in small oligomeric Fe_xO_y clusters [66] while bands above 450 nm arise from larger Fe_2O_3 particles as can be

seen, too, from the spectrum of the reference sample α-Fe_2O_3 (Fig. 6a). To facilitate band assignment, experimental spectra were deconvoluted into respective subbands (Fig. 3). For the deconvolution procedure, the lowest possible number of subbands has been used. Since the two CT transitions for the same Fe^{3+} species are experimentally not resolved, they have been fitted by one subband only for each type of Fe^{3+} species (tetrahedral and octahedral coordination). For deriving a quantitative estimate of the different Fe species coexisting in the zeolite samples, the percentage of the subbands with respect to the total area of the experimental spectrum has been multiplied by the overall Fe content (determined by ICP-OES) (Table 4.1). Being aware that the obtained values in Table 4.1 are an estimate only due to issues discussed below, they are nevertheless regarded to be helpful for a comparison of different samples.

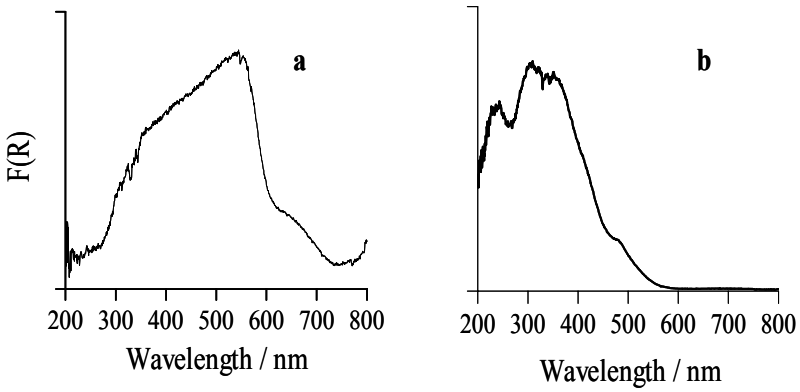

Fig. 4.1. UV/VIS-DR spectra of reference samples (a) α-Fe_2O_3 and (b) γ-Fe_2O_3 recorded at 298 K.

As seen from Fig. 4.1a, α-Fe_2O_3 does not contribute to the UV/VIS spectrum below 300 nm but γ-Fe_2O_3 (Fig. 4.1b), another reference sample, does contribute below 300 nm. This can cause some uncertainty when the area of deconvoluted subbands is used to derive the actual percentage of isolated sites in samples that contain also Fe_xO_y clusters because, depending on their structure, contributions of the particles in the wavelength region below 300 nm cannot be completely ruled out. In almost all particle containing samples, iron oxide particles are too small to be visible by XRD. However, EXAFS measurements of samples with higher Fe content (5.2 wt.%) point to the existence of oxide particles with an α-Fe_2O_3-like short range order [36]. Therefore, the existence of γ-Fe_2O_3 particles in the zeolites seems rather unlikely. However, to be on the safe side, the percentage of isolated and small oligonuclear Fe species in particle-containing samples (Table 4.1) has to be regarded as an upper limit.

In Fig. 2.3, light absorption above 300 nm occurs in a very broad range suggesting the superposition of CT bands for a variety of slightly different small oligonuclear Fe_xO_y clusters and larger Fe_2O_3 species. As mentioned above, for spectra deconvolution the lowest possible number of sub-bands in the range above 300 nm has been used that was needed to obtain a satisfactory fit of the experimental spectrum. This procedure is regarded to be acceptable, although a deconvolution of a broad and poorly structured experimental spectrum into sub-bands by mathematical means is always arbitrary to a certain extend. The subbands above 300

nm have to be understood in terms of reflecting a certain distribution of slightly different cluster geometries rather than representing a certain number of different individual cluster species.

In principle, *d-d* transitions of Fe^{3+} ions should also be considered between 350 and 550 nm. However, they are symmetry- and spin-forbidden and therefore, some orders of magnitude weaker than CT transitions. Hence, they are not visible and interpretation of the spectra is focused on the intense CT bands. Divalent iron does not contribute to the UV/VIS spectrum since its bands fall in the near-infrared range around 1000 nm [133]. However, Fe species in mixed valence iron oxides containing both Fe^{2+} and Fe^{3+} give rise to intervalence charge transfer (IVCT) transitions in the visible and near infrared region due electron delocalization between Fe^{2+} and Fe^{3+} ions.

The UV/VIS-DRS results of differently prepared Fe-zeolites are presented below with respect to the preparation method.

Chemical Vapor Deposition (CVD)

In the following section, the influence of washing, calcination steps and of use in catalysis as well as defect density of the parent ZSM-5 matrix (Si/Al ratio) on the UV/VIS spectra is described. The percentage of the different Fe species has been derived by spectra deconvolution for each sample (Table 4.1). However, for the sake of clarity, deconvoluted subbands are only shown in selected figures.

Influence of washing intensity

It has been reported in the literature that thorough washing is crucial for the formation of highly dispersed Fe structures [36,56]. In this study, the influence of the washing step was assessed by performing the washing procedure of A(CVD) with a total amount of 1 or 10 l water per 5 g catalyst (A(CVD,W1) and A(CVD,W10), respectively) (Fig. 4.2a).

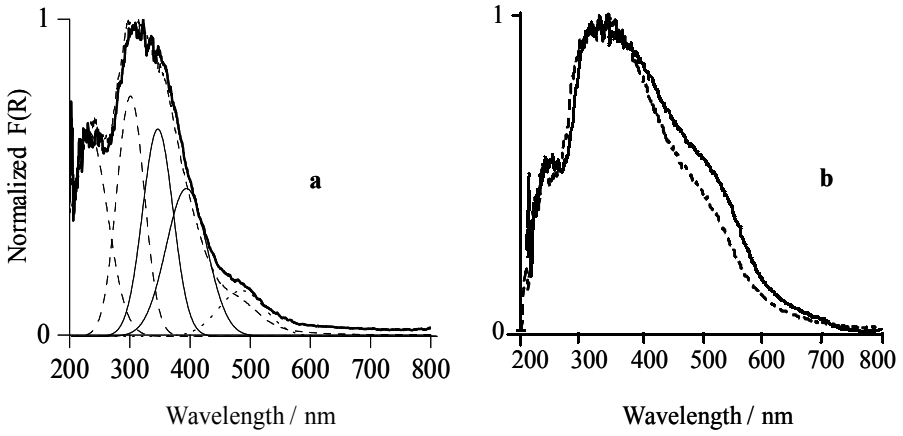

Fig. 4.2. UV/VIS-DR spectra of hydrated Fe-ZSM-5 samples at 293 K. (a) A(CVD,W1) (experimental spectrum, thick solid line) and deconvoluted subbands (thin lines), assignments: --- isolated Fe^{+3}, — small oligomeric Fe_xO_y moieties, …. Fe_2O_3-like clusters and A(CVD,W10) (experimental spectrum, broken line). (b) Experimental spectra of A(CVD,W1,C0.5) (solid line) and A(CVD,W10,C0.5) (broken line) after use in the SCR reaction. Samples were recalcined after catalysis in air at 823 K.

The UV/VIS spectrum of hydrated as-prepared A(CVD,W1) exhibits absorption mainly below 400 nm. The relative percentage of the deconvoluted subbands in Table 4.1 indicates that the majority of iron species is present as isolated ions and small oligomers. The band at ~500 nm suggests the presence of a certain amount of iron oxide particles which might have formed during the washing step.

In sample A(CVD,W10) light absorption above 400 nm is lower in comparison to sample A(CVD,W1) which indicates that intense washing diminishes the amount of large $Fe^{3+}_xO_y$ clusters slightly (Table 4.1). This effect is still clearly seen even in the calcined samples A(CVD,W1,C0.5) and A(CVD,W10,C0.5) after catalysis, although the calcination step itself forces cluster formation. This influence will be separately discussed below. This is in good agreement with earlier studies which show less clusters in A(CVD,W10,C0.5) as compared to A(CVD,W1,C0.5) [36].

Table 4.1. Percentage of the area of the sub-bands (I_1 at $\lambda < 300$ nm, I_2 at $300 < \lambda < 400$ nm, and I_3 at $\lambda > 400$ nm) derived by deconvolution of the UV/VIS-DRS spectra and corresponding Fe percentage derived from total Fe content determined by ICP [32,36,55,58,64,159,161].

Catalyst	I_1[a]/ %	Fe_1/wt.%	I_2[b]/ %	Fe_2/wt.%	I_3[c]/ %	Fe_3/wt.%	Total Fe Wt.%
A(CVD,W1)	47	2.53	45	2.43	8	0.43	5.4
A(CVD,W1,C0.5)	27	1.46	36	1.94	37	2.00	5.4
A(CVD,W1,C0.5) used	25	1.35	31	1.67	44	2.37	5.4
A(CVD,W1,C5)	27	1.46	35	1.89	38	2.05	5.4
A(CVD,W1,C5)used	22	1.19	30	1.62	48	2.59	5.4
A(CVD,W10)	46	2.30	47	2.35	7	0.35	5.0
A(CVD,W10,C0.5)used	27	1.35	36	1.80	36	1.8	5.0
A'(CVD,W1,C2)	44	2.19	45.2	2.25	10.8	0.54	5.0
B(CVD,W1)	28	0.73	45	1.17	27	0.70	2.6
B(CVD,W1,C5)	26	0.68	38	1.00	35	0.91	2.6
A(SSIE)5.2 uncalcined	32	1.66	37	1.90	31	1.62	5.2
A(SSIE)5.2	30	1.56	32	1.66	38	1.98	5.2
A(MR)0.5 uncalcined	91	0.45	9	0.05	-	-	0.5
A(MR)0.5	83	0.41	17	0.09	-	-	0.5
A(ILIE)0.2 uncalcined	100	0.2	-	-	-	-	0.2
A(ILIE)0.2	95	0.19	4.2	0.01	-	-	0.2
A(ILIE)0.3	95	0.28	5	0.01	-	-	0.3
A(ILIE)0.6	68.8	0.41	27.9	0.16	3.3	0.19	0.6
A(ILIE)0.7	60.7	0.42	35.7	0.25	3.5	0.02	0.7
A(ILIE)1.2 uncalcined	57.0	0.68	28	0.33	15	0.18	1.2
A(ILIE)1.2	40.8	0.48	41.7	0.5	17.5	0.21	1.2
Fe-ZSM-5(LIE)1.4	31.0	0.43	38.2	0.53	30.7	0.43	1.4
c-Fe-silicalite	100	0.68	-	-	-	-	0.68
ex-Fe-silicalite	93	0.63	7	0.04	-	-	0.68
ex-Fe-ZSM-5	44.3	0.29	41.5	0.27	14	0.09	0.67
c-Fe-beta	84	0.52	16	0.09	-	-	0.62
ex-Fe-beta	47	0.30	36	0.22	17	0.1	0.62
(Fe-SBA-I)0.95	89	0.88	11	0.11	-	-	0.95

[a] isolated Fe^{3+} in tetrahedral and higher coordination; [b] small oligomeric Fe_xO_y clusters; [c] large Fe_2O_3 particles.

Influence of calcination

It has been reported that the calcination step is crucial for the iron constitution in the final catalyst [57,116]. Hence, the influence of the calcination on the distribution of iron species was assessed by comparing UV/VIS spectra of sample A(CVD,W1) before calcination and after calcination in air at 873 K using heating rates of 0.5 and 5 K/min for A(CVD,W1,C0.5) and A(CVD,W1,C5), respectively (Fig. 4.3a). It is clearly seen from the UV/VIS spectra (Fig. 4.3a) that light absorption above 400 nm being characteristic of extended Fe_2O_3-like clusters increased considerably after calcination indicating the formation of Fe_2O_3 clusters upon calcination. This effect is somewhat higher after calcination with 5 K/min than with 0.5 K/min (Fig. 4.3a and Table 4.1).

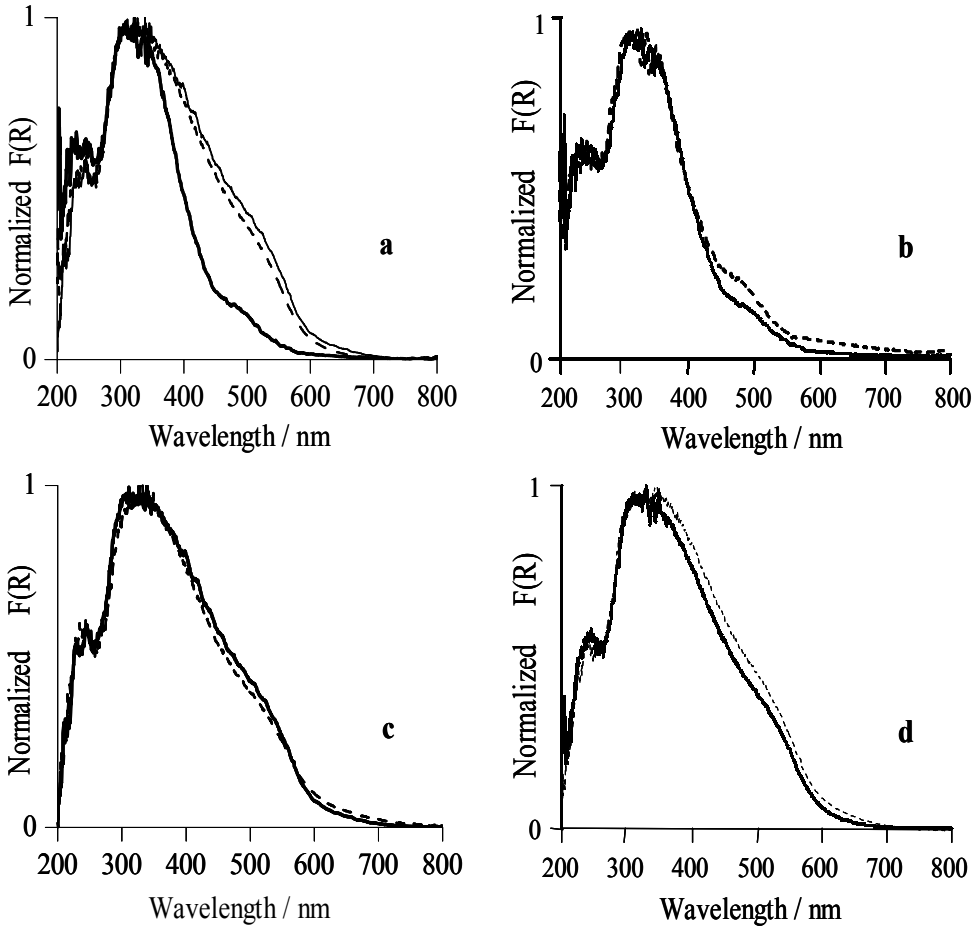

Fig. 4.3. UV/VIS-DR spectra of hydrated Fe-ZSM-5 samples recorded at 293 K. (a) A(CVD,W1) (thick solid line), A(CVD,W1,C0.5) (broken line) and A(CVD,W1,C5) (thin solid line). (b) B(CVD,W1) (broken line) and A(CVD,W1) (solid line); (c) B(CVD,W1,C5) (broken line) and A(CVD,W1,C5) (solid line). (d) A(CVD,W1,C0.5) before (thick line) and after (broken line) use in the SCR of NO, samples were recalcined after catalysis in air at 823 K.

Influence of the Al content and defect density of the parent ZSM-5 matrix

The effect of Si/Al ratio on the distribution of iron species in the parent ZSM-5 support was studied by subliming $FeCl_3$ into the ZSM-5 matrix B, which has a higher Si/Al ratio than matrix A (≈ 40 *vs.* ≈ 14). This, in turn, leads to a lower number of H^+ sites available for exchange by Fe ions, and a large amount of internal silanol groups, most likely silanol nests [36]. As expected, the total Fe content in sample B(CVD,W1) is lower than in sample A(CVD,W1) (Table 3.1), but the Fe/Al ratio of 1.13 [36] shows that sample B(CVD,W1) is even more overexchanged than A(CVD,W1) (Fe/Al ≈ 0.9). The UV/VIS spectra of as-prepared samples B(CVD,W1) and A(CVD,W1) are compared in Fig. 8b. It can be seen that there is a slightly higher percentage of extended Fe_2O_3-like clusters in sample B(CVD,W1) than in sample A(CVD,W1) (Fig. 4.3b and Table 4.1).

Interestingly, this trend is not retained for the calcined samples. Calcination with a heating rate of 5 K/min leads to a slightly less pronounced formation of large Fe_2O_3-like aggregates in sample B(CVD,W1,C5) compared to A(CVD,W1,C5) as evident from UV/VIS spectra in Fig. 4.3c. This may be explained by the presence of silanol nests in sample B(CVD,W1,C5), which may serve as additional nuclei for aggregation as has been suggested earlier on the basis of FT-IR, Mössbauer and EXAFS data [36]. In well-structured HZSM-5 matrices Fe_xO_y clusters being formed upon calcination have been shown to migrate towards the external crystal surface where they can grow further in size [57]. In contrast, silanol nests present in highly defective matrices could keep the clusters inside the crystal, thus, preventing their further growth.

Influence of the SCR reaction

In Figure 4.3d, UV/VIS spectra of catalyst A(CVD,W1,C0.5) before and after use in the SCR of NO with isobutane (duration 1 working day) are compared in order to trace structural changes that might occur in a precalcined catalyst under reaction conditions. The light absorption above 400 nm reflecting extended Fe_2O_3-like clusters is only slightly more pronounced after catalysis. The contribution of the sub-bands above 400 nm to the total intensity increases from 37 % to 44 % after the catalytic run (Table 4.1). This is almost exclusively at the expense of the subbands between 300 and 400 nm while the contribution of the isolated sites remains constant. Hence, during catalysis, large oxide particles are formed rather from small oligomeric moieties than from isolated Fe sites [55].

Solid-State Ion Exchange (SSIE)

The UV/VIS spectrum of sample A(SSIE)5.2 (uncalcined) is presented together with deconvoluted subbands in Fig. 4.4. From Fig. 4.4 and Table 4.1 it is evident that the sample contains a considerable amount of isolated Fe^{+3} ions (bands below 300) besides oligomeric $Fe^{3+}{}_xO_y$ moieties (bands between 300 to 400 nm) and large Fe_2O_3 particles (bands above 400 nm). This is in line with earlier studies in which α-Fe_2O_3 has been identified in the sample by both EXAFS and XRD [36]. Calcination causes additional clustering as evidenced by the increasing area of the subbands above 400 nm and the corresponding Fe percentage in Table 4.1.

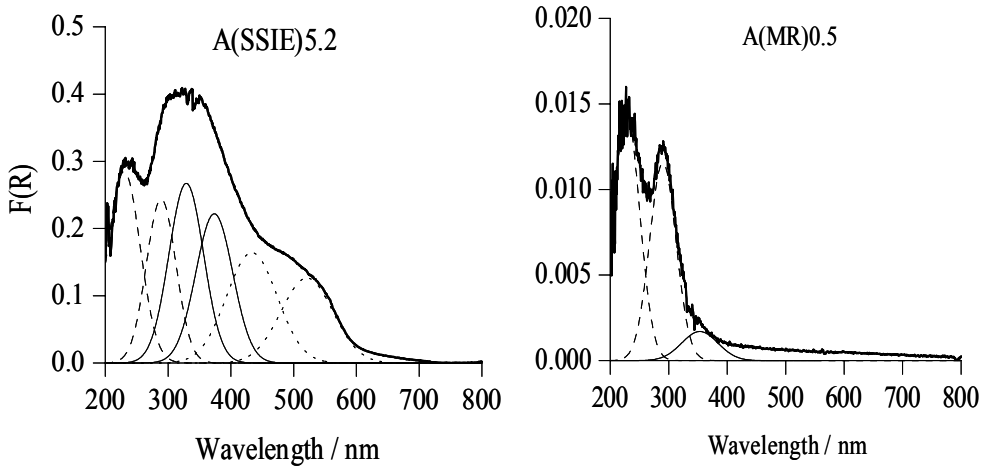

Fig. 4.4. UV/VIS-DR spectra and deconvoluted subbands of the hydrated uncalcined Fe-ZSM-5 zeolites recorded at 293 K, without pretreatment.

Mechanochemical Route (MR)

As discussed above, samples prepared by CVD and SSIE are highly heterogeneous with respect to the distribution of iron species which complicates assignment of catalytic activity in the SCR reaction to a particular iron species. Hence, it was essential to prepare a catalyst with preferably only isolated iron species. To this end Grünert et al. developed a so-called mechanochemical route to prepare highly dispersed iron species in the H-ZSM-5 matrix [32]. In the UV/VIS spectrum of the uncalcined sample A(MR)0.5 two intense bands appear at 228 and 290 nm (Fig. 4.4). Previous EXAFS measurements revealed that this sample is dominated by isolated Fe^{3+} sites with a mean coordination number between 4 and 6 suggesting that these Fe species are in both tetrahedral and higher coordination [32]. In agreement with these results the two strong bands in Fig. 4.4 are assigned to isolated Fe^{3+} sites in tetrahedral (228 nm) and higher coordination (290 nm). The band at 353 nm suggests the presence of a small amount of small oligomeric $Fe^{3+}_xO_y$ clusters. These species were earlier not found by EXAFS spectroscopy, since, obviously, this method is less sensitive to photon scattering from higher shells. These results illustrate the benefits derived from UV/VIS-DRS. As observed in samples CVD and SSIE, clusters are also formed in A(MR)0.5 upon calcination at the expense of isolated Fe species as evidenced by a decrease in the area of subbands and the corresponding Fe content (Table 4.1). However, the superior effectivity of this preparation route in creating mainly isolated Fe^{3+} sites is clearly evident.

Liquid ion exchange

The UV/VIS spectrum of Fe-ZSM-5(LIE)1.4 (Fig. 4.5) and the relative percentage of the deconvoluted subbands in Table 4.1 indicate that the majority of Fe^{3+} species is in the form of iron oxide clusters and iron oxide particles, besides about one third of the total iron content which is present as isolated Fe^{+3} ions. This is also in agreement with published HRTEM results [58], which indicated the presence of oxide particles with a size of ≈ 30 nm.

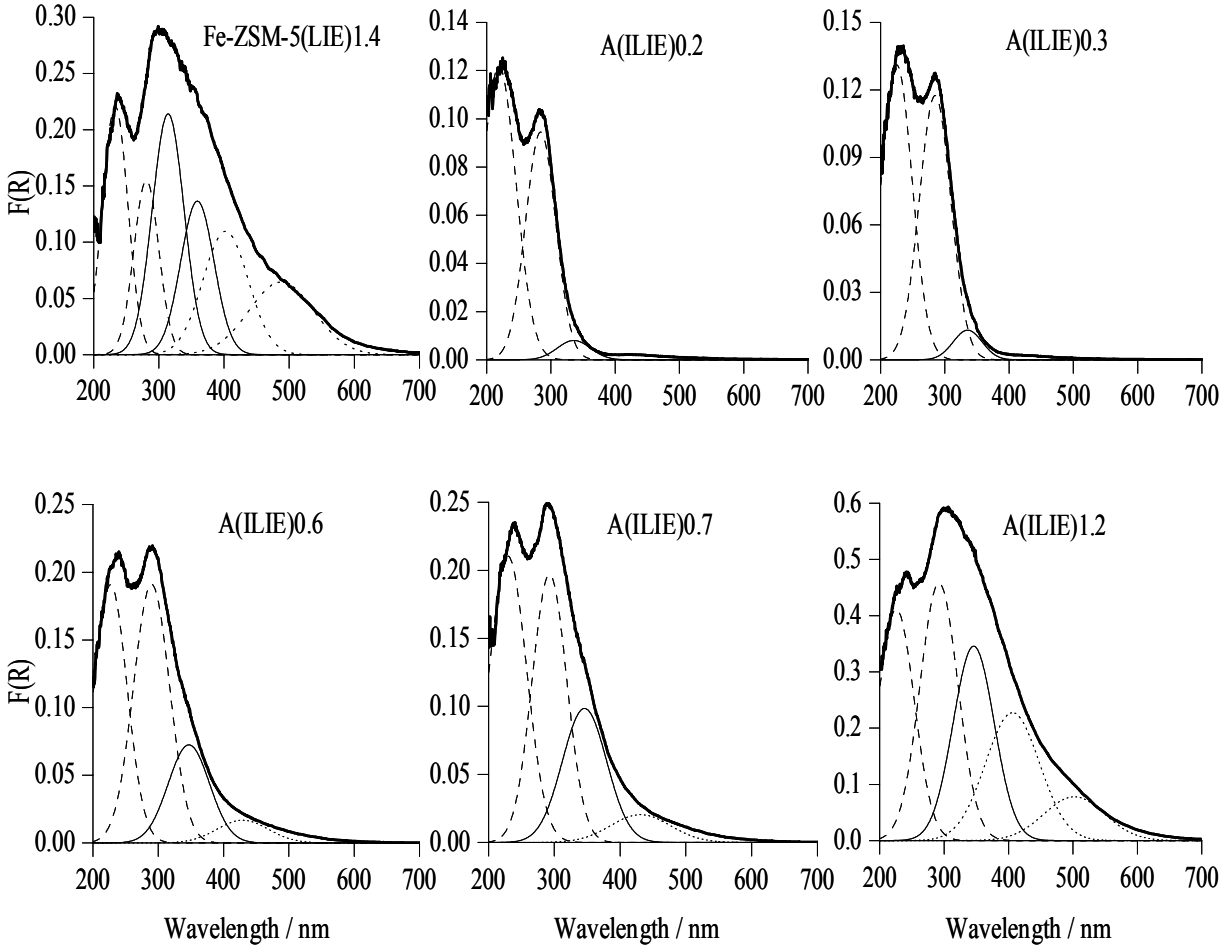

Fig. 4.5. UV/VIS-DR spectra and deconvoluted subbands of the hydrated Fe-ZSM-5 prepared by different liquid ion exchange procedures recorded at 293 K.

In contrast to conventional liquid ion exchange (LIE), improved liquid ion exchange (ILIE) produces samples with a high Fe dispersion as evidenced by the comparison of UV/VIS spectra of samples Fe-ZSM-5(LIE)1.4 and A(ILIE)1.2 with similar Fe content in Fig. 4.5 and Table 4.1. This is obviously due to the exchange of iron in the oxidation state +2. Therefore, this method was modified by Grünert and Schwidder for tuning the dispersion of Fe sites within a series of samples obtained after the same preparation route [64,164]. Deconvoluted UV/VIS spectra of calcined samples A(ILIE) are displayed in Fig. 4.5. The total spectral intensity as well as the relative intensity of the subbands strongly vary with the iron content as shown by Fig. 4.5 and Table 4.1. At low Fe content (A(ILIE)0.2 and A(ILIE)0.3) there is hardly any band above 400 nm indicating the absence of iron oxide particles. 95 % of the spectral intensity is accounted for by subbands below 300 nm (Table 4.1) indicating that the majority of Fe^{+3} species is well isolated. With increasing Fe content (A(ILIE)0.6 and A(ILIE)0.7), the percentage of Fe_xO_y clusters increases but still ca. 95 % of the spectral intensity is covered by subbands centered below 400 nm. This suggests that samples (A(ILIE)0.6 and A(ILIE)0.7) are dominated by isolated Fe^{+3} ions and small oligomers along with a negligible amount of large iron oxide particles (subband at ≈ 450 nm). Only the spectrum of A(ILIE)1.2 extends significantly to

wavelengths above 400 nm indicating the presence of considerable amounts of large iron oxide particles.

To elucidate whether the nature of the Fe species change during the calcination procedure, as-synthesized samples A(ILIE)0.2 and A(ILIE)1.2 were monitored by UV/VIS-DR spectroscopy during calcination as shown in Fig. 4.6. Interestingly, the whole spectral intensity increases upon calcination in comparison to the as-synthesized samples. This is due to the oxidation of divalent iron remaining in the sample after ILIE. After calcination the relative area of the subbands decreases below 300 nm and increases above 300 nm (Table 4.1) indicating the formation of iron oxide clusters at the expense of isolated Fe species. This is in line with the results of CVD, SSIE and MR samples where clustering was observed upon calcination, too.

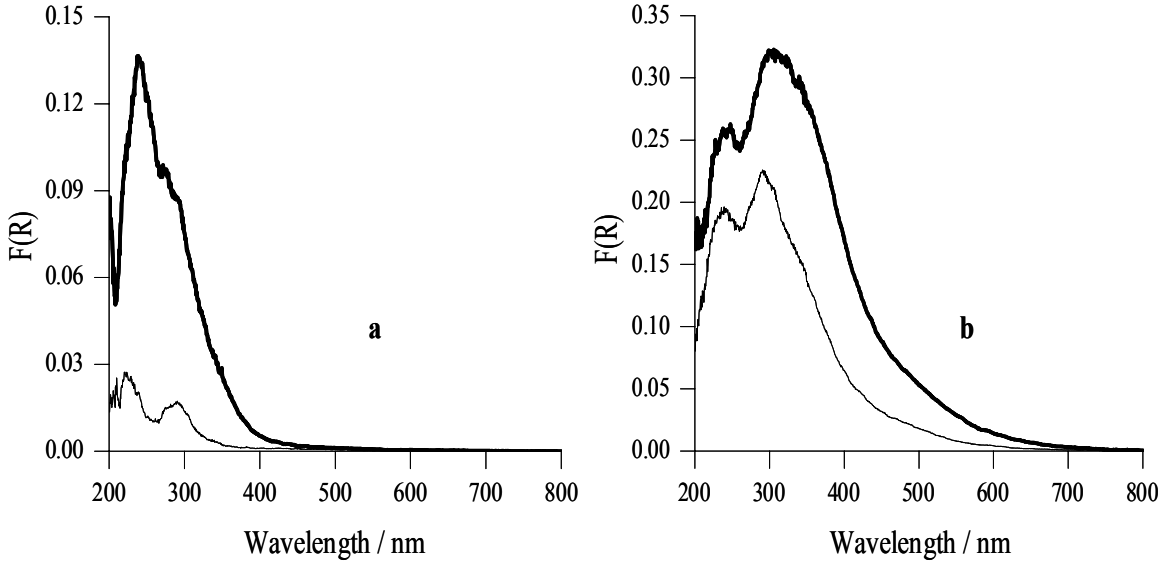

Fig. 4.6. In situ UV/VIS-DR spectra of (a) A(ILIE)0.2 and (b) A(ILIE)1.2 recorded at 298 K before (thin solid line) and after (thick solid line) calcination in air at 823 K with a heating rate of 5 K/min.

Since iron species are participating as active redox sites in the SCR reaction, their ability to be reduced and reoxidized is of crucial importance. For investigating this property, redox kinetics of isolated Fe^{+3} ions and iron oxide clusters were studied by following the time dependence of the absorbance at 238, 290 and 350 nm in reducing and oxidizing. Ex situ UV/VIS-DR spectra of uncalcined A(MR)0.5, A(ILIE)0.2 and A(ILIE)0.3 are very similar (Fig. 4.4 and 4.5), revealing the presence of mainly isolated Fe^{+3} ions, while A(ILIE)1.2 contains, too, a certain amount of oligomeric iron-oxo-clusters (Fig. 4.5). Therefore, A(ILIE)0.3 and A(ILIE)1.2 were used as model samples to assess the redox properties of different isolated Fe^{+3} ions and iron oxide clusters separately.

Isolated Fe^{+3} ions in tetrahedral and higher coordination give rise to two CT bands which are usually located below 300 nm. In the UV/VIS spectrum of sample A(ILIE)0.3 they fall around 225 nm and 285 nm respectively. This sample is ideal for redox studies of isolated Fe^{+3} ions, since only negligible contribution from agglomerated Fe_xO_y species is observed. The time

dependence of reduction and reoxidation at 673 K was followed at the maximum of these two CT bands separately. As an example, this is shown for the band at 238 nm in Fig. 4.7.

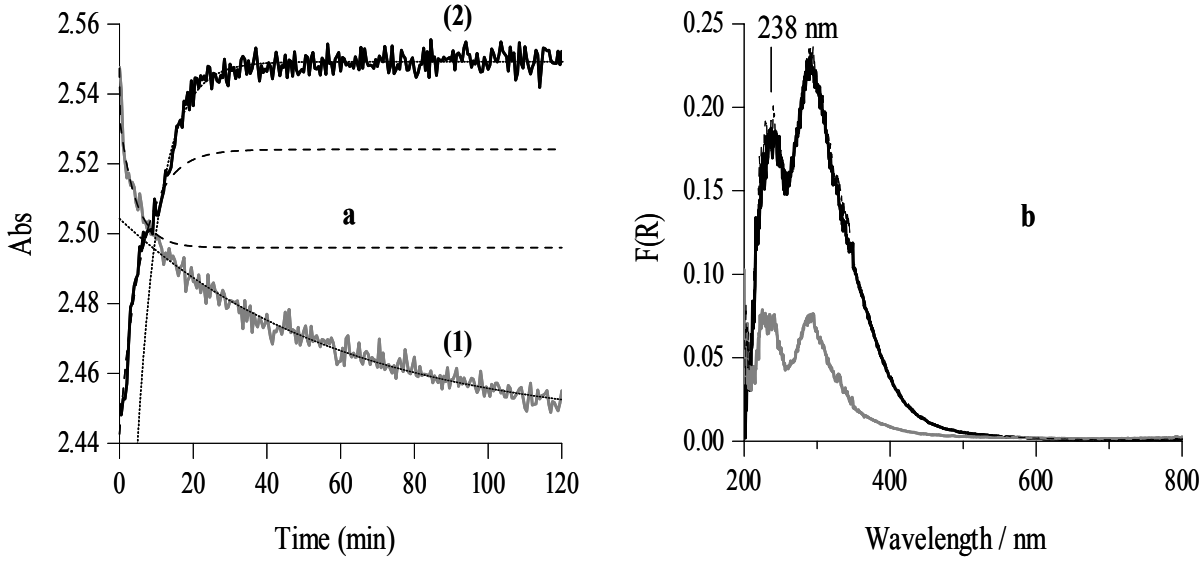

Fig. 4.7. Time dependence of reduction and reoxidation of sample A(ILIE)0.3: (a) Absorbance at 238 nm as a function of time at 673 K in a flow of (1) 1 vol.% NH_3/N_2 for 2 h (gray line) and (2) reoxidation in air for 2 h (solid line); (b) corresponding UV/VIS-DR spectra at 673 K after oxidative pretreatment in air at 773 K for 1 h (thick solid line), after reduction (gray line) and after reoxidation (thin solid line).

Table 4.2. Rate constants derived for reduction and reoxidation of Fe species by UV/VIS-DRS.

Sample	Treatment	Wavelength / nm	Time (min)	k (10^{-2} min^{-1})
A(ILIE) 0.3	Reduction	238	0 to 25	10.28
			25 to 120	1.22
	Reoxidation		0 to 10	16.61
			10 to 120	15.94
A(ILIE) 0.3	Reduction	290	0 to 25	17.49
			25 to 120	2.40
	Reoxidation		0 to 45	8.39
			45 to 120	8.83
A(ILIE) 1.2	Reduction	350	0 to 120	1.25
	Reoxidation		0 to 120	64.99

At 238 nm, the experimental reduction and reoxidation curves can be fitted by assuming two pseudo-first order processes each, with different rate constants (Table 4.2). This suggests the involvement of at least two kinds of isolated Fe^{+3} species in the redox process which are contributing to this band. Taking account of the rate constants, one kind of iron species is easily reduced and reoxidized in the first few minutes and the other type is more slowly reduced but relatively easily reoxidized as shown in Table 4.2 (Fig. 4.7). The reason for the different

reduction/reoxidation processes could be the presence of iron species at different pore positions in the zeolite matrix.

When comparing the results for the bands at 238 nm and 290 nm in sample A(ILIE)0.3 (Table 4.2), it is evident that both the bands show a similar behavior. However, the rate of reduction is somewhat higher for the latter representing octahedrally coordinated Fe^{3+}. Differently, the rate of reoxidation is slower. This indicates that the isolated Fe^{+3} ions in octahedral and tetrahedral coordination possess different redox properties. Thus, it can be concluded that the former species are somewhat easily reduced and slowly reoxidized as compared to the latter species (Table 4.2).

Sample A(ILIE)1.2 contains the highest iron percentage among the samples prepared by ILIE. Moreover, ex situ UV/VIS-DRS results show that this sample contains a considerable amount of oligonuclear iron-oxo clusters. For analyzing the redox behavior of these species, the time dependence of absorbance was followed at 350 nm, in the maximum of the band being characteristic of oligomeric clusters (Fig. 4.8). In contrast to the CT bands of isolated Fe^{+3} ions at 238 and 290 nm for which rate constants of reduction and reoxidation are in the same order of magnitude, reoxidation of clusters reflected by the band at 350 nm is more than one order of magnitude faster than reduction (Fig. 4.8). Moreover, both reduction and reoxidation can each be fitted with one rate constant only (Fig. 4.8 and Table 4.2). This suggests that the properties of iron species within clusters located in the channels may be more uniform than those of isolated sites.

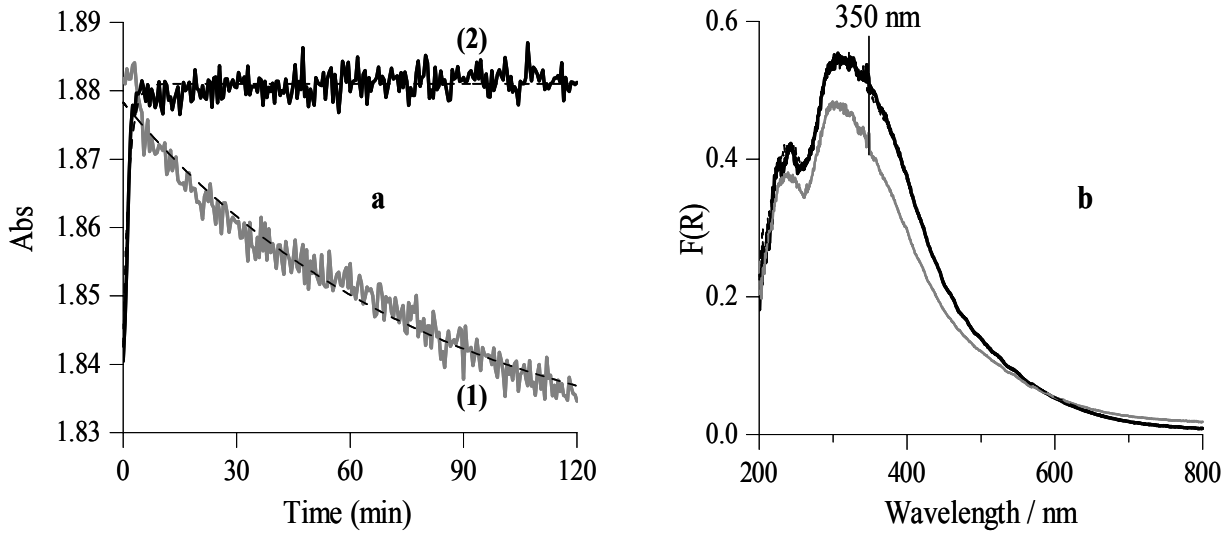

Fig. 4.8. Time dependence of reduction and reoxidation of sample A(ILIE)1.2: (a) Absorbance at 350 nm as a function of time at 673 K in a flow of (1) 1 vol.% NH_3/N_2 for 2 h (gray line) and (2) reoxidation in air for 2 h (solid line); (b) corresponding UV/VIS-DR spectra at 673 K after oxidative pretreatment in air at 773 K for 1 h (thick solid line), after reduction (gray line) and after reoxidation (thin solid line).

Interestingly, from the same experiment important additional information can be drawn on the redox properties of isolated Fe^{3+} ions in cluster containing samples. Fig. 4.8b shows

that bands below 300 nm, which were assigned to isolated iron species, follow the same reduction and reoxidation trend as for cluster bands above 300 nm. This is in contrast to the reduction and reoxidation of the CT bands of isolated Fe^{+3} ions at 238 and 290 nm in the cluster-free sample A(ILIE)0.3. This indicates that the redox properties of isolated Fe^{3+} species change with increasing cluster content in the sample and possess similar redox properties to that of clusters.

Hydrothermal Synthesis

Different from sublimation and ion exchange procedures which use a crystalline zeolite matrix for incorporating Fe in extra framework positions, hydrothermal synthesis is based on the incorporation of Fe in framework positions during crystallization of the zeolite matrix followed by subsequent extraction by steaming. Using this preparation procedure, Fe-zeolites of different composition and/or pore structure have been prepared by Javier Pérez-Ramírez [58,159].

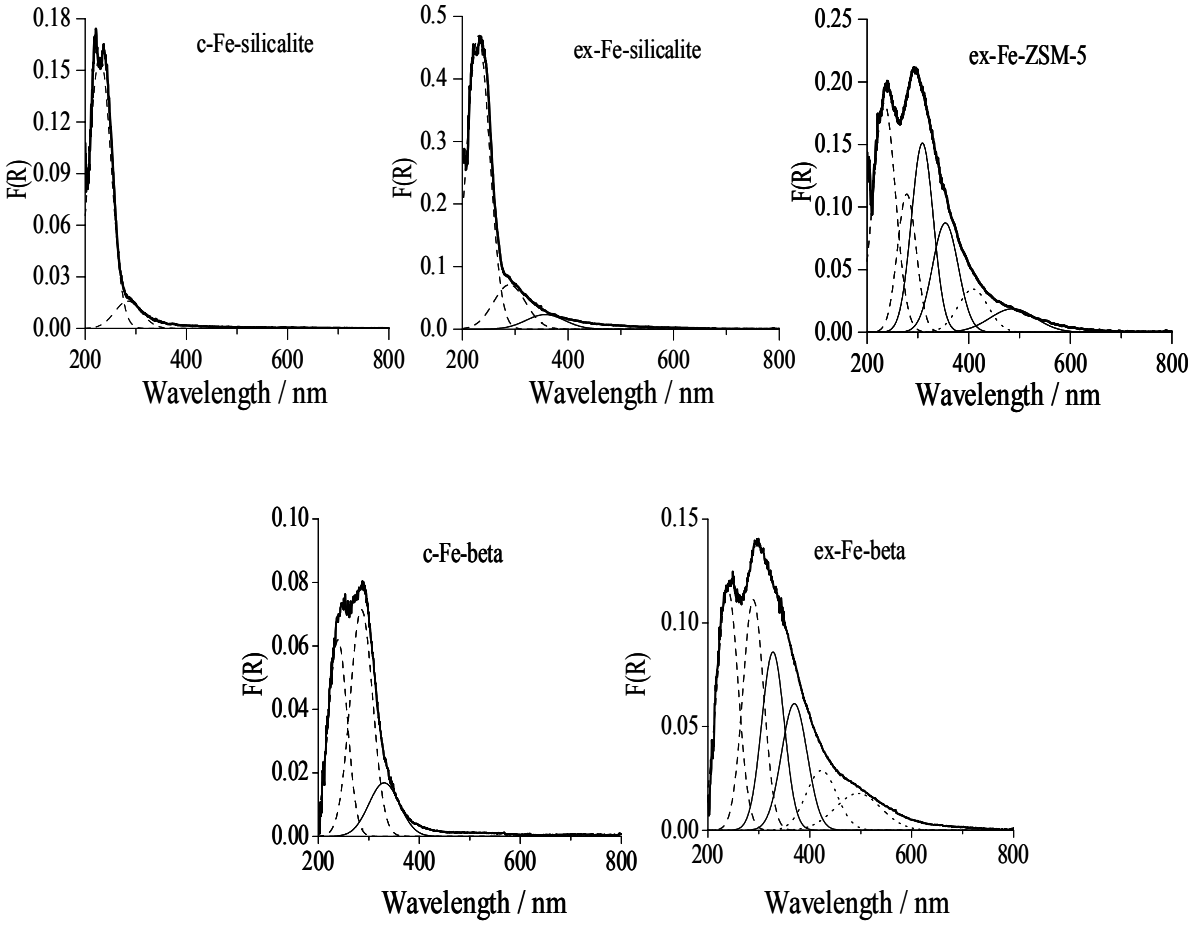

Fig. 4.9. UV/VIS-DR spectra and deconvoluted subbands of the hydrated samples recorded at 298 K without pretreatment.

The spectra of calcined and steamed Fe-silicalite in Fig. 4.9 and the relative percentage of the deconvoluted subbands in Table 4.1 indicate that the majority of Fe^{3+} species in the sample is well isolated. The band at ≈ 350 nm after steaming suggests that a relatively small fraction of iron is present as small oligonuclear species. This could be due to the dislodgement of

framework Fe^{3+} ions during calcination and/or a small fraction of iron which was not incorporated in the framework during the hydrothermal synthesis. No contribution >450 nm was observed, indicating the absence of large Fe_2O_3 particles in these samples.

In contrast to *ex*-Fe-silicalite, the percentage of isolated Fe^{3+} species is significantly lower in *ex*-Fe-ZSM-5, with extensive formation of $Fe^{3+}_xO_y$ clusters and a small fraction of Fe_2O_3 particles (Fig. 4.9 and Table 4.1). The latter particles have been also detected by HRTEM in this sample with an average size of 1-2 nm [58].

As observed for calcined Fe-silicalite, calcined Fe-beta also contains mainly isolated Fe^{3+} species (Table 4.1 and Fig. 4.9). Similar to *ex*-Fe-ZSM-5, the percentage of isolated Fe^{3+} species is significantly lower in steamed Fe-beta with extensive formation of $Fe^{3+}_xO_y$ clusters and a small fraction of Fe_2O_3 particles (Fig. 4.9 and Table 4.1) [159].

These results suggest that the framework composition of the zeolite plays an essential role in determining the iron speciation. Obviously, the presence of Al in the zeolite matrix partly prevents the incorporation of Fe in lattice positions since the latter are preferably occupied by Al. This might favour the formation of iron oxide clusters already during crystallization of the zeolite matrix [58].

Voltammetric characterization has shown that the extraction of framework iron in *ex*-Fe-silicalite is substantial after steam-treatment at 873 K, but not complete [155]. UV/VIS-DRS cannot discriminate between isolated Fe^{3+} ions in framework or extraframework positions just by the band position. Hence, the influence of Fe^{3+} reduction by H_2 and reoxidation by air on the UV/VIS spectrum of the calcined and steamed samples has been used to further analyze the degree of iron extraction in the steam-activated catalyst (Fig. 4.10). After hydrothermal synthesis and calcination at 823 K, Fe-silicalite shows typical CT bands at 250 and 280 nm, originating from tetrahedral and higher coordination. These species which are predominant (ca. > 95%) in the sample are most probably incorporated in Si lattice positions (Fig. 4.9). They are not sensitive to a reductive treatment (20 vol.% H_2 in N_2 at 773 K for 1 h), as expected from the nature of framework Fe^{3+} ions, which are well shielded in the zeolite and thus resistant against reduction. In contrast, calcined Fe-beta shows a small decrease in band intensity upon reductive treatment (Fig. 4.10). This could be due to the presence of a small fraction of extraframework isolated Fe^{+3} ions in this sample. This is also evident from a small shoulder at 350 nm observed in calcined Fe-beta which indicates that a small fraction of iron was not incorporated in the framework during the hydrothermal synthesis or was already extracted during the calcination step.

Contrarily, the same reductive treatment over the steamed samples clearly shows that reduction of Fe^{3+} to Fe^{2+} causes a marked decrease of the Fe^{3+} CT band intensity. Additionally *ex*-Fe-beta with extensive clusters exhibits increase of light absorption in the range above 500 nm. This can be attributed to an intervalence charge transfer (IVCT) transition, which is induced by electron delocalization between Fe^{+2} and Fe^{+3} ions in partially reduced iron oxide species such as Fe_3O_4-like clusters [58,165,159]. However, reduced iron species are completely reoxidized in air flow (Fig. 4.10).

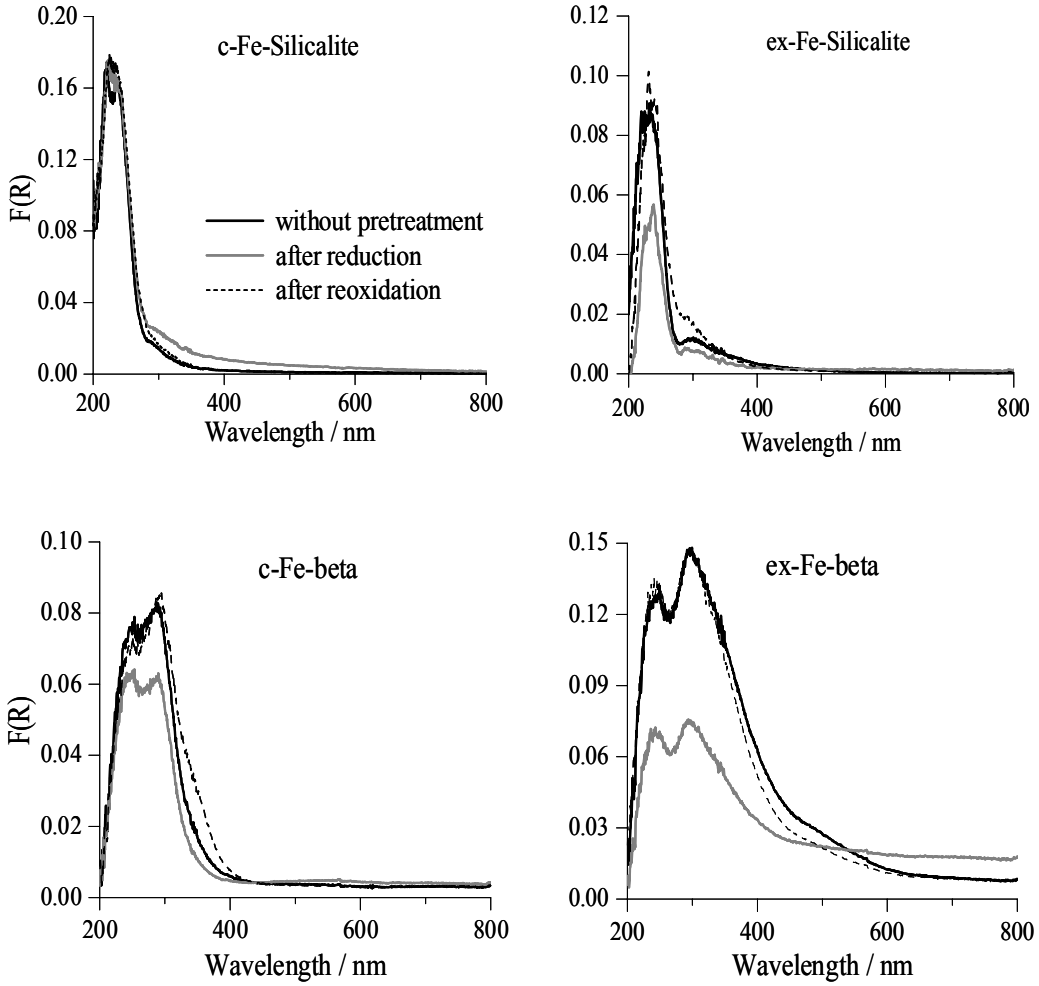

Fig. 4.10. UV/VIS-DR spectra of the calcined and steamed samples recorded at 293 K before reduction, after reduction in 20 vol.% H_2 in N_2 at 773 K for 1 h and after reoxidation in air at 773 K for 1 h.

Summarizing, the extraction of Fe^{3+} upon steaming at 873 K is significant in all samples. However, only in *ex*-Fe-silicalite the extraframework species remain well isolated while in Fe-beta and Fe-ZSM-5 iron extraction is connected with pronounced cluster formation.

Impregnation by incipient wetness

In the case of supported VO_x species it has been shown that almost exclusively isolated, fully accessible VO_x species can be deposited on the surface of mesoporous silica supports such as MCM-48 and SBA-15, due to their very high surface area [166]. Accordingly, the formation of highly dispersed FeO_x moieties should be favoured on these supports, too. Hence, Fe was deposited on an Al-free SBA-15 support by impregnation with iron acetylacetonate ($Fe^{3+}(acac)_3$). The corresponding UV/VIS spectra and the relative percentage of the deconvoluted subbands are shown in Fig. 4.11 and Table 4.1. These results indicate that in sample (FeSBA-I)0.95 the majority of Fe^{3+} species is well isolated. The band at ≈ 350 nm suggests that a relatively small fraction of iron is present as small oligonuclear species. No contribution >450 nm was observed, indicating the absence of large Fe_2O_3 particles [161].

Experimental UV/VIS spectra (thick solid lines) of hydrated and dehydrated (after pretreatment in air at 773 K for 1 h) samples in Fig. 16 show that in the latter a shoulder at ≈ 290 nm is completely missing which is clearly seen in the spectrum of the hydrated sample, which is assigned to isolated Fe^{3+} ions in environments with more coordinating ligands (5 or 6). This suggests that in the hydrated sample H_2O molecules are coordinating to Fe sites that contribute to a band at 290 nm. Upon dehydration, H_2O molecules are removed from the coordination sphere of Fe sites, which now contribute to a band below 250 nm, assigned to tetrahedrally coordinated isolated Fe^{3+} ions. This observation clearly supports the assignment of UV/VIS bands below 250 nm to tetrahedrally coordinated isolated Fe^{3+} ions and bands around 280 nm to higher coordination.

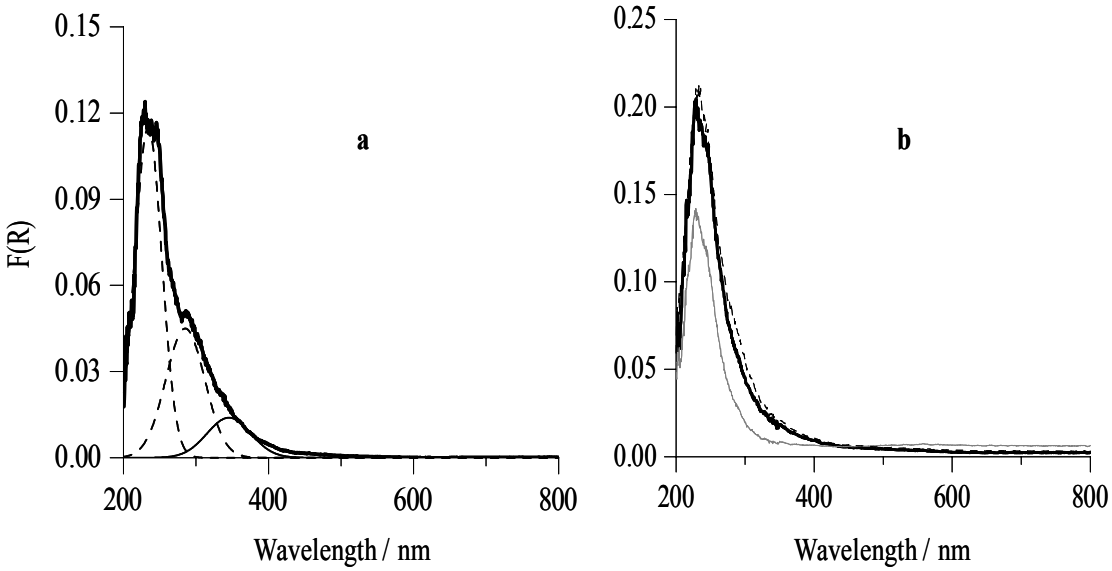

Fig. 4.11. UV/VIS-DR spectra of the calcined (Fe-SBA-I)0.95 sample recorded at 293 K: a) experimental spectrum of the hydrated sample (thick solid line) and deconvoluted subbands (thin lines). b) experimental spectrum after air treatment at 773 K for 1 h (thick solid line), after reduction in 20 vol.% H_2 in N_2 at 773 K for 1 h (gray line) and after reoxidation in air at 773 K for 1 h (broken line).

For comparative purposes, the calcined sample (Fe-SBA-I)0.95 with a similar distribution of iron species as compared to calcined and steamed Fe-silicalite and calcined Fe-beta was reduced by H_2 and reoxidized by air at 773 K for 1 h respectively [161]. In view of the preparation method of the sample (Fe-SBA-I)0.95, Fe^{+3} ions are expected to be present at extraframework positions. Accordingly, the reductive treatment clearly shows that reduction of Fe^{3+} to Fe^{2+} causes a marked decrease of the Fe^{3+} CT band intensity, which is completely reversible on reoxidation in air flow (Fig. 4.11).

4.1.2 EPR studies

Ex situ EPR spectra were recorded for all samples at 293 and 77 K. Additionally, temperature dependent spectra were recorded for selected samples between 90 and 673 K while heating in air to obtain information on the magnetic behavior of iron species. In addition, some of the samples were treated in vacuum to gather information about the ability of the Fe species to change their coordination state. On the basis of these results an attempt was made to assign the EPR signals to particular iron species. This is a matter of ongoing discussion in the literature. The EPR results of different Fe-samples studied in this work are presented below in the same order as for the UV/VIS-DRS results, e.g., related to the preparation method.

Assignment of EPR signals

EPR spectra of almost all samples show typical signals at effective g values of 2, 4.3, and 6 (Fig. 4.12). Such signals were frequently detected in Fe-ZSM-5 [63,121-129] and also with Fe^{3+} ions in the other matrices. However, their assignment is by no means straightforward. The number and position of EPR transitions for Fe^{3+} ions observable in a powder spectrum depends sensitively on the local crystal field symmetry of these sites (reflected by the magnitude of the zero field splitting parameters D and E) and possible magnetic interactions between them. Signals at $g' \approx 4.3$ and $g' \geq 6$ arise from the $| - ½ > \leftrightarrow < ½ |$ transition of isolated Fe^{3+} sites in strong rhombic ($D >> h\nu$, $E / D = 1/3$; $g' \approx 4.3$) or axial distortion ($D >> h\nu$, $E = 0$, $g' \approx 6$) when the zero-field splitting is large in comparison to the microwave energy $h\nu$ [63,120]. This implies that an Fe^{3+} species giving rise to a line at $g' \approx 4.3$ is more strongly distorted than an Fe^{3+} site represented by a signal at $g' \approx 6$ due to the difference in the magnitude of E.

In zeolites, the line at $g' \approx 4.3$ is frequently assigned to Fe^{3+} sites incorporated in tetrahedral framework positions while a line at $g' \approx 6$ is attributed to isolated Fe^{3+} species in higher coordination [63,121-123,125-127]. However, it must be stressed, that just from the signal position alone it is not possible to conclude whether the respective Fe ions are octahedrally or tetrahedrally coordinated since the signal position is governed by the magnitude of D and E, i.e., the extent of distortion of the Fe coordination. This distortion can arise from both tetrahedral and octahedral coordination. To draw conclusions on the number of ligands associated with the $g' \approx 4.3$ and 6 signals, additional aspects must be considered which are discussed in the following sections. Moreover, as will be shown below, an increase of the $g' \approx 4.3$ signal at the expense of $g' \approx 6$ and $g' \approx 2$ lines can be induced by dehydration, implying that the loss of water ligands leads to a lower coordination number. Therefore, we assign the EPR signal at $g' \approx 4.3$ to isolated tetrahedrally coordinated Fe^{3+} species and the line at $g' \approx 6$ to isolated higher coordinated Fe^{3+} species in less distorted extraframework positions [55].

Signals at $g' \approx 2$ can arise either from isolated Fe^{3+} in high symmetry ($D, E \approx 0$) or from Fe_xO_y clusters in which magnetic interactions between the Fe^{3+} ions average out the zero field splitting. For isolated, highly symmetric Fe^{3+} species, the signal intensity should follow the Curie-Weiss law, i.e., $I \sim 1/T$. It appears that both types of signal can be observed in the spectra of studied samples.

Chemical Vapor Deposition (CVD)

EPR spectra of the samples A(CVD,W1) and B(CVD,W1) measured at 293 K and 77 K are shown in Fig.4.12.

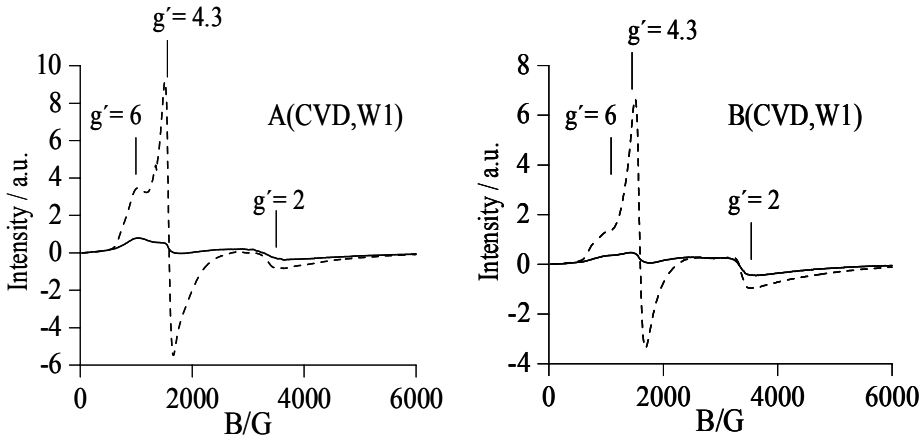

Fig. 4.12. EPR spectra of hydrated Fe-ZSM-5 zeolites at 298 K (solid line) and 77 K (broken line).

Both samples show typical signals at g'-values of 2, 4.3, and 6 however, signal intensities for sample B(CVD,W1), in particular at g' ≈ 6, are slightly weaker. Signals at g' ≈ 4.3 and g' ≈ 6 arise from isolated Fe^{3+} sites in strong rhombic and axial distortion respectively. As expected for pure paramagnetic behavior according to the Curie-Weiss law, their intensities increase with decreasing temperature. In contrast, the intensity of the line at g' ≈ 2 does not markedly increase upon cooling. This suggests that the Fe^{3+} sites responsible for this signal are coupled by antiferromagnetic interactions within oxidic clusters, which reduce the number of unpaired spins contributing to the EPR signal. The presence of oxidic clusters in samples A(CVD,W1) and B(CVD,W1) has been confirmed, too, by UV/VIS-DRS results (Figs. 4.2 and 4.3).

Additional information about mutual interaction between iron species can be obtained from temperature dependent EPR measurements. It has been shown earlier that the temperature dependence of the signal intensity bears valuable information on the presence of magnetically coupled phases [167,168]. While well ordered crystalline α-Fe_2O_3 is antiferromagnetic below T_N =960 K and, therefore, not EPR-active, it has been shown that nanoparticles of α-Fe_2O_3 (d ≈ 3 nm) do give rise to an EPR signal below T_N due to incomplete compensation of the spin moments [167].

Therefore, series of temperature dependent spectra were recorded for selected samples in a wide temperature range. EPR spectra of sample A(CVD,W1,C0.5) are displayed in Fig. 4.13. It can be seen that the EPR signals at g' ≈ 6 and g' ≈ 4.3 decrease with increasing temperature as expected for paramagnetic behavior, whereby the intensity loss of the g' ≈ 4.3 signal is stronger suggesting shorter relaxation times in comparison to the Fe^{3+} species reflected by g' ≈ 6. At T ≥ 373 K those signals become narrower and better resolved. This is attributed to the loss of water molecules from the pores which are assumed to be located in the coordination sphere of the Fe^{3+}

ions and give rise to a certain distribution of the zero field splitting parameters which enhances the line width.

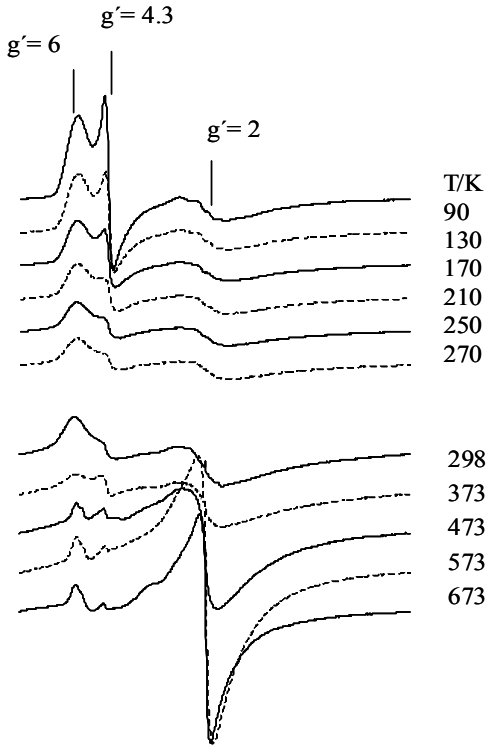

Fig. 4.13. EPR spectra of hydrated sample A(CVD,W1,C0.5) during heating in air flow.

The broad signal at g' ≈ 2 does not show Curie-like behavior. In the high-temperature range it increases and narrows suddenly. This suggests that the samples contain antiferromagnetically coupled Fe_xO_y species with a Neel temperature of $T_N > 373$ K. Above T_N those species become paramagnetic and contribute to the EPR signal. The line narrowing is most probably due to effective spin-spin exchange interactions between neighboring Fe^{3+} species within the clusters. However, the g' ≈ 2 signal is anisotropic, this suggests that the signal is not due to a particular species with defined geometry but to a superposition of Fe_xO_y species with a certain size distribution.

Influence of washing intensity

In analogy to UV/VIS-DRS analysis (section 4.1.1, Fig. 4.2), the effect of washing intensity on the nature of iron species was also studied by EPR spectroscopy (Fig. 4.14). The temperature-dependent EPR measurements for used samples of A(CVD,W1,C0.5) and A(CVD,W10,C0.5) after catalysis are shown in Fig. 4.14a and b. In the spectra of A(CVD,W1,C0.5) after catalysis, an intense narrow signal appears at g' ≈ 2 above 373 K indicating the presence of extended Fe_xO_y clusters with antiferromagnetic coupling (Fig. 4.14a). In contrast, the increase of this line in A(CVD,W10,C0.5) after catalysis is much less pronounced. This suggests a weaker antiferromagnetic coupling which may be due to a smaller cluster size (Fig. 4.14b). These results are in agreement with UV/VIS-DRS results, which also showed that intense washing diminishes the amount of large iron oxide clusters slightly (Fig. 4.2b).

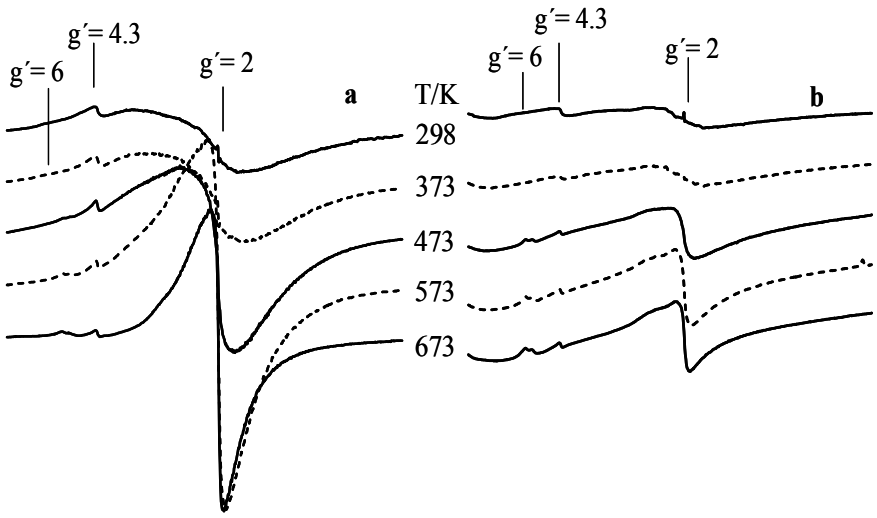

Fig. 4.14. EPR spectra of hydrated samples of used A(CVD,W1,C0.5) (a) and A(CVD,W10,C0.5) (b) during heating in air flow. Samples were recalcined after catalysis in air at 823 K.

Influence of calcination

EPR spectra of sample A(CVD,W1) are shown in Fig. 4.15 before calcination as well as after calcination in air at 873 K for 2 h using heating rates of 5 and 0.5 K min^{-1}. It is clearly seen that signals of isolated Fe^{3+} sites at g' ≈ 6 and g' ≈ 4.3 lose intensity upon calcination while the signal at g' ≈ 2 increases. This suggests that initially isolated Fe sites aggregate to form Fe_xO_y clusters. This effect seems to be slightly favored by higher heating rates as also observed by UV/VIS-DRS measurements (Fig. 4.3a and Table 4.1).

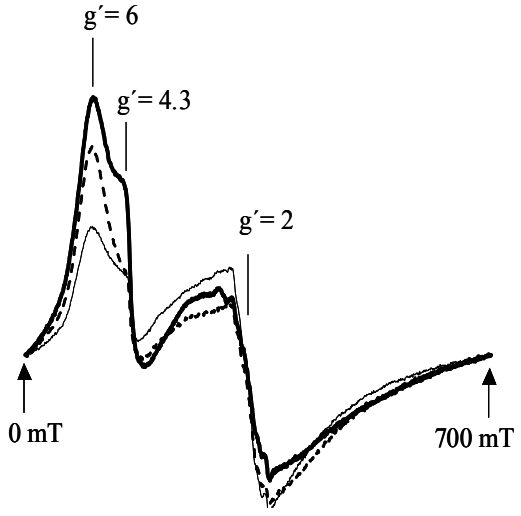

Fig. 4.15. EPR spectra of hydrated samples recorded at 293 K: before calcination A(CVD,W1) (thick solid line), after calcination at 873 K with a heating rate of 0.5 K/min A(CVD,W1,C0.5) (broken line) and after calcination at 873 K with a heating rate of 5 K/min A(CVD,W1,C5) (thin solid line).

Additional features of the calcination process are evident as shown by studying the effect of room-temperature evacuation and subsequent contact with ambient atmosphere for the uncalcined and the calcined samples A(CVD,W1) and A(CVD,W1,C0.5), where the latter had been rehydrated in ambient atmosphere between calcination and EPR experiment for an extended period of time (Fig. 4.16).

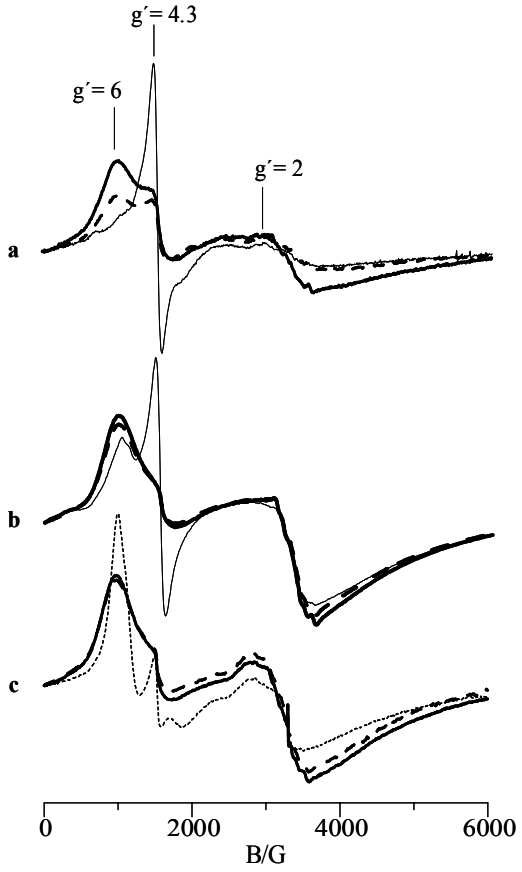

Fig. 4.16. Structural changes of the isolated Fe species in sample A(CVD,W1) during calcination; EPR spectra recorded at room temperature; initial hydrated state (thick solid line), after 2 h evacuation at 293 K (thin solid line), after 2 h calcination in air at 773 K (dotted line), and after reexposing to the ambient atmosphere (dashed line); initial states: (a) as-prepared sample A(CVD,W1); (b and c) calcined sample A(CVD,W1,C0.5) after long-term storage at the ambient atmosphere.

Fig. 4.16c shows the effect of thermal treatment in air at 773 K (instead of room-temperature evacuation) on the calcined and rehydrated sample A(CVD,W1,C0.5). It can be seen that evacuation of the uncalcined A(CVD,W1) material leads to complete disappearance of the signal at g' ≈ 6 while the one at g' ≈ 4.3 increases strongly (Fig. 4.16a). This shift is largely reversed by contact with ambient atmosphere. For the calcined but rehydrated sample A(CVD,W1,C0.5) the g' ≈ 6 signal remains upon room-temperature evacuation but has lost much intensity to that at g' ≈ 4.3 (Fig. 4.16b). When, instead of 2 h evacuation at room temperature, the latter sample is again thermally treated in air at 773 K, very different changes are induced (Fig. 4.16c): Now there is just a narrowing of the signals at g' ≈ 6 and g' ≈ 4.3 and the effect is completely reversible upon exposure to the ambient atmosphere.

An explanation of this behavior may set out from the assumption that $[FeCl_2]^+$ cations deposited on cation sites during the CVD step [31,56] [Eq. (4.1)] are hydrolyzed during the washing step. In this process, part of the iron species may acquire a distorted coordination sphere with a coordination number of 6 or 5 made up of water, charge-balancing OH groups and, possibly, oxygen of the zeolite wall, which is reflected in the signal at g' ≈ 6 [e. g., Eq. (4.2)].

$$H^+ + FeCl_3 \rightarrow [FeCl_2]^+ + HCl \qquad (4.1)$$

$$[FeCl_2]^+ + n\ H_2O + m\ O_z \rightarrow [Fe(H_2O)_n(O_z)_m(OH)_2]^+ + 2\ HCl \quad (m + n = 3 \text{ or } 4) \qquad (4.2)$$

Upon room-temperature evacuation, the water ligands may be reversibly removed, and the respective Fe species contribute to the signal at g' ≈ 4.3 which might arise from tetrahedral Fe species as frequently discussed in the literature (Fig. 4.16a). After calcination, however, if contact with the humid air is avoided, the coordination of most Fe ions is much different (Fig. 4.16c, dotted line). The difference is obviously caused by the more severe effect of the thermal treatment as opposed to room-temperature evacuation and consists presumably in a condensation of the charge-balancing OH groups on the Fe^{3+} ion. This process would lead to a cation with an extra-framework oxygen coordinated to 4 or 5 framework oxygens (Eq. (4.3), with a higher probability for p = 4 due to the steric conditions in the zeolite). This species is believed to give rise to the narrow signal at g' ≈ 6 after calcination (Fig. 4.16c), which is a typical feature of this type of mononuclear Fe sites in the dehydrated state. There is, however, also a minority species in tetrahedral coordination (g' ≈ 4.3).

$$[Fe(H_2O)_n(O_z)_m(OH)_2]^+ \rightarrow [(O_z)_pFeO]^+ \qquad (4.3)$$
$$(p = 4 \text{ or } 5 \text{ for } g' \approx 6, \text{ and } p = 3 \text{ for } g' \approx 4.3)$$

Upon contact with the humid ambient atmosphere, the outer coordination sphere of the Fe species is influenced by adsorbed water, which results in slightly different distortions at different lattice positions and causes the broadening of the signals, in particular that at g' ≈ 6, which can be seen in Fig. 21c. The reversal of the structural change upon dehydration (probably rehydration of the Fe=O units), however, appears to proceed much more slowly: This is suggested by a comparison of the spectra after 2h evacuation in Fig. 4.16a and 4.16b. In contrast to the initial sample in Fig. 4.16a, the one in Fig. 4.16b had been calcined but stored in ambient atmosphere for an extended period of time. The narrow g' ≈ 6 signal typical of the dehydrated structures is still left to an appreciable extent in the latter sample after 2 h evacuation (Fig. 4.16b), i.e. prolonged storage in the ambient atmosphere led to only incomplete rehydration of the dehydrated Fe site.

Influence of the Al content and defect density of the parent ZSM-5 matrix

Similar to the UV/VIS studies, the effect of Si/Al ratio on the nature of iron species in the catalyst was studied by EPR spectroscopy and the corresponding spectra are depicted in Fig. 4.17.

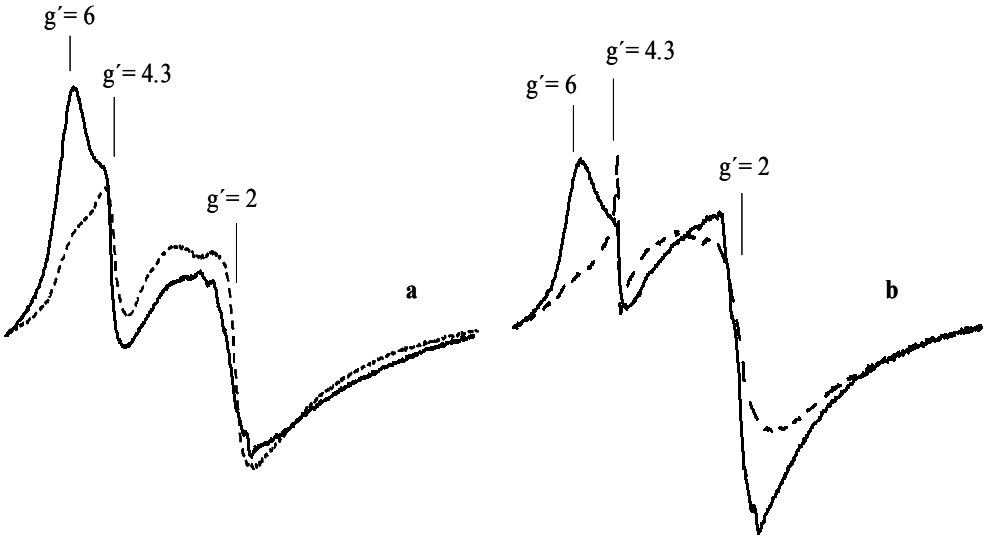

Fig. 4.17. EPR spectra recorded at 293 K: (a) as-prepared samples A(CVD,W1) (solid line) and B(CVD,W1) (broken line); (b) calcined samples A(CVD,W1,C5) (solid line) and B(CVD,W1,C5) (broken line).

The EPR signals for isolated Fe sites at low magnetic field are less intense for the uncalcined sample B(CVD,W1) than for A(CVD,W1) while the cluster signal at g' ≈ 2 is larger (Fig. 4.17a). A smaller percentage of isolated Fe^{3+} and slightly higher percentage of extended Fe_2O_3-like clusters in sample B(CVD,W1) is also evident from UV/VIS data (Fig. 4.3b, and Table 4.1).

In agreement with UV/VIS results (Fig. 4.3c), the opposite trend is observed for the calcined samples. Calcination with a heating rate of 5 K/min leads to a less pronounced formation of large Fe_2O_3-like aggregates in sample B(CVD,W1,C5) as evident from the signal g' ≈ 2 in EPR spectra in Fig. 4.17b.

Influence of the SCR reaction

Fig. 4.18 illustrates the effect of use in the catalytic reaction on a precalcined catalyst. The corresponding EPR spectra of A(CVD,W1,C0.5) before and after use in the SCR of NO with isobutane (duration 1 working day) are compared in Fig 4.18. In the EPR spectrum of used catalyst, the signal at g' ≈ 6 almost disappeared while the signal at g' ≈ 4.3 is virtually not effected. At the same time, the cluster signal at g' ≈ 2 grew enormously as compared to the fresh catalyst. These results do not agree with the corresponding UV/VIS results (Fig. 4.3d and Table 4.1) which indicate only a slight increase of the relative amount of iron oxide particles after use in catalysis. Obviously, the strong increase of the EPR signal at g' ≈ 2 after reaction is mainly due to intensified spin-spin exchange interactions between neighboring Fe sites which is probably caused by lattice ordering in larger Fe_xO_y clusters.

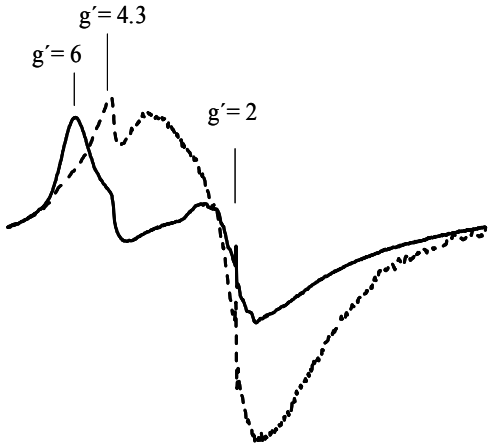

Fig. 4.18. EPR spectra of A(CVD,W1,C0.5) before (solid line) and after use in the isobutane-SCR of NO reaction (broken line) measured at 293 K.

The strong attenuation of the g' ≈ 6 line suggests that Fe species reflected by this signal, are modified in the catalytic reaction while those related to the g' ≈ 4.3 line remain unchanged. The UV/VIS data (Table 4.1), on the other hand, imply that this modification is not caused by cluster formation or reduction but just by a change in the Fe coordination geometry.

Solid-State Ion Exchange (SSIE)

EPR spectra of uncalcined A(SSIE)5.2 sample at 293 K and 77 K (Fig. 4.19) show signals at effective g values of 2, 4.3 and 6. The spectra are similar to those of sample A(CVD,W1) which has similar Fe content (Fig. 4.12).

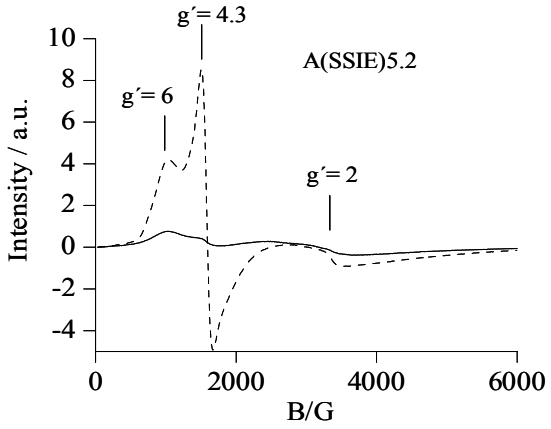

Fig. 4.19. EPR spectra of the uncalcined A(SSIE)5.2 sample (without pretreatment) at 293 K (solid line) and 77 K (broken line).

As observed from UV/VIS-DRS measurements, uncalcined A(SSIE)5.2 sample contains iron oxide clusters of different size along with a considerable amount of isolated iron ions (Fig. 4.4 and Table 4.1). While the isolated species are properly reflected by the signals at g' ≈ 6 and g' ≈ 4.3, the line at g' ≈ 2 is very weak, suggesting that the majority of the iron oxide clusters

might be EPR silent at T ≤ 293 K due to antiferromagnetic interactions. Therefore, to gather additional information about mutual magnetic interactions between Fe^{3+} ions and subsequently the size of the clusters, temperature dependent EPR measurements were performed as shown in Fig. 4.20.

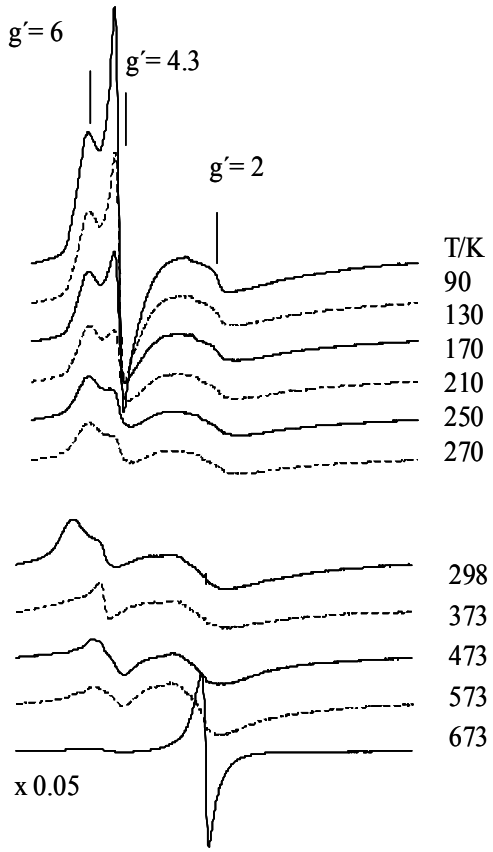

Fig. 4.20. EPR spectra of uncalcined A(SSIE)5.2 sample during heating in air flow.

The EPR spectra of sample A(SSIE)5.2 which were recorded in the low temperature range between 90-270 K show similar behavior to that of A(CVD,W1,C0.5) (Fig. 4.13). The signals at g' ≈ 6 and g' ≈ 4.3 decrease with rising temperature as expected for paramagnetic behavior.

Above 573 K a huge and very narrow signal appears at g' ≈ 2 which is much more intense than for sample A(CVD,W1,C0.5). This suggests that the A(SSIE)5.2 sample contains antiferromagnetically coupled Fe_xO_y species with a Neel temperature of $T_N > 573$ K. The strong increase in intensity and line narrowing of g' ≈ 2 signal in A(SSIE)5.2 indicates the presence of larger and/or better ordered clusters than in the sample A(CVD,W1,C0.5). Such species were also earlier detected in the unwashed and uncalcined Fe-ZSM-5 (prepared by SSIE), by XRD, TPR and XAFS [36]. It is not unexpected that they remain also in the washed material.

Mechano chemical route (MR)

EPR spectra of the uncalcined sample A(MR)0.5 at 293 K and 77 K (Fig. 4.21) show signals at effective g values of 2, 4.3 and 6.

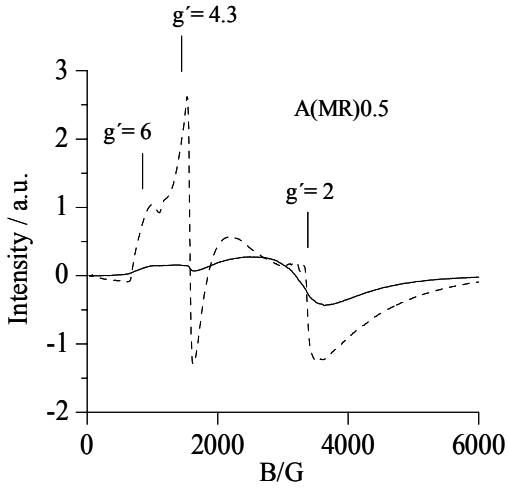

Fig. 4.21. EPR spectra of the uncalcined A(MR)0.5 sample (without pretreatment) at 293 K (solid line) and 77 K (broken line).

The signals at g' ≈ 4.3 and g' ≈ 6 show similar behavior as observed for other samples, e.g., A(CVD,W1), A(CVD,W1,C0.5) and uncalcined A(SSIE)5.2. Interestingly, the signal at g' ≈ 2 increased upon cooling from room temperature to 77 K, as expected for paramagnetic Fe^{3+} species obeying the Curie-Weiss law. This behaviour, typical for isolated sites, relates to the high degree of dispersion of iron in this catalyst. This is in agreement with UV/VIS results that indicate the presence of the majority of Fe^{+3} species in isolated form (Fig. 4.4 and Table 4.1). However, in the EPR spectrum of uncalcined A(MR)0.5 at 77 K, a rather narrow and a very broad line are superimposed in the range of g' ≈ 2. The former signal loses intensity upon heating. Most probably, this line arises from isolated Fe^{3+} ions in high symmetry. The latter is not typical for ideally isolated sites.

To check for the presence of magnetic interactions between Fe^{3+} sites in oxidic moieties, temperature dependent EPR measurements were also performed analogous to samples A(CVD,W1,C0.5) and uncalcined A(SSIE)5.2 as shown in Fig. 4.22. With the exception of the narrow signal at g' ≈ 2, the shape and behavior of the EPR signals in the low temperature range between 90-270 K are rather similar for uncalcined A(MR)0.5, A(CVD,W1,C0.5) and A(SSIE)5.2. This was expected, since the samples might contain isolated sites of similar nature giving rise to similar EPR signals at g' ≈ 6 and g' ≈ 4.3. However, above 373 K a slight increase of the broad signal at g' ≈ 2 is observed, too, though the effect is much less pronounced than in A(CVD,W1,C0.5) and uncalcined A(SSIE)5.2 (Fig. 4.22). This suggests the presence of antiferromagnetically coupled Fe_xO_y species with a Neel temperature of $T_N > 373$ K, although the lower intensity and the larger line width suggest that they are much less abundant and smaller than in samples uncalcined A(SSIE)5.2 and A(CVD,W1,C0.5). As mentioned above, these species were not detected by XAFS [32], illustrating the power of EPR spectroscopy for such investigations. Even the parent H-ZSM-5(A) which was measured for comparative purposes (Fig. 4.22b), and which contains only 0.05 % Fe shows a small g' ≈ 2 line with non-Curie behavior. This indicates that it is not free of small Fe_xO_y clusters. Moreover, signals at g' ≈ 4.3

and 6 were not detected in the parent H-ZSM-5(A). This shows clearly that the respective Fe^{3+} species are introduced by the various Fe loading procedures.

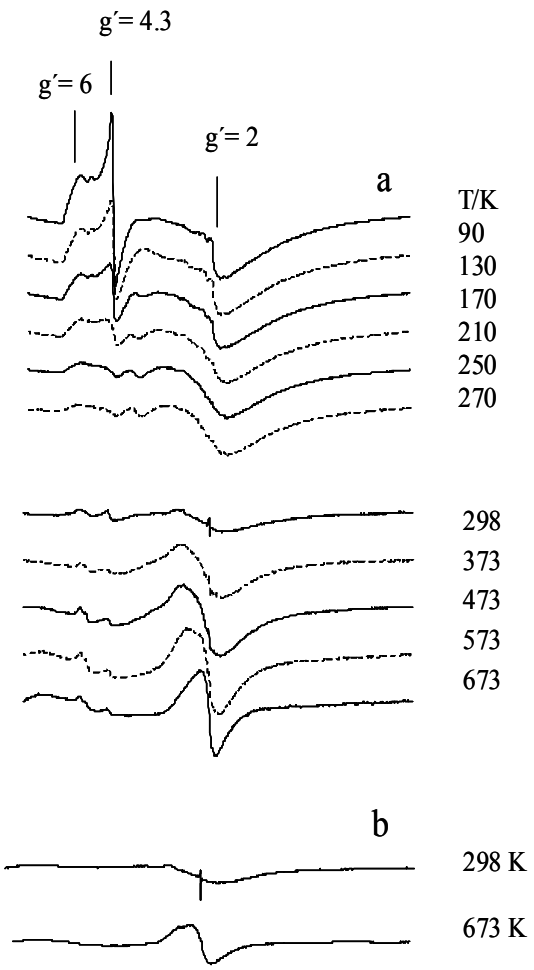

Fig. 4.22. EPR spectra of hydrated uncalcined samples A(MR)0.5 (a) and parent H-ZSM-5(A) (b) during heating in air flow.

Liquid Ion Exchange

In Fig. 4.23, ex situ EPR spectra recorded at 77 K and room temperature of calcined samples are presented. In the spectra, typical signals at effective g values of 2, 4.3, 6 and 9 can be distinguished. In addition, a narrow and a broad signal at g' ≈ 2 can be discerned. In samples A(ILIE)0.2 and A(ILIE)0.3 the g' ≈ 2 EPR signal increases markedly upon cooling to 77 K which is typical for pure paramagnetic behaviour according to the Curie-Weiss law. Therefore, this line is assigned to isolated Fe^{3+} ions in highly symmetric environment. This is also in agreement with UV/VIS-DRS results that indicate the presence of almost exclusively isolated Fe species in those samples (see Fig. 4.5 and Table 4.1). In ILIE samples with 0.6 and 0.7 % Fe, for which UV/VIS-DR spectra indicate the presence of a certain amount of oligomers and even some Fe_2O_3 nanoparticles (bands above 300 and 400 nm in Fig. 4.5) a broad line with a low field maximum around 2350 G at 298 K is superimposed on the narrow signal at g' ≈ 2 which might be due to Fe_xO_y clusters (Fig. 4.23). In sample A(ILIE)1.2 for which UV/VIS-DRS showed a pronounced trend to the formation of Fe_2O_3 particles (Fig. 4.5), the line width of

this broad signal is even larger shifting the low field maximum to about 880 G while the narrow line, though well visible, does not increase with rising temperature which indicates a deviation from paramagnetic (isolated) nature (Fig. 4.23).

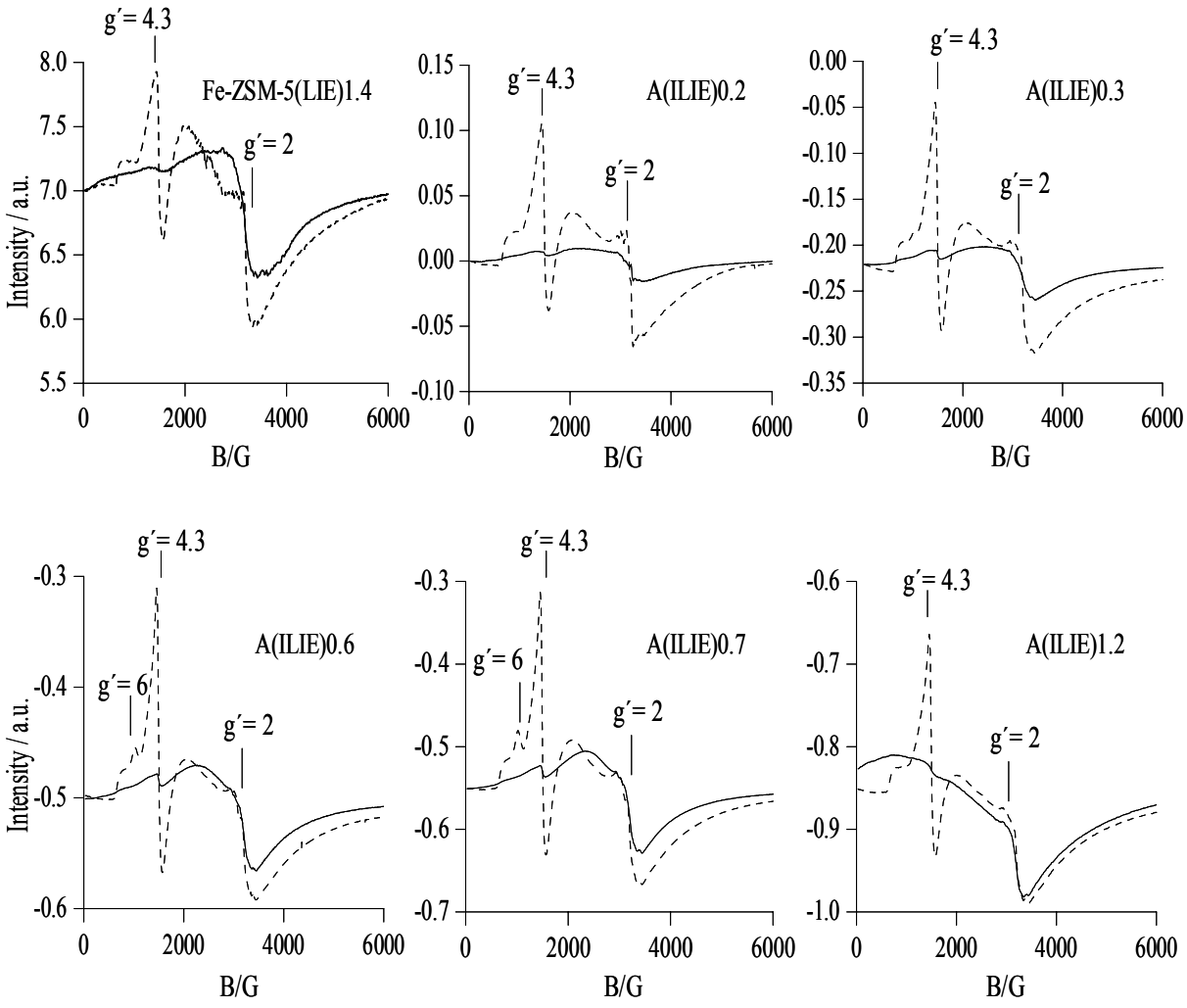

Fig. 4.23. EPR spectra of the hydrated samples at 293 K (solid line) and 77 K (broken line).

As mentioned earlier, the temperature dependence of the signal intensity bears valuable information on the presence of magnetically coupled phases. In view of this, temperature-dependent EPR measurements have been performed with samples A(ILIE)0.6 and A(ILIE)1.2 (Fig. 4.24). From Fig. 4.24 it can be seen that the signal at g' ≈ 2 of sample A(ILIE)0.6 narrows slightly and follows a Curie-like temperature dependence which is typical for both isolated Fe^{3+} ions but also for oxide nanoparticles in the superparamagnetic state. UV/VIS-DRS measurements (Fig. 4.5) suggest that this sample is dominated by isolated Fe^{3+} ions with a small contribution of oligomers. Due to their location inside the pore system, these oligomers are assumed to consist of only a few Fe atoms which is probably not enough to create superparamagnetic behaviour. Therefore, the g' ≈ 2 in sample A(ILIE)0.6 is regarded as arising from both highly symmetric isolated Fe^{3+} species as well as small oligomers with weak dipolar coupling.

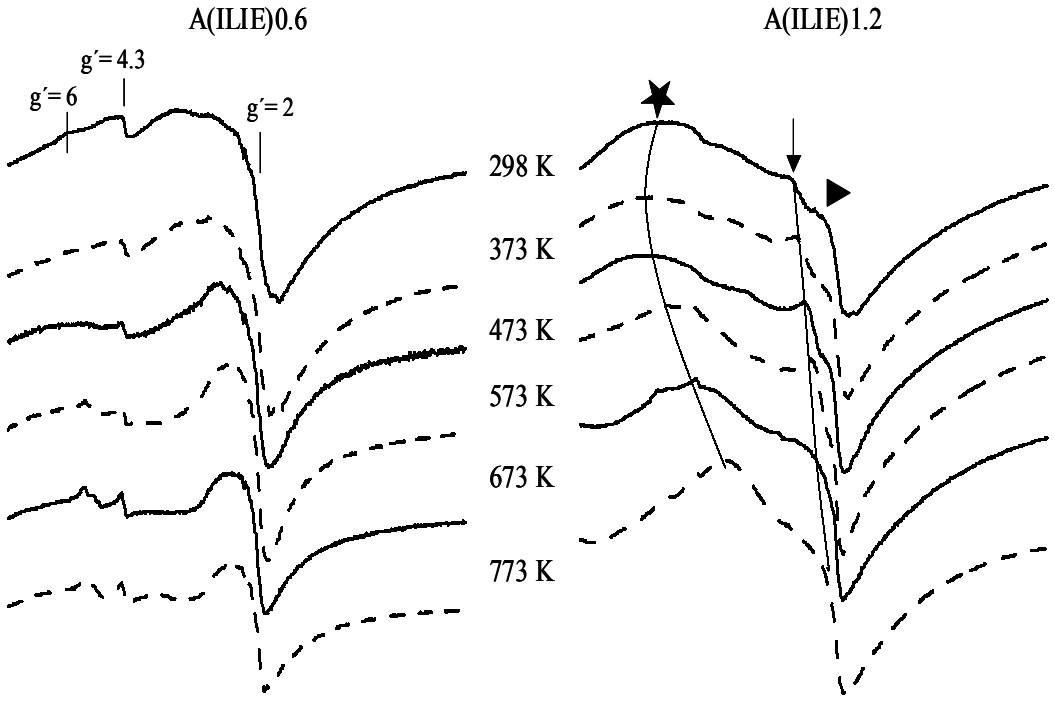

Fig. 4.24. EPR spectra of hydrated samples during heating in air flow.

The EPR spectrum of sample A(ILIE)1.2 at 298 K is characterized by a very broad anisotropic line and two narrow features at g' ≈ 2 (Fig. 4.24). The broad line (marked with star) narrows and shifts to higher resonance field with increasing temperature. The same holds for one of the narrow lines (marked with an arrow). It has been shown that very small α-Fe_2O_3 particles of only a few nm size, in contrast to crystalline bulk α-Fe_2O_3, are EPR-active at low temperature and show ferrimagnetic behaviour [167]. In the EPR spectra, this is reflected by broad anisotropic signals, since the resulting magnetic moment vectors of the particles tend to align with the direction of the external magnetic field. With rising temperature, thermal fluctuations lead to the collapse of the ferrimagnetic order and the particles become superparamagnetic above the so-called blocking temperature. As a result, the EPR signal narrows and shifts towards g' ≈ 2 as the temperature increases [168]. Based on this, these two signals can be assigned to ferrimagnetic/superparamagnetic Fe_2O_3 particles of different size while the second narrow signal at g' ≈ 2 (marked with triangle) might be due to isolated and weakly interacting Fe^{3+} sites.

Interestingly, sample Fe-ZSM-5(LIE)1.4, which shows extensive clustering as evidenced by UV/VIS-DRS, does contain a small amount of highly symmetric isolated Fe^{3+} ions besides iron oxide clusters as evidenced by the temperature dependent g' ≈ 2 signal behaviour (Fig. 4.23). The g' ≈ 2 signal is a superposition of a narrow and a broad line. With decreasing temperature the narrow line increases in intensity (77 K spectrum in Fig. 4.23) as expected for paramagnetic isolated Fe^{3+} sites, while the broad line does not indicating the presence of clusters.

Hydrothermal Synthesis

Ex situ EPR spectra of *ex*-Fe-silicalite, *ex*-Fe-ZSM-5, *c*-Fe-beta and *ex*-Fe-beta were recorded at 77 K and room temperature as shown in Fig. 4.25. As observed for the other Fe-zeolites, too, samples show three signals at effective g values of 2, 4.3 and 6 and they can be assigned to similar species as for ILIE samples. The intensity of the line at g' ≈ 2 in the EPR spectra of the *ex*-Fe-ZSM-5 and *ex*-Fe-beta containing clusters, as evident from UV/VIS results (Fig. 4.9 and Table 4.1), at room temperature and 77 K is very similar, and does not follow the Curie-Weiss law as expected for paramagnetic species. This suggests that the Fe^{3+} sites responsible for this signal are coupled by antiferromagnetic interactions within oxidic clusters, which reduce the number of unpaired spins contributing to the EPR signal.

The g' ≈ 2 signal in *ex*-Fe-silicalite and *c*-Fe-beta increased upon cooling from 293 K to 77 K, as observed for A(MR)0.5 and ILIE samples with low Fe content, which is characteristic of paramagnetic isolated Fe^{3+} species. This indicates the high degree of iron dispersion in the catalysts. This is in excellent agreement with UV/VIS-DRS results which showed the presence of almost exclusively isolated Fe^{3+} ions besides a small fraction of oligomeric moieties (Fig. 4.9 and Table 4.1). Similar to A(MR)0.5 and ILIE samples with low Fe content, these samples, too, show a narrow and a very broad line in the range of g' ≈ 2 (see EPR spectra at 77 K). The latter line indicates the presence of weak dipolar interaction between the Fe^{3+} sites contributing to this signal. Considering these effects and similar to the assignment of g' ≈ 2 signal in A(MR)0.5 and ILIE samples, the signal at g' ≈ 2 in these samples is assigned, too, to highly symmetric Fe^{3+} species rather than isolated Fe sites that have weak dipolar interactions.

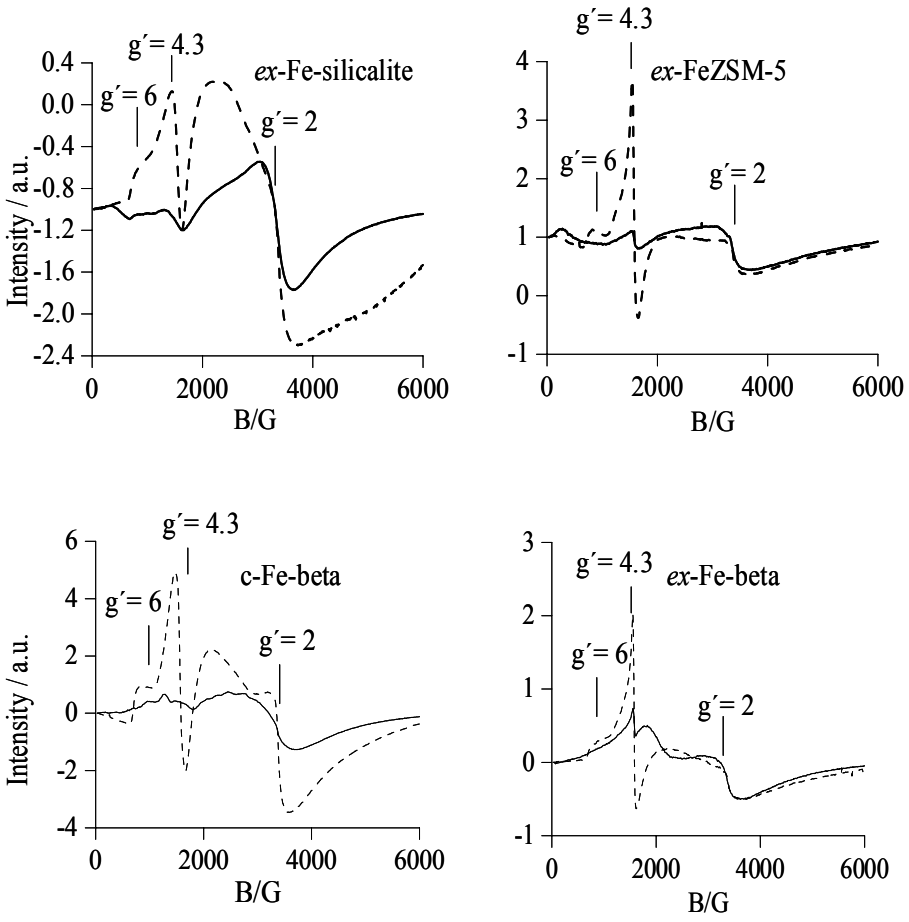

Fig. 4.25. EPR spectra of Fe-zeolites at 293 K (solid line) and 77 K (broken line).

Further support for this assignment was gathered by measuring the EPR spectrum of *ex*-Fe-silicalite after evacuation at ambient temperature for 2 h (Fig. 4.26). This treatment causes a dramatic decrease of the g' ≈ 2 line, together with the appearance of additional signals in the low-field range. This can be attributed to the removal of water molecules from the pore network of the zeolite adsorbed on Fe^{3+} species responsible of the g' ≈ 2 signal. Upon evacuation this leads to isolated Fe^{3+} sites in a lower symmetry (higher zero-field splitting) that give rise to additional signals in the low-field range. These spectral changes are slowly reversible when exposing the sample to ambient conditions. A very similar behaviour for the g' ≈ 2 signal upon evacuation and rehydration at room temperature was also observed by Berlier *et al.* [62] on iron silicalite (Si/Fe = 90) activated at 773-1073 K in vacuum. These authors assigned the g' ≈ 2 signal to isolated Fe^{3+} ions, which are solvated by water molecules in ambient atmosphere. Following their assignment, the result in Fig. 4.26 suggests that the majority of the Fe^{3+} species contributing to the g' ≈ 2 line in *ex*-Fe-silicalite are well isolated in extraframework positions, being accessible to gaseous molecules.

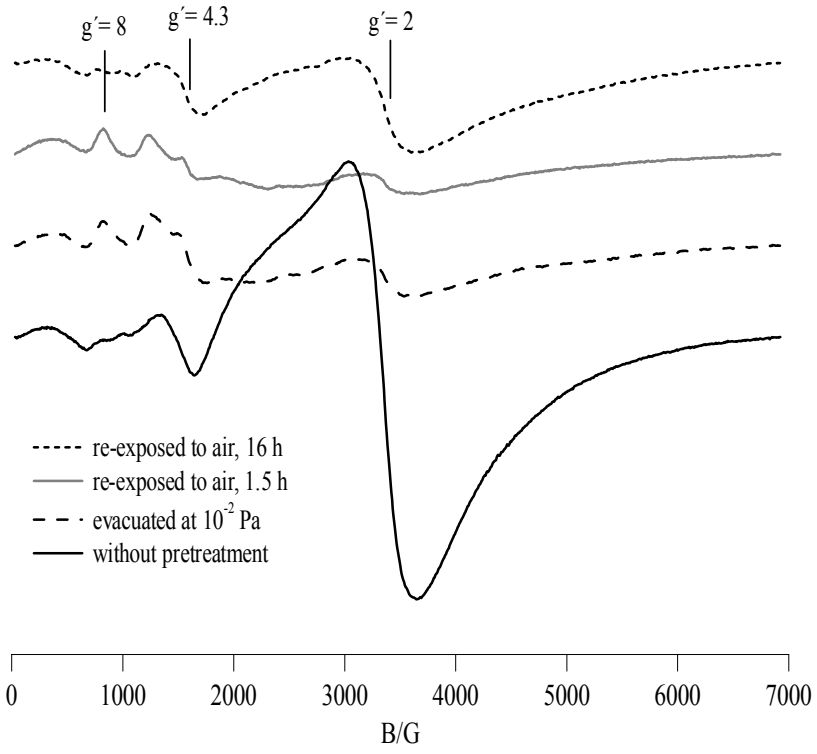

Fig. 4.26. EPR spectra of *ex*-Fe-silicalite recorded at 298 K before and after evacuation for 2 h and after re-exposure to ambient atmosphere for 1.5 and 16 h.

Impregnation by incipient wetness

In Fig. 4.27, ex situ EPR spectra of calcined (Fe-SBA-I)0.95 at 293 K and 77 K are depicted. The spectra not only show similar EPR signals at effective g values of 2, 4.3 and 6 but also similar behavior to that of uncalcined A(MR)0.5, A(ILIE)0.2, A(ILIE)0.3 and *ex*-Fe-silicalite, which show almost exclusively isolated Fe^{3+} ions besides a small fraction of oligomeric iron oxo clusters (see Figs. 4.21, 4.23 and 4.25 and Table 4.1). Hence, similar to

these samples, the EPR signals in sample (Fe-SBA-I)0.95 can be attributed to differently distorted isolated Fe^{3+} ions. However, the broad line in the g' ≈ 2 range indicates the presence of weak dipolar interaction between the Fe^{3+} ions. These results are in line with UV/VIS-DRS which show a majority of iron in the sample as isolated iron species and a small fraction of iron association as oligomeric iron oxo species (Fig. 4.11 and Table 4.1).

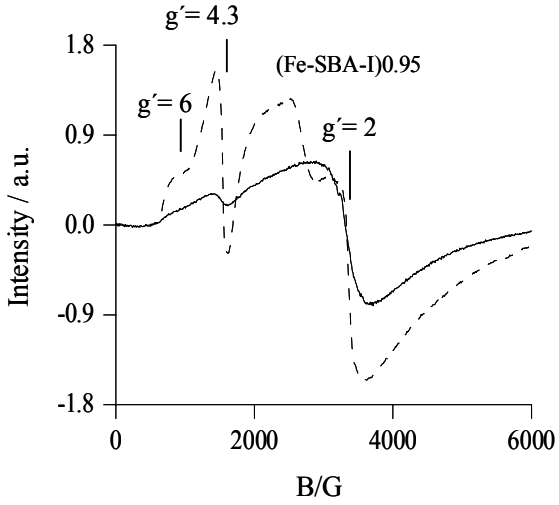

Fig. 4.27. EPR spectra of (Fe-SBA-I)0.95 at 293 K (solid line) and 77 K (broken line).

4.2 Analysis of acidic properties of Fe-zeolites by FT-IR investigation of adsorbed pyridine

FT-IR spectroscopic measurements of adsorbed pyridine were carried out to elucidate the nature and relative amount of the acid sites in selected iron zeolites. The infrared spectra of the various samples (Figs. 4.28, 4.29 and 4.30) exhibit a band at 1545 cm^{-1} unequivocally assigned to Brønsted acid sites [148,159]. Bands around 1445 cm^{-1} arise from pyridine adsorbed on Lewis acid sites [148,159]. Bands around 1600 cm^{-1} are also due to pyridine adsorbed on Lewis sites and can be considered a measure of the strength of the Lewis sites [148]. Bands at 1581 and 1598-1596 cm^{-1} are attributed to weak and medium Lewis acid sites, respectively, while bands at 1612-1607 and 1623 cm^{-1} originate from strong and very strong Lewis acid sites, respectively [148]. However, the band at 1623 cm^{-1} is ambiguously discussed [148,150]. In zeolites this band is attributed to Brønsted acid sites [150], while the same band is ascribed to pyridine adsorbed on Al Lewis acid sites of γ-Al_2O_3 and amorphous Al_2/SiO_2. [148]. The latter assignment is supported by the fact that the FT-IR spectrum of the Al-free *ex*-Fe-silicalite (Si/Al ≈ ∞ and 0.68 wt.% Fe) after pyridine adsorption does not show a band at 1623 cm^{-1} (Fig. 4.30). According to infrared studies over iron supported on silica [149], the band at 1595-1598 cm^{-1} can be assigned to weakly adsorbed pyridine on Si Lewis acid sites in Fe-zeolites. The presence of different types of Lewis acid sites in Fe-zeolites can be inferred from the splitting of the bands at high wavenumbers (≈1600 cm^{-1}), which is not the case in *ex*-Fe-silicalite, showing a single absorption band in this region (Fig. 4.30).

The ratio of Brønsted-to-Lewis acid sites can be estimated from the area of the bands at 1545 (pyridium ions, $PyrH^+$) and 1445 cm^{-1} (pyridine coordinated to Lewis sites, PyrL), respectively, since the ratio of the extinction coefficients of these two absorption bands is ≈ 1 [169-172]. The integral intensities of Brønsted (1567-1515 cm^{-1}) and Lewis (1467-1426 cm^{-1}) acid sites of the samples are normalized on their surface area. As shown in Table 4.3, the ratio of Brønsted-to-Lewis acid sites depends on the zeolite type, Fe-content, preparation route and the corresponding treatment.

Attending to the intensity of the infrared bands at around ≈1600, 1545 and 1445 cm^{-1} in Fig. 4.28, samples A(CVD,W1,C0.5), A(CVD,W10,C0.5) and A(CVD,W1,C5) contain similar Brønsted and Lewis acidity (Table 4.3). The Brønsted acidity of the samples is similar to that of the parent H-ZSM-5(A) but the samples contain much higher amount of Lewis acidity. The latter can be attributed to the presence of iron oxide clusters in the samples A(CVD) which are not present in the parent H-ZSM-5(A) as evidenced by ex situ UV/VIS-DRS and EPR spectroscopic results (sections 4.1.1 and 4.1.2). These spectra show that A(CVD) samples consist of similar nature and distribution of iron species, however, with different size of clusters as shown by temperature dependent EPR spectra in Fig. 4.14 and as reported earlier in [36,55]. Therefore, it can be concluded that iron oxide clusters form additional Lewis sites on the sample. H-ZSM-5(A) shows additional bands at 1621 and 1596 cm^{-1} while in samples A(CVD) these two bands are extinguished and a new band at 1614 cm^{-1} arises. These observations indicate the change in the nature of the Lewis acidity of the A(CVD) samples as compared to the parent H-ZSM-5(A) which might be due to the presence of iron oxide clusters. Accordingly, a band in the same range (1612 cm^{-1}) is observed for sample A(SSIE)5.2 which is dominated by clusters (Fig. 4.29).

Table 4.3. Areas of FT-IR bands normalized on the BET surface area of adsorbed pyridine associated with Brønsted and Lewis acidity and their corresponding ratio.

Sample	Band at 1545 cm^{-1} Brønsted sites	Band at 1445 cm^{-1} Lewis sites	Ratio of Brønsted / Lewis acidity
H-ZSM-5(A)	3.4	1.8	188.8
A(CVD,W1,C0.5)	3.9	2.7	144
A(CVD,W10,C5)	3.1	2.9	106
A(CVD,W1,C5)	3.7	3.0	123
B(CVD,W1,C5)	0.8	1.58	50
A(SSIE)5.2	7.1	3.2	221
A(MR)0.5	5.0	1.8	277
A(ILIE)0.2	3.69	2.1	175.7
A(ILIE)1.2	2.78	3.14	87
ex-Fe-silicalite	0.15	0.9	16.6
c-Fe-beta	0.35	3.1	11.3
ex-Fe-beta	0.23	1.8	12.7

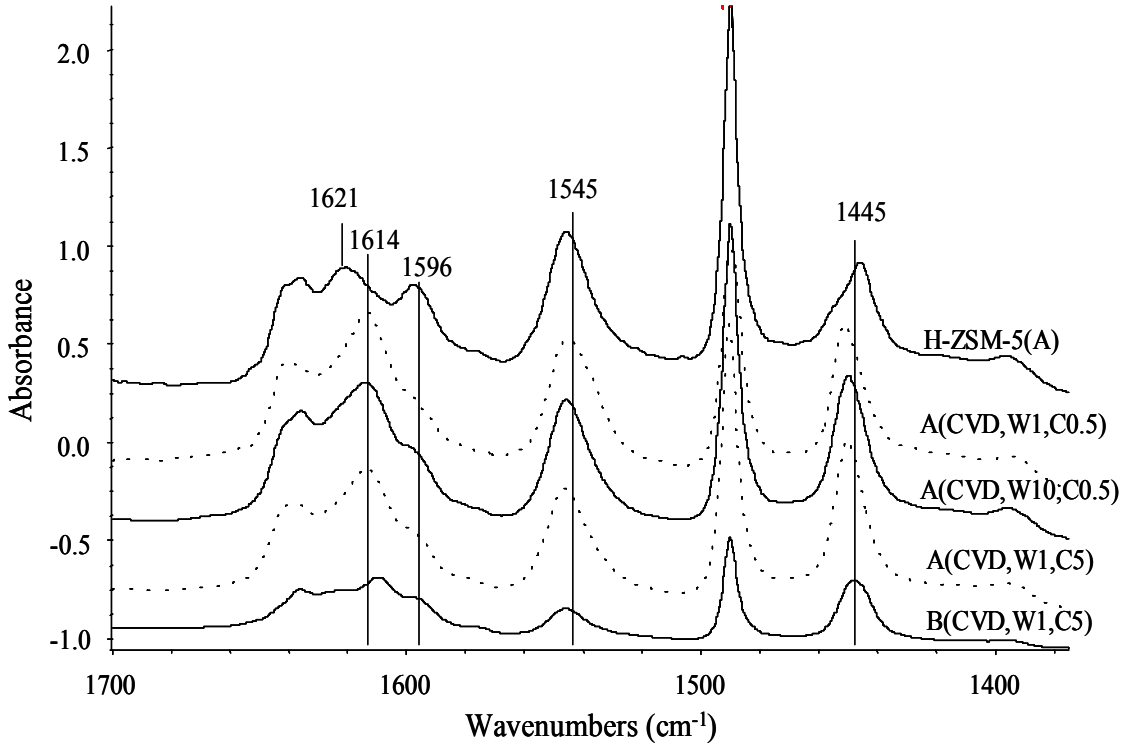

Fig. 4.28. Difference FT-IR spectra of pyridine adsorbed on Fe-ZSM-5 zeolites at 373 K, obtained by subtraction of the FT-IR spectrum of the bare zeolite after pretreatment at 673 K for 1 h.

The effect of Si/Al ratio (≈ 40 *vs* ≈ 14) on the nature of iron species is significant as evidenced, too, by ex situ UV/VIS-DRS and EPR (Fig. 4.3 and 4.17) which show that higher Si/Al ratio (≈ 40, sample B(CVD,W1,C5)) favors cluster formation during CVD. However, after calcination the clusters in sample B(CVD,W1,C5) seem to be smaller than in samples A(CVD) with lower Si/Al ratio since they may be trapped in silanol nests which restrict their further growth. As expected, the FT-IR spectrum of adsorbed pyridine of sample B(CVD,W1,C5) shows low Brønsted acidity but contains a considerable amount of Lewis sites (Fig. 4.28 and Table 4.3). The low Brønsted acidity is obviously due to the higher Si/Al ratio and the observed Lewis acidity is due to the presence of intra zeolite iron oxide clusters and/or framework Al sites [36,55]. On the basis of these results it can be concluded that the higher Si/Al ratio (≈ 40) leads to lower acidity of the sample as compared to lower Si/Al ratio (≈ 14).

Interestingly, the sample prepared by solid state ion exchange, A(SSIE)5.2 contains the highest density of Brønsted acid sites among the investigated Fe-zeolites including H-ZSM-5(A) besides a considerable amount of Lewis acid sites (Table 4.3 and Fig. 4.29). The acidity (Brønsted and Lewis) of the sample is almost double the amount as compared to the parent H-ZSM-5(A) (Table 4.3), while compared to the A(CVD) samples, A(SSIE)5.2 shows almost double the amount of Brønsted acidity but similar amount of Lewis acidity. This indicates that the SSIE preparation method creates additional Brønsted acid sites as compared to the CVD procedure. This conclusion is further supported by the similar Brønsted acidity in the parent H-ZSM-5(A) and A(CVD) samples (Table 4.3). Similar to A(CVD) samples, A(SSIE)5.2 shows an intense band at 1612 cm^{-1} while bands at 1621 and 1596 cm^{-1} are completely missing

which are present in the parent H-ZSM-5(A) as shown in Fig. 4.28 and 4.29. This indicates the presence of similar nature of Lewis acid sites in A(SSIE)5.2 and A(CVD) samples. This is in good agreement with ex situ UV/VIS-DRS and EPR results which show similar nature and distribution of iron species, however, with different degrees of iron agglomeration. This indicates that the size of the clusters may not affect the Lewis acidity of the sample.

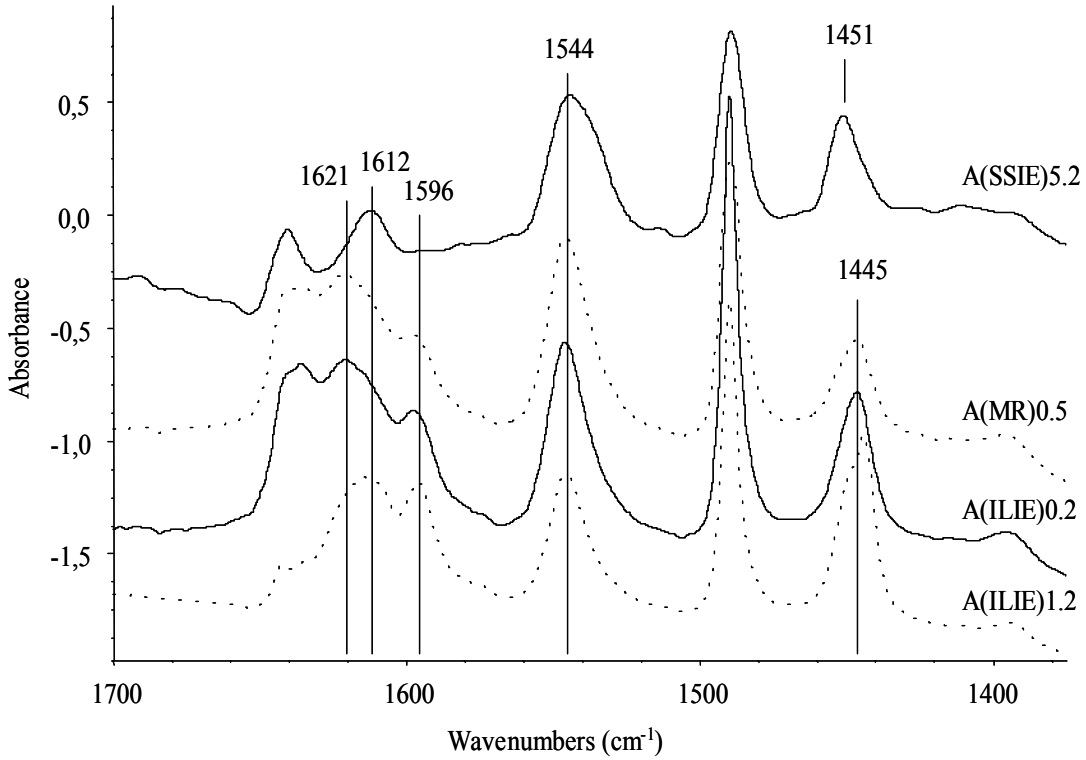

Fig. 4.29. Difference FT-IR spectra of pyridine adsorbed on Fe-ZSM-5 zeolites at 373 K, obtained by subtraction of the FT-IR spectrum of the bare zeolite after pretreatment at 673 K for 1 h.

The amount of Brønsted acid sites in the A(MR)0.5 (Si/Al ≈ 14 and 0.5 wt.% Fe) is increased as compared to the parent H-ZSM-5(A) and is between A(SSIE)5.2 and A(CVD) samples while the Lewis acidity of the sample is considerably lower than in the latter samples but is similar to that of parent H-ZSM-5(A) (Table 4.3 and Fig. 4.29). From the above observations it can be concluded that, similar to the SSIE preparation procedure, MR technique also creates additional Brønsted acid sites. However, at this point it cannot be conclusively stated how they are created by these two techniques. As shown by ex situ UV/VIS-DRS and EPR, the sample A(MR)0.5 contains almost exclusively isolated Fe^{3+} ions with a small fraction of oligomeric moieties (Table 4.1). Accordingly, additional Lewis acidity from iron oxide clusters cannot be expected for this sample as observed for cluster containing samples A(CVD) and A(SSIE)5.2. In agreement with these results sample A(MR)0.5 shows similar Lewis bands as the parent H-ZSM-5(A). This suggests that the nature of Lewis acidity of A(MR)0.5 is similar to that of H-ZSM-5(A) and mainly related to Al and Si sites.

Different from SSIE and MR techniques, ILIE does not create additional Brønsted acid sites as evidenced by samples A(ILIE)0.2 and A(ILIE)1.2 which show similar Brønsted

acidity to that of H-ZSM-5(A) and A(CVD) samples. Lewis acidity of the A(ILIE)0.2 is similar to that of H-ZSM-5(A). This is in good agreement with ex situ UV/VIS-DRS and EPR results which show almost exclusively isolated Fe^{3+} ions in the A(ILIE)0.2. Accordingly, additional Lewis acidity is not expected for this sample. In contrast to this sample, A(ILIE)1.2 with extensive clustering as evidenced by ex situ UV/VIS-DRS and EPR results shows higher Lewis acidity as compared to H-ZSM-5(A), A(MR)0.5 and A(ILIE)0.2 and is similar to that of cluster containing A(CVD) and A(SSIE) samples. This further supports that iron oxide clusters provide additional Lewis acidity in the sample. Additional bands in the high wavenumber range at 1621 and 1596 cm^{-1} are observed over cluster free A(ILIE)0.2 similar to H-ZSM-5(A) and A(MR)0.5 but no band at 1612 cm^{-1} which was typically observed for cluster containing samples as in A(ILIE)1.2. In the latter sample the band at 1621 cm^{-1} is almost completely missing or may be present as a shoulder to 1612 cm^{-1} band but a band at 1596 cm^{-1} is observed.

Calcined *c*-Fe-beta contains weak Brønsted acidity but considerable Lewis acidity as evidenced by Fig. 4.30 and Table 4.3.

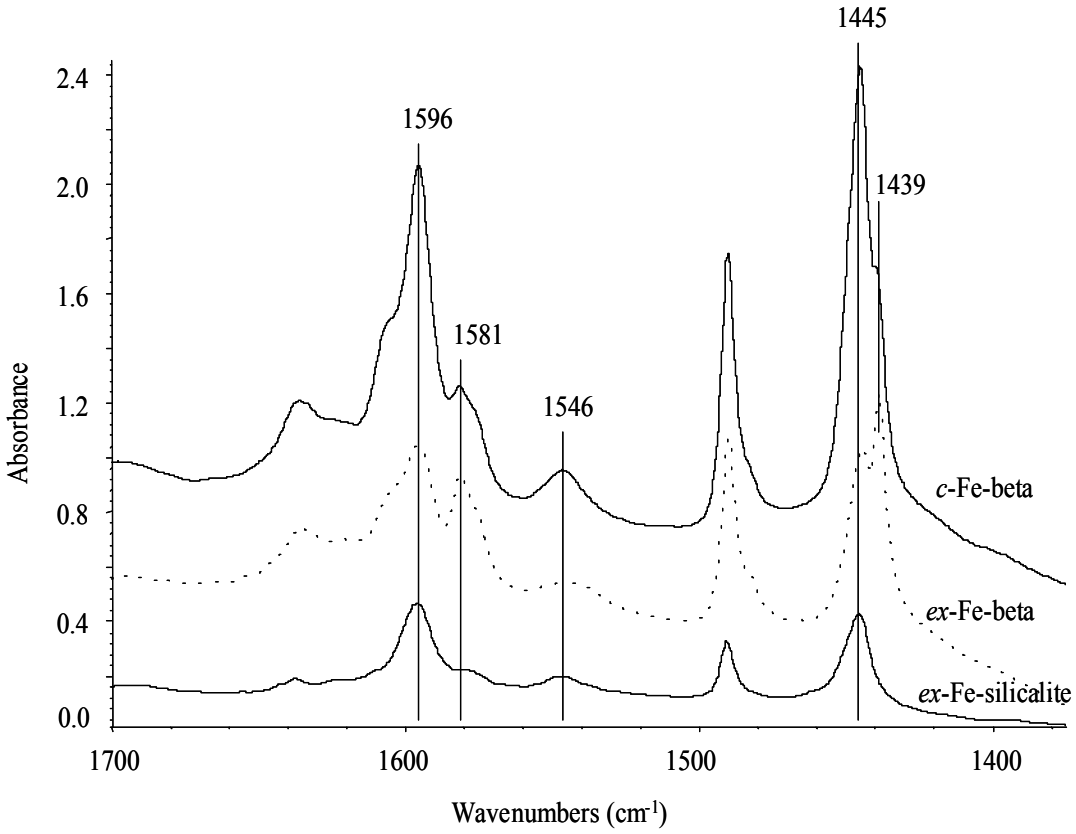

Fig. 4.30. Difference FT-IR spectra of pyridine adsorbed on Fe-ZSM-5 zeolites at 373 K. Difference spectra are obtained by subtraction of the FT-IR spectrum of the bare zeolite after pretreatment at 673 K for 1 h.

As compared to B(CVD,W1,C5) with similar Si/Al ratio, *c*-Fe-beta shows lower Brønsted acidity (Table 6). This can be attributed to the dealumination of Al^{3+} sites from framework positions upon calcination in the latter sample as reported in [159]. A decrease of Brønsted and Lewis acid sites is observed upon steaming of *c*-Fe-beta as evidenced by the reduced intensity

of bands at 1546 and 1445 cm^{-1} in Fig. 4.30 and Table 4.3. Besides dealumination, the steam activation of calcined zeolites induces dislodgement of framework iron. This should in principle contribute to the acidity differences observed, despite the relatively low iron content compared to Al. This observation is in good agreement with ex situ UV/VIS-DRS and EPR results which show that *c*-Fe-beta contains the majority of iron as isolated Fe^{3+} ions probably in the framework positions while *ex*-Fe-beta shows extensive clustering. On the basis of these observations it can be concluded that the *c*-Fe-beta and *ex*-Fe-beta with Si/Al ≈ 36 possesses poor acidity even lower than that of the B(CVD,W1,C5) sample with higher Si/Al ≈ 40. Finally, as expected, *ex*-Fe-silicalite without Al in the framework exhibits poor Brønsted and Lewis acidity as evidenced by less intense FT-IR bands as compared to *ex*-Fe-beta in Fig. 4.30 and the corresponding areas of the bands in Table 4.3.

In summary, samples prepared using H-ZSM-5(A) support with Si/Al ≈ 14 show considerable amount of Brønsted and Lewis acidity. Interestingly, samples prepared by SSIE and MR techniques using this support show more Brønsted acidity than that of CVD and ILIE and even higher than H-ZSM-5(A). However, it is not yet clear how SSIE and MR techniques create additional Brønsted acidity. Sample prepared by CVD technique using H-ZSM-5(B) support with Si/Al ≈ 40 shows, as expected, poor Brønsted acidity as compared to samples prepared using H-ZSM-5(A). Interestingly, the Brønsted acidity of the sample is much higher than that of calcined and steamed Fe-beta samples which contain lower Si/Al ratio (≈ 36) than the H-ZSM-5(B). This is due to the dislodgement of framework Al and Fe even upon calcination and obviously after steam treatment in Fe-beta samples. Consequently, the reduced surface acidity is observed in the latter samples. However, in agreement, calcined and steamed Fe-beta samples show higher Lewis acidity than H-ZSM-5(B) due to lower Si/Al ratio.

4.3 Studies of the behaviour of Fe species in the presence of feed components by in situ techniques

In situ UV/VIS-DR, EPR and FT-IR spectroscopic studies were performed to identify active iron species and the adsorbed NO_x species or reaction mechanism in the SCR of NO by NH_3 and isobutane, the SCR of N_2O by CO as well as N_2O decomposition over Fe-zeolites, based on the propensity of the iron sites to undergo redox processes. To this end, the interaction of NH_3, isobutane, NO, CO, N_2O, CO+N_2O and SCR reaction mixtures with the iron species in the catalysts has been investigated at 623 K. At this temperature, all catalysts have shown substantial activity in steady-state catalysis experiments (see section 4.4). Additionally, samples A(MR)0.5 and A(ILIE)0.3 were subsequently treated with NH_3 and NO at 773 K to study the effect of temperature on the redox activity of different isolated Fe sites by EPR. Also, the interaction of NH_3 and NO with the iron species in the catalysts was investigated at 293 K to study the influence of these probe molecules on the Fe sites and also to investigate the nature of adsorbed species. Hence, in this section results of EPR, UV/VIS-DR and FT-IR spectroscopic studies are described.

4.3.1 EPR, UV/VIS-DR and FT-IR spectroscopic studies during interaction of feed components in NH_3-SCR of NO

Interaction of NH_3 with pre-oxidized samples A(MR)0.5 and A(CVD,W1,C0.5) at 293 K

Upon NH_3 treatment at room temperature for 1 h, the EPR signal at $g' \approx 6$ completely disappeared while the one at $g' \approx 2$ slightly increased in intensity and the signal at $g' \approx 4.3$ slightly decreased in A(MR)0.5 or is hardly affected in A(CVD, W1,C0.5) (Fig. 4.31).

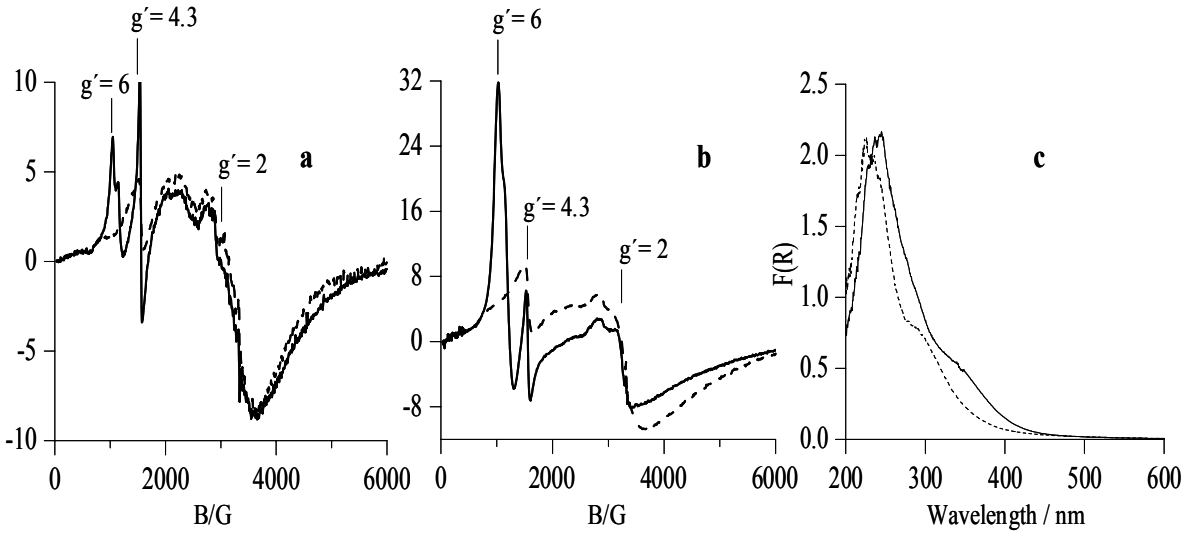

Fig. 4.31. In situ EPR spectra of samples A(MR)0.5 (a) and A(CVD,W1,C0.5) (b) and in situ UV/VIS-DR spectra of A(MR)0.5 (c) recorded at 293 K after oxidative treatment at 773 K for 1 h (solid line) and after treatment in a flow of 1% NH_3/He at 293 K for 1 h followed by flushing with He at 293 K for 15 min (dotted line).

In principle, this could be due to two reasons: i) reduction of Fe^{3+} to Fe^{2+} or ii) coordination of NH_3 to these Fe^{+3} species which increases the local crystal field symmetry and shifts the signal towards $g' \approx 2$. Considering the experimental conditions, i.e., room temperature and 1% NH_3/He, the suppression of the EPR signal at $g' \approx 6$ may not be due to the reduction of Fe^{+3} species but could be due to the coordination of NH_3 to coordinatively unsaturated iron species that increases the site symmetry. This may be the reason for a slight increase in intensity at $g' \approx 2$, which is more clearly seen for sample A(CVD,W1,C0.5) than for sample A(MR)0.5. This is due to the fact that in sample A(MR)0.5 the $g' \approx 6$ signal is smaller than in sample A(CVD,W1,C0.5). Therefore, less NH_3 ligated Fe^{3+} species contribute to the $g' \approx 2$ signal in the former sample. Hence, this could explain the low intensity gain of $g' \approx 2$ signal in sample A(MR)0.5 than in A(CVD,W1,C0.5). After NH_3 treatment the samples were purged by pure He at 293 K temperature, which did not restore the original EPR spectra. This could be due to strong linking between Fe^{+3} sites and NH_3 ligands. However, it is difficult to decide whether reduction of Fe^{3+} or coordination of NH_3 is the reason for the spectral changes only from EPR. To clarify these results, UV/VIS-DR spectroscopy is a suitable technique since it provides information about simultaneous electronic and coordination changes.

In the corresponding UV/VIS-DRS spectra of sample A(MR)0.5, NH_3 treatment causes a shift in the band position to a lower wavelength as observed in Fig. 4.31c. Interestingly, the band intensity is more or less similar which indicates that NH_3 may considerably not reduce the iron species at room temperature but links to coordinatively unsaturated isolated iron species. Therefore, after NH_3 treatment the band position slightly shifted to lower wavelength as compared to the oxidatively pretreated sample. This is expected since NH_3 is a stronger field ligand than oxygen. Consequently, for electronic transitions higher energy is required. On the basis of these results it can be concluded that the disappearance of EPR signal at $g' \approx 6$ is, probably, not due to the reduction of Fe sites but due to the change in the Fe site symmetry. However, reduction of a small amount of Fe species cannot be completely ruled out. The corresponding UV/VIS experiments have also been performed on sample A(CVD,W1,C0.5), but the effects are hardly visible since this sample is rather dominated by iron oxide clusters (not shown).

Interaction of NO with pre-oxidized and pre-reduced catalysts at 293 K studied by FT-IR spectroscopy

These experiments were performed to investigate the nature of the interaction of NO with Fe sites in Fe-ZSM-5 as well as the nature of adsorbed species on the pre-oxidized and pre-reduced surface of Fe-ZSM-5 zeolites.

Interaction of NO with pre-oxidized catalysts at 293 K

FT-IR spectra of samples A(MR)0.5, A(ILIE)0.3, A(ILIE)1.2, A(CVD,W1,C0.5) and pure support H-ZSM-5(A) after oxidative pretreatment and adsorption of 1% NO/He are shown in Fig. 4.32. The spectra obtained after 30 min adsorption of NO and before evacuation show bands at 2198, 2134, 1882, 1743, 1627, 1605 and 1574 cm^{-1}. Similar bands have been observed previously upon adsorption of NO by several authors. An overview on their assignment is given in Table 2.2. Based on these studies, bands at 2198 and 2134 cm^{-1} are assigned to $[NO^+][N_2O_4]$ and NO^+, respectively, while the band at 1743 cm^{-1} is ascribed to adsorbed N_2O_4 [86-89]. A band around 1880 cm^{-1} has always been observed for NO adsorbed on an iron site, although the nature of this Fe site is controversially discussed (Table 2.2). Taking into account that the catalysts in Fig. 4.32 have been pre-oxidized before NO adsorption, it is likely that the band at 1880 cm^{-1} arises from NO adsorbed at Fe^{3+} sites. However, N_2O_3 can also contribute to this band as it gives two bands at around 1880 and 1555 cm^{-1} [86]. Thus, the latter band probably also contribute to the nitrato band at 1575 cm^{-1}. Interestingly, bands above 1700 cm^{-1} disappear completely upon evacuating the sample for 30 min (Fig. 4.33). This indicates that these bands arise from weakly adsorbed species only. In contrast, bands below 1700 cm^{-1} do not disappear completely upon evacuation, although differences in intensities are observed (Fig.4.33). However, it must be noted that the band at 1575 cm^{-1} over H-ZSM-5 completely vanished. This suggests the contribution of N_2O_3 to some extent to 1880 and 1575 cm^{-1} bands in the spectra of samples before evacuation (Fig. 4.32). This is in particular true for H-ZSM-5 since these bands disappeared completely after evacuation.

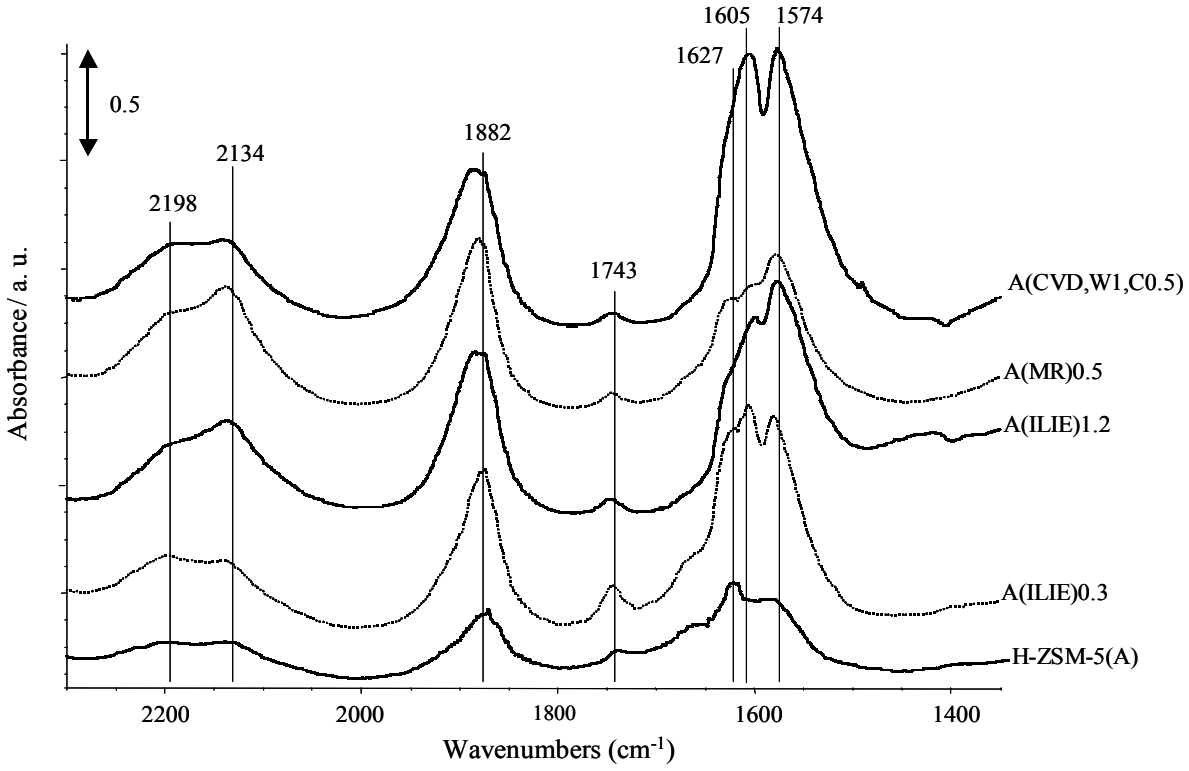

Fig. 4.32. In situ FT-IR spectra at 293 K after adsorption of 1% NO/He on oxidized surfaces and before evacuation; oxidative pretreatment in air at 673 K for 1 h followed by evacuation and cooled to 293 K.

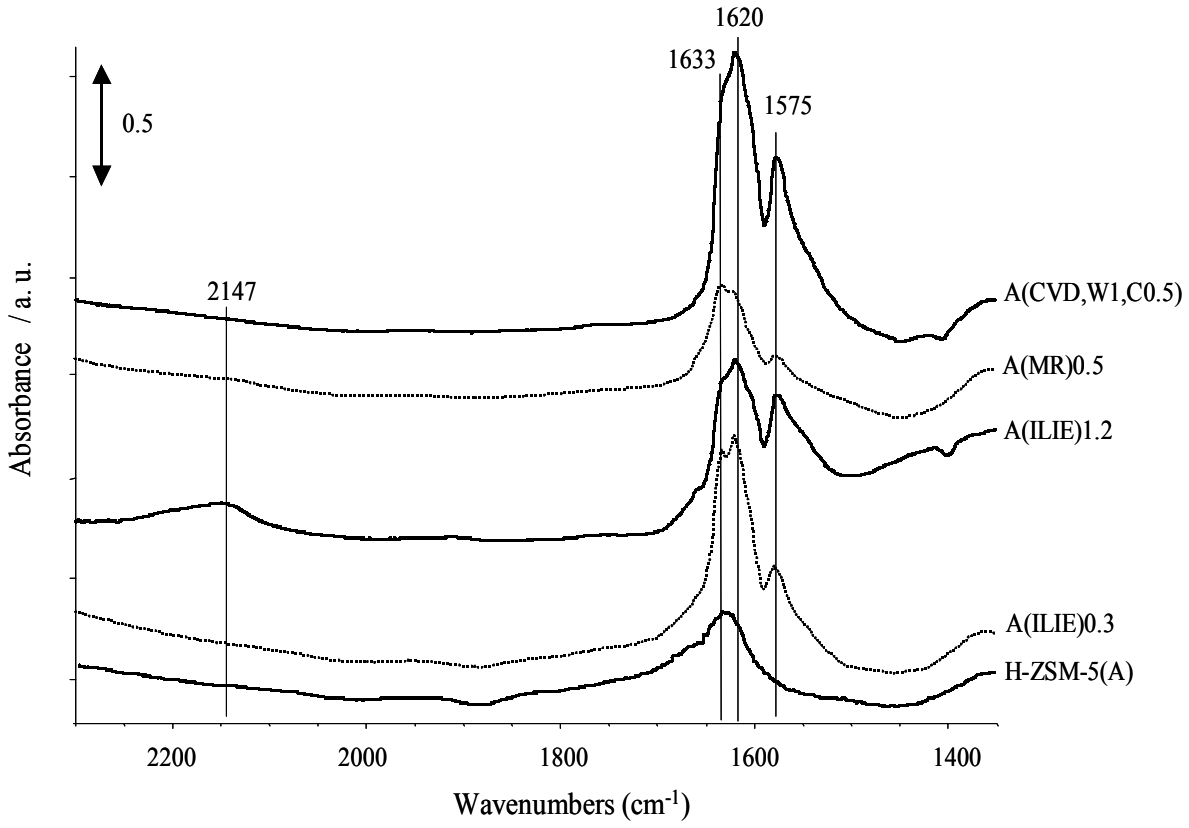

Fig. 4.33. In situ FT-IR spectra at 293 K after adsorption of 1% NO/He on oxidized surfaces and after evacuation; oxidative pretreatment in air at 673 K for 1 h followed by evacuation and cooled to 293 K.

The band at 1605 cm^{-1} is no longer observed for the evacuated samples, suggesting that the respective species might be only weakly adsorbed. Chen et al. [86] assigned this band to weakly adsorbed NO_2 since it is close to the asymmetric stretching frequency of gaseous NO_2 (1610 cm^{-1}). Bands at 1634, 1625 and 1570 cm^{-1} were assigned by the same authors [86,87] and Lobree et al. [88] to NO_2/NO_3 species whereby a more detailed description of their nature was not given. In contrast, Hadjiivanov et al. [89] and Davidov [153] assigned bands between 1650-1600 cm^{-1} to bridging bidentate nitrato and a band at 1575 cm^{-1} to chelating bidentate nitrato species. It is well known, that NO_3^- and NO_2^- anions give rise to bands at 1380 and 1260 cm^{-1}, respectively [153]. For NO_3 and NO_2 species which are not purely ionic, an increase of the bond strength and, thus, a blue shift of the bands should be expected. This is in agreement with the results of Davidov [153], who reported bands of differently bound NO_3 species to occur between 1480 and 1650 cm^{-1} while those of NO_2 species were observed at lower wavenumbers between 1205 and 1520 cm^{-1}. Based on these considerations, bands at 1633, 1620 and 1575 cm^{-1} in the spectra of evacuated samples (Fig. 4.33) are assigned to differently bound nitrato species. By comparing the band intensities in Fig. 4.33, it turns out that the relative intensity at 1575 cm^{-1} is higher on samples A(CVD,W1,C0.5) and A(ILIE)1.2 with the higher Fe content. This could suggest that the NO_3 species reflected by the latter band are preferably adsorbed on Fe species. This is also supported when comparing the spectra of the different Fe-ZSM-5 samples with the one of H-ZSM-5. Band intensities over the bare H-ZSM-5 and samples with low Fe content do not differ much in intensity suggesting that bands associated with NO in the latter samples need not necessarily arise from NO adsorbed on Fe sites. Interestingly, H-ZSM-5 does not show a band at 1575 cm^{-1}.

In summary, it can be stated that on pre-oxidized Fe-ZSM-5 samples weakly adsorbed $[NO^+][N_2O_4]$ (2198 cm^{-1}), NO^+ (2134 cm^{-1}), Fe^{3+}-NO (1882 cm^{-1}), N_2O_4 species (1743 cm^{-1}) and N_2O_3 species (1882 and 1555 cm^{-1}) are formed that, however, can be easily removed by evacuation at 293 K. In addition, stable nitrato species reflected by bands between 1633 and 1575 cm^{-1} are formed, that persist evacuation, whereby the latter arises most likely exclusively from nitrate bound to Fe sites.

Interaction of NO with pre-reduced catalysts at 293 K

To learn more about the influence of the Fe valence state on the interaction with NO, the same experiments were performed with reductively pretreated samples. The adsorption of NO on samples A(MR)0.5, A(ILIE)0.2, A(ILIE)1.2, A(CVD,W1,C0.5) and H-ZSM-5(A) after reduction with NH_3 was investigated at 293 K. The spectra obtained after adsorption of NO for 30 min and before evacuation are reported in Fig. 4.34. In contrast to the NO adsorption on oxidatively pretreated samples, the bands above 1635 cm^{-1} are only weakly present and the bands between 1635-1575 cm^{-1} decreased in intensity. In particular, sample A(CVD,W1,C0.5) with extensive clusters shows an intense band at 1465cm^{-1} which is completely missing in A(MR)0.5 and A(ILIE)0.2 (with almost exclusively isolated iron sites) and A(ILIE)1.2 (with relatively small clusters).

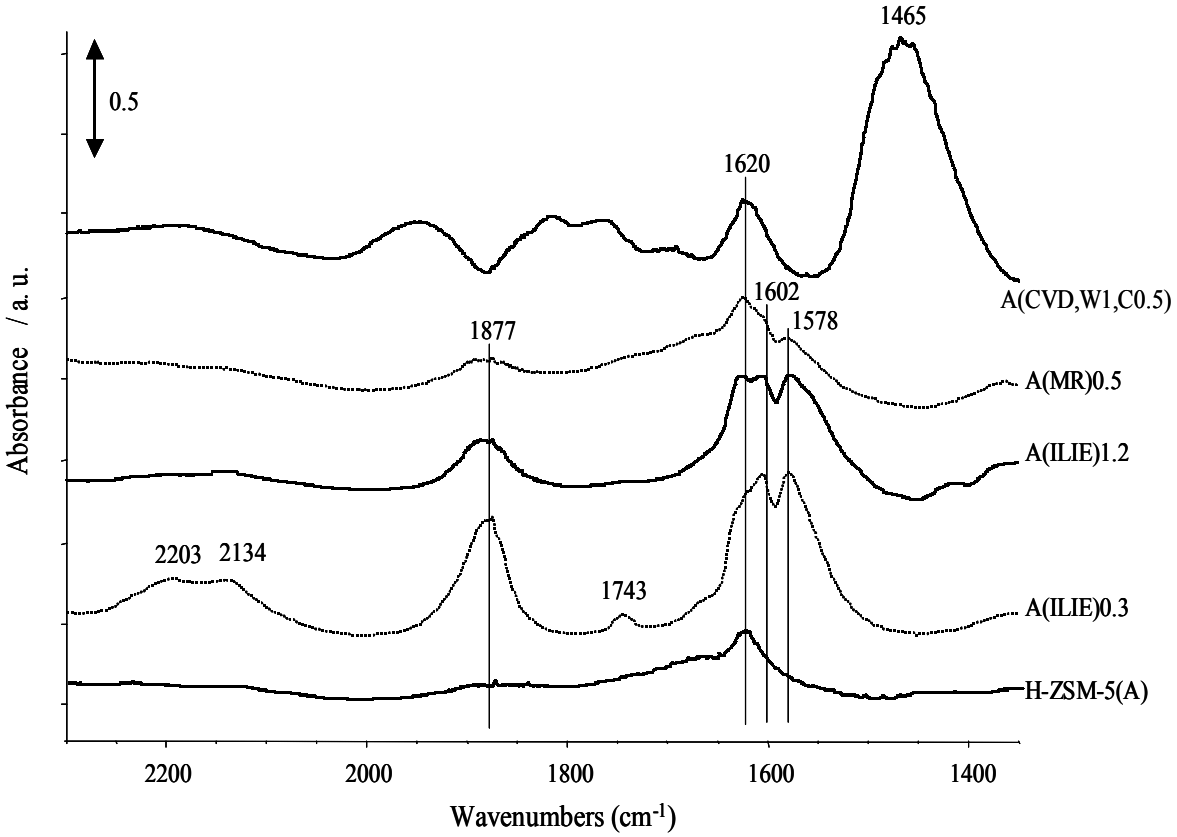

Fig. 4.34. In situ FT-IR spectra at 293 K after adsorption of 1% NO/He on pre-reduced surfaces and before evacuation; reductive pretreatment in 1% NH_3/He at 673 K for 1 h followed by evacuation and cooled to 293 K.

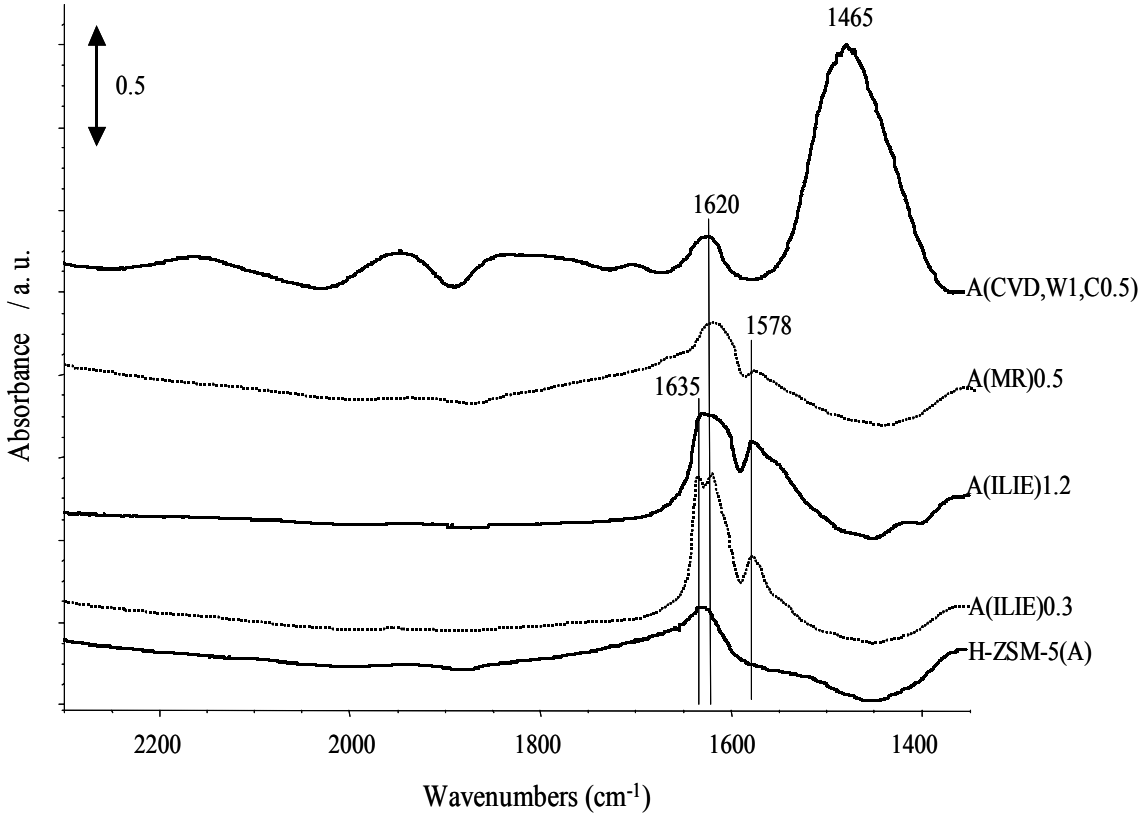

Fig. 4.35. In situ FT-IR spectra at 293 K after adsorption of 1% NO/He on pre-reduced surfaces and after evacuation; reductive pretreatment in 1% NH_3/He at 673 K for 1 h followed by evacuation and cooled to 293 K.

Furthermore, in sample A(CVD,W1,C0.5) the band at 1575 cm^{-1} and a shoulder at 1630 cm^{-1} completely disappeared and the one at 1620 cm^{-1} drastically decreased in intensity. Additionally, upon evacuation, the band at 1578 cm^{-1} drastically decreases in intensity in all samples and weak features above 1635 cm^{-1} completely disappear as shown in Fig. 4.35. These results suggest that Fe^{2+} species assumed to be formed upon pretreatment in 1% NH_3/He do not favor neither the formation of weakly adsorbed species reflected by bands at 2198, 2134, 1882 and 1743 cm^{-1} nor the formation of nitrato species. This suggests that Fe^{3+} ions are essential for the activation of NO either by direct oxidation or by the intermediate formation of N_2O_4 (disproportionation). The band at 1465 cm^{-1} can be ascribed to the formation of nitrito species (-O-N=O) upon adsorption of NO on reduced iron sites, probably on reduced iron oxide clusters [153].

Interaction of NH_3-SCR feed components with catalysts at elevated temperature

While FT-IR results described above provide information mainly on the nature of adsorbed species formed upon contact with NO, these experiments were performed to learn more about the behavior of the Fe sites in the presence of feed components. Samples are described in the order of increasing Fe_xO_y cluster formation, starting with samples that are dominated by isolated Fe sites.

A(MR)0.5

As shown by ex situ UV/VIS and EPR measurements (sections 4.1.1 and 4.1.2) this sample contains almost exclusively isolated Fe species in tetrahedral and higher oxygen coordination. Changing the flow at 623 K from air to NH_3-SCR feed causes a substantial decrease of CT bands of isolated Fe^{3+} species in the UV/VIS-DR spectrum (Fig. 4.36a). This is due to the reduction of Fe^{+3} to Fe^{+2} ions. This suggests that the mean oxidation state of isolated iron ions under typical NH_3-SCR conditions is probably slightly lower than +3. Interestingly, the reduced iron species were not completely reoxidized during 1 h air treatment (not shown), therefore, the sample was reoxidized in air at 773 K for 15 min and cooled to the reaction temperature of 623 K again. On subsequent switching of the flow from air to 0.1% NH_3/He at 623 K the intensity of the two CT bands decreased much stronger than in the complete SCR feed (Fig. 4.36a). This decrease is even more pronounced for the band at 291 nm which is assigned to octahedrally coordinated Fe^{3+}. This is in line with the iron redox kinetics (Table 4.2), which shows that octahedrally coordinated isolated Fe^{3+} ions are faster reduced than tetrahedrally coordinated ones. These reduced iron species are partly reoxidized by subsequent NO/He treatment.

In the corresponding EPR measurements, changing the flow from air to NH_3-SCR feed causes a strong decrease of the signal at $g' \approx 6$ and a less pronounced decrease of the line at $g' \approx 4.3$ (Fig. 4.36b). Different from the $g' \approx 6$ and $g' \approx 4.3$ signals, the signal at $g' \approx 2$, which is attributed to highly symmetric isolated iron species in this sample (see section 4.1.2), changes only very slightly. This suggests that Fe^{+3} species contributing to this signal are hardly reducible at this temperature or that the presence of redox cycle keeps the mean oxidation state of Fe at

+3. To check this, the sample was subjected to subsequent 0.1% NH_3 and 0.1% NO treatments at 773 K (Fig. 4.37).

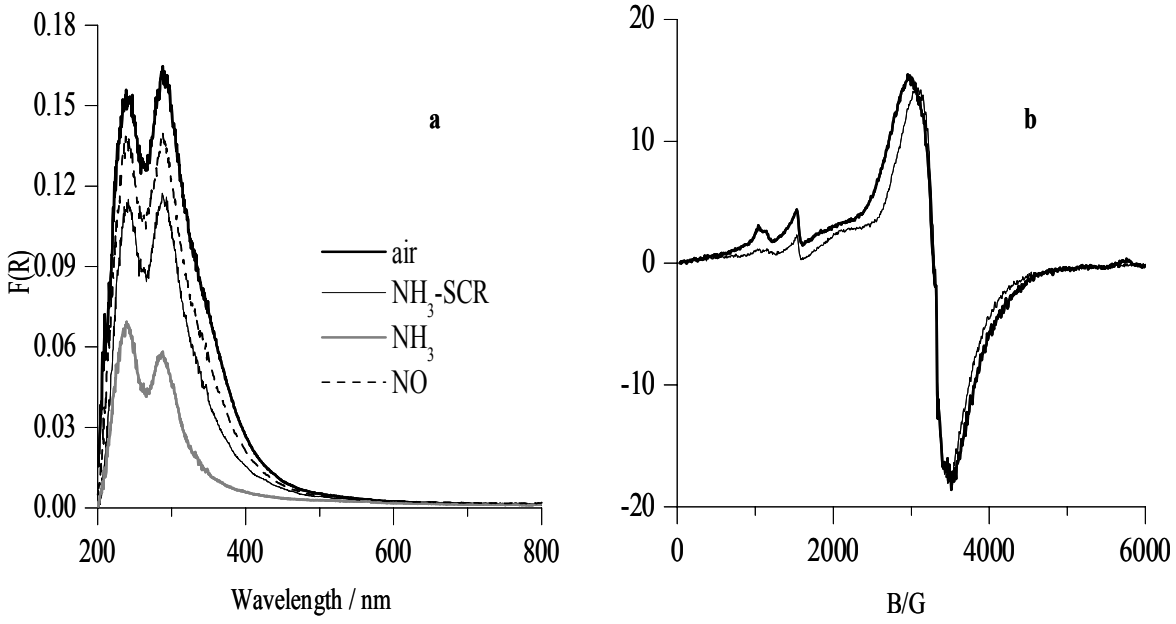

Fig. 4.36. In situ UV/VIS-DRS (a) and in situ EPR (b) spectra of A(MR)0.5 at 623 K in different gas mixtures: air, NH_3-SCR (0.1% NO, 0.1% NH_3, 2% O_2/He), 0.1% NH_3/He and 0.1% NO/He. For UV/VIS measurements, samples were regenerated in airflow (20 ml/min) for 15 min at 773 K to restore the original spectra after NH_3-SCR and cooled to 623 K. Spectra were measured after treatment of the samples in the respective mixtures at 623 K for 1 h. Catalyst pretreatment in air at 773 K for 1 h.

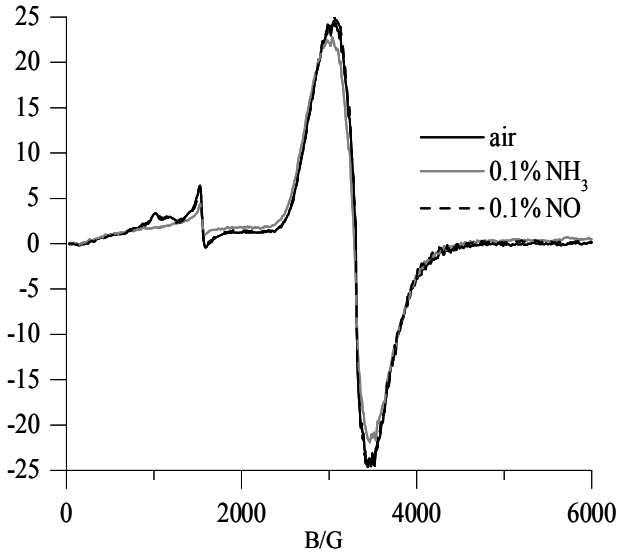

Fig. 437. In situ EPR spectra of A(MR)0.5 at 773 K in different gas mixtures: air (pretreatment), 0.1% NH_3/He and 0.1% NO/He. Spectra were measured after treatment of the sample in the respective mixtures at 773 K for 1 h.

After 1 h NH_3 treatment at 773 K, different from complete SCR feed treatment at 623 K, the intensity of the g' ≈ 2 and g' ≈ 4.3 signals decreased slightly while the one at g' ≈ 6 completely disappeared. Interestingly, subsequent NO treatment almost completely restored the original EPR spectrum. These results clearly demonstrate the different sensitivity of isolated Fe sites against reduction that decreases in the order g' ≈ 6 > g' ≈ 4.3 > g' ≈ 2. Accordingly, isolated Fe sites reflected by g' ≈ 6 which are most probably octahedrally coordinated (see section 4.1.2) are reduced already at lower temperatures compared to Fe sites reflected by g' ≈ 4.3 and g' ≈ 2. This is also suggested by the UV/VIS spectra in which the band at 291 nm being characteristic for octahedral Fe^{3+} decreases stronger already at 623 K than the one at 241 nm assigned to tetrahedral Fe^{3+} (Fig. 4.36a).

A(ILIE)0.2 and A(ILIE)0.3

Similar to sample A(MR)0.5 it has been shown that these two samples are dominated by isolated Fe^{3+} sites. Figure 4.38 demonstrates the in situ UV/VIS-DRS and EPR spectra of samples A(ILIE)0.2 and A(ILIE)0.3 under different feed composition. UV/VIS-DRS spectra are characterized by isolated Fe^{+3} species with CT band maxima below 300 nm. The spectral intensity is markedly decreased under typical NH_3-SCR conditions as compared to the UV/VIS-DR spectra of the samples in air (Fig. 4.38) due to a reduction of isolated Fe^{+3} ions. This behaviour is similar to that of A(MR)0.5 with similar nature and distribution of Fe species (Fig. 4.36). Interestingly, in agreement with Fe redox kinetics (Table 4.2), the intensity loss is more pronounced for the band at 290 nm representing Fe^{3+} in higher than fourfold coordination. As observed for A(MR)0.5, the reduced iron species were not completely reoxidized during subsequent 1 h air treatment at 623 K (not shown). Therefore, the samples were reoxidized at 773 K for 15 min and cooled to the reaction temperature of 623 K. On switching the flow from air to 0.1% NH_3/He at 623 K the intensity of the whole spectrum decreased stronger than in the complete SCR feed indicating further reduction of Fe^{3+}. However, the reduction of the bands at 240 and 290 nm follow the same trend as observed in the complete SCR feed and also as seen for A(MR)0.5, in agreement with the Fe redox kinetics (Fig. 4.7 and Table 4.2). The reduced iron species were partly reoxidized by subsequent NO/He treatment.

In the corresponding EPR spectra of A(ILIE)0.2 and A(ILIE)0.3, changing the flow from air to NH_3-SCR feed causes a slight decrease of the signal at g' ≈ 4.3 and strong decrease of the line at g' ≈ 6, while the line at g' ≈ 2 is hardly influenced (Fig. 4.38). As for sample A(MR)0.5 this suggests that Fe^{3+} sites which are surrounded by more than 4 oxygen ligands and reflected by the signal at g' ≈ 6 are easier to reduce than tetrahedral Fe^{3+} represented by the line at g' ≈ 4.3. This is in agreement with the corresponding UV/VIS-DRS results which show under complete NH_3-SCR feed slightly more reduction of octahedral Fe sites reflected by 290 nm band than tetrahedral Fe sites reflected by 240 nm band. Similar to sample A(MR)0.5 (Fig. 4.36) Fe^{3+} reduction is more pronounced in NH_3/He flow and only partially reversible upon subsequent treatment with NO/He. In particular, the CT band at 290 nm does not return to its original intensity and this is also true for the EPR signal at g' ≈ 6. This is different when the experiment is performed at 773 K (Fig. 4.39).

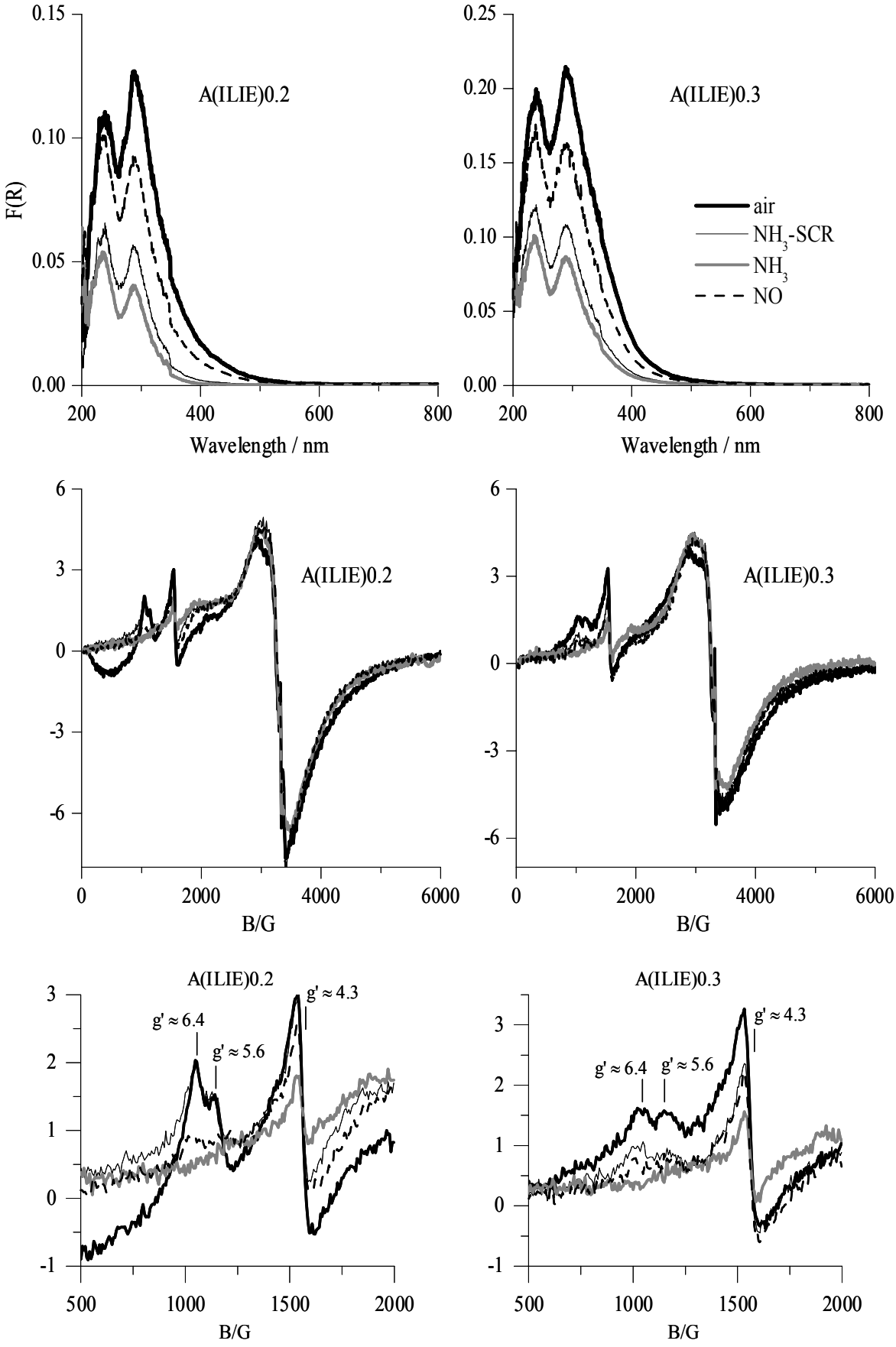

Fig. 4.38. In situ UV/VIS-DRS and EPR spectra at 623 K in different gas mixtures, conditions as in Fig. 4.36. Bottom figures are enlarged EPR spectra.

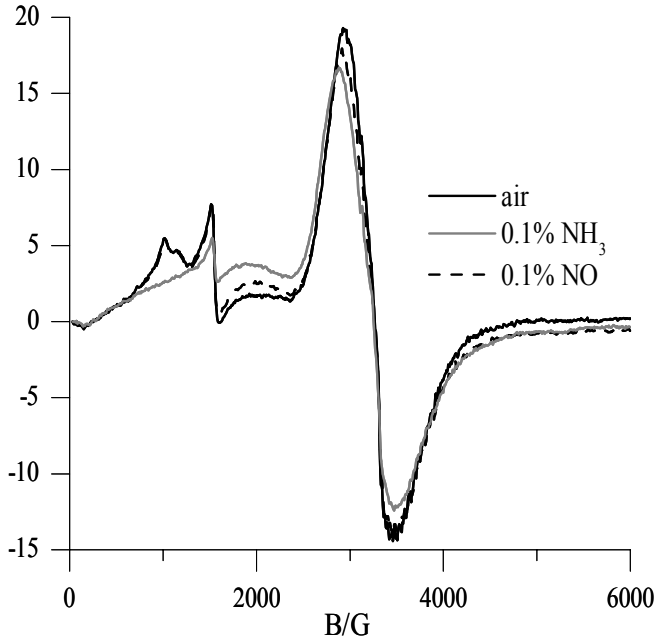

Fig. 4.39. In situ EPR spectra of A(ILIE)0.3 at 773 K in different gas mixtures, conditions as in Fig. 4.37.

In this case the EPR spectrum is completely restored after NO/He treatment. Moreover, a small but significant change of the g' ≈ 2 EPR signal is also seen at 773 K, suggesting that Fe sites reflected by this line might become active at higher temperature compared to those reflected by the g' ≈ 6 and g' ≈ 4.3 signals. In analogy to the A(MR)0.5 catalyst, these results also indicate that the isolated Fe species are stable and do not aggregate upon reduction as observed by Kucherov et al. during reduction of Fe-ZSM-5 already at 523 K in 1% H_2/He [119].

A(ILIE)0.7 and A(ILIE)1.2

In contrast to sample A(MR)0.5 and the two A(ILIE) samples with lower Fe content discussed above, samples A(ILIE)0.7 and A(ILIE)1.2 contain, besides isolated Fe, a certain amount of oligonuclear Fe_xO_y clusters. Sample A(ILIE)0.6 is very similar to sample A(ILIE)0.7 with respect to the nature and distribution of iron species as discussed in sections 4.1.1 and 4.1.2. Moreover, under typical SCR conditions this sample behaves like A(ILIE)0.7. Hence, the following discussion is focused on the latter sample only.

On switching the flow from air to NH_3-SCR feed the intensity of the whole UV/VIS spectrum slightly decreased in A(ILIE)0.7 while in A(ILIE)1.2 the intensity of the band above 300 nm slightly decreases and the band below 300 nm hardly changes (Fig. 4.40). Interestingly, the reduction of isolated iron species in the samples is not as significant as observed for samples A(ILIE)0.2 and A(ILIE)0.3. This suggests that redox properties of isolated Fe^{3+} sites might change with increasing Fe_xO_y cluster content in the sample. It is well known from the literature [59] and has been demonstrated in section 4.1.1 and Fig. 8 that isolated Fe^{3+} can migrate out of their positions and be incorporated in Fe_xO_y clusters during calcination. It has also been shown that migration of isolated Fe^{3+} out of the pores to form clusters is particularly favoured for easily reducible sites [103,173]. Thus, it can be assumed that in samples with higher Fe content,

preferentially those Fe^{3+} sites that are rather resistant against reduction might withstand the tendency to form clusters.

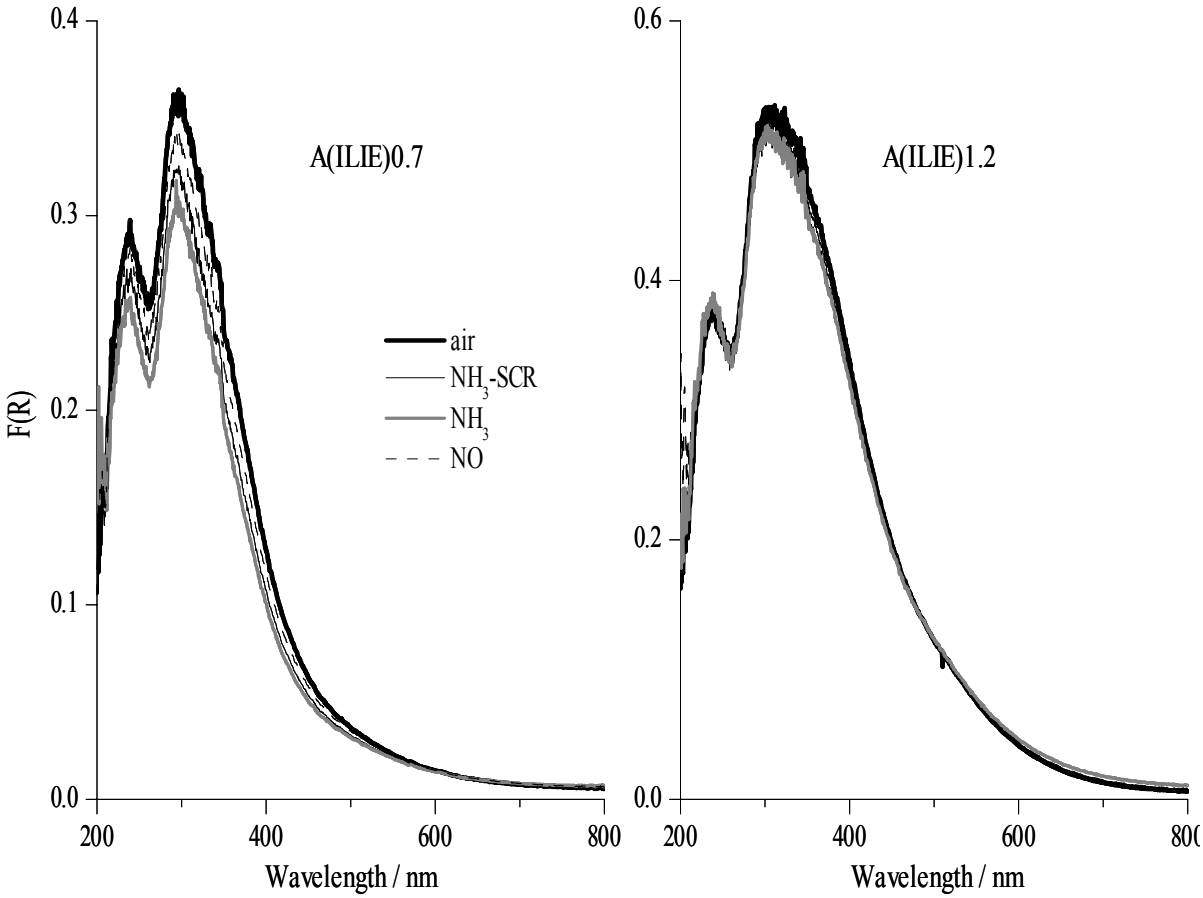

Fig. 4.40. In situ UV/VIS-DR spectra at 623 K in different gas mixtures, conditions as in Fig. 4.36.

When comparing the EPR spectra of sample A(ILIE)0.7 with those of samples A(ILIE)0.2 and A(ILIE)0.3 recorded under the same conditions, a rather similar behavior can be observed for the signals at low magnetic filed (Fig. 4.41). However, it must be noted that the total intensity of the lines at g' ≈ 6 and g' ≈ 4.3 in sample A(ILIE)0.7 is similar to that in samples A(ILIE)0.2 and A(ILIE)0.3 although the iron content is more than twice as high. This shows clearly that the relative percentage of (more easily reducible) isolated Fe^{3+} species represented by the signals at g' ≈ 6 and g' ≈ 4.3 decreases with rising iron content. This effect is even more pronounced for sample A(ILIE)1.2 in which those signals are hardly visible (Fig. 4.41). This result supports the conclusion derived from the UV/VIS-DRS measurements (Fig. 4.40) that, with increasing Fe content, only reduction resistant isolated Fe^{3+} sites might survive.

Considering the signal at g' ≈ 2, significant differences are observed for samples A(ILIE)0.7 and A(ILIE)1.2 upon treatment in 0.1% NH_3/He in comparison to samples A(ILIE)0.2 and A(ILIE)0.3 (Fig. 4.38). These are most obvious for sample A(ILIE)1.2, in which the g' ≈ 2 signal is a superposition of at least two contributions, an intense broad line and a less intense narrower line. Possibly the two signals in the g' ≈ 2 range arise from oxidic clusters of different sizes.

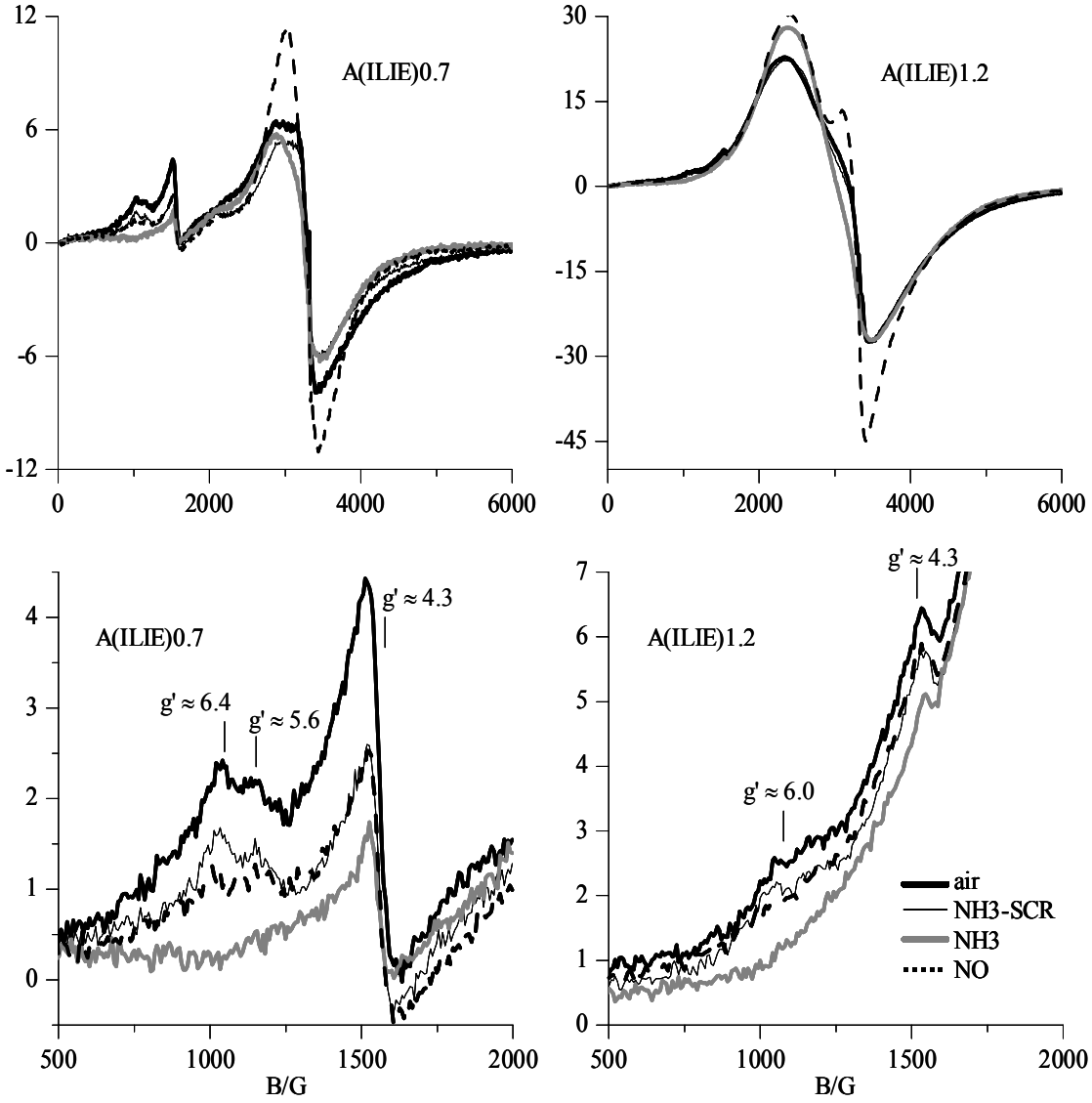

Fig. 4.41. In situ UV/VIS-DR spectra at 623 K in different gas mixtures, conditions as in Fig. 4.36. Bottom figures are enlarged spectra.

Switching from air to NH_3-SCR feed virtually does not change the EPR spectra, suggesting that cyclic reduction/reoxidation keeps the mean valence state of the oxidic cluster species unchanged at +3. This is in good agreement with the results of UV/VIS kinetic studies that revealed very fast reoxidation of $Fe^{3+}{}_xO_y$ clusters (Fig. 4.8) and with in situ UV/VIS-DRS studies (Fig. 4.40). Changing the flow from NH_3-SCR feed to NH_3/He reduces the intensity of the narrow signal in the g' ≈ 2 range while the broad line increases. Increasing intensity upon partial reduction is characteristic of the formation of Fe_3O_4-like species with ferrimagnetic interaction [58,119]. The decrease of the narrow signal in sample A(ILIE)1.2 suggests that the oxidic moieties giving rise to this line might be smaller in comparison to those responsible for the broad line. Thus, reduction of Fe^{+3} to Fe^{+2} just reduces the number of EPR-active Fe^{+3} sites but does not give rise to ferrimagnetic order. In A(ILIE)0.7, the increase in intensity of the broad line is hardly seen indicating the presence of very few and/or small oligomeric $Fe^{3+}{}_xO_y$ clusters in the sample which show less effective magnetic ordering. Isolated Fe^{3+} sites in sample A(ILIE)1.2 as reflected by the UV/VIS spectrum (Fig. 4.40) might contribute to the line at g' ≈

2, too, but are hardly distinguished from the cluster signals. Switching from 0.1% NH_3 to 0.1% NO/He flow restores the narrower subsignal even above its original value. This could be due to a change of the intrinsic magnetic interactions within the Fe_3O_4-like domains.

A(CVD,W1,C0.5)

As shown by ex situ studies (section 4.1.1) sample A(CVD,W1,C0.5) is characterized by pronounced formation of Fe_xO_y clusters. In the UV/VIS spectrum, a switch from air to NH_3-SCR feed does not cause any significant changes (Fig. 4.42a). This suggests that cyclic reduction/reoxidation keeps the mean valence state of the iron species in steady state unchanged at +3. Accordingly, also the EPR spectrum under NH_3-SCR feed does not change very much (Fig. 4.42b and d). It is interesting to compare the behavior of the EPR lines at g' ≈ 6 and g' ≈ 4.3 with those in the A(ILIE) samples discussed above. During treatment with the complete NH_3-SCR mixture, the intensity of these lines decreases less and less as Fe_xO_y clusters become more and more dominant from A(ILIE)0.2 to A(ILIE)0.7. In sample A(CVD,W1,C0.5) with extended cluster formation, EPR signals at g' ≈ 6 and g' ≈ 4.3 remain almost constant during NH_3-SCR (Fig. 4.42b).

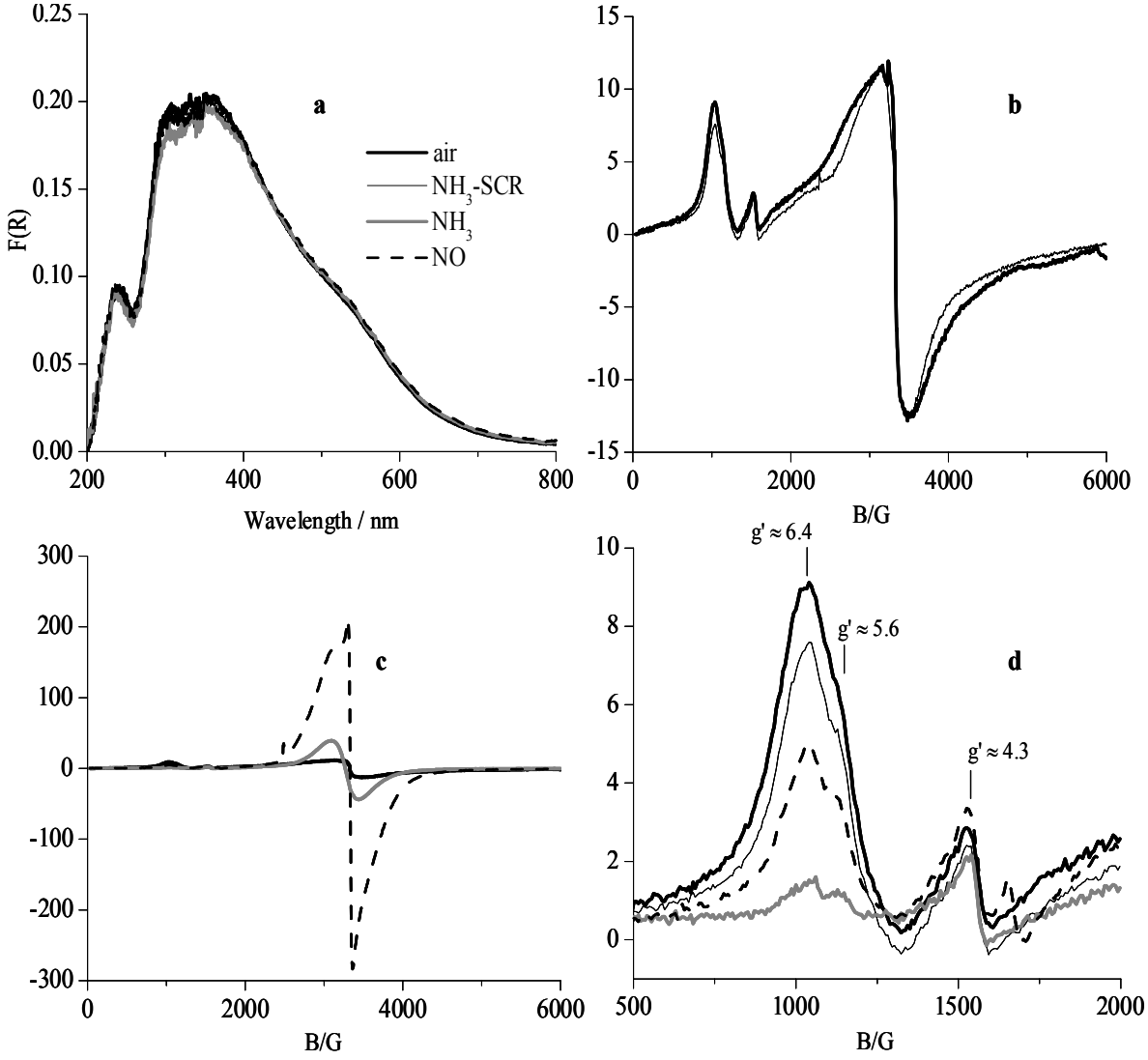

Fig. 4.42. In situ UV/VIS-DRS (a) and in situ EPR (b, c and d) spectra of A(CVD,W1,C0.5) at 623 K in different gas mixtures, conditions as in Fig. 4.36.

Even upon switching from NH_3-SCR to NH_3/He flow the g' ≈ 6 signal does not completely disappear as it is observed for A(ILIE) samples without Fe_xO_y clusters (Fig. 4.42), and the line at g' ≈ 4.3 decreases only slightly. This is again a clear indication that isolated Fe sites in samples characterized by extensive cluster formation change their redox behavior as discussed above for samples A(ILIE)0.7 and A(ILIE)1.2. At the same time, the signal at g' ≈ 2 becomes broad, increases in intensity and shifts to a slightly lower magnetic field (Fig. 4.42c). Such behavior is typical for partially reduced iron oxide clusters with ferrimagnetic interaction [58,119]. Subsequent NO treatment shifts the signal back and increases the intensity markedly (Fig. 4.42c) and the signal at g' ≈ 6 is only partially restored (Fig. 4.42d), indicating the partial reoxidation of the reduced iron species. The increase in intensity of the g' ≈ 2 signal could be due to the change in intrinsic magnetic properties of the iron oxide clusters.

In summary, isolated Fe sites reflected by EPR signals at g' ≈ 6, g' ≈ 4.3 and g' ≈ 2 possess different redox properties and, hence, they behave differently under typical SCR conditions as revealed by in situ EPR experiments. Under typical NH_3-SCR of NO, isolated Fe sites are partly reduced in cluster free samples (such as A(MR)0.5 and A(ILIE) with low Fe content) while in clustered samples (like A(ILIE)1.2 and A(CVD,W1,C0.5)) Fe sites are essentially in +3 oxidation state as evidenced by both in situ EPR and UV/VIS-DRS measurements.

4.3.2 EPR, UV/VIS-DRS and FT-IR spectroscopic studies during SCR of NO with isobutane

To elucidate differences in the behavior of the Fe species when isobutane is used as reducing agent instead of NH_3, similar in situ investigations have been performed as described in section 4.3.1. The results are discussed below in the order of increasing cluster formation, starting with samples dominated by isolated Fe species.

A(MR)0.5

In the UV/VIS spectrum, switching flow from air to isobutane-SCR feed causes an increase of absorption in the whole UV/VIS spectral region (Fig. 4.43). This unexpected result could be due to the formation of N-containing organic deposits in the pores. Formation of N-containing organic species in the SCR of NO by hydrocarbons has been extensively discussed in the literature [87,90,174-178]. Based on in situ FT-IR results, the formation of several N-containing organic species such as alkyl nitrites, alkyl nitrates, alkyl nitriles, cyanates, isocyanates and alkyl radicals has been proposed. Most of these species are UV/VIS active and give bands below 400 nm hence, it is difficult to conclude which N-containing species is responsible for such behavior from UV/VIS only. Therefore, in situ FT-IR experiments have been performed for selected samples. These results will be discussed in the corresponding sections below. After treatment with the complete SCR feed, sample A(MR)0.5 was calcined in air at 773 K for 15 min to restore the initial UV/VIS spectrum in order to continue with the further steps.

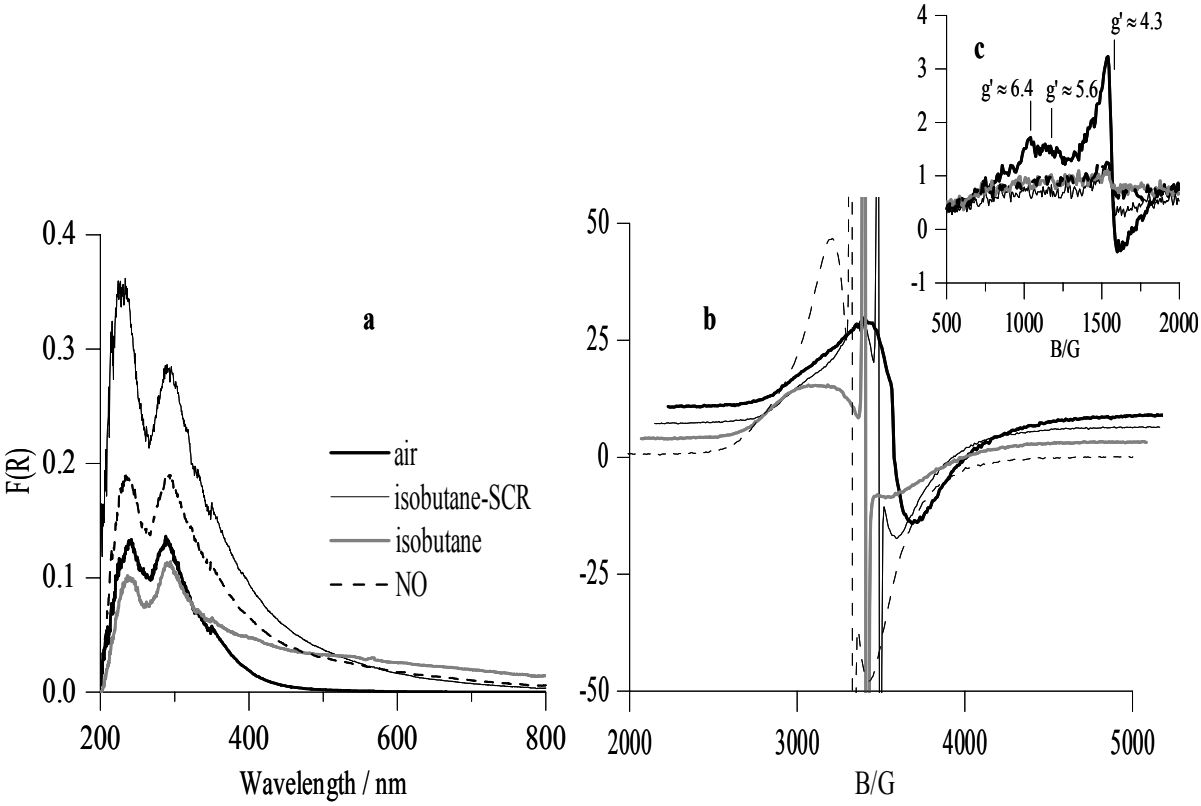

Fig. 4.43. In situ UV/VIS-DRS (a) and EPR spectra at 623 K in different gas mixtures (b and c): air, isobutane-SCR (0.1% NO, 0.1% isobutane, 2% O_2/He), 0.1% isobutane/He and 0.1% NO/He. Spectra were measured after treatment of the samples in the respective mixtures at 623 K for 1 h. Catalyst pretreatment in air at 773 K for 1 h.

On changing the gas flow from air to isobutane/He at 623 K, the intensity of the bands below 300 nm slightly decreases and higher absorption above 400 nm can be observed. The former effect is due to the reduction of iron species and the latter effect might be due to the formation of carbonaceous deposits. The formation of carbonaceous deposits in the pores might proceed on acidic sites due to incomplete oxidation of isobutane. However, in contrast to isobutane/He treatment, a much stronger reduction of bands below 300 nm and no increase of absorbance above 400 nm were observed in the presence of NH_3 (Fig. 4.36). This suggests that polymeric carbonaceous deposits probably also contribute to the UV/VIS spectrum below 300 nm. Hence, it is noteworthy that the real degree of reduction of isolated Fe sites below 300 nm can be underestimated by UV/VIS-DRS. After flushing with He for 15 min, the flow was changed to NO/He. The UV/VIS band intensity again increases below 400 nm but decreases above 500 nm. This suggests the formation of N-containing species upon reaction of NO with carbonaceous deposits formed in the previous isobutane/He treatment.

In the corresponding EPR spectrum, changing the flow from air to isobutane-SCR feed causes almost complete disappearance of the signal at g' ≈ 6 and a marked decrease in intensity at g' ≈ 4.3 (Fig. 4.43b inset). The observed changes of EPR signals at g' ≈ 6 and g' ≈ 4.3 are attributed to the reduction of Fe^{+3} to Fe^{+2} ions. Different from the low field signals, the signal at g' ≈ 2 practically does not change (Fig. 4.43b). This suggests that the Fe^{+3} species

contributing to this signal are probably not easily reducible at 623 K as discussed in the NH_3-SCR section for this sample (Fig. 4.36b). However, an additional sharp signal is superimposed in the g' ≈ 2 range (Fig. 4.43b) which was not observed in the EPR spectrum of this sample during NH_3-SCR (Fig. 4.36b). This indicates the formation of some kind of carbon-containing radicals under isobutane-SCR. Changing the flow from isobutane-SCR feed to isobutane/He causes a further decrease of the EPR signal at g' ≈ 4.3 and the one at g' ≈ 2 decreases substantially. Note that upon NH_3/He treatment only a very small intensity loss of the g' ≈ 2 line was observed at an even higher temperature (773 K, Fig. 4.37). These results clearly show that under isobutane/He feed isolated Fe sites are more strongly reduced than in NH_3/He feed. This, however, is not detectable by UV/VIS-DRS due to the contribution of carbonaceous deposits as discussed above. These observations again demonstrate the benefits of using these two techniques for such studies and show that they are complimentary to a certain extent. Upon switching from isobutane/He to NO/He, the EPR signal at g' ≈ 4.3 slightly increases and the g' ≈ 6 remains completely missing while the one at g' ≈ 2 is enhanced even above its original intensity. The radical signal at g' ≈ 2 still retains similar intensity as observed in isobutane/He feed. So far, no conclusive explanation can be given for the increase of the g' ≈ 2 signal upon treatment with NO/He. Possibly, isolated Fe^{3+} species tend to agglomerate into larger clusters upon treatment with isobutane/He which revealed to be stronger reducing than the NH_3/He mixture. Subsequent treatment with NO/He which causes partial reoxidation of those clusters could then give rise to a change in the intrinsic magnetic interaction as discussed similarly for the partially reduced sample A(ILIE)0.7 upon NO/He treatment (Fig. 4.41).

A(ILIE)0.2

As demonstrated by ex situ UV/VIS and EPR investigations the nature of the Fe species in sample A(ILIE)0.2 is almost the same as in A(MR)0.5, despite the fact that A(MR)0.5 contains slightly more oligomeric clusters than A(ILIE)0.2 (Table 4.1). Consequently, the behavior in the UV/VIS and EPR in situ experiments is also very similar (compare Fig. 4.43 and 4.44) and can be explained in the same way as for sample A(MR)0.5:

Again, the increasing UV/VIS intensity under isobutane-SCR feed suggests the formation of N-containing deposits being UV-active below 400 nm while the isobutane/He mixture alone causes Fe reduction (intensity loss below 400 nm) and carbon deposition (intensity gain above 400 nm). As observed for A(MR)0.5, the latter react with NO/He forming N-containing deposits (repeated intensity increase below 400 nm).

Also the EPR signals at g' ≈ 6 and g' ≈ 4.3 show virtually the same strong reduction as in the experiment with sample A(MR)0.5 which is even stronger than in the presence of NH_3 indicating that isobutane is a stronger reducing agent (Fig. 4.38).

Furthermore, a narrow signal is superimposed on the Fe^{3+} line at g' ≈ 2 in isobutane-SCR which could be due to alkyl radicals as reported earlier in the SCR of NO by hydrocarbons [174]. However, it is more probable that carbon radicals in the carbon deposits contribute to this signal. This is supported by the fact that the radical signal intensity increases during

isobutane/He treatment in which the amount of such deposits increases as evidenced by UV/VIS-DRS.

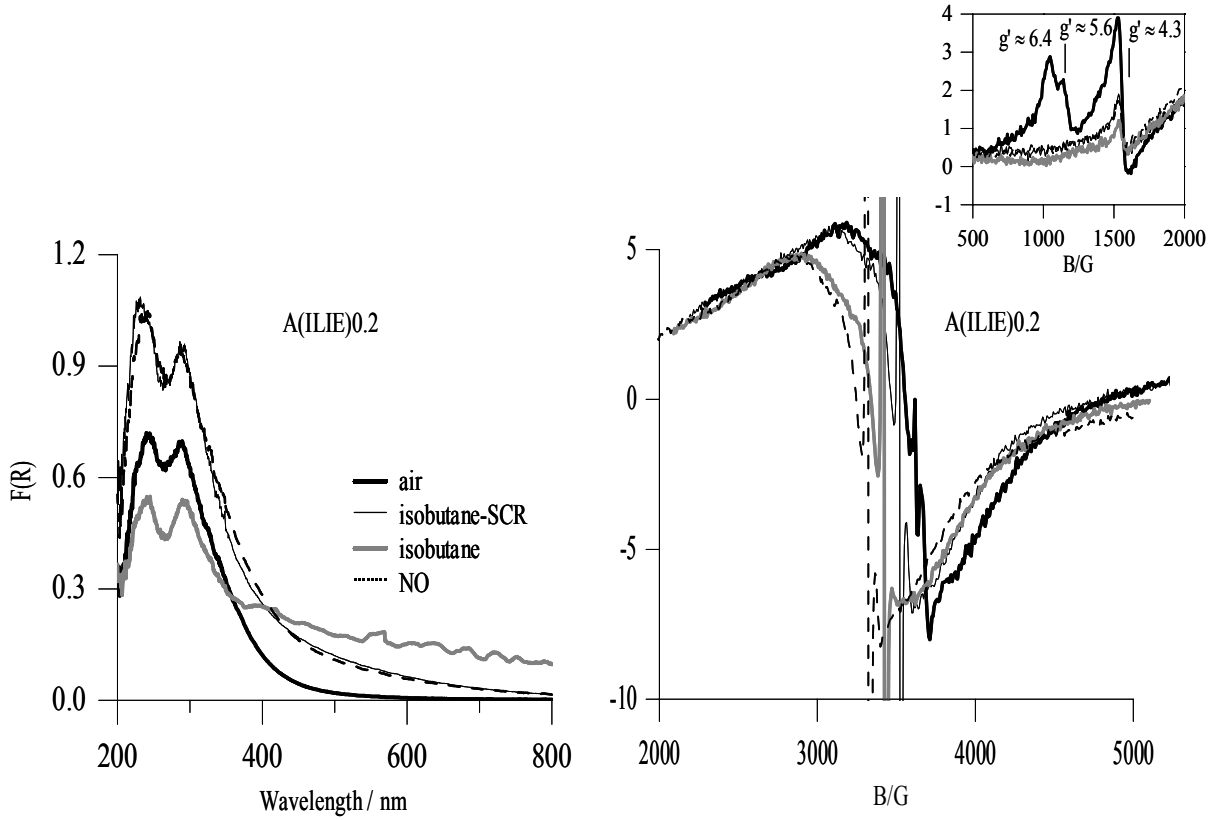

Fig. 4.44. In situ UV/VIS-DRS (left) EPR (right) spectra at 623 K in different gas mixtures: Conditions as in legend of Fig. 4.43.

In contrast to sample A(MR)0.5, the signal at g' ≈ 2 of isolated Fe^{3+} ions does virtually not change during SCR reaction and in isobutane/He feed it decreases a little less than in the case of A(MR)0.5 (Fig. 4.43). This suggests that the Fe^{+3} species contributing to this signal are hardly reducible at this temperature. Compared to A(ILIE)0.2 in which 95% of Fe is present as mononuclear Fe sites, in A(MR)0.5 only 83% of Fe is present as isolated Fe sites (Fig. 4.43 and Table 4.1), while 17% of Fe is present as small oligomers. Obviously, these clustered species are partially reduced upon isobutane/He treatment while the isolated Fe sites also contributing to the signal at g' ≈ 2 are harder to reduce.

To obtain more information about the nature of adsorbates detected already during the in situ-UV/VIS experiment described above, in situ FT-IR measurements were performed at 623 K under SCR conditions. Fig. 4.45 includes spectra measured after oxidative pre-treatment, after 1 h treatment in SCR feed followed by evacuation and after subsequent 1 h reoxidation at 673 K. For comparison, the same experiment was also performed with the bare H-ZSM-5(A).

It can be seen that the FT-IR spectra after SCR feed treatment are rather similar for H-ZSM-5(A) and A(ILIE)0.2. The strong band at 1630 cm^{-1} clearly indicates the formation of nitrate species [89,153] while bands below 1470 cm^{-1} point to the formation of adsorbed nitrite species [153]. However, it must be mentioned that bands in the latter range can also arise from deformation vibrations of adsorbed ammonium species [87,90]. In particular, for the ILIE

samples this cannot be excluded, since an additional weak and broad band is observed at 3132 cm^{-1} (not shown) in the range for ν(N-H) vibrations, which is not visible for H-ZSM-5(A). Moreover, it is known that the intermediate formation of NH_3 can occur during SCR of NO with hydrocarbons [90,179].

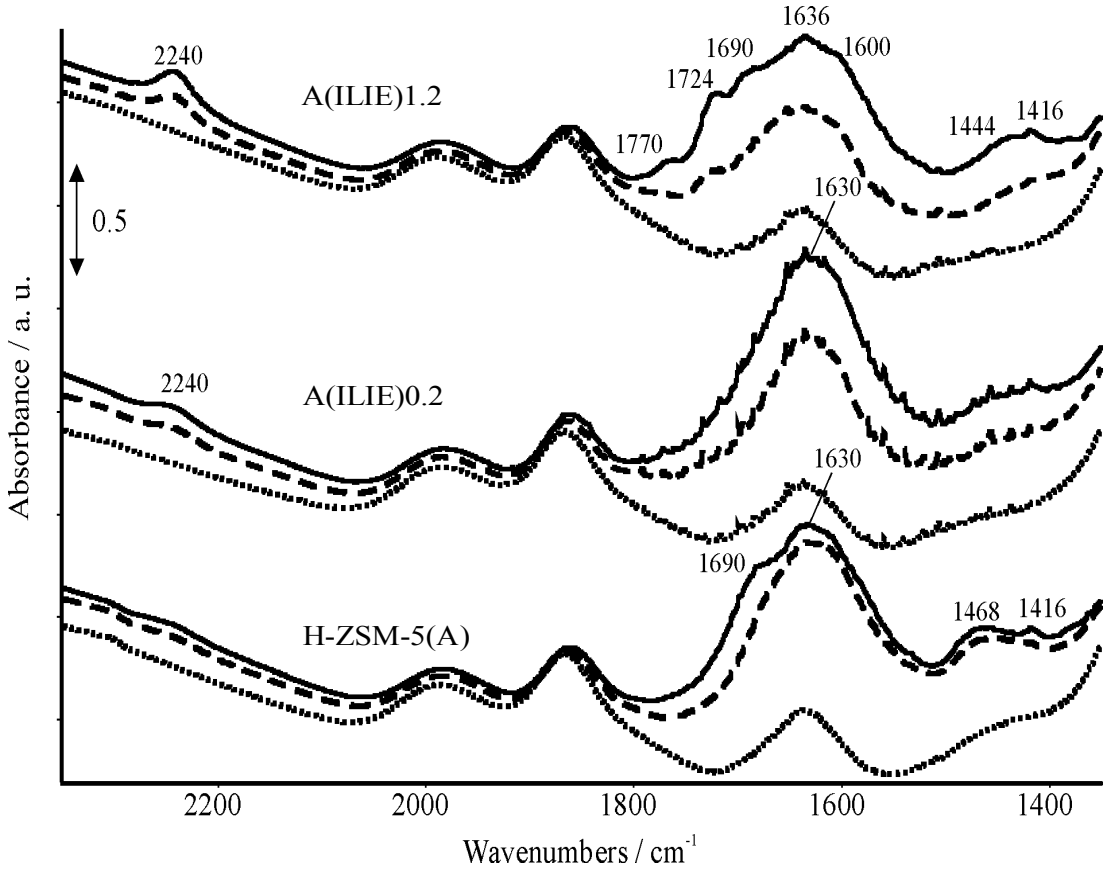

Fig. 4.45. In situ FT-IR spectra at 623 K after pretreatment (dotted line), isobutane-SCR for 1 h followed by evacuation (thick solid line) and after subsequent air treatment at 673 K for 60 min (broken line). Catalyst pretreatment in air at 673 K for 1 h and evacuation.

The band at 2240 cm^{-1} is certainly due to ν(C≡N) of nitrile, cyanate and/or isocyanate species which can only be formed upon reaction of NO with i-butane. Interestingly, this band is not observed over H-ZSM-5(A), suggesting that this reaction requires the presence of a sufficient amount of Fe species. Obviously, the very small Fe impurity of 0.05 % present in the commercial H-ZSM-5 is not enough to catalyse this process. In contrast, the formation of adsorbed nitrates and nitrites on zeolites can occur without participation of a transition metal site [180].

After subsequent treatment in air at 400 °C, the band at 2240 cm^{-1} almost disappeared due to the oxidative degradation of nitrile, cyanate and/or isocyanate species. The bands below 1700 cm^{-1} are markedly diminished in sample A(ILIE)0.2 but remain almost unchanged in H-ZSM-5(A). This suggests that in the former sample those bands might largely arise from oxidizable organic (alkyl) nitrates and nitrites while in H-ZSM-5(A) they may originate from inorganic species, the thermal degradation of which is probably not favoured at this temperature.

Interestingly, a band at 1690 cm^{-1} in the range of ν(C=O) [181] is also observed over H-ZSM-5(A) which disappears upon reoxidation. This suggests that on the bare commercial H-ZSM-5(A) partial oxidation of the hydrocarbon is catalyzed to a certain extend by redox active impurities such as Fe.

A(ILIE)1.2

In contrast to samples A(MR)0.5 and A(ILIE)0.2, this sample contains a significant amount of Fe_xO_y clusters of different sizes. Switching the flow from air to isobutane-SCR feed does virtually not change the intensity of the UV/VIS spectrum (Fig. 4.46). This indicates that the average oxidation state of iron under typical isobutane-SCR conditions is +3 due to the presence of redox process. A similar behavior of this sample has been observed, too, under NH_3-SCR feed (Fig. 4.40).

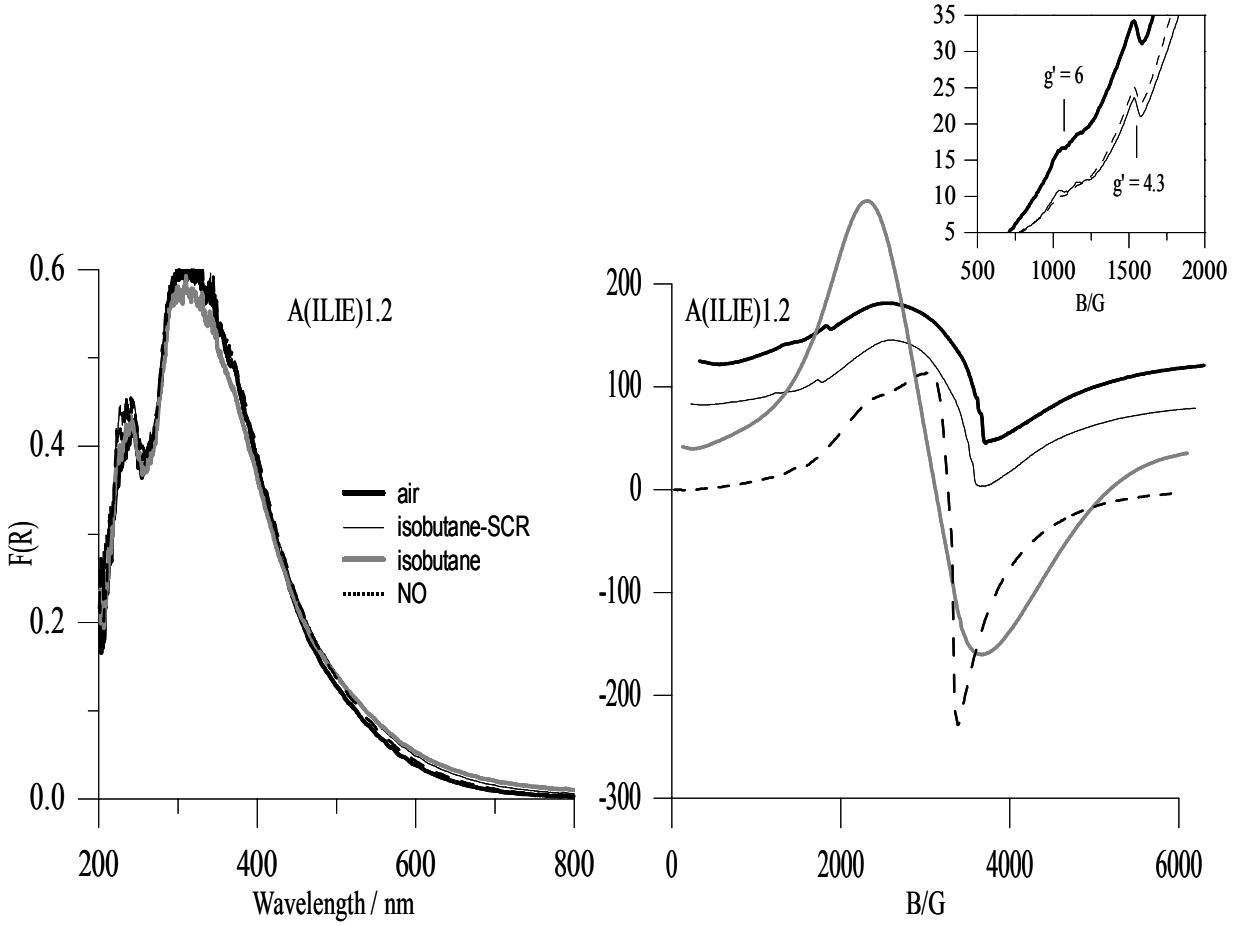

Fig. 4.46. In situ UV/VIS-DRS (left) EPR (right) spectra at 623 K in different gas mixtures, conditions as in Fig. 4.43.

In contrast to A(ILIE)0.2, no marked increase of absorbance is observed that could be attributed to the formation of N-containing species and/or carbon deposits. This might be due to the fact that such deposits are rapidly oxidized by the Fe_xO_y clusters being dominant in sample A(ILIE)1.2 and, thus, are easily removed from the surface. Changing feed flow from isobutane-SCR to isobutane/He does not form carbon deposits in the zeolites as observed for sample A(ILIE)0.2 but isobutane interacts with iron oxide clusters leading to a partial reduction of

iron oxide clusters to Fe_3O_4-like clusters as evidenced by a slight decrease in intensity above 300 nm and a slight increase in the absorption in the visible region. The latter effect is associated with the lower wavelength tail of an intervalence charge transfer (IVCT) transition. Such a phenomenon is characteristic for mixed-valence iron oxides and has been observed in Fe_3O_4 nanoparticles [58,165], where the tail of the IVCT transition extends to the visible range and contributes to light absorption above 450 nm. Upon NO/He treatment the spectrum is partly restored, indicating that NO is able to reoxidize the clusters only partially.

In the EPR spectra (Fig. 4.46), on switching from air to isobutane-SCR feed, the decrease of the g' ≈ 6 and g' ≈ 4.3 signals is markedly less pronounced than for sample A(ILIE)0.2 (Fig. 4.44). This might be due to the fact that in sample A(ILIE)1.2, due to the influence of the higher Fe content and the dominating Fe_xO_y clusters, only more or less reduction-resistant isolated Fe^{3+} species persist. This agrees well with the respective in situ UV/VIS-DRS results (Fig. 4.46). The signal at g' ≈ 2 does not change indicating that the Fe ions remain essentially trivalent in time average due to the fast reoxidation of the clusters. This is in line with the results of UV/VIS kinetic measurements (section 4.1.1 and Fig. 4.8) which revealed that the reoxidation of clusters is more than one order of magnitude faster than their reduction.

Changing flow from isobutane-SCR feed to isobutane/He leads to the formation of a broad intense signal at g' ≈ 2.05 which indicates the formation of ferrimagnetic Fe_3O_4-like species. This behavior is similar to the one upon treatment with NH_3/He, however the intensity increase is higher. This is probably due to a more pronounced reduction of the clusters by isobutane in comparison to NH_3 and, consequently, a more pronounced formation of ferrimagnetic domains. By subsequent treatment in NO/He flow, the g' ≈ 2.05 signal narrows and shifts to g' ≈ 2 due to the partial reoxidation of reduced iron species as observed, too, in UV/VIS-DRS. However, the initial spectrum was not restored, indicating that just with NO alone a complete reoxidation of the ferrimagnetic clusters is not possible. Moreover, the signal at g' ≈ 2 reflects the superposition of two signals which probably represent ferrimagnetic clusters of different size.

The corresponding in situ FT-IR spectrum under isobutane-SCR conditions is shown in Fig. 4.45. Treatment of the sample for 1 h under SCR feed flow followed by evacuation gives rise to a band at 2240 cm^{-1} assigned to ν(C≡N) of nitrile, cyanate and/or isocyanate species, which was also observed for A(ILIE)0.2, however, with a markedly lower intensity. Again, this is a strong indication for the participation of Fe species in this process. Additionally, a series of bands at 1770, 1724 and 1690 cm^{-1} is observed which are typical for carbonyl stretching vibrations [181]. Carbonyl-like adsorbates can occur as intermediates in the oxidation of the hydrocarbon. Those bands are not visible on A(ILIE)0.2 which contains almost exclusively isolated Fe species. Therefore, it seems likely that the oxidative degradation of the hydrocarbon, which proceeds via intermediate formation of C=O moieties, is promoted by the presence of Fe_xO_y clusters and particles which are dominating species in A(ILIE)1.2.

A(CVD,W1,C0.5)

Similar to sample A(ILIE)1.2 (Fig. 4.46), a switch from air to isobutane-SCR feed does virtually not change the UV/VIS spectrum of A(CVD,W1,C0.5) (Fig. 4.47a). A similar behavior of the sample has been observed, too, under NH3-SCR feed (Fig. 4.42). This suggests the occurrence of redox cycle that keeps the mean valence state of the iron species unchanged at +3 in the sample.

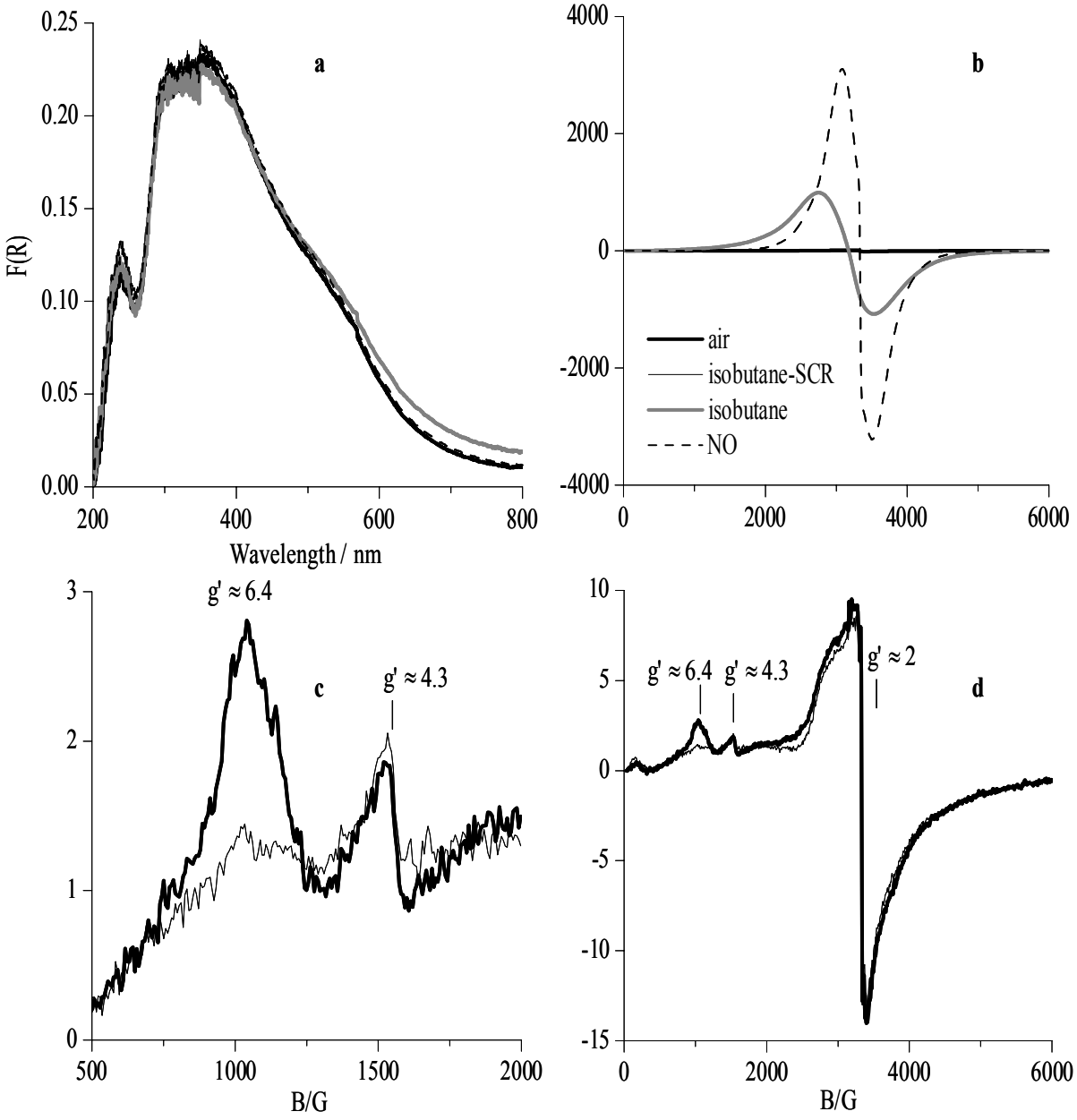

Fig. 4.47. In situ UV/VIS-DRS (a) EPR (b, c and d) (c and d are enlarged spectra) spectra of A(CVD,W1,C0.5) at 623 K in different gas mixtures, conditions as in Fig. 4.43.

Subsequent change of gas flow from air to isobutane/He lowers the intensity of the band above 300 nm and increases absorption slightly in the visible region while the band below 300 nm hardly changes (Fig. 4.47a). The decrease in intensity above 300 nm and higher absorption above 400 nm is due to the partial reduction of iron oxide clusters to Fe_3O_4-like clusters as

evidenced by the IVCT transition between neighboring Fe^{+2} and Fe^{+3} ions in partly reduced Fe_3O_4-like clusters [58,165]. Subsequent NO/He treatment causes the partial reoxidation of the reduced clusters. This behavior is similar to that of sample A(ILIE)1.2 (Fig. 4.46). However, the significant difference between these two samples is the pronounced formation of Fe_3O_4 like clusters in A(CVD,W1,C0.5) than in A(ILIE)1.2 as evidenced by the stronger light absorption in the visible range after isobutane treatment. This is due to the presence of larger iron oxide clusters in the former sample than the latter.

Switching from air to isobutane-SCR feed causes substantial decrease of the EPR signal at g' ≈ 6 while the signals at g' ≈ 4.3 and g' ≈ 2 practically do not change (Fig. 4.47c and d). These results are similar to NH_3-SCR results of this sample and other cluster-containing samples such as A(ILIE)1.2 (Fig. 4.46). On changing the flow from SCR mixture to isobutane/He a broad singlet develops in the range of g' ≈ 2. This behavior is typical for partially reduced iron oxide clusters and formation of Fe_3O_4-like species with ferrimagnetic interaction [58] as discussed earlier. This is in good agreement with the corresponding UV/VIS results (Fig. 4.47a), which show IVCT in partially reduced Fe_3O_4 clusters. In agreement with the corresponding in situ UV/VIS, the intensity of the broad singlet around g' ≈ 2 is much higher in the sample as compared to the similar signal in A(ILIE)1.2 (Fig. 4.46). This confirms the presence of larger and higher amount of iron oxide clusters in the sample as also evidenced by ex situ results (section 4.1. and 4.1.2, Table 4.1). Subsequent NO treatment gives rise to an intense signal in the g' ≈ 2 range while the signal at g' ≈ 6 is weakly and at g' ≈ 4.3 is partially restored, indicating the partial reoxidation of the reduced iron species. As discussed for this sample and other clustered samples in NH_3-SCR, the increase in the intensity of the g' ≈ 2 signal could be due to the change in intrinsic magnetic properties of the iron oxide clusters.

In summary, in situ UV/VIS-DRS and EPR studies show a similar behaviour of the Fe sites under NH_3- and isobutane-SCR, although isobutane seems to be stronger reducing than NH_3. This is particularly evident by comparing the EPR spectra of sample A(CVD,W1,C0.5) in Fig. 4.42 and 4.47. While the g' ≈ 6 signal is still well visible under NH_3-SCR feed, it has almost disappeared under isobutane-SCR feed. Besides, the more pronounced reducing power of isobutane-SCR conditions is also evident for Fe_xO_y clusters. While the respective EPR signal at g' ≈ 2 in cluster-containing samples like A(ILIE)1.2 and A(CVD,W1,C5) only slightly increases in NH_3-SCR feed (Figs. 4.41 and 4.42), the strong increase under isobutane-SCR mixture in the same samples (Fig. 4.46 and 4.47) indicates a pronounced reduction of Fe_2O_3 to ferrimagnetic Fe_3O_4-like species.

In situ FT-IR results show that under isobutane-SCR conditions nitrate, nitrite and N-containing organic deposits such as nitrile, cyanate and/or isocyanate species are formed. Interestingly, the latter species are not formed over the bare H-ZSM-5(A) support while at low Fe content like in A(ILIE)0.2 they are much less pronounced. In contrast, these species are more pronounced over iron rich sample A(ILIE)1.2. This indicates the importance of Fe sites for the oxidation of NO and its subsequent reduction by isobutane via organic N-containing intermediates.

4.3.3 EPR and UV/VIS-DR spectroscopic studies during decomposition and SCR of N_2O with CO

The abatement of N_2O has been studied over Fe-MFI catalysts that are characterized by a similar distribution of differently structured Fe sites as observed for catalysts used in the SCR of NO. The only difference is that some of the Fe-MFI zeolites used for N_2O abatement were prepared by other methods (section 3.1.1). Thus, *ex*-Fe-silicalite contains virtually only isolated Fe species as it is the case, too, for A(MR)0.5 and A(ILIE) with low Fe content, while the other three samples [A(ILIE)1.2, A'(CVD,W1,C2) and Fe-ZSM-5(LIE)1.4] contain, besides isolated Fe ions, a significant percentage of Fe_xO_y clusters and particles. In analogy to section 4.3 on SCR of NO, the behavior of the Fe catalysts in the abatement of N_2O is described in the order of increasing Fe agglomeration, starting with *ex*-Fe-silicalite which contains isolated Fe sites only.

Steam-activated ex-Fe-silicalite

Upon changing the gas flow from air to CO/He, the UV/VIS spectrum does practically not change (Fig. 4.48). This suggests that isolated Fe^{3+} species in *ex*-Fe-silicalite, which are mainly tetrahedrally coordinated, are hardly sensitive to reduction by CO at this temperature. In principle, a comparable trend has also been observed upon NH_3-treatment of samples with low Fe content such as A(MR)0.5 and A(ILIE). In those samples which, however, contain isolated Fe in both tetrahedral and octahedral coordination, the former species revealed to be more resistant against reduction (Fig. 4.36 and 4.37) than the latter.

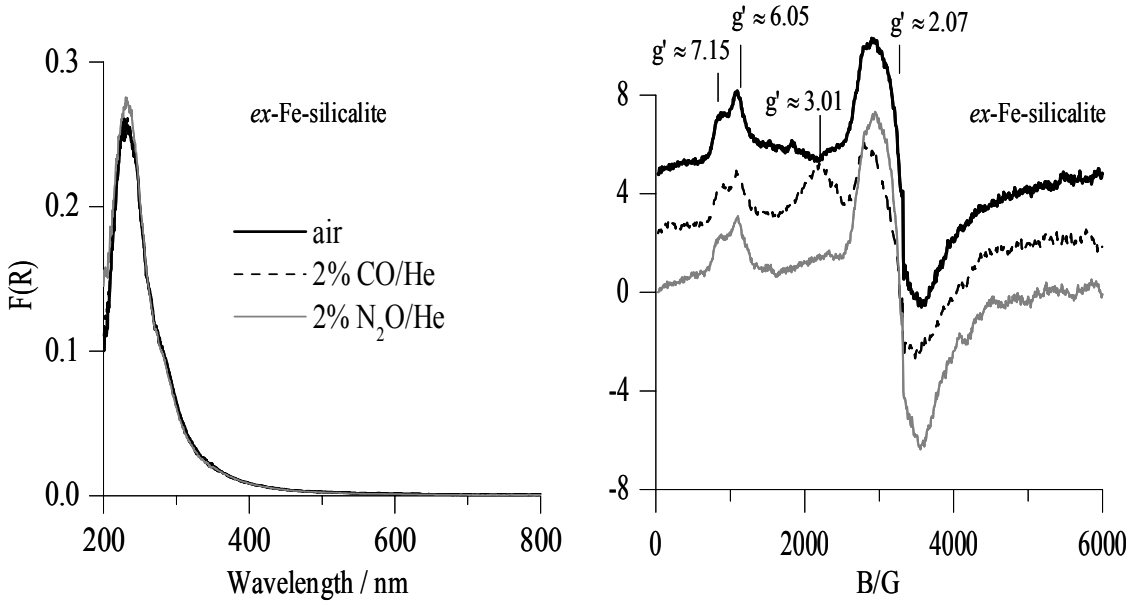

Fig. 4.48. In situ UV-VIS-DRS (left) and EPR (right) spectra of *ex*-Fe-silicalite measured at 623 K upon subsequent treatment in different gas mixtures. Spectra were measured after treatment of the samples in the respective mixtures at 623 K for 1 h. Catalyst pretreatment in air at 773 K for 1 h.

The EPR spectrum of *ex*-Fe-silicalite changes significantly upon interaction with CO (Fig. 4.48). The signals at g' ≈ 7.15, 6.05, and 2, representative for differently distorted isolated iron sites, decrease in the presence of CO and a new broad signal at g' ≈ 3.01 appears. A signal at g' ≈ 4.3 in Fig. 53 is not observed at 623 K, probably due to short relaxation times at high temperature. Considering the UV/VIS results, the decrease of the EPR lines at g' of 7.15, 6.05, and 2 should not be due to reduction of Fe^{3+}. Rather, it is probable that CO is chemisorbed on extraframework Fe^{3+} isolated ions, causing changes of the local symmetry and thus altering the position of the EPR signals. A similar shift of the Fe^{3+} signal upon changing ligands was observed for Fe-ZSM-5 zeolites prepared by impregnation of H-ZSM-5 with a $FeCl_3$ solution [119]. In the as-prepared zeolites, a line at g' ≈ 3.65 was assigned to isolated $(FeCl_2)^+$ species. Upon calcination in air, this line disappeared due to the transformation of $(FeCl_2)^+$ into differently distorted FeO^+ species, giving rise to EPR signals at g' ≈ 6.5, 5.6, and 4.27.

For *ex*-Fe-silicalite, the EPR changes are reversible upon switching from CO to N_2O (compare EPR spectra in Fig. 4.48). The intensity of the band at 240 nm in the UV/VIS spectrum of *ex*-Fe-silicalite is slightly higher after contact with N_2O, as compared to the initial spectrum of the sample in air (Fig. 4.48). This suggests that some Fe^{2+} ions could be present even after pretreatment in air, which can be oxidized by N_2O but not by O_2.

A(ILIE)0.3

The interaction of CO and N_2O with A(ILIE)0.3 leads to important differences compared to *ex*-Fe-silicalite (Fig. 4.49). The UV/VIS spectrum of the sample increases in intensity upon switching from air to N_2O/He. This might be due to the oxidation of Fe^{2+} ions by N_2O, which remain even after pretreatment in air (Fig. 4.49).

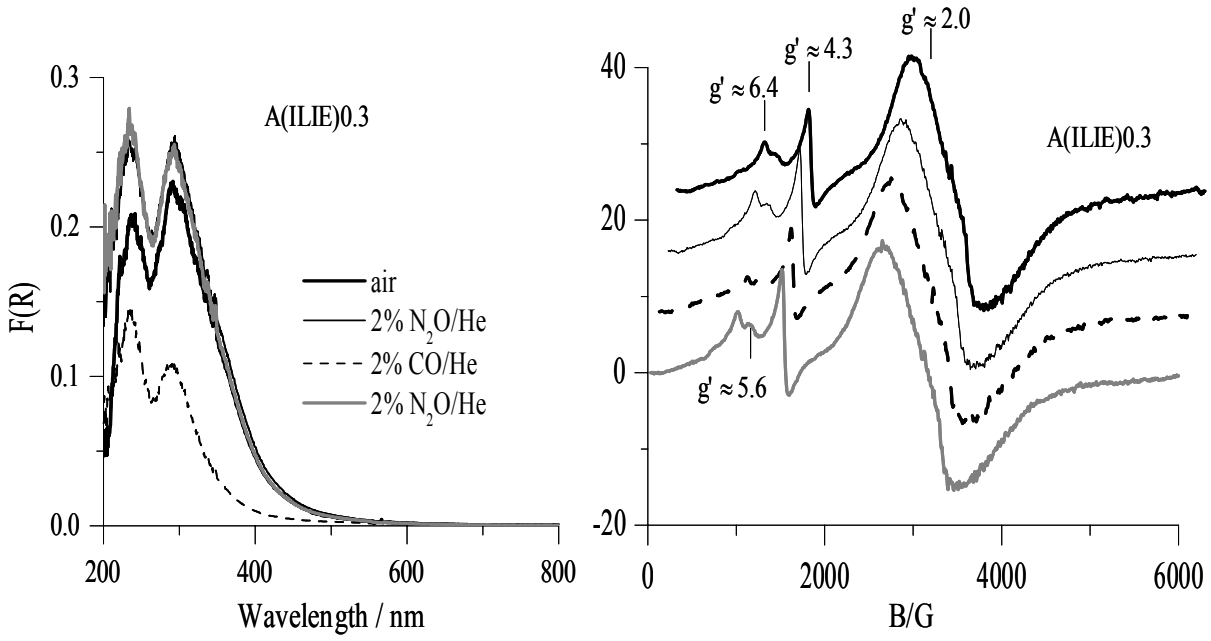

Fig. 4.49. In situ UV-VIS-DRS (left) and EPR (right) spectra measured at 623 K upon subsequent treatment in different gas mixtures. Conditions as in legend of Fig. 4.48.

Subsequent treatment in CO/He decreases partly the intensity of the bands at 230 and 290 nm, which are assigned to isolated Fe sites in tetrahedral and octahedral coordination respectively. This effect is more pronounced for the latter band than the former (Fig. 4.49). The decrease of the band at 230 nm is surprising since this band was not reduced by CO at this temperature in *ex*-Fe-silicalite which is governed by mainly tetrahedrally coordinated isolated Fe sites. A possible explanation for the slight decrease of the band at 230 nm in A(ILIE)0.3 could be that the CT band of octahedral Fe sites at 290 nm extends below 250 nm and contributes to the overall intensity at 230 nm. Therefore, the reduction of the band at 290 nm could influence to a certain extent also the band at 230 nm. Another reason could be that tetrahedral Fe^{3+} sites in *ex*-Fe-silicalite and A(ILIE)0.3 are located in different pore positions. Note that the former sample was prepared by extraction of Fe from framework positions. These results suggest that octahedral isolated Fe sites are partly reduced by CO while tetrahedral isolated Fe sites are hardly sensitive against reduction by CO. This is highly likely, since tetrahedral isolated Fe can extend their coordination state rather than releasing an oxygen atom from the coordination sphere to undergo reduction. Differently, octahedral isolated Fe sites, which are coordinatively saturated, can give away an oxygen atom from the coordination sphere to undergo reduction rather than extend their coordination state. This could explain the different behavior of A(ILIE)0.3 and *ex*-Fe-silicalite. However, subsequent N_2O treatment restores the UV/VIS spectrum similar to that of initial N_2O spectrum.

In the corresponding EPR spectra of A(ILIE)0.3 (Fig. 4.49), switching from air to N_2O causes a slight increase of the signals at g' ≈ 6 and 4.3. Taking into account of UV/VIS results, the observed changes can be attributed to oxidation of Fe^{2+} sites by N_2O. Upon switching from N_2O to CO, the signals at g' ≈ 2 and 4.3 are almost not affected. In contrast to these signals, signals at g' ≈ 6.4 and 5.6 decreased slightly in intensity indicating that isolated Fe sites with 5 or 6 coordinating ligands are partly reduced by CO. This is in line with the corresponding UV/VIS measurements which show that octahedral Fe sites are partly reduced by CO (Fig. 4.49).

These finding are different as compared to the results observed for *ex*-Fe-silicalite. The decrease of the EPR signals at g' ≈ 6.4 and 5.6 in A(ILIE)0.3 corresponds to octahedral isolated Fe^{3+} which are reduced by CO as concluded from in situ UV/VIS. Different from *ex*-Fe-silicalite, no pronounced signal at g' ≈ 3 was observed in A(ILIE)0.3 upon interaction with CO. Furthermore, EPR signals in the low-field range appear at slightly different g'-values in A(ILIE)0.3, suggesting that the distortion of the local symmetry of the isolated sites might differ slightly in comparison to *ex*-Fe-silicalite. Thus, the interaction of CO with such sites can lead to complexes of slightly different geometry in both samples, causing a shift of the EPR signal. This could also explain the absence of the g' ≈ 3 signal in A(ILIE)0.3. Finally, the reduced Fe sites are reoxidized upon switching from CO to N_2O (Fig. 4.49).

A(ILIE)1.2

On switching the flow from air to N_2O/He the UV/VIS bands below 300 nm slightly increased in intensity but bands above 300 nm did not change (Fig. 4.50). This suggests the

oxidation of isolated Fe^{2+} sites as observed in A(ILIE)0.2. Subsequent treatment in CO/He decreases slightly the intensity of the bands between 250-300 nm assigned to octahedral Fe sites. Similar to *ex*-Fe-silicalite, the band at 250 nm, characteristic of tetrahedral isolated Fe^{3+} species, remains almost unaltered. This indicates that octahedral isolated Fe sites are partly reduced by CO but not tetrahedral isolated Fe^{3+} species. Differently, light absorption above 300 nm decreases strongly and the light absorption above 450 nm increases significantly. The former effect is due to the reduction of oligomeric clusters and consequently the latter effect is observed, due to the IVCT transition in partly reduced iron oxide clusters [58,165]. These results suggest a different behaviour of Fe^{3+} species upon interaction with carbon monoxide. Obviously, CO reduces oligonuclear $Fe^{3+}{}_xO_y$ clusters at typical reaction temperatures. This differs from observations in the SCR of NO in which no marked reduction of Fe_xO_y clusters could be detected at this temperature (Figs. 4.40 and 4.46). It suggests that CO might be slightly more effective in reducing iron oxide clusters than NH_3 and/or isobutane. Switching back from CO to N_2O reoxidizes the reduced Fe sites.

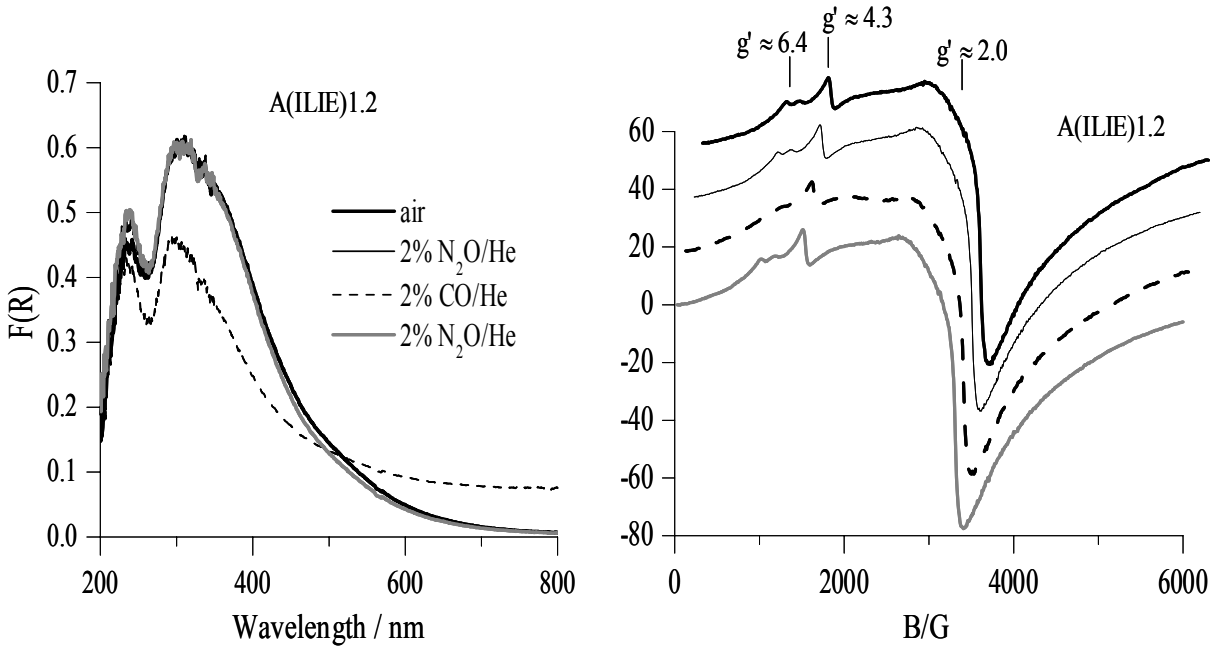

Fig. 4.50. In situ UV-VIS-DRS (left) and EPR (right) spectra of A(ILIE)0.2 measured at 623 K upon subsequent treatment in different gas mixtures. Conditions as in legend of Fig. 4.48.

In the corresponding EPR spectra of the sample, switching from air to N_2O causes a slight increase of the signals at g' ≈ 6 and 4.3. This is due to the oxidation of divalent Fe sites as observed in the corresponding UV/VIS-DRS. CO treatment causes slight decrease of the signal at g' ≈ 6 while the one at g' ≈ 4.3 is almost not affected and the signal at g' ≈ 2 becomes slightly broader. The latter effect is due to the reduction of iron oxide clusters. These results are in line with the corresponding UV/VIS results, which show reduction of octahedral isolated Fe sites and oxidic clusters upon CO treatment. These reduced Fe sites are reoxidized by subsequent N_2O treatment.

Steam-activated ex-Fe-ZSM-5

The subsequent interaction of CO and N_2O with *ex*-Fe-ZSM-5 leads to similar results as in A(ILIE)1.2, which are associated with similar iron constitution. However, the UV/VIS spectrum of *ex*-Fe-ZSM-5 did not change upon switching from air to N_2O/He indicating that the sample does not contain divalent Fe species unlike ILIE samples. But, treatment in CO/He decreases the intensity of the bands above 290 nm (Fig. 4.51). Similar to A(ILIE)1.2, the band around 250 nm is virtually not effected. These observations can be explained as for A(ILIE)1.2. Octahedral isolated Fe sites are slightly and clusters are stronger reduced by CO, whereas tetrahedral isolated Fe sites are not. Switching back from CO to N_2O restores the band above 280 nm in *ex*-Fe-ZSM-5 and surprisingly, enhances the band around 250 nm above the maximum reached during the first N_2O treatment. This result can be tentatively explained by assuming that the coordination of some of the Fe^{3+} species formed upon reoxidation by N_2O is different from their initial state before reduction with CO. Phenomena like the partial dissolution of larger clusters and/or symmetry changes might lead to an increased absorbance around 250 nm. However, in any case, the changes are very small and the amount of Fe species involved in these processes is not significant.

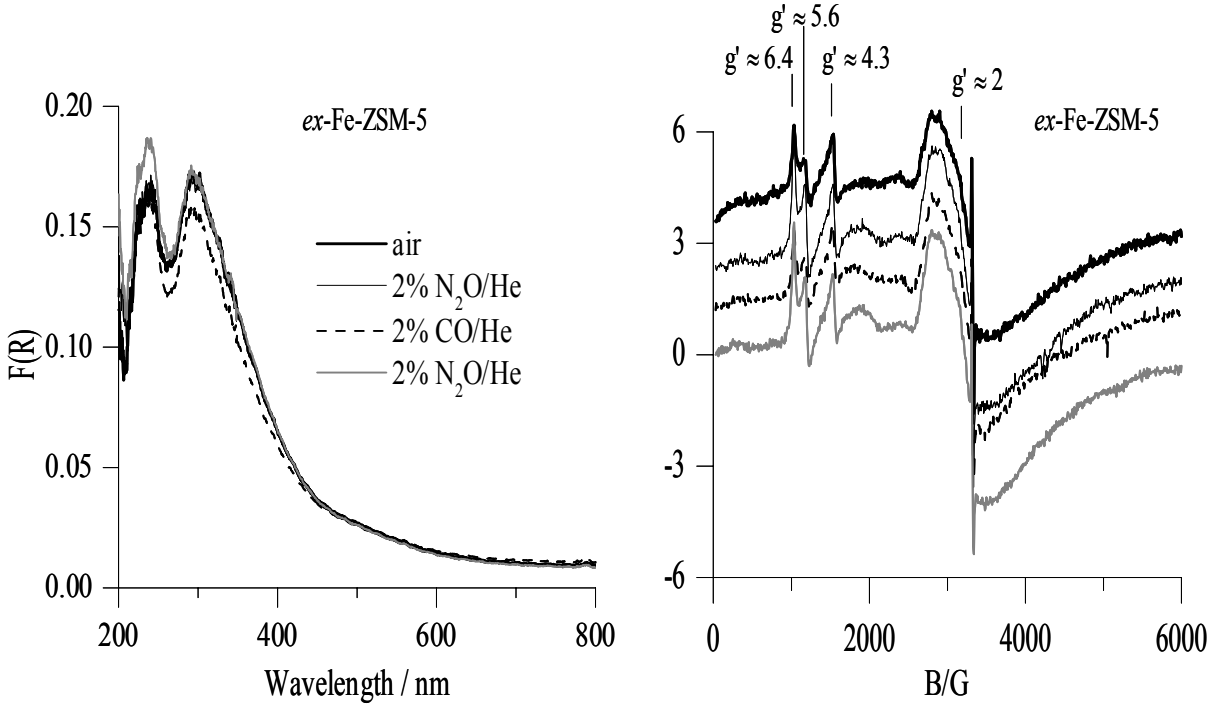

Fig. 4.51. In situ UV-VIS-DRS (left) and EPR (right) spectra of *ex*-Fe-ZSM-5 measured at 623 K upon subsequent treatment in different gas mixtures. Conditions as in legend of Fig. 4.48.

In the corresponding EPR spectra of *ex*-Fe-ZSM-5 (Fig. 4.51), switching from air to N_2O causes a slight increase of the signals at $g' \approx 6.4$, 5.6 and 2.0. This can be associated to the change from a mixture containing a paramagnetic gas (O_2) to a diamagnetic one (N_2O), which causes line narrowing since the magnetic interaction between Fe^{3+} and O_2 is suppressed. Interestingly, the signal at $g' \approx 4.3$ is almost not influenced by this change, suggesting that the Fe^{3+} species contributing to this line are probably not accessible by gas-phase components.

The signals at g' ≈ 6.4, 5.6 and 2.0 in *ex*-Fe-ZSM-5 decrease upon switching from N_2O to CO (Fig. 4.51). Based on the ex situ characterizations in section 4.1 (UV/VIS, and the temperature dependence in the EPR spectra), the signal at g' ≈ 2 in this sample is mainly assigned to oxidic iron clusters. Accordingly, its decrease upon CO treatment is associated to the reduction of clustered Fe^{3+} species. As observed in A(ILIE)1.2, the decrease of the EPR signals at g' ≈ 6.4 and 5.6 in *ex*-Fe-ZSM-5 is due to the reduction of octahedral isolated Fe^{3+} species as concluded from in situ UV/VIS. In agreement with the previous results and with the corresponding in situ UV/VIS results, tetrahedral isolated Fe sites are hardly effected by CO treatment as evidenced by a negligible change in the signal intensity at g' ≈ 4.3. Finally, the EPR signals at g' ≈ 6.4, 5.6 and 2 were restored upon switching from CO to N_2O (Fig. 4.51).

Sublimed A'(CVD,W1,C2)

As shown in Fig. 4.52, the UV/VIS spectra of A'(CVD,W1,C2) in air and N_2O were identical. Upon CO treatment, the intensity of the whole spectrum was substantially reduced and completely recovered by switching back to N_2O. The intensity reduction in CO was expected for the bands above 280 nm, arising from octahedral isolated Fe sites and clustered iron species. However, the decrease of the band intensity below 250 nm (tetrahedral isolated Fe^{3+} species) was not anticipated, since these species were not reduced by CO in *ex*-Fe-silicalite and in other samples described above. It should be noted that the tail of the CT subbands arising from octahedral isolated Fe sites and $Fe^{3+}_xO_y$ clusters in the sample extends into the low-wavelength range, contributing to the overall intensity below 300 nm. Thus, the marked reduction of the band above 280 nm influences the intensity of the signal at lower wavelengths. However, subsequent N_2O treatment restores the original UV/VIS spectrum.

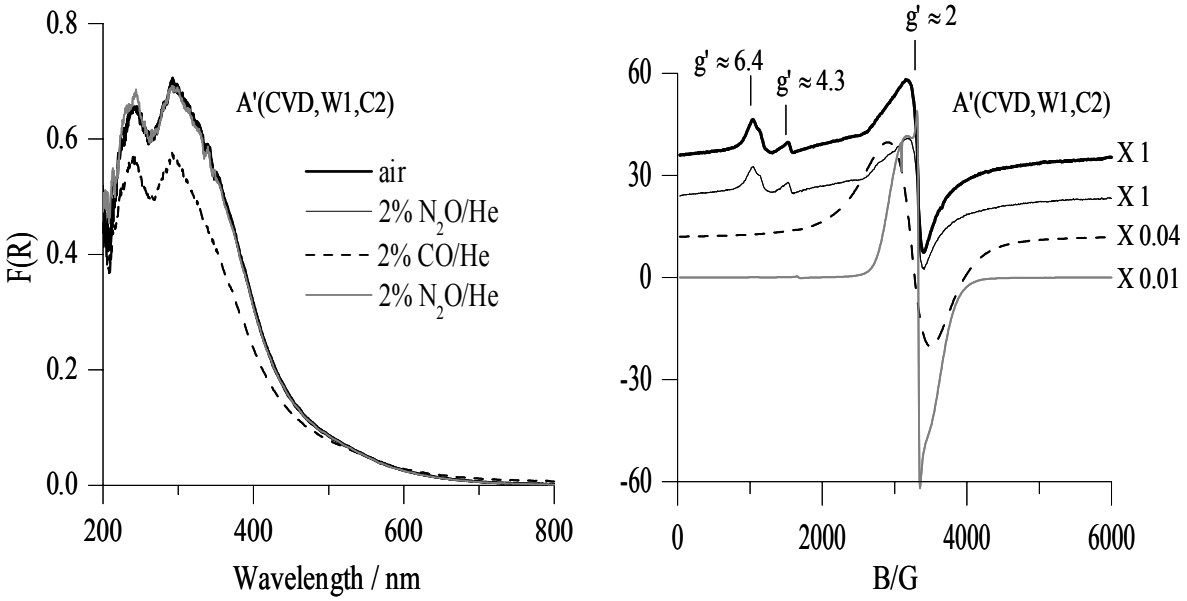

Fig. 4.52. In situ UV-VIS-DRS (left) and EPR (right) spectra of A'(CVD,W1,C2) measured at 623 K upon subsequent treatment in different gas mixtures. Conditions as in legend of Fig. 4.48.

The EPR spectra of A'(CVD,W1,C2) show a slight decrease of the signal at g' ≈ 2 upon switching from air to N_2O, while the signals of isolated Fe^{3+} sites at low field remain practically unchanged (Fig. 4.52). Subsequent admission of CO leads to a very large broad singlet at g' ≈ 2.07 in the sample, which is typical of ferrimagnetic Fe_3O_4-like species that can only form by partial reduction of sufficiently large oxidic particles as present in this sample. Similar to the behavior observed for A(ILIE) samples and *ex*-Fe-ZSM-5, isolated octahedral Fe sites reflected by EPR signal at g' ≈ 6.4 are reduced. As shown in Fig. 4.52, switching back from CO to N_2O narrows and shifts the g' ≈ 2 line to a higher magnetic field. Since the reduced Fe^{2+} sites are almost completely reoxidized by N_2O, as concluded from UV/VIS-DRS, the change of the EPR signal should be related to changes of the intrinsic magnetic interactions within the ferrimagnetic clusters. In N_2O, a very narrow signal at g' ≈ 2.003 is observed too. Such signal is typical for radical species rather than for Fe^{3+} ions. Panov [100] attributed the unique performance of iron-containing ZSM-5 in the N_2O-mediated oxidation of benzene to phenol to the formation of α-oxygen, the charge of which has been a matter of discussion. The ability of N_2O to deposit paramagnetic O^- species on partially reduced oxide surfaces is well known [182]. Such species originate narrow EPR signals near the free-electron g values, having an anisotropic g tensor with $g_\perp > g_\parallel$ [182,183]. However, when they become mobile, e.g., at high temperatures, *g* anisotropy averages out [183]. To the best of our knowledge, neutral oxygen atoms have never been detected by EPR, due to the short lifetime imposed by the their high reactivity [184]. In a recent work, Starokon et al. [185] have concluded that α-oxygen is an anion-radical species, designated as O_α^-. It has also been shown that O^- species, when encaged in the micropores of CaO/Al_2O_3 crystals with zeolite-like structure can be rather stable [183]. Based just on its *g* value, the narrow isotropic line in Fig. 4.52 cannot be conclusively assigned to O^- species, since different radical species lead to similar signals in this region. However, considering that the signal appears only in the presence of N_2O and/or after partial reduction of the sample with CO, i.e., under favorable conditions for formation of O^- species, it does not seem unlikely that the signal arises from these radical species, being mobile within the zeolite pore network.

Finally, an in situ EPR experiment was performed by exposing A'(CVD,W1,C2) to different N_2O-CO mixtures at 623 K (Fig. 4.53). A change from air to a reaction mixture containing of $CO/N_2O = 1$ causes a slight decrease of the signals at g' ≈ 6.4 and g' ≈ 2, while the line at g' ≈ 4.3 remains unchanged. The N_2O conversion in the experiment was 82%, in good agreement with the steady-state tests as reported in [58]. This result indicates that in the presence of equimolar amounts of N_2O and CO, the average valence of active Fe species is +3 under steady-state conditions, with no formation of ferrimagnetic Fe_3O_4-like particles. This occurs when CO is added in excess ($CO/N_2O = 2$), while the obtained N_2O conversion is slightly increased by 5% (i.e., 87%).

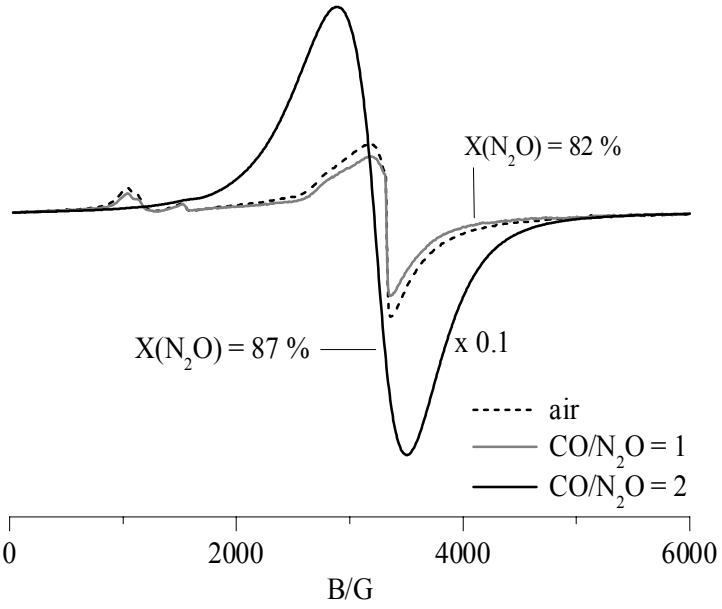

Fig. 4.53. In situ EPR spectra of A'(CVD,W1,C2) in different gas mixtures: air at 773 K, 10 mbar N_2O + 10 mbar CO in He (CO/N_2O = 1) at 623 K, and 6.6 mbar N_2O + 13.4 mbar CO in He (CO/N_2O = 2) at T = 623 K and P = 1 bar. The N_2O conversion obtained is shown in the figure.

Ion-exchanged Fe-ZSM-5(LIE)1.4

The in situ UV/VIS spectra of Fe-ZSM-5(LIE)1.4 shows similar behaviour to that of A(ILIE)1.2 (Fig. 4.54). As observed for sample A(ILIE)1.2, interaction with CO leads to an increase of light absorption above 450 nm. This is due to an IVCT transition by electron delocalization between Fe^{2+} and Fe^{3+} ions in mixed-valence iron oxides [58,165].

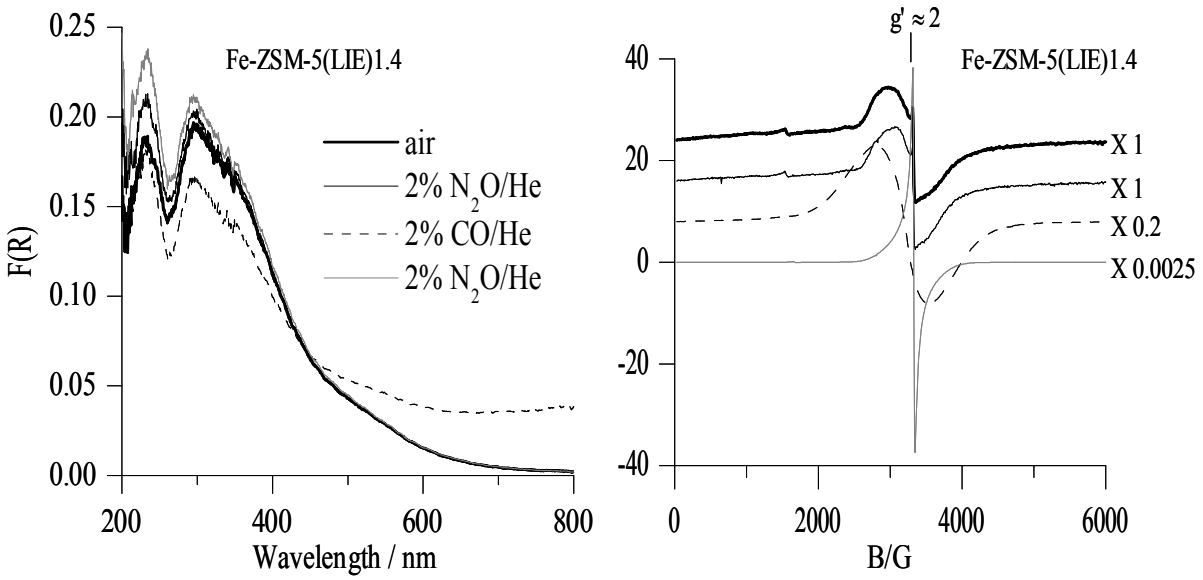

Fig. 4.54. In situ UV-VIS-DRS (left) and EPR (right) spectra of Fe-ZSM-5(LIE)1.4 measured at 623 K upon subsequent treatment in different gas mixtures. Conditions as in legend of Fig. 4.48.

This was observed neither for *ex*-Fe-ZSM-5 nor for A'(CVD,W1,C2) (Fig. 4.51 and 4.52) and could be attributed to the significantly larger Fe_2O_3 particles in Fe-ZSM-5(LIE)1.4, which can form typical Fe_3O_4-like species upon reduction of large Fe_2O_3 with a certain long range order. Furthermore, the mutual distribution of Fe^{3+} and Fe^{2+} species in A'(CVD,W1,C2) and Fe-ZSM-5(LIE)1.4 may differ which in turn can alter the exact position, intensity, and/or line width of the IVCT transition.

In the EPR spectra of Fe-ZSM-5(LIE)1.4, low filed signals for isolated Fe^{3+} species are hardly visible, in agreement with the high degree of clustering evidenced by this sample. Large iron oxide particles give rise to the broad EPR signal at $g' \approx 2$ which does not change upon switching from air to N_2O. In the presence of CO, the broad line accounting for ferrimagnetic Fe_3O_4-like particles develops. A similar EPR signal was observed in A'(CVD,W1,C2) (Fig. 4.52). However, in the latter sample, the intensity of this line is five times higher than in Fe-ZSM-5(LIE)1.4, although the total Fe content is only 3.5 times higher (see Table 3.1, in section 3.1.1). This is likely due to differences in the domain microstructure of the ferrimagnetic particles and not to a higher degree of Fe^{3+} reduction by CO in A'(CVD,W1,C2), since UV/VIS-DRS clearly shows a more pronounced reduction in Fe-ZSM-5(LIE)1.4 (Fig. 4.54). Upon contact with N_2O, a narrow EPR signal around $g' \approx 2.003$ arises in Fe-ZSM-5(LIE)1.4. This signal, attributed to O^- species, is 17 times larger than in A'(CVD,W1,C2), despite the lower iron content in Fe-ZSM-5(LIE)1.4. These various observations further evidence the markedly different nature of this Fe-oxide phase in both catalysts.

4.4 Catalytic behaviour

Catalytic tests of the Fe-zeolites described in this section have not been performed within this thesis but in the laboratories of Prof. W. Grünert (SCR of NO), and Prof. Javier Pérez-Ramírez (direct decomposition and SCR of N_2O). However, since knowledge of the catalytic behavior is essential for the discussion of structure-reactivity relationships (section 5.2), the results which have widely been published [36,55,58,64,161,162] are shortly mentioned blow.

4.4.1 Selective Catalytic Reduction (SCR) of NO with NH_3 and isobutane

In this section, the catalytic performance of selected Fe-containing samples is described that have been chosen to illustrate the influence of particular properties: 1) increasing Fe content and, thus, increasing degree of Fe site agglomeration (series of ILIE samples in comparison to A(CVD,W1,C5)). 2) Different Al content and, thus, different acidity of the MFI matrix (sample A(CVD,W1,C5), B(CVD,W1,C5) and *ex*-Fe-silicalite in comparison to A(ILIE) samples with low Fe content. 3) Different pore sizes (*ex*-Fe-silicalite and (Fe-SBA-I)0.95). Detailed results of the catalytic behavior of all samples studied in this thesis can be found elsewhere [36,55,64].

Fig. 4.55 shows the temperature dependence of the NO conversion in NH_3-SCR over these Fe containing samples. NO conversions increase with increasing reaction temperature in all samples. For the series of ILIE samples it can be clearly seen that with increasing amount of isolated Fe sites from A(ILIE)0.2 to A(ILIE)0.3 (Table 4.1) activity increases gradually. Accordingly, sample A(MR)0.5 which is not included in Fig. 4.55 shows similar activity to

that of A(ILIE)0.3. As the concentration of oligomeric sites increases with rising Fe content from A(ILIE)0.3 to A(ILIE)0.6 (Table 4.1), the NO conversion improves, too. Accordingly, A(ILIE)1.2 shows the highest activity within the ILIE series below 750 K while above this temperature NO conversion drops again. These results clearly demonstrate the contribution of both isolated and small oligomeric iron sites to the SCR reaction while the drop of NO conversion at high temperatures for sample A(ILIE)1.2 suggests that larger Fe_xO_y clusters could contribute to the non selective oxidation of the NH_3 reductant.

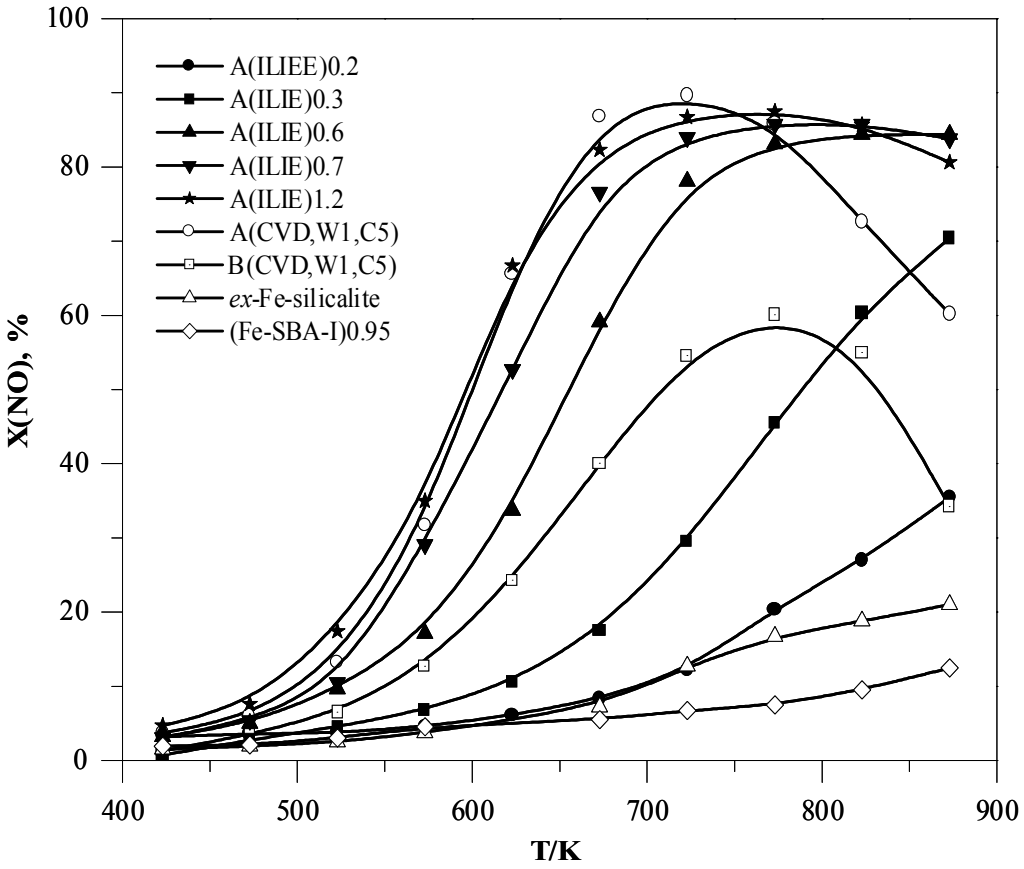

Fig. 4.55. NO conversions in the selective catalytic reduction of NO with NH_3 over different Fe-containing catalysts. Comparison of different preparation techniques, acidity and pore structures of the support. Feed composition: 1000 ppm NO, 1000 ppm NH_3, 2% O_2 in He at 750,000 h^{-1} [55,64].

Sample A(CVD,W1,C5) shows similar activity to that of A(ILIE)1.2 below 700 K but above this temperature activity drastically decreases which is much less pronounced over the latter. This is due to the oxidation of NH_3 by iron oxide clusters. This is obviously much more pronounced over A(CVD,W1,C5) due to the presence of more and larger clusters than in A(ILIE)1.2 (Table 4.1). In agreement with this, sample A(SSIE)5.4 which contains similar Fe content but more or less the similar nature and distribution of Fe sites as that of A(CVD,W1,C5), exhibits similar catalytic activity (not shown).

To study the effect of acidity on the NH_3-SCR of NO, the performance of B(CVD,W1,C5) and A(CVD,W1,C5) is compared (Fig. 4.55). These two samples were

prepared by the same preparation method using different H-ZSM-5 supports with Si/Al ratio 40 and 14 respectively. Accordingly, B(CVD,W1,C5) shows poor acidity as compared to A(CVD,W1,C5) as evidenced by FT-IR studies of pyridine adsorption (Fig. 4.28). B(CVD,W1,C5) shows much less SCR activity than A(CVD,W1,C5) indicating that acidity may play an important role in the SCR. Furthermore, in spite of containing much higher Fe content and, consequently, higher amount of oligomeric clusters (Table 4.1), B(CVD,W1,C5) shows lower activity at all temperatures as compared to A(ILIE)0.6. This further supports that acidity, probably Brønsted acidity, is required for this reaction. Finally, despite high Fe content, Al free *ex*-Fe-silicalite shows very poor activity as compared to A(ILIE)0.2 and A(ILIE)0.3 with similar nature and distribution of Fe species (Table 4.1). This is, obviously, due to poor acidity. This is in excellent agreement with the above conclusion.

By comparing the catalytic performance of Al free *ex*-Fe-silicalite and (Fe-SBA-I)0.95, the influence of the framework structure on NH_3-SCR reaction is studied (Fig. 4.55). Despite similar nature and distribution of Fe species in the samples (section 4.1), *ex*-Fe-silicalite shows poor activity whereas (Fe-SBA-I)0.95 completely failed. This indicates that the framework structure and/or pore geometry are crucial for determining the SCR activity. Thus, it was found that microporous materials like MFI structure is favorable for SCR reaction than mesoporous material like SBA-15.

Fig. 4.56 shows the temperature dependence of the NO conversions obtained in isobutane-SCR over the series of ILIE samples. First of all it must be noted that the ILIE samples are markedly less active with isobutane than with NH_3 as a reactant since a much lower GHSV was required to reach similar NO conversions with isobutane. With increasing reaction temperature, the NO conversions increase in all samples and passes through a maximum. With increasing Fe content in the samples from A(ILIE)0.2 to A(ILIE)1.2 the NO conversion at the lowest reaction temperature (523 K) increases strongly from 10 to 40%. The NO conversion maximum decreases and shifts to lower temperatures, from 680 K (A(ILIE)0.2) to 620 K (A(ILIE)1.2).

A(ILIE)0.3 which contains almost exclusively isolated Fe sites as evidenced by ex situ EPR and UV/VIS-DRS results (Table 4.1), exhibits the best catalytic performance. This indicates that isolated Fe sites are playing a major role in the reaction. With increase in the concentration of oligomeric moieties in A(ILIE)0.6 (Table 4.1), the NO conversion drastically decreases at higher temperatures. This is mainly due to the unselective total oxidation of isobutane by oligomeric sites which are essentially in +3 oxidation state under typical SCR conditions as evidenced by in situ EPR and UV/VIS-DRS (section 4.3.2). This effect is even more pronounced for A(ILIE)1.2 which contains extensive clusters. It must be mentioned that NO conversion drops much more than in NH_3-SCR as oxidic clusters gain influence in the samples. This indicates that isobutane is much more sensitive against total oxidation than NH_3.

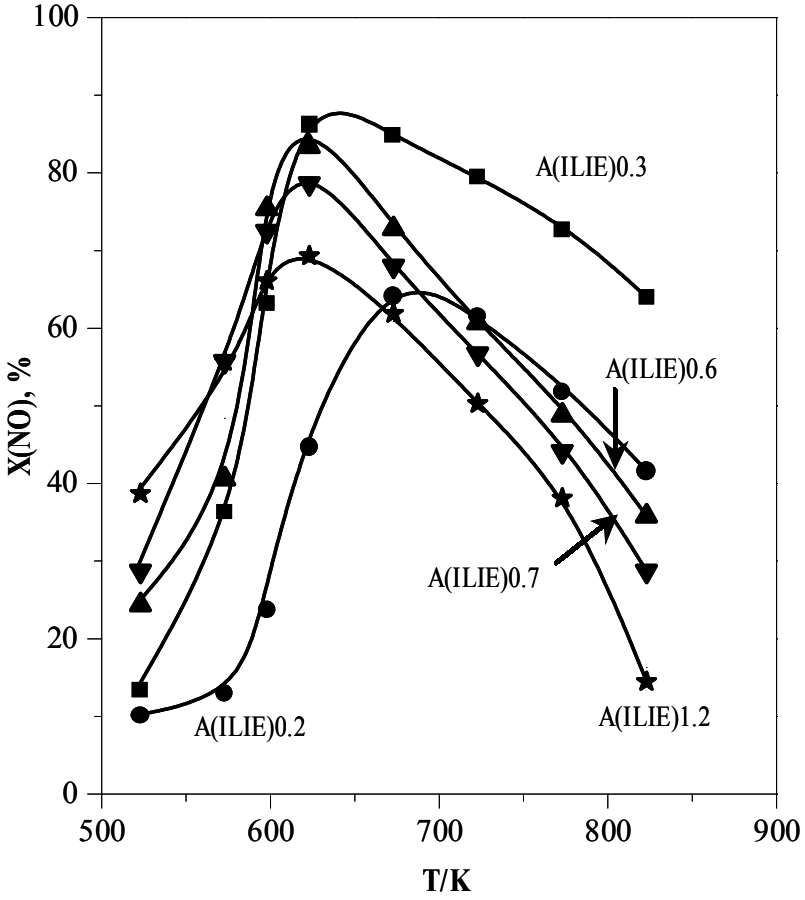

Fig. 4.56. NO conversions in the selective catalytic reduction of NO with isobutane over a series of ILIE samples. Comparison of different nature and distribution of Fe sites. Feed composition: 2000 ppm NO, 2000 ppm isobutane, 2% O_2 in He at 42,000 h^{-1} [64].

Fig. 4.57 demonstrates the effect of the nature and distribution of Fe sites, framework composition and structure of the support on the isobutane-SCR activity. As compared to the performance of A(ILIE)1.2 in Fig. 4.56, the peak NO conversion shifts slightly to lower temperatures and NO conversion also increases slightly. This is due to the difference in the reaction conditions. Samples A(ILIE)1.2 and A(CVD,W1,C5) which contain extensive clusters show similar behavior on the whole. However, over A(CVD,W1,C5), in which clusters are more abundant than A(ILIE)1.2, NO conversion above 650 K decreases slightly more. With respect to the nature and distribution of Fe sites, samples A(CVD,W1,C5) and A(SSIE)5.4 are more or less similar. Accordingly, the latter sample shows similar activity as compared to the former (not shown).

In contrast to these samples, B(CVD,W1,C5) which contains higher Si/Al ratio (40 *vs* 14) shows poor activity as compared to A(CVD,W1,C5). This can be attributed to the lack of acidity, mainly due to the poor Brønsted acidity as concluded in NH_3-SCR. This is further supported by comparing the catalytic performance of A(ILIE)0.2 with Si/Al ≈ 14 (Fig. 4.56) and Al free *ex*-Fe-silicalite (Fig. 4.57). Accordingly, the former sample shows pronounced acidity while the latter shows poor acidity (Figs. 4.29, 4.30 and Table 4.3). However, both samples contain almost exclusively isolated iron sites (Table 4.1). In spite of containing only one

third of the isolated Fe sites, which are believed to play a crucial role in the SCR reaction, A(ILIE)0.2 exhibits much higher activity than *ex*-Fe-silicalite. This confirms that Brønsted acidity is essential for this reaction.

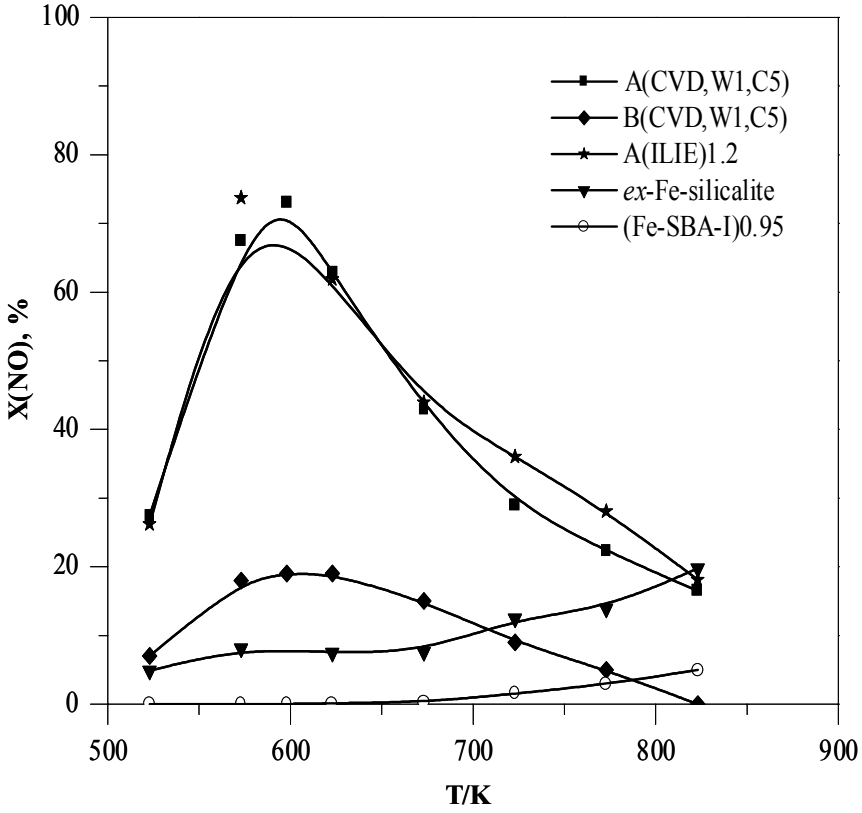

Fig. 4.57. SCR of NO with isobutane over Fe containing catalysts. Comparison of different nature and distribution of Fe sites, framework composition and structure of the support. Feed composition: 1000 ppm NO, 1000 ppm isobutane, 2% O_2 in He at 30,000 h^{-1} [55,64].

To investigate the effect of framework structures on the isobutane-SCR reaction, the catalytic performance of *ex*-Fe-silicalite and (Fe-SBA-I)0.95 is compared. Both samples do not contain Al in the framework but have very similar nature and distribution of iron species (Table 4.1). Interestingly, although *ex*-Fe-silicalite shows poor activity the activity of sample (Fe-SBA-I)0.95 is even worth showing almost negligible NO conversion in the whole temperature range. This clearly demonstrates that the intrinsic activity of MFI structure is an additional asset for this reaction.

In summary, SCR activity either with NH_3 or with isobutane increases with increasing Fe concentration at low temperature, suggesting that accessible Fe sites in isolated and oligomeric form play an active role. However, oligomers cause total oxidation of the reductant. This is much more severe even at lower temperatures for isobutane than for NH_3. Therefore, the NO conversion drastically deteriorated above 600 K over cluster containing samples in isobutane SCR whereas this effect is much less pronounced in NH_3-SCR. This suggests a more favorable role of small oligomeric clusters in NH_3-SCR. Consequently, sample A(ILIE)1.2

shows superior activity at almost all temperatures as compared to the cluster-free sample A(ILIE)0.3. This is opposite in isobutane-SCR, where the cluster-free sample A(ILIE)0.3 exhibits the highest activity in a wide temperature window since clusters that can cause total oxidation of the reductant are missing.

The poor SCR activity of B(CVD,W1,C5) and *ex*-Fe-silicalite indicates that acidity is essential for these reactions. The SCR activity of sample (Fe-SBA-I)0.95 is almost negligible in both the reactions as compared to *ex*-Fe-silicalite, despite a very similar nature and distribution of iron species. From this it can be concluded that the intrinsic activity of MFI structure is favorable for these reactions.

4.4.2 Decomposition and Selective Catalytic Reduction (SCR) of N_2O with CO

N_2O conversion has been studied over *ex*-Fe-silicalite, *ex*-Fe-ZSM-5, A'(CVD,W1,C2) Fe-ZSM-5(LIE), A(ILIE)0.2, A(ILIE)1.2 and (Fe-SBA-I)0.95. These catalysts were prepared by different procedures and, hence, contain different nature and distribution of Fe species. Besides, some of the catalysts contain different amounts or no aluminum in the lattice, which gives rise to different acidic properties. Therefore, it allows us to study the effect of the nature and distribution of Fe species, acidic properties and framework structure on N_2O decomposition and SCR of N_2O with CO.

Fig. 4.58 shows the N_2O conversion *vs*. temperature resulting from steady-state experiments over *ex*-Fe-silicalite, *ex*-Fe-ZSM-5 and A'(CVD,W1,C2) in direct N_2O decomposition.

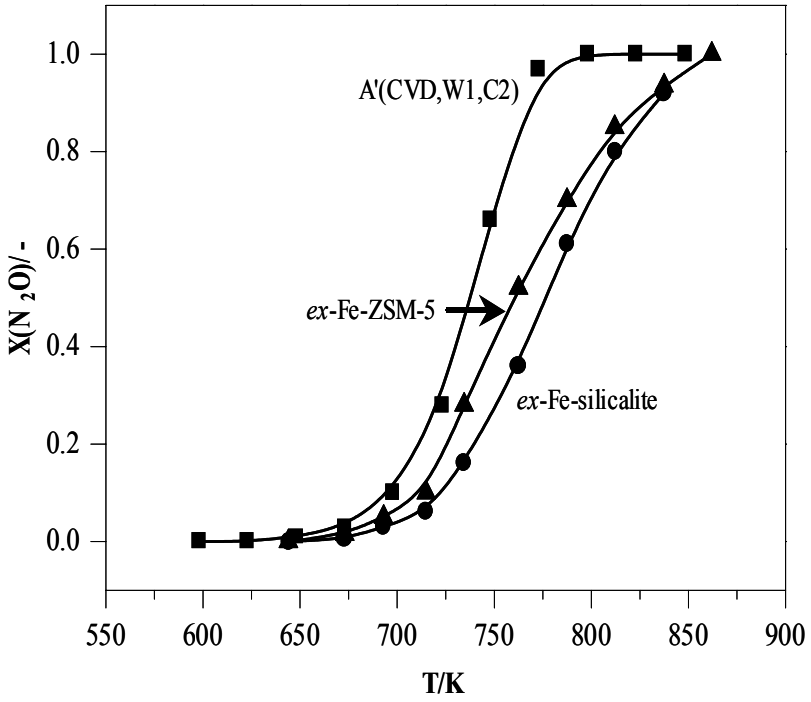

Fig. 4.58. Conversions of N_2O vs temperature in direct N_2O decomposition at 9×10^5 g s mol^{-1}. Partial N_2O pressure was fixed at 1.5 mbar; balance He [58,96].

A'(CVD,W1,C2) shows the highest activity followed by *ex*-Fe-ZSM-5 and *ex*-Fe-silicalite. Furthermore, different activation energies were obtained for *ex*-Fe-ZSM-5 and *ex*-Fe-silicalite (≈ 140 and ≈ 155 kJ mol^{-1} respectively) as reported elsewhere [96]. It should be noted that despite similar Fe content, *ex*-Fe-silicalite contains almost isolated Fe sites while *ex*-Fe-ZSM-5 shows extensive clustering. Differently, A'(CVD,W1,C2) contains both isolated and oligomeric Fe sites almost equally (Table 4.1). As mentioned earlier (section 2.1.2), oxygen desorption is a rate limiting step in the direct N_2O decomposition. Thus, for direct N_2O decomposition oligomeric sites are preferred over isolated Fe sites due to easier oxygen recombination over Fe sites which are close together.

Fig. 4.59 compares the activity of *ex*-Fe-silicalite and (Fe-SBA-I)0.95 in direct N_2O decomposition. This is especially interesting, since the two catalysts contain Fe species of very similar structure as shown in section 4.1. Thus, for the first time, it is possible with these two samples to study the influence of the pore network explicitly. *Ex*-Fe-silicalite shows significant conversion in direct N_2O decomposition at T > 650 K and the N_2O conversion is complete at 800 K. The different behavior of this sample as compared to the one in Fig. 4.58 is due to the difference in the reaction condition. The conversion profile over (Fe-SBA-I)0.95 is similar but shifted by 200 K to higher temperatures indicating considerably lower activity than *ex*-Fe-silicalite [161].

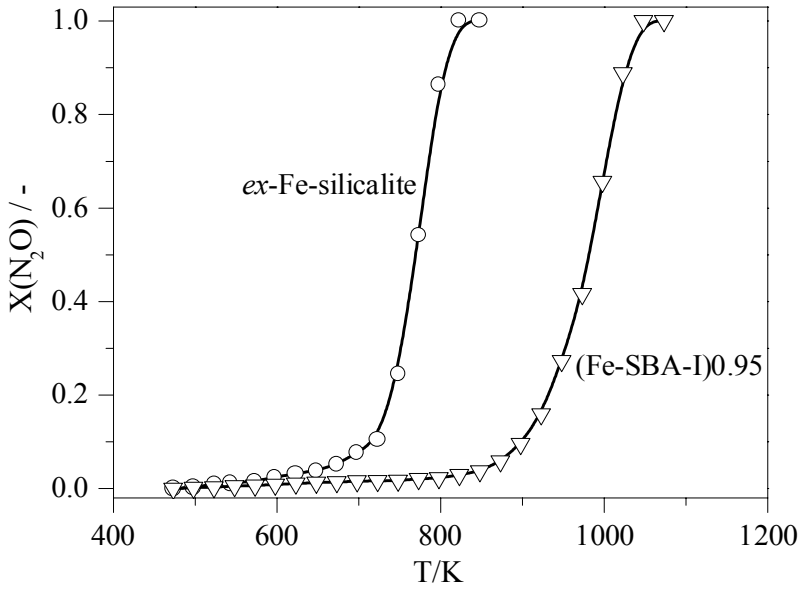

Fig. 4.59. N_2O conversion vs temperature in direct N_2O decomposition at 3×10^5 g s mol^{-1}. Partial N_2O pressure was fixed at 1.5 mbar; balance He [161].

The SCR of N_2O with CO was performed over the same samples used for direct N_2O decomposition as well as over A(ILIE)0.2 and A(ILIE)1.2. The catalytic performance of *ex*-Fe-silicalite and *ex*-Fe-ZSM-5 in CO/N_2O at a molar ratio of 0.6 is compared with A'(CVD,W1,C2) at molar feed ratios of 0.5 and 0.75 (see in the Fig. 4.60). In comparison to direct N_2O decomposition (Fig. 4.58), reduction of N_2O with CO starts at significantly lower temperatures over all samples. N_2O conversion over A'(CVD,W1,C2) increases with increasing CO/N_2O

molar ratio from 0.5 to 0.75 indicating that the reaction is stoichiometric as shown by Eq. (4.4).

$$N_2O + CO \rightarrow N_2 + CO_2 \qquad (4.4)$$

This is also suggested by the profile of the N_2O conversion curves. N_2O conversion over A'(CVD,W1,C2) sample rapidly increases in the temperature range of 500-600 K. Above 600 K CO becomes exhausted over this catalyst and hence, N_2O conversion remains practically unchanged until 700 K. Above this temperature N_2O conversion curves shift to that of the pure N_2O decomposition.

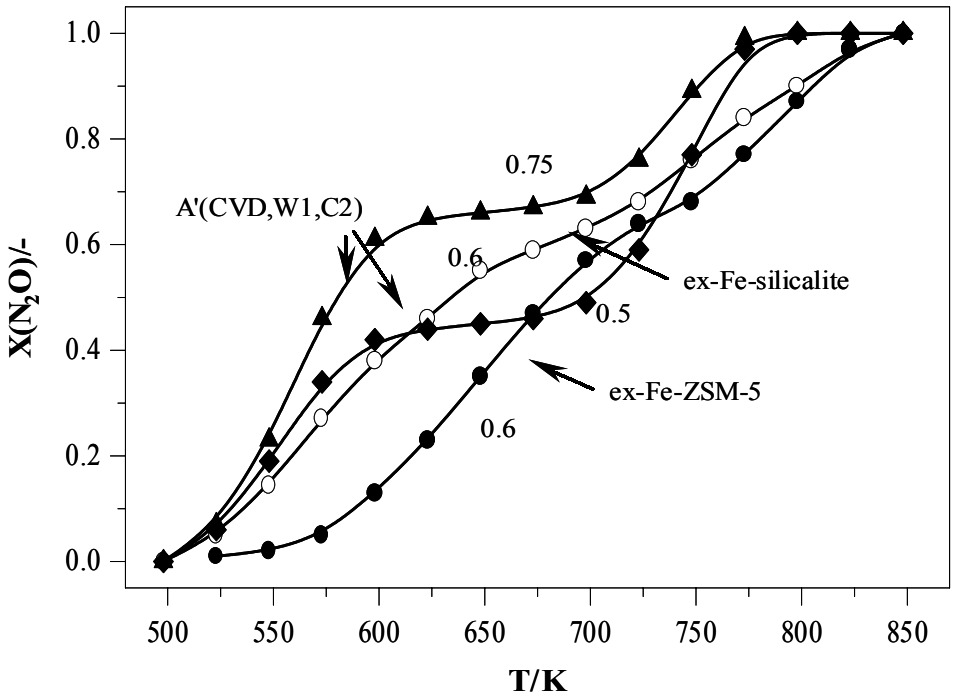

Fig. 4.60. N_2O conversion vs temperature at $W/F(N_2O) \approx 9\times10^5$ g s mol^{-1} and P = 1 bar. Partial N_2O pressure was fixed at 1.5 mbar and CO/N_2O ratios at 0.5-0.75 were used, balance He [58,96].

Despite the fact that both *ex*-Fe-silicalite and *ex*-Fe-ZSM-5 contain almost the same amount of iron, the former is markedly more active in the entire temperature range studied. While in *ex*-Fe-silicalite almost all Fe sites are well isolated, *ex*-Fe-ZSM-5 is characterized by a considerable amount of Fe_xO_y clusters which form at the expense of isolated Fe sites. Thus, the different behavior of the two samples shows clearly the superior catalytic performance of isolated Fe sites in the SCR of N_2O. In principle, this is also confirmed by the behavior of sample A'(CVD,W1,C2). Although this sample contains roughly ten times more iron than *ex*-Fe-silicalite, it is only slightly more active in the low-temperature range, probably since most of the additional Fe is incorporated in oxidic clusters.

Fig. 4.61 compares the activity of different catalysts in the N_2O reduction with CO at CO/N_2O molar ratio of one. Both *ex*-Fe-silicalite and A(ILIE)0.2 contain almost exclusively

isolated Fe sites. However, the occurrence of differently coordinated Fe sites (octahedral and tetrahedral) differs markedly in the samples. Thus, the former sample is dominated by tetrahedrally coordinated Fe sites besides a small amount of octahedral Fe sites, whereas the latter sample contains both types of Fe sites equally. However, despite lower Fe content, sample A(ILIE)0.2 shows slightly higher activity than *ex*-Fe-silicalite. This could be due to the differences in the occurrence of differently coordinated isolated Fe sites in the samples and/or presence of Al in the framework of A(ILIE)0.2. Interestingly, in spite of containing extensive clusters with relatively low amount of isolated Fe sites (Table 4.1), sample A(ILIE)1.2 shows higher activity at all temperatures as compared to *ex*-Fe-silicalite and (Fe-SBA-I)0.95. Therefore, the superior catalytic performance of the sample A(ILIE)1.2 should be related to the contribution of oligomeric sites along with isolated Fe sites.

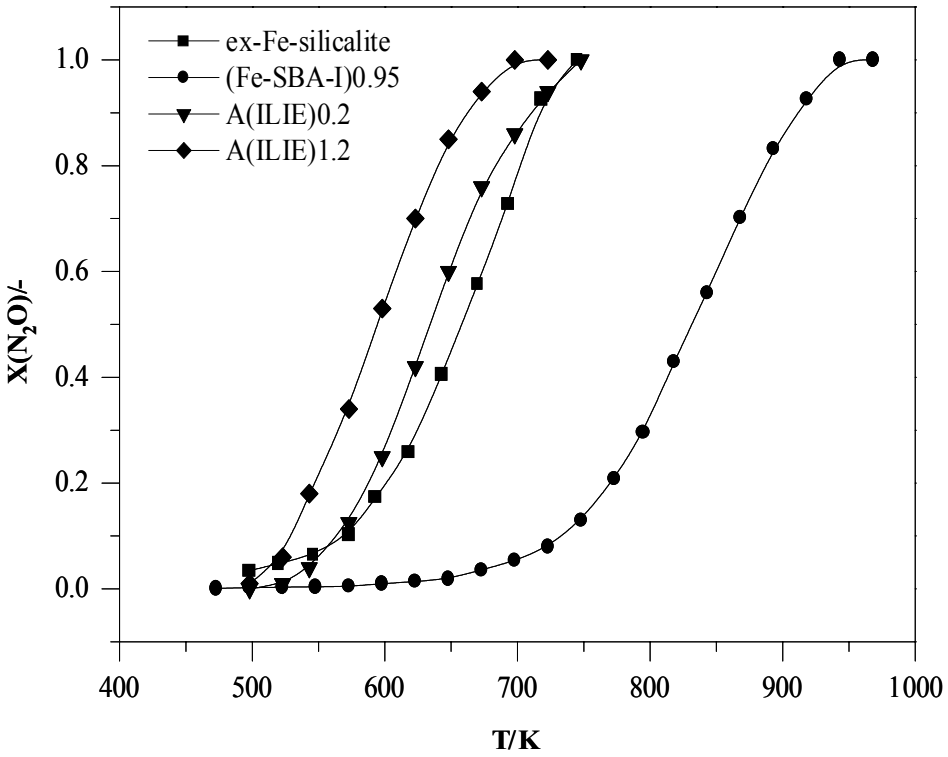

Fig. 4.61. N_2O conversion vs temperature over different catalysts in the N_2O reduction with CO at $CO/N_2O=1$. Conditions: $W/F^o(N_2O) = 3\times10^5$ g s mol^{-1} and P = 1 bar; balance He [161,162].

Finally, despite of similar nature and distribution of Fe sites in *ex*-Fe-silicalite and (Fe-SBA-I)0.95, the latter sample shows considerably lower activity than the former. This indicates clearly that it is not the nature of the Fe sites but their confinement in the micropores of the MFI structure that accounts for the superior activity of *ex*-Fe-silicalite.

In summary, for direct decomposition of N_2O, cluster-containing samples A'(CVD,W1,C2) and *ex*-Fe-ZSM-5 show higher performance than the cluster-free sample *ex*-Fe-silicalite. Thus, it can be concluded that oligomeric sites are preferred over isolated Fe sites for this reaction. In SCR of N_2O with CO, A(ILIE)0.2 and *ex*-Fe-silicalite with almost exclusively isolated Fe sites show higher activity per mol of Fe than any other catalyst tested

in this study. Therefore, it can be concluded that isolated Fe sites are essential for this reaction. However, contribution of oligomeric sites to the reaction cannot be completely ruled out as evidenced by the catalytic performance of sample A(ILIE)1.2. Contrarily, in spite of containing a slightly higher amount of isolated Fe sites (Table 4.1), (Fe-SBA-I)0.95 shows lower catalytic activity in both the direct decomposition as well as in the SCR of N_2O in comparison to *ex*-Fe-silicalite. This observation is a clear evidence for the contribution of the intrinsic activity of MFI structure for these reactions than mesoporous SBA-15. Finally, from the catalytic behavior of A(ILIE)0.2 (Si/Al ≈ 14) and *ex*-Fe-silicalite (Si/Al ≈ ∞), which contain similar nature and distribution of Fe species, it can be concluded that surface acidity of the Fe-zeolites has negligible effect on these reactions.

5. Discussion

5.1 Influence of synthesis conditions, framework composition and SCR reaction on the nature of Fe species

Fe-containing zeolites prepared by various techniques can be classified into two categories: (i) postsynthesis insertion of iron via ion exchange in liquid and solid state as well as by CVD and by impregnation and (ii) isomorphous substitution of Fe^{+3} into the framework of MFI and beta structure followed by extraction by steaming to extrafamework positions. The samples have been characterized by EPR and UV/VIS-DRS after synthesis, calcination, steaming and use in catalysis as well as in situ during calcination to assess the nature and distribution of iron species and their role in the catalytic reaction. In this section, the EPR and UV/VIS-DRS results of the influence of the mode of Fe insertion, washing and calcination procedure, Al content of the parent zeolite matrix and use in the SCR reaction on the iron species are discussed.

5.1.1 Mode of Fe incorporation

The results of UV/VIS-DRS and EPR characterization show that the distribution of iron species, as isolated iron ions, oligomeric iron oxo species and iron oxide particles, is a function of the sample genesis. According to EPR results it can be concluded that almost all samples contain at least two kinds of strongly distorted isolated Fe^{+3} ions, probably in tetrahedral and higher coordination as reflected by EPR signals at $g' \approx 4.3$ and $g' \approx 6$. A third kind of isolated Fe^{+3} ions in less distorted environment contributes to the EPR signal at $g' \approx 2$. In UV/VIS-DRS rather the different coordination geometry (tetrahedral and octahedral) but not the distortion of the isolated Fe site is reflected by two signals below 300 nm. Beside the different isolated Fe^{+3} ions, Fe_xO_y aggregates are formed, the amount and size of which varied from sample to sample. In UV/VIS-DRS they are reflected by bands above 300 nm while in EPR spectra they give rise to a signal around $g' \approx 2$.

Chemical vapor deposition (CVD) is one of the most effective postsynthesis methods, since it is easy to obtain high iron loading ($Fe/Al \approx 1$). A complete insertion of iron at ion exchanged positions has been claimed, forming diferric (hydr)oxo-bridge binuclear clusters [31,56,57]. The presence of almost exclusively such Fe dimers in Fe-ZSM-5 zeolites prepared by CVD has been claimed by several authors using different spectroscopic techniques, mainly EXAFS [56,57,110,111]. However, recently, Heinrich et. al. [36] have shown that EXAFS seriously underestimates scattering contributions from higher shells. Thus, it is much less sensitive to FeO_x clusters (dimers being the smallest possible cluster species) than to isolated Fe. Moreover, EXAFS gives average values for the scattering contributions from all Fe species making the identification of particular species in samples with several types of coexisting Fe species difficult. In an EPR study, Chen et al. assigned such dimer species to the signal at $g' \approx 2.03$ in the spectra recorded at 293 K. It is unlikely that such dimer species gives an EPR signal at this temperature since, it requires much lower temperatures (e.g. 8 K) to be detected [55,186].

In the present study, the UV/VIS-DRS and EPR results in sections 4.1.1 and 4.1.2 respectively show the presence of iron in the sample as isolated, oligomeric iron oxo species and large iron oxide particles. Furthermore, the semi-quantitative data obtained by UV/VIS-DRS show the occurrence of these three kinds of Fe species in almost equal amounts (Table 4.1). Hence, a uniform distribution of iron species was certainly not achieved in the studied CVD samples, prepared according to the procedure described by Chen and Sachtler [31]. Therefore, the almost exclusive presence of Fe dimers in Fe-ZSM-5 as claimed by some authors is not appropriate. The hydrolysis and calcination steps were proven to be the key steps in order to control the formation of large iron oxide particles after sublimation of $FeCl_3$ into zeolite matrix. The results will be discussed in detail in the corresponding sections.

Similar to CVD, solid-state ion exchange (SSIE) leads to the formation of both isolated iron ions and iron oxo clusters of different sizes. However, large iron oxide particles with long range magnetic ordering as evidenced by temperature dependent EPR results (Fig. 4.20) are markedly more pronounced than with CVD. These particles are at the external surface of the zeolite as evidenced by XRD and EXAFS [36].

UV/VIS-DRS and EPR results show that the mechanochemical route (MR) leads to the formation of highly dispersed isolated Fe^{+3} ions besides a small amount of oligomeric Fe_xO_y moieties. Semi-quantitative UV/VIS-DRS data show that almost 83% of the Fe is distributed as isolated iron sites and 17% of the Fe is present as oligomeric Fe_xO_y. Interestingly, XAFS data of sample A(MR)0.5 do not reflect any Fe_xO_y clusters although they are clearly detected by EPR and UV/VIS-DRS. This illustrates the benefit of the two techniques for the characterization of complex solid materials like Fe-ZSM-5.

The sample prepared by conventional liquid ion exchange (LIE) shows extensive formation of iron oxide clusters and particles as evidenced by UV/VIS-DRS and EPR results, which is also in line with HRTEM results [58] although the Fe content is rather low. On the other hand, improved liquid ion exchange (ILIE) in dilute HCl with iron powder was proven to be a more effective post synthesis method, since iron clustering into large particles is largely suppressed as compared to samples obtained by other techniques. UV/VIS-DRS and EPR data revealed that at low iron content in the zeolite matrix iron is mainly in the form of isolated Fe^{+3} ions and a uniform distribution of iron species was achieved in A(ILIE)0.2 and A(ILIE)0.3. At an iron content ≤ 0.3 wt-%, ca. 95 % of the iron is present as mononuclear sites. This conclusion rests mainly on the UV/VIS-DRS data (Fig. 4.5, Table 4.1). It is, however, confirmed by the EPR results (Fig. 4.23) where all signals observed in A(ILIE)0.2 and A(ILIE)0.3 could be assigned to isolated sites and exhibit paramagnetic behavior. Previous EXAFS results also support this conclusion qualitatively by a very low sum coordination number of the neighboring Fe shells [64]. On increasing iron percentage more and more oligomeric Fe_xO_y moieties are formed in A(ILIE)0.6 and A(ILIE)0.7. Increasing clustering tendency is also supported by EXAFS, where the Fe sum coordination number increases above 3 [64]. The coexistence of isolated Fe^{3+} ions and weakly interacting Fe sites within low oligomers is also suggested from the temperature dependence of the EPR spectra (Fig. 4.24). However, the missing ferrimagnetic/super-paramagnetic behaviour confirms that the formation of extended oxide particles does not take place at Fe contents of 0.6 %. At a Fe content of 1.2 %, the

aggregation into larger particles is obvious as evidenced by UV/VIS-DRS and EPR results. The temperature dependence of EPR spectra of A(ILIE)1.2 is typical for ferrimagnetic/super-paramagnetic Fe_2O_3 nanoparticles (Fig. 4.24), the formation of which is further supported by TEM measurements [64].

Finally, the observed differences in the distribution of Fe species between samples prepared by LIE and ILIE can be explained as: In LIE, Fe^{3+} ions are exchanged with NH_4^+ ions (NH_4-ZSM-5 with Si/Al ≈ 37). Thus, one Fe^{3+} ion compensates three spatially separated negative charges of the zeolite matrix which were balanced by NH_4^+ ions. Accordingly, only a small amount of Fe^{3+} could be deposited at cationic sites (ca. Fe/Al ≈ 0.33). The additional Fe^{3+} ions tend to precipitate and form Fe_xO_y clusters upon subsequent washing and calcination which leads to a highly heterogeneous distribution of Fe species in the final catalyst. Differently, in ILIE procedure Fe^{2+} ions replace two H^+ (H-ZSM-5 with Si/Al ≈ 14). Obviously, this leads to the incorporation of more Fe ions at cationic sites in the zeolite matrix. Accordingly, the possibility for the formation of Fe_xO_y clusters is reduced and a more uniform distribution of Fe species was achieved, in particular at low Fe content. Furthermore, low Al content NH_4-ZSM-5 support (Si/Al ≈ 37) used for LIE provides lower number of cation exchange sites than high Al content H-ZSM-5 (Si/Al ≈ 14) used for ILIE. This can be another reason for the formation of more pronounced clusters in LIE than in ILIE samples.

Steam activated *ex*-Fe-silicalite, *ex*-Fe-ZSM-5 and *ex*-Fe-beta are highly diluted samples, with Si/Fe ≈ 150. The migration of iron from framework to extraframework positions upon steaming is complex and can be envisaged as a clustering process in the latter two samples [155]. An appropriate comparison of the iron constitution in these samples can be established, since the preparation and activation procedures, as well as the iron content in the catalysts are similar. A better-defined distribution of iron species was attained upon steam treatment of Fe-silicalite. The color of this sample was nearly white, suggesting the more isolated nature of the iron species in the catalyst, while *ex*-Fe-ZSM-5 and *ex*-Fe-beta were light brownish. Indeed, the majority of iron in *ex*-Fe-silicalite was found as isolated Fe^{3+} ions in extraframework positions. A very minor degree of iron aggregation is present, as concluded from UV/VIS-DRS. EPR spectroscopy evidences the paramagnetic behaviour of Fe^{3+} species in *ex*-Fe-silicalite following the Curie-Weiss law, as typically observed for highly symmetric isolated species ($g' \approx 2$). However, a certain degree of weak dipolar interactions between Fe^{3+} sites is also identified, indicative of certain iron association. The UV/VIS-DRS and EPR results of *ex*-Fe-ZSM-5 and *ex*-Fe-beta are similar, showing a variety of iron species including the formation of small iron oxide nanoparticles. Hence a remarkable uniformity of iron species and the absence of extensive clustering are a priori not guaranteed by this method. Of course, the size of the particles is significantly smaller than in the Fe-zeolites prepared by post-synthesis methods as evidenced by (HR)TEM [58,64], which indicates a higher iron dispersion. However, this is also associated to the lower iron content in the sample (e.g., ≈ 7 times lower than in the catalyst prepared by CVD and SSIE).

Additionally the above results indicate the importance of framework composition of the zeolite in determining the iron distribution. As shown in results (section 4.1.1 and page no. 62), the presence of Al in the framework structure favors the formation of oligonuclear Fe_xO_y clusters and even Fe_2O_3 particles upon steaming. By comparing the UV/VIS-DR spectra of *c*-Fe-beta and *ex*-Fe-beta (Fig. 4.9) it is evident that this undesired process takes partly place already during synthesis and/or calcination. However, it is largely suppressed in Al-free Fe-silicalite. This suggests that Al and Fe might compete for the same Si lattice positions, whereby the isomorphous substitution of Al is obviously favored. This agrees with previous observations [96,61] on Fe-MFI and also with recent results of Berlier et al. [187] who observed that the presence of Al in the framework of Fe-ZSM-5 promotes the formation of extraframework Fe upon vacuum treatment at higher temperature in comparison to Al-free Fe-silicalite. The *ex*-Fe-silicalite results presented here and in previous studies on this system [155], using steam as activation atmosphere (more effective for iron dislodgment than vacuum treatment), show that the higher stability of iron in the framework of silicalite enables a better control of iron extraction upon steam activation, since iron clustering can be largely prevented. Still, by a proper selection of the steaming temperature (873 K), a substantial degree of Fe extraction can be accomplished, although not being complete. This has been demonstrated by the different reduction characteristics of framework and extraframework isolated iron species (irrespective of the zeolite structure) during in situ UV/VIS-DRS in H_2 at 773 K (Fig. 4.10), and previously by voltammetric response studies [155].

The Fe content as well as the BET surface area of *ex*-Fe-silicalite and (Fe-SBA-I)0.95 are rather similar. Significant differences exist in the pore structure. While *ex*-Fe-silicalite is dominated by micropores of 0.55 nm diameter resulting from the well-known MFI structure which is confirmed by the XRD powder pattern [161], (Fe-SBA-I)0.95 contains mesopores, the mean diameter of which amounts to 7.5 nm as derived from N_2 adsorption measurements [161]. Taking into account the results obtained by UV/VIS-DRS and EPR and also by other characterization techniques obtained over these two samples [161], it can be concluded that both Fe-silicalite and (Fe-SBA-I)0.95 contain almost exclusively isolated Fe^{3+} sites of very similar structure. Moreover, very similar reduction/reoxidation behaviour of iron species in H_2 and in air is observed, too, for both samples (Fig. 4.11). This suggests that Fe sites of almost the same structure and very similar redox properties can be created in matrices of very different pore structure by using suitable preparation techniques.

In summary, the characterization results indicate that improved liquid ion exchange and the mechanochemical route are the most effective postsynthesis techniques to introduce preferably isolated Fe^{+3} species into pore positions of ZSM-5. Chemical vapor deposition and solid-state ion exchange methods are also effective to create isolated Fe sites but, besides, cluster formation cannot be avoided. Differently, conventional liquid ion exchange creates preferably large iron oxide clusters/particles. On the other hand, hydrothermal synthesis followed by steam activation leads to extensive clustering of Fe in Al containing Fe-ZSM-5 and Fe-beta but remarkably, this method leads to formation of exclusively extraframework isolated

Fe^{+3} species in Al free Fe-silicalite. Finally, mesoporous supports like SBA-15 are certainly favorable for the formation of highly dispersed Fe species.

5.1.2 Washing intensity

The washing procedure after sublimation of $FeCl_3$ into the ZSM-5 matrix, certainly, has influence on the distribution of iron species. As evidenced by UV/VIS-DRS spectra of samples A(CVD,W1) and A(CVD,W10), intense washing diminishes the amount of large Fe_xO_y clusters slightly (Fig. 4.2 and Table 4.1). This has been supported earlier from TPR and Mössbauer measurements although these measurements had been performed with the respective A(CVD,W1,C0.5) and A(CVD,W10,C0.5) samples after use in the SCR reaction [36]. For comparison, these (used) samples were also studied by UV/VIS-DRS (Fig. 4.2b) and EPR spectroscopy (Fig. 4.14). Thermal stress (calcination or use in the SCR reaction, which is initiated by a thermal activation/stabilization process) favors aggregation of isolated Fe sites markedly. However, even after use in catalysis the better dispersion of the iron species in the intensely washed material can be traced by a decreased absorption above 400 nm (solid line) in UV/VIS-DRS (Fig. 4.2) and a less intense g' ≈ 2 signal above 373 K in EPR spectra (Fig. 4.14). The latter effect indicates a weaker antiferromagnetic coupling due to a smaller cluster size. This confirmed that intense washing diminishes the amount of large Fe_xO_y clusters slightly and leads to slightly higher dispersion as compared to the washing procedure using a 10-fold smaller amount of water.

5.1.3 Calcination procedure

Heat treatment, e.g. the calcination in air at 873 K, usually performed before catalytic experiments [32,36] causes significant structural changes. It is seen from the UV/VIS-DRS and EPR spectra that initially isolated Fe sites aggregate to form Fe_xO_y clusters (see also Table 4.1). This effect seems to be slightly favored by higher heating rates. It has been reported that mild calcination (0.5 K/min and 1000 ml/min O_2/He (20% O_2 + 80% He)) favours high Fe dispersion and formation of large iron oxide clusters is strongly suppressed, while severe calcination (5 K/min and 200 ml/min O_2) leads to large Fe oxide clusters [57]. These calcination procedures are similar to those used for the samples in this thesis (e.g. samples A(CVD,W1,C0.5) and A(CVD,W1,C5). Different from the above authors observations, in both cases extensive iron oxide clusters including larger ones are formed as evidenced by EPR and UV/VIS but the clustering slightly lowered in A(CVD,W1,C0.5) (Figs. 4.3 and 4.15). Clustering of isolated Fe species upon calcination in air has been observed for almost all Fe-containing samples (Table 4.1). It appears that Fe_xO_y cluster formation is favored by moisture remaining in the zeolites after washing as evidenced by dehydration and re-hydration experiments (Fig. 4.16). After deposition of $[FeCl_2]^+$ at cationic sites of the zeolite matrix, the chloride ligands from the coordination sphere of Fe sites are replaced by OH or H_2O during the washing procedure (Eq. (4.2)). The latter can be reversibly removed from the Fe coordination either by evacuation or by mild thermal treatment (< 423 K) as evidenced in Fig. 4.16a [55]. EPR signal at g' ≈ 6 which is assigned to isolated Fe sites with 5 or 6 coordinating ligands (Eq. (4.2)) lose intensity to g' ≈ 4.3 (due to isolated Fe sites with 3 or 4 ligands) upon room temperature evacuation (Fig. 4.16a).

This is due to the removal of OH or H_2O ligands from the coordination sphere of Fe sites that are responsible for the g' ≈ 6 signal. These effects are almost completely reversible upon contact with ambient atmosphere due to the adsorption of moisture. Calcination at 873 K initiates the condensation of these ligands (OH or H_2O) between different Fe coordinations as well as between Fe and framework OH groups. The former leading to Fe association as evidenced by decrease in the amount of isolated Fe sites after calcination (Fig. 4.15 and Table 4.1) and the latter attaches the Fe site to the framework via oxygen bridge (Fig. 4.16b and c). Accordingly, it is also likely that iron oxy hydroxo clusters, which most probably form after the washing step, lose moisture (H_2O/OH) upon calcination and form Fe_xO_y clusters as evidenced UV/VIS (Table 4.1).

5.1.4 Al content and defect density of the parent zeolite matrix

The effect of Si/Al ratio in the zeolite matrix on the distribution of iron species was studied using two different zeolite matrices with Si/Al ≈ 40 and 14. ZSM-5(A) with Si/Al ≈ 14 shows higher acidity than ZSM-5(B) with Si/Al ≈ 40 as evidenced by FT-IR of pyridine adsorption (Fig. 4.28 and Table 4.3). UV/VIS-DRS and EPR results of uncalcined samples B(CVD,W1) and A(CVD,W1) show that the ZSM-5(B) matrix favours the formation of iron oxide clusters (Fig. 4.3b and 4.17a). Surprisingly, the opposite is observed after calcination as evident from both UV/VIS-DRS and EPR results (Fig. 4.3c and 4.17b). This might be due to the presence of silanol nests in the defective matrix (ZSM-5(B)) which serve as additional nuclei for iron condensation and keep the iron inside the pores. In contrast, in well-structured ZSM-5(A), iron oxide species may migrate out of the pores toward the external crystal surface where they can grow further in size [57]. Hence, in calcined B(CVD,W1,C5) the formation of large iron oxide clusters is less pronounced compared to sample A(CVD,W1,C5).

5.1.5 Use in the SCR reaction

UV/VIS-DR spectra of A(CVD,W1,C0.5) and A(CVD,W1,C5) before and after use in the SCR of NO with isobutane have shown that further structural changes occur in a precalcined catalyst under reaction conditions (Fig. 4.3d and Table 4.1). The relative intensity of bands above 400 nm increases after use in the SCR reaction mainly at the expense of bands between 300 and 400 nm, while bands below 300 nm decrease only slightly. This is particularly evident for sample A(CVD,W1,C0.5) (Table 4.1). It suggests that, under reaction conditions, the growth of iron oxide particles is supported mainly by further agglomeration of oligonuclear clusters [55]. However, it cannot be excluded, that some isolated Fe sites are also involved in this agglomeration process.

In the EPR spectra (Fig. 4.18), those isolated Fe sites might be reflected by the signal at g' ≈ 6 which is completely missing after use in catalysis. Alternatively, the disappearance of the g' ≈ 6 signal may also be due to a reduction and/or a change of the coordination of the respective isolated Fe sites during reaction. In any case, the change of the isolated Fe sites reflected by the vanishing g' ≈ 6 signal does obviously not lead to a loss of catalyst activity since in the catalytic tests no deactivation was observed with time on stream.

By comparing the EPR and UV/VIS spectra for sample A(CVD,W1,C0.5) before and after use in the SCR of isobutane an apparent contradiction is evident (Figs. 4.3d and 4.18). While a huge increase of the EPR signal at g' ≈ 2 is observed after reaction, UV/VIS intensity in the range characteristic of agglomerated iron oxide species rises only slightly. This suggests that the observed changes are rather due to modified magnetic interactions within the oxidic clusters than to a marked increase of their concentration. The fact that the amount of small oligonuclear clusters decreases in favour of large oxide particles while isolated Fe sites mainly persist during reaction suggests that the latter are the active Fe sites of the SCR reaction. However, the changes between the amounts of oligomers and large aggregates (Table 4.1) are too small to safely exclude a contribution of the clustered phases. On the other hand, since EPR reflects a strong ordering tendency in the clustered phase and it is unlikely that the catalytic activity of clusters will be improved by increasing structural perfection, the structural changes observed on the whole support the view that isolated Fe sites play a deciding role in the SCR reaction as proposed, for instance, in [32,36,91]. However, this aspect will be discussed in detail in the following sections.

5.2 Structure-reactivity relationships in Fe-containing zeolites

Spectroscopic ex situ studies described in section 4.1 revealed that a variety of Fe species ranging from isolated ions via low oligonuclear clusters to large Fe_2O_3 particles may be formed in zeolites depending on peculiarities of the synthesis procedures and the nature of the matrices. Catalytic results described in section 4.4 together with findings from in situ EPR, UV/VIS-DRS and FT-IR studies suggest that the various Fe species play a different role in the three reactions studied in this work. Those relations between the nature of the Fe sites and their catalytic role are discussed separately for the abatement of NO and N_2O in this section.

5.2.1 Low temperature interaction of NH_3 and NO with Fe-ZSM-5 zeolites

Interaction of NH_3 with samples A(MR)0.5 and A(CVD,W1,C0.5) at 293 K

Interaction of NH_3 with Fe-ZSM-5 zeolites at 293 K leads to the disappearance of EPR signals at g' ≈ 6 and shifts the UV/VIS band to a lower wavelength as observed in Fig. 4.31. The observed effects are most likely due to linking of NH_3 to coordinatively unsaturated isolated Fe^{3+} ions without considerable reduction of the latter. This is evidenced by UV/VIS-DR spectra (Fig. 4.31c), which show similar spectral intensity before and after interaction of NH_3. This indicates that isolated Fe^{3+} ions, in particular those reflected by EPR signal at g' ≈ 6 can extend their coordination while this is less pronounced for those iron species reflected by the signal at g' ≈ 4.3. It is difficult to discern between these two kinds of isolated Fe^{3+} ions by UV/VIS-DRS but it can be clearly seen from Fig.36c that part of the isolated Fe^{3+} ions are coordinated with NH_3 as evidenced by a shift in the band position. However, considering differences in the area of UV/VIS spectra before and after NH_3 treatment, reduction of a small amount of Fe^{3+} spices cannot be completely ruled out. Kucherov et al. have observed similar effects during in situ EPR

studies over Fe-ZSM-5 prepared by sublimation [59]. In that study the EPR signals at g' ≈ 6.5 and g' ≈ 5.6 were suppressed upon adsorption of H_2O, NO or NO_2 at 293 K while the signal at g' ≈ 4.3 did virtually not change. They ascribed this behavior to a change in the symmetry of iron species, reflected by EPR signals at g' ≈ 6.5 and g' ≈ 5.6, from lower to higher symmetry and designated them as active Fe sites in the SCR reaction.

Adsorption of NO on oxidized and reduced surfaces of Fe-ZSM-5 at 293 K studied by FT-IR spectroscopy

FT-IR spectra in Fig. 4.32 and 4.33 show the formation of $[NO^+][N_2O_4]$, NO^+, Fe^{3+}-NO, N_2O_4, N_2O_3 and differently bound nitrato species upon adsorption of 1% NO/He on pre-oxidized Fe-ZSM-5 samples. This suggests the occurrence of oxidation, dimerization and disproportionation reactions over oxidized surface of the catalyst. The fact that they are found, though weakly, also after adsorption of NO on the bare H-ZSM-5 suggests that these processes can occur even in the presence of residual traces of gaseous O_2 and/or Fe impurities (ca. 500 ppm) in the commercial H-ZSM-5 used for the preparation of the Fe-samples. The formation of the above mentioned species could follow as:

NO is obviously oxidized by Fe^{3+} ions as shown by Eq. (2.3) (page no. 18). The other possible route for the oxidation of NO is by traces of oxygen which might be present on the catalyst surface (Eq. (5.1)).

$$2NO + O_2 \rightarrow 2NO_2 \qquad (5.1)$$

It is well known that NO_2 can undergo dimerization to form N_2O_4 [86,180] as evidenced by a band at 1743 cm^{-1} in Fig. 4.32 (Eq. (5.2)).

$$2NO_2 \rightarrow N_2O_4 \qquad (5.2)$$

Subsequently, N_2O_4 disproportionates to form NO^+, as evidenced by a band at 2134 cm^{-1}, and NO_3^- (Eq. (5.3)) [86,180]. However, the formation of NO_3^- cannot be seen within the spectral region recorded for this study (Fig. 4.32).

$$N_2O_4 \rightarrow NO^+ + NO_3^- \qquad (5.3)$$

Note that the reaction via the intermediate formation of N_2O_4 with subsequent disproportionation is only one of the routes for the formation of NO^+ and NO_3^- species. The other routes for the formation of these species are well documented in the literature [86-90,180]

The disproportionation of NO and NO_2 leads to formation of N_2O_3 (Eq. (5.4)) [180].

$$NO + NO_2 \rightarrow N_2O_3 \qquad (5.4)$$

However, upon evacuation the weakly adsorbed $[NO^+][N_2O_4]$, NO^+, Fe^{3+}-NO, N_2O_4, N_2O_3 species are removed. In contrast, differently bound nitrato species (bands at 1633, 1620 and 1575 cm^{-1}) remain even after evacuation indicating the higher stability of these species. This is likely due to the involvement of oxygen species that are directly connected to the Fe sites. Furthermore, the band at 1575 cm^{-1} is missing on the bare H-ZSM-5 and increases with rising Fe content from sample A(ILIE)0.3 to A(CVD,W1,C5) via A(ILIE)1.2. This indicates that NO_3 species reflected by this band are preferably adsorbed on Fe species. The presence of traces of Fe might be responsible for the observed nitrate band around 1620 cm^{-1} on H-ZSM-5.

Adsorption of NO on reduced surface leads to different spectral features as compared to NO adsorption on oxidized surface (Figs. 4.32, 4.33, 4.34 and 4.35). Here, $[NO^+][N_2O_4]$, NO^+, Fe^{3+}-NO, N_2O_4, N_2O_3 species are almost completely absent and nitrato species are only weakly present. In contrast, the nitrito (1465 cm^{-1}) species are formed over cluster containing sample A(CVD,W1,C5). This indicates the strong suppression of oxidation, dimerization and disproportionation of NO and NO_2 reactions over reduced catalyst surface (Eqs. (2.3),(5.1)-(5.4)). Hence, the bands for nitrato species are only weakly present in A(CVD,W1,C0.5), A(ILIE)1.2 and A(MR). However, this is different over A(ILIE)0.3 as evidenced by the corresponding FT-IR bands in Fig. 4.34. This could be due to the possible contact of prereduced sample with air. Interestingly, the only sample with high iron content and with extensive iron oxide clusters (A(CVD,W1,C0.5)) shows nitrito species, at 1462 cm^{-1}, upon adsorption of NO over reduced surface. This may be due to the differently linked NO or NO_2 species to reduced iron species, presumably to reduced iron oxide clusters. However, it has to be taken into account that the severity of the reductive pretreatment for FT-IR measurements was only moderate (NH_3/He at 673 K for 1 h) as compared for in situ UV/VIS and EPR (NH_3/He or H_2/He at 773 K for 1 h). In situ UV/VIS and EPR experiments revealed that even after 1 h at 773 K in NH_3/He or H_2/He flow no complete reduction of Fe^{3+} was possible (Figs. 4.10, 4.37 and 4.39). Nevertheless, the drop in band intensities in the in situ FT-IR spectra after reductive pretreatment is obvious. This suggests that, in the SCR reaction, trivalent Fe species are preferred as active sites in comparison to Fe^{2+} ions due to their ability to activate/oxidize NO to the corresponding NO_2 or NO_3. In agreement, it has been reported that reaction between NO and activated reductant (NH_3 or isobutane) is almost negligible [37,46]. The activation of the reductant proceeds via surface acidity of the zeolite [37,46,49,162]. In contrast, oxidized NO (NO_2 or NO_3) readily reacts with activated reductants to form N_2. Thus, it can be proposed that Fe^{3+} sites and acidity of the zeolite is essential for SCR of NO by NH_3 and isobutane. The possible reaction between activated NO and reductants proceeds similarly as that described earlier in section 2.1.1 (Eqs. (2.1)-(2.10)).

5.2.2 SCR of NO with NH_3 and isobutane

Relation between structure of Fe sites and catalytic performance in SCR of NO

Ex situ UV/VIS-DRS and EPR results show that the series of ILIE samples comprises both samples with only isolated Fe sites (A(ILIE)0.2 and A(ILIE)0.3) as well as samples that are characterized by an increasing amount of additional Fe_xO_y clusters (A(ILIE)1.2) (Table 4.1).

Therefore, it is possible to investigate the catalytic role of isolated Fe^{3+} sites discretely and iron oxide clusters, however, along with isolated Fe sites, by comparing the catalytic activity of these samples.

In NH_3-SCR, activity increases with increasing amount of isolated Fe sites in samples A(ILIE)0.2 to A(ILIE)0.3 (Fig. 4.55), which contain almost exclusively isolated Fe sites (Table 4.1). This indicates the participation of isolated sites in the catalytic reaction. Accordingly, A(MR)0.5 with mainly isolated Fe sites showed similar catalytic behaviour as sample A(ILIE)0.3. However, the dramatic increase of the concentration of oligomeric sites from A(ILIE)0.3 to A(ILIE)0.6 improves the activity much more than the gradual growth of the isolated site concentration (Table 4.1 and Fig. 4.55). This suggests a remarkable contribution of the oligomers to the SCR of NO with NH_3. This is further supported by correlating the percentage of different Fe sites (isolated, oligomers and particles) as derived by UV/VIS-DRS (Table 4.1) and first order rate constants of the SCR reaction [64]. Fig. 5.1 shows the results for different correlation attempts for NH_3-SCR at 523 K, which is well below the conversion maximum.

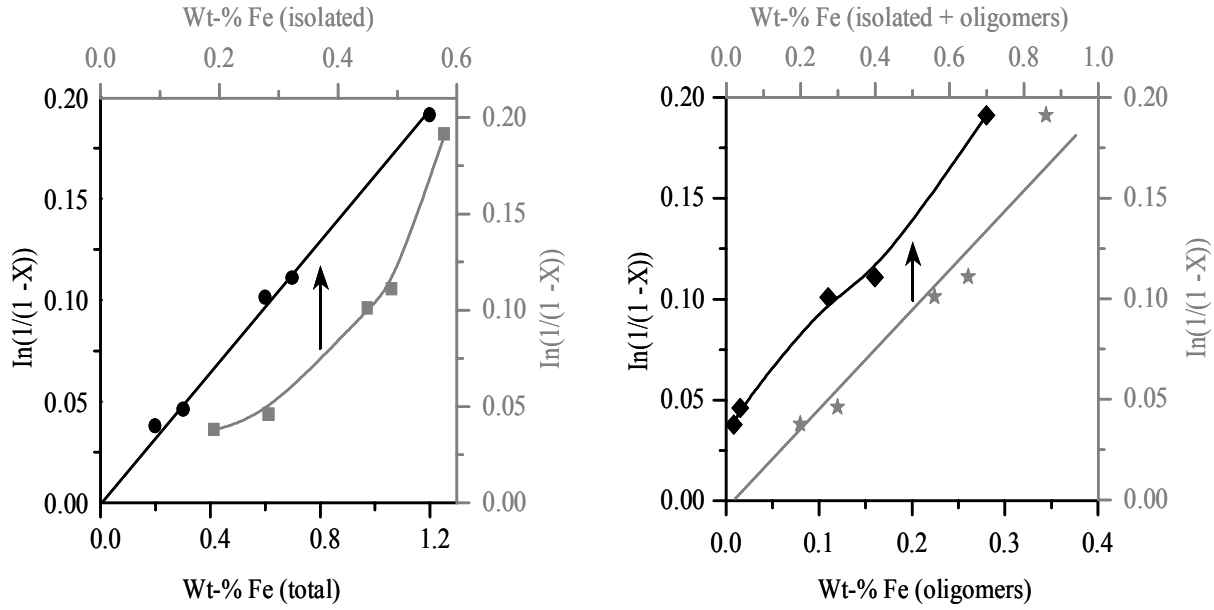

Fig. 5.1. Correlation of SCR rates (first order rate constants) with the concentration of different Fe species detected by UV/VIS-DRS (Table 4.1) [64].

It is clear from Fig. 5.1 that the rate constants do not correlate neither with the amount of isolated Fe sites nor with the amount of Fe_xO_y oligomers alone. There is a much better correlation with the percentage of both isolated and oligomeric Fe sites. However, the best correlation is obtained with the total Fe content. This suggests that all accessible Fe sites including, besides isolated and low oligomeric Fe, also Fe sites on the surface of oxidic particles participate in selective reduction at temperatures below 700 K (Fig. 4.55). At higher temperatures (T > 700 K) NO conversion was observed to level off or even to drop down for those samples that are characterized by a remarkable percentage of oxidic clusters (Fig. 4.55,

sample A(CVD,W1,C5)). Since this undesired behavior is not observed for Fe samples free of clusters, it suggests that Fe_xO_y agglomerates play a detrimental role at high temperatures by favoring the total oxidation of the NH_3 reductant which is then no longer available for the SCR of NO. Differently, isolated Fe^{3+} species of different coordination are efficient for reducing NO in a whole range of temperature as evidenced by the catalytic behavior of cluster free samples (Fig. 4.55). However, these Fe species behave differently under steady-state SCR conditions as evidenced by in situ UV/VIS and in situ EPR studies. Thus, it was found that in cluster free samples, octahedral Fe^{3+} sites reflected by EPR signal around g' ≈ 6 and UV/VIS band around 290 nm are more sensitive to reduction. In comparison, tetrahedral Fe^{3+} sites shown by EPR signal at g' ≈ 4.3 and a UV/VIS band around 230 nm are less sensitive. Differently, Fe^{3+} sites reflected by EPR signal at g' ≈ 2, for which coordination state cannot be simply specified, are hardly reduced. The amount of these Fe species preferably increases with rising Fe content from sample A(ILIE)0.3 to A(ILIE)1.2 as evidenced by a comparison of the UV/VIS spectral intensities below 300 nm under steady-state SCR conditions (Figs. 4.38 and 4.40). On the other hand, in situ FT-IR results show preferential reaction of NO with Fe^{3+} to form oxidized products which are important intermediates in the SCR reaction (Fig. 4.32). Based on these considerations it can be concluded that among isolated Fe sites, the hardly reducible Fe sites are the active sites for SCR of NO. In agreement, the NO conversion increases with increasing the amount of hardly reducible Fe sites from samples A(ILIE)0.2 to A(ILIE)1.2 (Fig. 4.55).

By comparing the isobutane-SCR activity data of A(ILIE)0.2 and A(ILIE)0.3 the participation of isolated sites in the reaction is obvious (Fig. 4.56). In particular, A(ILIE)0.3, which does not contain particles and only a very small amount of oligomers, shows even the highest NO conversions in a broad temperature range. Apparently, particles can be therefore safely rejected as active sites which is in agreement with observations made earlier by other research groups [36,86]. At the same time the extremely low quantity of oligomers (more than an order of magnitude less than in the cluster-containing catalysts such as A(ILIE)1.2) strongly discourages an assignment of the catalytic activity exclusively to oligomers. The data imply rather that mononuclear Fe species govern the activity in SCR catalysis, probably together with a certain contribution of oligomeric entities. This is also suggested by a correlation of the SCR rate with the concentration of different Fe species (Fig. 5.2). It is clear from this figure that the rate constant correlates best with the sum of the iron in isolated and oligomeric sites, whereas there is no proportionality with the concentration of the oligomeric sites alone. Therefore, a major contribution of the isolated Fe sites can be identified. The correlation of the rate constant with the concentration of isolated sites yields a bent curve, which implies the participation of a second type of Fe site, the oligomers. Apparently, the surface of the particles does not contribute to the SCR reaction as evidenced by the correlation of the rate constants with the total Fe content, which does not go through the origin. The increase of the concentration of oligomeric sites from A(ILIE)0.3 to A(ILIE)1.2 (Table 4.1) enhances the activity below 600 K but above this temperature NO conversion drastically deteriorates (Fig. 4.56). This suggests that oligomeric sites, which are present in highly oxidized state under typical SCR conditions as evidenced by in situ spectroscopic studies (section 4.3.2), do contribute to SCR reaction below 600 K but above this temperature they promote the unselective total oxidation of isobutane.

This tendency has been observed, too, for NH_3-SCR. However, it is much more pronounced for isobutane-SCR.

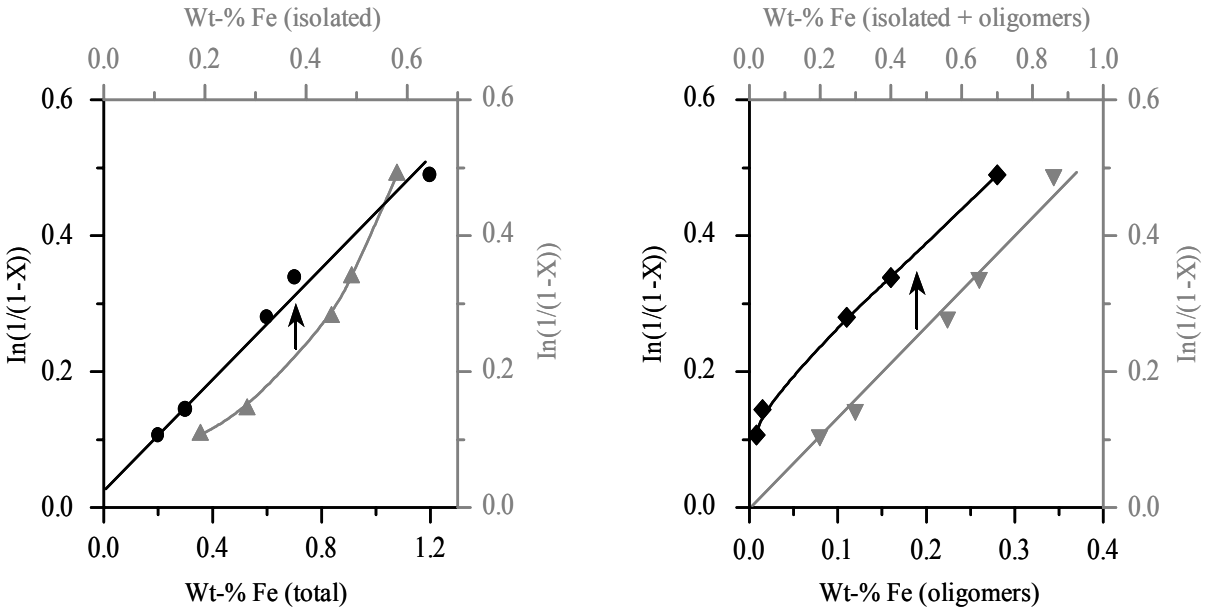

Fig. 5.2. Correlation of SCR rates (first order rate constants) with the concentration of different Fe species detected by UV/VIS-DRS (Table 3) [64].

In summary, hardly reducible isolated Fe sites reflected by EPR signals at g' ≈ 2 and partly also by g' ≈ 4.3 are the active Fe sites for both the SCR reactions. Whereas, easily reducible isolated Fe sites reflected by the signal at g' ≈ 6 are already reduced at 623 K under typical SCR conditions as evidenced by in situ EPR. Therefore, it cannot be excluded that these sites are only spectator species at and/or above 623 K. Consequently, the role of isolated Fe sites in the SCR may increase in the following order: g' ≈ 6 < g' ≈ 4.3 < g' ≈ 2. Oligomers including dimers are also active sites for both SCR reactions, in particular for NH_3-SCR. However, these species are only selective at lower temperatures but at higher temperatures they are unselective and contribute to total oxidation of the reductant, which is much more pronounced for isobutane than for NH_3. Therefore, for isobutane-SCR clustered-type active sites are not essential and must be avoided, while these species play, to a certain extent, a constructive role in NH_3-SCR.

Influence of the acidity on the SCR of NO

The role of acidity on the SCR of NO either by NH_3 or by isobutane is not much studied. Hence, in this work an effort is made to shed some light on this aspect as well [161,162]. For this purpose, the catalytic behavior of samples *ex*-Fe-silicalite, A(ILIE)0.2, A(ILIE)0.3, A(ILIE)1.2 and B(CVD,W1,C5) was compared. Samples *ex*-Fe-silicalite, A(ILIE)0.2 and A(ILIE)0.3 contain almost exclusively isolated Fe sites, while A(ILIE)1.2 and B(CVD,W1,C5) are dominated by clusters (Table 4.1). However, framework composition of the samples is different (Table 3.1). *Ex*-Fe-silicalite does not contain any Al in the framework whereas B(CVD,W1,C5) is prepared with silica rich matrix H-ZSM-5(B) (Si/Al ≈ 40). Accordingly, *ex*-

Fe-silicalite shows very poor acidity as evidenced by FT-IR of pyridine adsorption (Fig. 4.30 and Table 4.3). As expected, B(CVD,W1,C5) contains a very low Brønsted acidity but considerable amount of Lewis acidity. The latter acidity is mainly due to the presence of iron oxide clusters in the sample as concluded in the results section (Fig. 4.28 and Table 4.3). Samples A(ILIE)0.2 and A(ILIE)1.2 with Si/Al ≈ 14 show much higher acidity (Fig. 4.29. Although the acidity was measured for sample A(ILIE)0.2, the same acidity can be expected for A(ILIE)0.3 since both the samples contain similar Si/Al ratio (14) and show similar nature and distribution of Fe species (section 4.1).

In both NH_3- and isobutane-SCR, in spite of lower amount of isolated Fe entities with respect to the iron content (Table 4.1), A(ILIE)0.2 and A(ILIE)0.3 exhibit the highest activity. Contrarily, *ex*-Fe-silicalite, which contains a higher amount of isolated Fe sites than the most active A(ILIE)0.3 (Table 4.1), shows a very poor activity in both SCR reactions (Fig. 4.55 and 4.57). This strongly indicates that the presence of Fe sites in high dispersion is not a sufficient criterion for high activity. Definitely, acidic sites are inevitable as well. Additionally, by comparing the catalytic behavior of B(CVD,W1,C5) and A(ILIE)1.2, which both contain heterogeneous distribution of Fe sites, the importance of Brønsted and Lewis acidity even in the presence of active sites of the isolated and clustered-type for the SCR is discussed. Despite containing double the amount of Fe content (Table 3.1) as compared to A(ILIE)1.2, B(CVD,W1,C5) shows moderate activity in NH_3-SCR while it completely failed in isobutane-SCR. This suggests that the presence of clusters, which can also act as Lewis sites, compensates the low Brønsted acidity to some extent in NH_3-SCR but this is not the case in isobutane-SCR. However, the observed NH_3-SCR activity for sample B(CVD,W1,C5) is still markedly lower than that of A(ILIE)1.2 despite the higher Fe content of the former due to the absence of sufficient acidity.

In summary, on the basis of these observations it can be concluded that for both NH_3- and isobutane-SCR, acidity (Brønsted and Lewis acidity) is compulsory even in the presence of active sites of isolated and clustered-type. Since, acidic sites are required for the activation of reductants which can only then further react with NO_x ($x > 2$) and NO to form N_2.

Influence of the pore structure on the SCR of NO

The influence of the pore structure on the SCR of NO is evident by comparing the behavior of *ex*-Fe-silicalite and (Fe-SBA-I)0.95. These two catalysts have comparable Fe contents, comprise almost exclusively isolated Fe sites and show almost no acidity (section 4.1 and 4.2). Due to this low acidity, both catalysts are much less active than ZSM-5 based materials (Fig. 4.55 and 4.57). Nevertheless, a clear difference is seen that reveals higher catalytic activity for *ex*-Fe-silicalite than (Fe-SBA-I)0.95. This is line with the earlier studies on this topic which revealed that open mesoporous framework structures such as SBA-15 are less favorable for the SCR of NO as compared to microporous structures like MFI [158]. Therefore, it is reasonable to conclude that the mesoporous structure such like SBA-15 is not favorable for this reaction. In contrast, the unique pore structure of the MFI is certainly an additional asset for this reaction.

On the basis of the above discussion and observations, an uniform concept for tailoring new Fe-ZSM-5 zeolites for SCR of NO can be drawn. The increase in the concentration of clustered sites from samples A(ILIE)0.2 and A(ILIE)0.3 to samples A(ILIE)0.7, A(ILIE)1.2 and CVD leads to a continuous deterioration of the catalytic behavior in isobutane-SCR at temperatures above 600 K (Fig. 4.56). The bridging oxygen, be it in binuclear complexes as favored by [31,56,57] or in oligomers of a wide range of nuclearities as suggested in [36], probably participates in the SCR at low temperatures. However, at high temperatures, it tends to attack the reductant unselectively leading to its total oxidation. This can be easily understood from reduction/reoxidation kinetic measurements of A(ILIE)0.3 and A(ILIE)1.2 (see section 4.1.1) which show that iron oxide clusters are hardly reduced but fastly reoxidized. In agreement with these results, in situ spectroscopic studies (sections 4.3.1 and 4.3.2) show that iron oxide clusters are essentially in +3 oxidation state under typical SCR conditions which has a higher oxidation potential than reduced Fe valence state. Therefore, on the basis of these experimental evidences it is reasonable to ascribe the unselective total oxidation of isobutane to iron oxide clusters.

In NH_3-SCR, the same trend can be seen, however at much higher temperatures. With the catalysts containing almost exclusively isolated sites, unselective NH_3 oxidation cannot be detected up to 873 K. With increasing content of clustered sites, the NO conversion starts to level off under more and more moderate conditions (Fig. 4.55). In situ spectroscopic studies show that under SCR conditions the iron sites are much less reduced in NH_3-SCR than in isobutane-SCR feed. Furthermore, studies of subsequent interaction of isobutane or NH_3 and NO with Fe-zeolites show that Fe species are stronger reduced by isobutane than by NH_3 as clearly evidenced by in situ EPR spectroscopy (sections 4.3.1 and 4.3.2). These results indicate that NH_3 is not as easily oxidized than isobutane. This could explain why clustered sites play a rather constructive role in NH_3-SCR but not in isobutane-SCR.

The above observations form the basis for optimization strategies for Fe-ZSM-5 in these reactions. For isobutane-SCR, the concentration of isolated sites has to be increased avoiding clustered sites. For NH_3-SCR, a high dispersion of iron should be sought as well to increase the number of accessible Fe sites. However, in contrast to isobutane-SCR, these sites may be part of low oligomeric clusters, too. Acidity is essential for both SCR reactions to activate the reductant.

5.2.3 Decomposition and SCR of N_2O with CO

For this study, differently prepared Fe-catalysts (*ex*-Fe-silicalite, *ex*-Fe-ZSM-5, A'(CVD,W1,C2), Fe-ZSM-5(LIE)1.4, A(ILIE)0.2, A(ILIE)1.2 and (Fe-SBA-I)0.95) with different framework composition, nature and distribution of Fe sites and pore structures have been used to investigate the role of these properties on the decomposition and SCR of N_2O. The nature and distribution of Fe species in these materials strongly depend on the framework composition and preparation route as evidenced by UV/VIS-DRS and EPR (section 4.1).

In direct N_2O decomposition, O_2 desorption is the rate-determining step, which can be accelerated at a high temperature, in the presence of NO [41], and also by addition of reductants. Interestingly, in spite of containing similar Fe content *ex*-Fe-ZSM-5 and *ex*-Fe-silicalite show significant differences in the activity of N_2O decomposition. This is attributed to the distinct Fe constitution in the samples and, thus, *ex*-Fe-ZSM-5 with extensive clusters was found to be a more effective catalyst than *ex*-Fe-silicalite with exclusively isolated Fe sites [96,155]. In this case, the isolated nature of iron in *ex*-Fe-silicalite makes the recombination of N_2O deposited oxygen (O*), which is the rate-determining step, difficult according to Eq. 2.13, even though the rate of Eq. 2.11 is higher than over *ex*-Fe-ZSM-5 [58]. Differently, the oligomeric Fe sites facilitate the recombination of O* due to the presence of Fe ions in a closer vicinity. In agreement with this, A'(CVD,W1,C2) which contains both isolated and oligomeric Fe sites in a larger quantity than the former two samples (Table 4.1) shows the best activity.

In the SCR of N_2O, CO efficiently removes atomic oxygen from the catalyst surface and leads to a substantially decreased operation temperature with respect to the direct N_2O decomposition. The reaction of N_2O with CO is stoichiometric as shown by Eq. 4.4 and the N_2O conversion increases linearly with the molar feed CO/N_2O ratio (Fig. 4.60) [58].

The remarkably uniform distribution of iron in *ex*-Fe-silicalite as isolated Fe ions connected to its high catalyst activity is a strong indication of the importance of mononuclear iron ions in the reduction of N_2O with CO. Fig. 5.3 shows the derived correlation between the relative fraction of isolated Fe sites estimated from the relative intensity of the UV/VIS-DRS subbands below 300 nm (Table 4.1) and the relative N_2O conversion derived from the catalytic activity at 600 K.

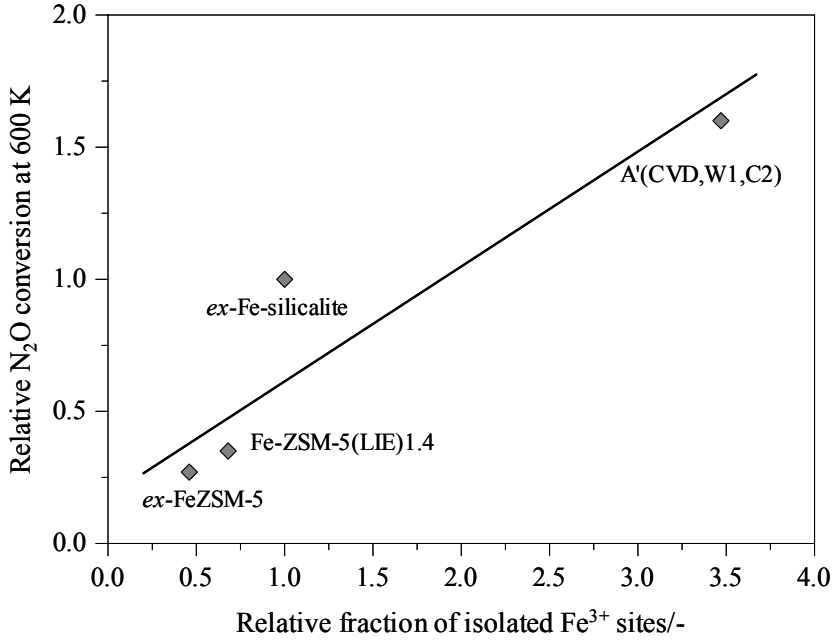

Fig. 5.3. Correlation between the relative N_2O conversion at 600 K (CO/N_2O=1 and W/F (N_2O) = 9 X 10^5 g s mol^{-1}) and the relative fraction of isolated Fe^{3+} sites (from Table 4.1) in the Fe-MFI zeolites investigates. Values are referred to ex-Fe-silicalite [58].

The N_2O conversion and the percentage of isolated Fe^{3+} sites of the catalysts (normalized to the values of *ex*-Fe-silicalite) follow the sequence:

$$A'(CVD,W1,C2) > ex\text{-Fe-silicalite} > ex\text{-Fe-ZSM-5} \approx \text{Fe-ZSM-5(LIE)1.4}$$

The poor catalytic performance of Fe-ZSM-5(LIE)1.4 and *ex*-Fe-ZSM-5 is due to the formation of iron oxide particles which render the majority of Fe sites inaccessible and, thus, inactive. Iron clustering also occurs in the catalyst prepared by sublimation (A'(CVD,W1,C2)), but the high iron content together with a relatively high fraction of iron in intrazeolitic positions makes it the most active formulation in terms of absolute N_2O conversions. The activity of *ex*-Fe-ZSM-5 is largely reduced compared to *ex*-Fe-silicalite, which correlates with the decreased concentration of isolated iron species due to clustering in the former sample.

Finally, it should be noted that the correlation in Fig. 5.3 assumes that all isolated sites in the steam-activated samples are in extraframework positions. This is the case for *ex*-Fe-ZSM-5, as concluded in [154,155]. For *ex*-Fe-silicalite, a certain (small) fraction of redox inactive framework iron cannot be excluded. This fraction was not quantified here, since framework and extraframework species cannot be discriminated in UV/VIS-DRS. In rigorous terms, the fraction of remaining framework iron in *ex*-Fe-silicalite should be subtracted from the total fraction of isolated sites in Fig. 5.3, since Fe^{3+} ions in tetrahedral framework positions do not contribute to the catalytic activity [188].

However, the participation of cluster species in the SCR of N_2O cannot be excluded. In situ UV/VIS-DRS and EPR spectroscopic studies revealed important differences in the redox behaviour of the iron species in the catalysts upon interaction with O_2, N_2O, and CO, suggesting that both isolated Fe^{3+} sites as well as oligonuclear $Fe^{3+}{}_xO_y$ species are active in the reaction of N_2O with CO at 623 K. The reaction mechanism associated with these species differs substantially. In situ UV/VIS-DRS analyses have clearly shown that Fe^{3+} in oligonuclear $Fe^{3+}{}_xO_y$ clusters can be preferably reduced by CO and can be completely reoxidized by N_2O. In combination with EPR results, it can be proposed that the reduction of N_2O with CO over these sites occurs according to Eqs. (5.5) and (5.6), i.e., via intermediate formation of O^- radicals. This mechanism agrees with the classical hypothesis stating that CO purely acts as an O-scavenger leading to CO_2 (Eq. 5.5) and regenerating the active site (□) for subsequent N_2O activation [96,117,118].

$$Fe^{3+}–O–Fe^{3+} + CO \rightarrow Fe^{2+}–□–Fe^{2+} + CO_2 \quad (5.5)$$

$$Fe^{2+}–□–Fe^{2+} + N_2O \rightarrow Fe^{3+}–O^-–Fe^{3+} + N_2 \quad (5.6)$$

Differently, the (dominant) tetrahedral isolated Fe^{3+} ions in extraframework positions of *ex*-Fe-silicalite suffer no reduction by CO at 623 K (Fig. 4.48). The relatively weak interaction between CO and iron ions is commonly accepted [62]. However, the changes of the local symmetry and altered position of the signals in the EPR spectra suggest that CO coordinates to ferric ions in *ex*-Fe-silicalite.

Attending to these results, the mechanism represented by Eqs. (5.7) and (5.8) can be proposed for the N_2O reduction with CO over tetrahedral isolated Fe sites.

$$Fe^{3+}–□ + CO \rightarrow Fe^{3+}–CO \quad (5.7)$$

$$Fe^{3+}–CO + N_2O \rightarrow Fe^{3+}–□ + N_2 + CO_2 \quad (5.8)$$

This mechanism implies that the involved isolated Fe species must be coordinatively unsaturated in order to chemisorb CO. This holds for species associated with the $g' \approx 2$ as well as the $g' > 5$ signals in *ex*-Fe-silicalite (Fig. 4.48). The observations related to the latter group of signals are in excellent agreement with various EPR studies, where the reactivity of the EPR signals around $g' \approx 6$ is elaborated. Kucherov et al. [59] determined by in situ EPR that the signals at $g' \approx 5.6$ and 6.5 observed in Fe-ZSM-5 catalysts prepared by sublimation disappear upon contact with NO or NO_2. The corresponding signals were assigned to very reactive coordinatively unsaturated Fe^{3+} species. Volodin et al. [189] also attributed the disappearance of this line (in vacuum and in the presence of H_2O and NO) as an indication for the reactivity of an ion-exchanged Fe-ZSM-5 with N_2O. Ribera et al. [60] found that the signals at $g' \approx 6.4$ and 5.7 in steam-activated Fe-ZSM-5 disappear upon addition of β-mercaptoethanol, concluding their participation in redox processes. In a recent study, Kubánek et al. [190] have correlated the intensity of the signals at $g' \approx 6.0$ and 5.6 and the activity of H-ZSM-5 zeolites with low Fe concentrations in the oxidation of benzene to phenol with N_2O. These signals were assigned to distorted T_d-coordinated isolated ions with a complex oxo-structure in cationic sites.

In agreement with this discussion, A(ILIE)0.2 which contains almost exclusively isolated Fe sites shows similar behavior to that of *ex*-Fe-silicalite. Furthermore, with increasing amount of isolated and oligomeric sites in the A(ILIE)1.2 the activity increases considerably than the former two samples. This confirms that isolated Fe sites are determining the SCR activity. However, besides isolated Fe sites oligomeric sites are also participating in the reaction.

In conclusion, isolated Fe sites and oligomeric sites are active Fe centers for both decomposition and SCR of N_2O. However, the isolated Fe sites are more effective in the latter reaction. Differently, oligomeric Fe sites are more active in the decomposition due to the easier oxygen recombination over these species, which is the rate-determining step. However, these two types of active Fe sites involve differently in the SCR of N_2O. Coordinatively unsaturated isolated Fe sites coordinate the CO without being reduced. The reaction over oligomeric sites proceeds via a redox Fe^{3+}/Fe^{2+} process probably via intermediate formation of O^- radicals.

Influence of the acidity on the decomposition and SCR of N_2O

To study the role of acidity on these reactions the catalytic performance of *ex*-Fe-silicalite, A(ILIE)0.2, A'(CVD,W1,C2) and *ex*-Fe-ZSM-5 is compared. *Ex*-Fe-silicalite does not contain any lattice Al sites and thus a weak surface acidity was measured by FT-IR

spectroscopy (Fig. 4.30). A(ILIE)0.2 with Si/Al ≈ 14 shows markedly higher acidity (Fig. 4.29). Although the acidity was not measured for A'(CVD,W1,C2) and *ex*-Fe-ZSM-5, similar acidity can be expected as observed for A(CVD,W1,C5) and *ex*-Fe-beta respectively (Table 4.3 and Figs. 4.28, 4.30). Since, A'(CVD,W1,C2) and *ex*-Fe-ZSM-5 contain similar Si/Al ratio, Fe content and nature and distribution of Fe sites as that of A(CVD,W1,C5) and *ex*-Fe-beta respectively (section 4.1). Accordingly, A'(CVD,W1,C2) should contain much higher acidity than *ex*-Fe-ZSM-5. In spite of containing roughly ten times lower Fe content, *ex*-Fe-ZSM-5 shows comparable activity in direct N_2O decomposition to that of A'(CVD,W1,C2) (Fig. 4.58). In SCR of N_2O with CO, *ex*-Fe-silicalite shows similar activity to that of A(ILIE)0.2 (Fig. 4.61). Thus, it is clear that the surface acidity of the catalyst is not essential for these reactions.

Influence of the pore structure on the decomposition and SCR of N_2O

The effect of micro and mesoporous framework structure on the catalytic N_2O decomposition and N_2O reduction with CO has been nicely illustrated by the performance of *ex*-Fe-silicalite and (Fe-SBA-I)0.95. From UV/VIS-DRS and EPR characterization results it is evident that content and nature of iron sites in the two catalysts are very similar (section 4.1). Both *ex*-Fe-silicalite and (Fe-SBA-I)0.95 contain almost exclusively isolated Fe^{3+} sites of very similar structure but differ markedly in their pore structure. While *ex*-Fe-silicalite is characterized by the well known MFI structure consisting of intersecting straight and sinusoidal channels of 0.55 nm, the structure of (Fe-SBA-I)0.95 is dominated by parallel linear pores, the diameter of which is more than ten times as large as in *ex*-Fe-silicalite [161]. *Ex*-Fe-silicalite revealed to be much more active than (Fe-SBA-I)0.95 in both direct N_2O decomposition and N_2O reduction with CO. This is certainly due to the difference in the pore structure. Obviously, the large pores in (Fe-SBA-I)0.95 do not support an intimate contact between active iron sites and reactant molecules, most of the latter passing the pore system of (Fe-SBA-I)0.95 without approaching active sites and, consequently, give rise to low activity. Furthermore, *ex*-Fe-ZSM-5 and *ex*-Fe-beta with similar Fe content, nature and distribution of iron sites and pore structure (section 4.1) exhibit similar activity in both SCR and direct decomposition of N_2O (not shown) as reported elsewhere [159]. Therefore, it can be concluded that the micropore structure like MFI is favorable for these reactions since it facilitates intimate contact between active Fe sites and reactants.

Optimization strategies for preparing Fe-MFI zeolites for decomposition and SCR of N_2O

On the basis of these results it is possible to draw an unified concept for the behaviour of Fe-zeolites in both reactions. The high specific activity of *ex*-Fe-silicalite, with a remarkable uniform distribution of isolated iron ions, is essential to conclude the importance of mononuclear iron ions in the reduction of N_2O by CO. In agreement, in situ UV/VIS-DRS and in situ EPR studies evidenced the participation of isolated Fe sites in the reaction, however, they also support the involvement of oligomeric Fe sites (section 4.3.3).

In direct N_2O decomposition, samples A'(CVD,W1,C2) and *ex*-Fe-ZSM-5 which are dominated by oligomeric clusters show higher activity than *ex*-Fe-silicalite. It indicates the preference of bridging oxygens, be it in binuclear complexes or in oligomers of a wide range

of nuclearities, over isolated iron ions in the reaction. This is obviously due to the easier oxygen recombination, which is the rate-determining step in the reaction, of two iron centers that are close together. On the basis of the poor performance of Fe-ZSM-5(LIE)1.4 with extensive clustering, mainly large iron oxide particles, particles can be safely rejected as active sites in SCR and direct decomposition of N_2O.

The results are evidence for the requirement of quite different optimization strategies for the tailoring of Fe-MFI zeolites for these two reactions. For the reduction of N_2O with a reducing agent, the concentration of extraframework isolated iron ions has to be increased avoiding clustered sites as concluded for isobutane-SCR of NO. For N_2O decomposition, a high dispersion of iron should be required as well but along with small oligomeric iron oxide clusters. This is a similar strategy as concluded for NH_3-SCR of NO. Finally, the acidity is not mandatory for both reduction and direct decomposition of N_2O.

6. Conclusions

In this study, Fe-zeolites prepared by different techniques (CVD, SSIE, MR, LIE, ILIE, hydrothermal synthesis followed by steam activation and incipient wetness impregnation) using different framework compositions and structures and different pretreatment strategies have been used to probe their influence on the nature and distribution of Fe species. To this end, these samples have been characterized by EPR and UV/VIS-DRS-ex situ (after preparation, after calcination, after use in the selective catalytic reduction of NO) and in situ (during calcination and interaction of feed components with Fe sites of the catalysts at 293 K and at typical SCR temperature (623 K)). Iron redox kinetics of different isolated Fe^{3+} species and $Fe^{3+}{}_xO_y$ clusters have been studied by UV/VIS-DRS to evaluate the impact of redox properties of different Fe species on the SCR of NO and N_2O as well as on the decomposition of N_2O. Acidity of selected Fe-zeolites was analyzed by FT-IR of pyridine adsorption. This information has been used to study the role of acidity on the SCR of NO either by NH_3 or by isobutane and SCR of N_2O with CO as well as N_2O decomposition. In situ FT-IR was also used to investigate the surface species formed during the adsorption of NO on oxidized and reduced surfaces at 293 K as well as during isobutane-SCR of NO at 623 K. It has been found that combined EPR and UV/VIS-DRS techniques are effective tools for elucidating the nature of coexisting Fe species formed in the Fe-containing catalysts investigated. The results have been discussed in relation to the catalytic performance. In this section, the main conclusions for structure-reactivity relationships will be summarized.

Structure, distribution and redox behaviour of Fe species

In the studied Fe-zeolites, at least three different isolated sites have been identified by EPR spectroscopy, which have been assigned to Fe^{3+} in tetrahedral ($g' \approx 4.3$) and higher coordination ($g' \approx 6$), and to Fe^{3+} in a highly symmetric environment ($g' \approx 2$). The latter has been separately observed only in the samples A(MR)0.5, A(ILIE)0.2, A(ILIE)0.3, *ex*-Fe-silicalite, *c*-Fe-beta, (Fe-SBA-I)0.95. In the remaining samples (CVD, SSIE, *ex*-Fe-ZSM-5, *ex*-Fe-beta) an intense signal of aggregated iron oxide species is superimposed at the same g' value of 2. UV/VIS-DRS differentiates between isolated Fe^{3+} sites of different coordination, small (oligomeric) Fe oxide clusters and large Fe oxide aggregates. The degree of aggregation and the magnetic ordering of the aggregates were studied by temperature-dependent EPR measurements. Based on these results, the following conclusions could be derived:

All Fe-MFI preparations (including MR, ILIE and hydrothermal synthesis followed by steam activation) lead to the coexistence of different iron species. In all cases, isolated Fe sites are found. They are predominant after the MR, ILIE and hydrothermal synthesis (only in Al free silicalite) followed by steam activation while, in the other preparations, they are formed together with Fe_xO_y clusters of different size.

In the CVD preparation, clustered species occur already after the washing step, but their quantity and size increase strongly during calcination, with low heating rates resulting in higher Fe dispersions. Intense washing of the material after the CVD step also favors higher Fe dispersion but does not prevent clustering. With a matrix of low Al content and low density

of Brønsted sites but high defect density, clusters are preferentially created in both uncalcined and calcined samples. However, the cluster size is somewhat restricted in the calcined sample as compared to samples with a matrix containing high Al content and low defect density, probably due to the internal defects providing additional aggregation nuclei. By the SSIE technique, clustered species are formed already during the preparation and their quantity and size increase even more after calcination. Remarkably, the MR preparation method leads to formation of mainly isolated Fe^{3+} species and iron association is largely suppressed even after calcination. Similarly, the ILIE method favours high Fe dispersion for low Fe content (≤ 0.3 wt.%) for which Fe is mainly in the form of mononuclear Fe sites. With increasing Fe content from 0.3 to 1.2 wt.% formation of isolated Fe sites level off at a certain Fe content, after which oligomeric iron-oxo species and poorly ordered iron oxide aggregates are formed. Contrarily, the conventional LIE method favours the formation of iron oxide clusters of different size, particularly the larger ones already at rather low Fe content (Table 4.1).

Samples with desired framework composition can be prepared using hydrothermal synthesis and framework cations can be extracted to extraframework positions by steam activation. Framework Fe^{3+} species either in the MFI or in the beta are well shielded in the zeolite framework and are not reducible upon reductive treatment with H_2 (Fig. 4.10). The presence of Al in the zeolite framework destabilizes framework iron and promotes extraction and clustering of extraframework iron to oxide clusters upon steaming or even after calcination to some extent. Accordingly, Al free *ex*-Fe-silicalite shows almost exclusively isolated Fe^{3+} ions even after steam activation and iron association is largely prevented. Al containing *ex*-Fe-ZSM-5 and *ex*-Fe-beta with relatively low Fe content show extensive degree of iron clustering in the form of oligomers and large iron oxide particles (Table 4.1).

The very high surface area of mesoporous silica supports such as SBA-15 favours the formation of highly dispersed, almost exclusively isolated Fe species upon incipient wetness preparation (Table 4.1).

In cluster free samples, extraframework isolated Fe^{+3} ions in tetrahedral and octahedral coordination possess different redox properties as evidenced by the time dependence of reduction and reoxidation at 673 K by UV/VIS-DRS (Table 4.2). The former species are slightly slower reduced and faster reoxidized than the latter. In contrast, iron oxide clusters are hardly reduced but fastly reoxidized in cluster containing samples. Interestingly, Fe^{3+} sites that remain isolated in samples dominated by Fe_xO_y clusters, change their redox behaviour and become highly reduction resistant in comparison to those in samples without oxide clusters. Additionally, isolated Fe sites reflected by EPR signals at $g' \approx 6$, $g' \approx 4.3$ and $g' \approx 2$ are easily, moderately and hardly reduced respectively, whereas the reoxidation takes place the other way around, i.e., hardly, moderately and easily respectively as evidenced by in situ EPR studies.

Acidic properties and the nature of adsorbed species

Brønsted acidity of the samples decreases with increasing Si/Al ratio as evidenced by FT-IR studies of adsorbed pyridine over catalysts with different Si/Al ratio (Table 4.3). It was also found that iron oxide clusters provide additional Lewis acidity.

In situ FT-IR spectroscopy revealed that adsorption of NO on the pre-oxidized surface of Fe-ZSM-5 zeolites forms mainly adsorbed nitrate species presumably on Fe sites. However, the adsorbed nitrate species are also found over H-ZSM-5(A) support which might proceed over Fe sites that are present as impurities and/or extraframework Al sites. The formation of N_2O_4 species was observed. Therefore, besides oxidation of NO by Fe species, the disproportionation reaction of N_2O_4 to NO^+ and NO_3^- was proposed as one of the reaction pathways for the formation of nitrates. This was further supported by the formation NO^+ (2134 cm^{-1}) and $[NO^+][N_2O_4]$ (2198 cm^{-1}) species. Differently, adsorption of NO on pre-reduced surface of Fe-ZSM-5 zeolites lowers the formation of nitrate species by oxidation as evidenced by the lower intensity of the respective FT-IR bands. This leads to formation of nitrito species on the cluster containing samples. Thus, it can be concluded that Fe^{3+} sites are essential for the oxidation/activation of NO species.

Active sites for SCR of NO with NH_3 and isobutane

Under typical NH_3 and isobutane-SCR conditions, the different isolated iron ions show a different sensitivity versus reduction/reoxidation. Accordingly, in cluster free samples (e.g., A(ILIE)0.3) isolated Fe^{3+} ions are partially reduced under steady-state SCR conditions, however, to different extents. Octahedral Fe^{3+} reflected by EPR signals around g' ≈ 6 and a UV/VIS band at 291 nm are most sensitive to reduction followed by tetrahedral Fe^{3+} (g' ≈ 4.3, 241 nm) while Fe^{3+} ions evidenced by the EPR signal at g' ≈ 2, for which the coordination geometry cannot be easily specified, are hardly reduced. With increasing Fe content, the amount of these hardly reducible isolated Fe^{3+} sites increases as evidenced by a comparison of the UV/VIS intensity below 300 nm under steady-state conditions. Regarding the relative intensities of the different EPR signals, it appears that hardly reducible sites comprise the majority of the isolated Fe species and are mainly reflected by the signal at g' ≈ 2. In contrast, easily reducible sites give rise to the line at g' ≈ 6 and partly also to the signal at g’ ≈ 4.3 and seem to be much less abundant. Taking account of the in situ FT-IR results that revealed a preferred reaction of NO with oxidized Fe^{3+} species, it is straightforward to conclude that, among the isolated Fe species, it might be just the hardly reducible Fe^{3+} ions which are essential for the oxidation of NO to form NO_2/NO_3 as intermediates for the reaction with the reductant. In contrast, Fe sites that are irreversibly reduced under SCR conditions do probably not belong to active sites. This is also supported by the fact that in used Fe-ZSM-5 catalysts the g' ≈ 6 signal disappeared completely, however, no deactivation was observed during the SCR reaction [55]. Since the amount of hardly reducible isolated Fe increases with rising Fe content, it is not surprising that the activity of the Fe-samples has been observed to increase, too (section 4.4).

However, attempts to correlate the rate of the SCR reaction with the number of Fe sites in the Fe-catalysts (Figs. 4.62 and 4.63) show the involvement of isolated Fe ions and oligonuclear Fe_xO_y clusters in both SCR reactions. Additionally, it was also found that in NH_3-SCR probably even Fe ions accessible on the surface of oxide particles also participate. In situ UV/VIS studies including those of the redox kinetics have shown that Fe_xO_y clusters are much faster reoxidized than isolated Fe sites and, thus, can immediately enter in another redox cycle.

It is therefore plausible to assume that they contribute to the selective catalytic process at lower reaction temperature, too. At higher temperature these agglomerates, due to their higher oxidation potential in comparison to isolated Fe^{3+} species, give rise to unselective total oxidation of the reductant, thus, limiting the temperature window of selective NO reduction. This effect is much more pronounced for isobutane-SCR since Fe_xO_y clusters oxidize the isobutane to CO_x already at temperatures as low as 623 K, whereas in NH_3-SCR they are selective up to temperatures of about 700 K. This is also evident from carbonyl-containing species detected by in situ FT-IR preferentially on cluster containing A(ILIE)1.2 but not on cluster free A(ILIE)0.2. These species are regarded as intermediates in the total oxidation of isobutane. As a result of this unselective oxidation behaviour of the Fe_xO_y agglomerates, the NO conversion drops dramatically above 600 K in case of isobutane. Hence, the catalyst performing best in this reaction (A(ILIE)0.3) is almost void of clusters. With the NH_3 reductant, the unselective attack occurs at much higher temperature and to a much lower extent. Thus, the limitation of the selective temperature region is of little practical importance. Hence, the best catalyst for NH_3-SCR was the one with the highest number of accessible Fe sites (A(ILIE)1.2).

The acidity of the zeolite is essential for both NH_3 and isobutane-SCR as evidenced by the catalytic performance of cluster free *ex*-Fe-silicalite and A(ILIE)0.3 and cluster containing B(CVD,W1,C5) and A(ILIE)1.2 (Figs. 4.55 and 4.57). In situ FT-IR studies show that isobutane-SCR of NO over Fe-ZSM-5 mainly proceeds via nitriles, cyanates and/or isocyanates. Interestingly, the formation of nitriles, cyanates and/or isocyanates seem to proceed preferentially on isolated Fe sites, the amount of which increases from sample A(ILIE)0.2 to A(ILIE)1.2 (Fig. 4.45). Therefore, it can be regarded as another reason for the superior catalytic performance of isolated Fe sites in the isobutane-SCR. Finally, the microporous MFI structure of the Fe-catalysts is much more favorable for the SCR of NO than the mesoporous SBA-15 structure, since the confined pore structure of the former favors the intimate contact between active Fe sites and reactants (Figs. 4.55 and 4.57).

The following preparation strategies are necessary for tailoring Fe-catalysts for isobutane- and NH_3-SCR. For the former reaction the Fe-ZSM-5 with mainly isolated Fe sites is desirable and the amount of Fe sites should be increased without imposing the formation of clusters. The same strategy applies also for designing Fe-ZSM-5 catalyst for NH_3-SCR, however, in the course of increasing the amount of isolated Fe sites the formation of highly dispersed oligomeric Fe sites may be acceptable to some extent. The rational catalyst for both SCR reactions is the one with strong Brønsted and Lewis acidity.

Active sites for Decomposition and SCR of N_2O with CO

By correlation of N_2O conversions in direct decomposition and SCR of N_2O with different iron species detected by UV/VIS-DRS it was found that in direct N_2O decomposition oligomers are preferred over isolated Fe^{3+} ions in view of the easier oxygen recombination (rate determining step in the process) of two iron centers that are close together. Hence, the best catalyst for the decomposition of N_2O was the one with high amount of oligomers, A'(CVD,W1,C2) (Fig. 4.58).

For SCR of N_2O by CO, isolated Fe^{3+} are the active iron centers. The importance of the mononuclear iron sites in the reduction of N_2O by CO was strongly evidenced by the high specific activity of A(ILIE)0.2 and *ex*-Fe-silicalite, with a remarkable uniform distribution of isolated iron ions. Furthermore, a correlation between the N_2O conversion and the fraction of isolated Fe^{3+} ions in the catalysts was found (Fig. 5.3). In situ UV/VIS-DRS and EPR studies further evidenced the participation of mononuclear iron ions in the SCR of N_2O with CO, however, they also support the involvement of oligomeric species. The interaction of N_2O and CO and the reaction mechanism is iron site dependent. Over tetrahedral isolated iron sites, which are coordinatively unsaturated and, thus, can extend their coordination sphere, the reduction of N_2O with CO occurs via coordinated CO species on Fe^{3+} ions, not involving change of oxidation state (Eqs. (5.7) and (5.8)). In contrast, octahedrally coordinated isolated Fe^{3+} sites convert N_2O in the presence of CO by involving a Fe^{3+}/Fe^{2+} redox process (Eqs. (5.5) and (5.6)). The reaction over oligomers proceeds, too, via a redox Fe^{3+}/Fe^{2+} process and involves the intermediate formation of O^{-} radicals.

The acidity of the zeolite has probably no effect on both the decomposition and SCR of N_2O as evidenced by the catalytic performance of *ex*-Fe-silicalite and A(ILIE)0.2 (Figs. 4.58, 4.60 and 4.61).

In contrast, pore structure of the Fe-catalyst strongly influences the catalytic activity as shown by *ex*-Fe-silicalite and (Fe-SBA-I)0.95 (Figs. 4.59 and 4.61). Thus, it was found that microporous structure such as MFI is more favorable than mesoporous material.

Finally, for tailoring Fe-MFI catalysts for SCR and direct decomposition of N_2O, the same strategies can be followed as drawn for isobutane and NH_3-SCR respectively. Thus, Fe-MFI catalysts for SCR of N_2O should contain mainly extraframework isolated Fe sites, while for decomposition highly dispersed oligomeric moieties are required.

7. References

1. S. N. Orlik., Theoretical and Experimental Chemistry 37 (2001) 135.
2. R. Q. Long and R. T. Yang., J. Am. Chem. Soc. 121 (1999) 5595.
3. L. Lietti, I. Nova and P. Forzatti., Topics in Catalysis 11/12 (2000) 111.
4. D. A. Peña, B. S. Uphade and P. G. Smirniotis., J. Catal. 221 (2004) 421.
5. H. Bosch, F. Janssen., Catal. Today 2 (1988) 369.
6. J. N. Armor., Catal. Today 26 (1995) 99.
7. R. W. van den Brink, S. Booneveld, J. R. Pels, D. F. Bakker, M. J. F. M. Verhaak., Appl. Catal. B. 32 (2001) 73.
8. Javier Pérez-Ramírez, F. Kapteijn, K. Schöffel, J. A. Moulijn., Appl. Catal. B. 44 (2003) 117.
9. M. D. Amiridis, T. Zhang, R. J. Farrauto., Appl. Catal. B. 10 (1996) 203.
10. Y. Traa, B. Burger, J. Weitkamp., Micropor. Mesopor. Mater. 30 (1999) 3.
11. M. S. Wain wright, N. R. Foster., Catal. Rev 19 (1979) 211.
12. A. Kato, S. Matsuda, F. Nakajima, M. Imanari, Y. Watanabe., J. Phys. Chem. 85 (1981) 1710.
13. M. A. Vuurman, I. E. Wachs, A. M. Hirt., J. Phys. Chem., 95 (1991) 9928.
14. L. Singoredjo, R. Korver, F. Kapteijn, J. A. Moulijn., Appl. Catal. B 1 (1992) 409.
15. G. Ramis, L. Yi, G. Busca, M. Turco, E. Kotur, R. J. Willey., J. Catal. 157 (1995) 523.
16. M. Yoshikawa, A. Yasutake, L. Mochida., Appl. Catal. A 173 (1998) 239.
17. M. Iwamoto, H. Furukawa, H. Kagawa., Stud. Surf. Sci. Catal. 28 (1986) 943.
18. H. Hamada, Y. Kintaichi, M. Sasaki, T. Ito, M. Tabata., Appl. Catal. 64 (1990) L1.
19. Y. Li, W. K. Hall., J. Catal. 129 (1991) 202.
20. Y. Li, J. N. Armor., J. Catal. 150 (1994) 356.
21. H. Hamada., Catal. Today 22 (1994) 21.
22. K. Shimizu, A. Satsuma, T. Hattori., Catal. Surv. Jpn. 4 (2000) 115.
23. R. Q. Long, R. T. Yang, R. Chang., J. Chem. Soc., Chem. Commun. (2002) 452.
24. G. Qi, R. T. Yang., J. Chem. Soc., Chem. Commun. (2003) 848.
25. R. Burch, P. J. Millington., Catal. Today 26 (1995) 185.
26. F. Janssen, F. Van den Kerkhof, H. Bosch and J. R. H. Ross., J. Phys. Chem. 91 (1987) 5921.
27. G. Ramis, G. Busca and F. Bregani., Catal. Lett. 18 (1993) 299.
28. S. C. Wood., Chem. Eng. Progr. 90 (1994) 32.
29. J. A. Dumesic, N.-Y. Topsoe, H. Topsoe and T. Slabiak., J. Catal. 163 (1996) 409.
30. G. Busca, L. Lietti, G. Ramis, F. Berti., Appl. Catal. B 18 (1998) 1.
31. H.-Y. Chen, W. M. H. Sachtler., Catal. Today 42 (1998) 73.

32. F. Heinrich, C. Schmidt, E. Löffler, W. Grünert., Catal. Commun. 2 (2001) 317.
33. Q. Sun, Z.-X. Gao, H.-Y. Chen, W. M. H. Sachtler., J. Catal. 201 (2001) 88.
34. A.- Z. Ma, W. Grünert., J. Chem. Soc., Chem. Comm. (1999) 71.
35. A. A. Battiston, J. H. Bitter, D. C. Koningsberger., J. Catal. 218 (2003) 163.
36. F. Heinrich, C. Schmidt, E. Löffler, M. Menzel, W. Grünert., J. Catal. 212 (2002) 157.
37. R. Q. Long, R. T. Yang., J. Catal. 207 (2002) 224.
38. in R. J. Meyer and E. Pietsch (Editors), Gmelins Handbuch der Anorganischen Chemie, Vol. 4, Verlag Chemie, Berlin, 1936, pp. 558-597.
39. F. Kapteijn, J. R. Mirasol, J. A. Moulijn., Appl. Catal. B. 9 (1996) 25.
40. C. M. Fu, V. N. Korchak, W. K. Hall., J. Catal. 68 (1981) 166.
41. Javier Pérez-Ramírez, F. Kapteijn, G. Mul, J. A. Mouljin., J. Catal. 208 (2002) 211.
42. Javier Pérez-Ramírez, F. Kapteijn, G. Mul, J. A. Mouljin., Appl. Catal. B. 35 (2002) 227.
43. Javier Pérez-Ramírez, F. Kapteijn, G. Mul, J. A. Mouljin., J. Chem. Soc., Chem. Comm. (2001) 693.
44. H.-Y. Chen, X. Wang, W. M. H. Sachtler., Appl. Catal. A. 194 (2000) 159.
45. R. Q. Long and R. T. Yang., J. Catal. 188 (1999) 332.
46. R. Q. Long and R. T. Yang., J. Catal. 207 (2002) 274.
47. O. A. Anunziata, A. R. Beltramone, Z. Juric, L. B. Pierella, F. G. Requejo., Appl. Catal. A. 264 (2004) 93.
48. M. Mauvezin, G. Delahay, F. Kisslich, B. Coq, S. Kieger., Cat. Lett. 62 (1999) 41.
49. M. Mauvezin, G. Delahay, B. Coq, S. Kieger., Appl. Catal. B. 23 (1999) L79.
50. B. Coq, M. Mauvezin, G. Delahay, J.-B. Butet, S. Kieger., Appl. Catal. B. 27 (2000) 193.
51. X. Xu, H. Xu, F. Kapteijn, J. A. Moulijn., Appl. Catal. B. 53 (2004) 265.
52. R. T. Yang, T. J. Pinnavaia, W. Li, W. Zhang., J. Catal. 172 (1999) 488.
53. S. Sato, H. Hirabayashi, H. Yahiro, N. Mizuno, M. Iwamoto., Catal. Lett. 12 (1992) 193.
54. T. Ishihara, M. Kagawa, F. Hadama, Y. Takita., J. Catal. 169 (1997) 93.
55. M. Santhosh Kumar, M. Schwidder, W. Grünert, A. Brückner., J. Catal. 227 (2004) 384.
56. P. Marturano, L. Drozdova, A. Kogelbauer, R. Prins., J. Catal. 192 (2000) 236.
57. A. A. Battiston, J. H. Bitter, F. M. F. de Groot, A. R. Overweg, O. Stephan, J. A. van Bokhoven, P. J. Kooyman, C. van der Spek, G. Vanko, D. C. Koningsberger., J. Catal. 213 (2003) 251.
58. Javier Pérez-Ramírez, M. Santhosh Kumar, A. Brückner., J. Catal. 223 (2004) 13.

59. A. V. Kucherov, C. N. Montreuil, T. N. Kucherova, M. Shelef., Catal. Lett. 56 (1998) 173.
60. A. Ribera, I. W. C. E. Arends, S. de Vries, Javier Pérez-Ramírez, R. A. Sheldon., J. Catal. 195 (2000) 287.
61. A. Brückner, R. Lück, W. Wieker, B. Fahlke, H. Mehner., Zeolites 12 (1992) 380.
62. G. Berler, G. Spoto, S. Bordiga, G. Ricchiardi, P. Fisicaro, A. Zecchina, I. Rossetti, E. Selli, L. Forni, E. Giamello, C. Lamberti., J. Catal. 208 (2002) 64.
63. D. Goldfarb, M. Bernardo, K.G. Strohmaier, D.E.W. Vaughan, H. Thomann, J. Am. Chem. Soc. 116 (1994) 6344.
64. M. Schwidder, M. Santhosh Kumar, K, Klementiev, M. M. Pohl, A. Brückner, W. Grünert., J. Catal. 231 (2005) 328.
65. A. Brückner, G,-U. Wolf, M. Meisel, R. Stösser, H. Mehner, F. Majunke, M. Baerns, J. Catal. 154 (1995) 11.
66. S. Bordiga, R. Buzzoni, F. Geobaldo, C. Lamberti, E. Giamello, A. Zecchina, G. Leofanti, G. Petrini, G. Tozzola, G. Vlaic., J. Catal. 158 (1996) 486.
67. M. Iwamoto et al., Tenth International Congress on Catalysis: Prepr. and Abstr. Book, Budapest (1992) p.212.
68. M. Iwamoto, H. Furukawa, Y. Mine, F. Uemura, S. Mikuriya, S. Kagawa., J. Chem. Soc., Chem. Commun. (1986) 1272.
69. M. Shelef., Catal. Rev. Sci. Eng. 11 (1975) 1.
70. T. Komatsu, M. Nunokawa, I. S. Moon, T. Takahara, S. Namba, T. Yashima., J. Catal. 148 (1994) 427.
71. J. O. Petunchi, W. K. Hall., Appl. Catal. B 3 (1994) 239.
72. K. Segawa, K. Watanabe, R. Kunugi., Trans. Mater. Res. Soc. Jpn. A. 15 (1994) 131.
73. X. Feng, W. K. Hall., J. Catal. 166 (1997) 368.
74. M. Iwamoto, H. Yahiro., Catal. Today 22 (1994) 5.
75. Z. Chajar, M. Primet, H. Praliaud, M. Chevrier, C. Gauthier, F. Mathis., Appl. Catal. B 4 (1994) 199.
76. K. C. C. Kharas, D.-J. Liu and H. J. Robota., Catal. Today 26 (1995) 129.
77. Y. Li, T. L. Slager, J. N. Armor., J. Catal. 150 (1994) 388.
78. Avelino Corma., J. Catal. 216 (2003) 298.
79. K. C. C. Kharas, H. J. Robota, D. J. Liu., Appl. Catal. B. 2 (1994) 225.
80. J. Y. Yan, G.-D. Lei, W. M. H. Sachtler, H. H. Kung., J. Catal. 161 (1996) 43.
81. X. Feng, W. K. Hall., Catal. Lett. 41 (1996) 45.
82. G. Centi and F. Vazzana., Catal. Today 53 (1999) 683.
83. R. Q. Long, R. T. Yang., J. Catal. 194 (2000) 80.

84. J. Eng, C.H. Bartholomew., 171 (1997) 27.
85. Q. Sun, Z,-X Gao, B. Wen, W. M. H. Sachtler., Catal. Lett. 78 (2002), 1.
86. H.-Y. Chen, El-M. El-Malki, X. Wang, R. A. van Santen, W. M. H. Sachtler., J. Mol. Catal. A: Chemical 162 (2000) 159.
87. H.-Y Chen, T. Voskoboinikov, W. M. H. Sachtler, J. Catal. 180 (1998) 171.
88. L. J. Lobree, In-chul Hwang, A. R. Jeffrey, A. T. Bell, Catal. Lett. 63 (1999) 233.
89. K. Hadjiivanov, H. Knözinger, B. Tsyntsarski, L. Dimitrov, Catal. Lett. 62 (1999) 35.
90. H.-Y Chen, T. Voskoboinikov, W. M. H. Sachtler, J. Catal. 186 (1999) 91.
91. Z. Sobalik, A. Vondrova, Z. Tvaruskova, B. Wichterlova., Catal. Today 75 (2002) 347.
92. Q. Zhu, B. L. Mojet, R. A. J. Janssen, E. J. M. Hensen, J. van Grondelle, P. C. M. M. Magusin, R. A. van Santen., Catal. Lett. 81 (2002) 205.
93. El-M. El-Malki, R. A. van Santen, W. M. H. Sachtler., J. Catal. 196 (2000) 212.
94. L. K. Minsker, D. A. Bulushev, A. Renken., J. Catal. 219 (2003) 273.
95. G. Delahay, M. Mauvezin, Coq, S. Kieger., J. Catal. 202 (2001) 156.
96. Javier Pérez-Ramírez, F. Kapteijn, A. Brückner., J. Catal. 218 (2003) 234.
97. B. R. Wood, J. A. Reimer, A. T. Bell., J. Catal. 209 (2002) 151.
98. M. A. Rodkin, V. I. Sobolev, K. A. Dubkov, N. H. Watkins, G. I. Panov., Stud. Surf. Sci. Catal. 130 (2000) 875.
99. G. I. Panov, A. K. Uriarte, M. A. Rodkin, V. I. Sobolev, Catal. Today 41 (1998) 365.
100. G. I. Panov., CATTECH 4 (2000) 18.
101. C. Pophal, T. Yogo, K. Yamada, K. Segawa., Appl. Catal. B. 16 (1998) 177.
102. G. Delahay, M. Mauvezin, A. G. Vargas, B. Coq., Catal. Commun. 3 (2002) 385.
103. L. J. Lobree, In-chul Hwang, A. Jeffrey, A. Reimer, A. T. Bell., J. Catal. 186 (1999) 242.
104. P. Ratnasamy, R. Kumar., Catal. Today 9 (1991) 329.
105. R. Joyner, M. Stockenhuber., J. Phys. Chem. B 103 (1999) 5963.
106.R. Q. Long, R. T. Yang., Catal. Lett. 74 (2001) 201.
107.W. K. Hall, X. Feng, J. Dumesic, R. Watwe., Catal. Lett. 52 (1998) 13.
108. E. J. M. Hensen, Q. Zhu, M. M. R. M. Hendrix, A. R. Overweg, P. J. Kooyman, M. V. Sychev, R. A. van Santen., J. Catal. 221 (2004) 560.
109. Javier Pérez-Ramírez, F. Kapteijn., Appl. Catal. B. 47 (2004) 177.
110. A. A. Battiston, J. H. Bitter, D. C. Koningsberger., Catal. Lett. 66 (2000) 75.
111. J. Jia, Q. Sun, B. Wen, L. X. Chen, W. M. H. Sachtler., Catal. Lett. 82 (2002), 7.
112. Y. Nishizaka, M. Misono., Chem. Lett. (1994) 2237.
113. C. Yokoyama, M. Misono., J. Catal. 160 (1996) 95.
114. R. L. Garten, W. N. Delgass, M. Boudart., J. Catal. 18 (1970) 90.

115. J. O. Petunchi, W. K. Hall., J. Catal. 78 (1982) 327.
116. A. A. Battiston, J. H. Bitter, W. H. Heijboer, F. M. F. De Groot, D. C. Koningsberger., J. Catal. 215 (2003) 279.
117. G. I. Panov, V. I. Sobolev, K. A. Dubkov, A. S. Kharitonov., in "Proceedings, 11th International Congress on Catalysis, Baltimore, 1996" (J. Hightower, W. N. Delgass, E. Iglesia, A. T. Bell, Eds), P.O Elsevier, Amsterdam, Stud. Surf. Sci. Catal. 101 (1996) 493.
118. K. A. Dubkov, N. S. Ovanesyan, A. A. Shteinman, E. V. Starokon, G. I. Panov., J. Catal. 207 (2002) 341.
119. A. V. Kucherov, M. Shelef., J. Catal. 195 (2000) 106.
120. R. Aasa, J. Chem. Phys. 52 (1983) 3919.
121. P.N. Joshi, S.V. Awate, V.P. Shiralkar, J. Phys. Chem. 97 (1993) 9749.
122. T. Inui, H. Nagata, T. Takeguchi, S. Iwamoto, H. Matsuda, M. Inoue, J. Catal. 139 (1993) 482.
123. A. Brückner, U. Lohse, H. Mehner, Micropor. Mesopor. Mater. 20 (1998) 207.
124. A.V. Kucherov, A.A. Slinkin, Zeolites 8 (1988) 110.
125. B. Wichterlová, P. Jiru, React. Kinet. Catal. Lett. 13 (1980) 197.
126. A.F. Ojo, J. Dwyer, R.V. Parish, Stud. Surf. Sci. Catal. 49 (1989) 227.
127. P. Wenquin, Q. Shilun, K. Zhiyun, P. Shaoyi, Stud. Surf. Sci. Catal. 49 (1989) 281.
128. G. Catana, J. Pelgrims, R.A. Schoonheydt, Zeolites 15 (1995) 475.
129. A. Brückner in B.M. Weckhuysen, P. Van Der Voort, G. Catana (Eds.), Spectroscopy of Transition Metal Ions on Surfaces, Leuven University Press, Leuven, 2000, p. 69.
130. A. M. Ferretti, C. Oliva, L. Forni, G. Berlier, A. Zecchina, C. Lamberti., J. Catal. 208 (2002) 83.
131. K. Dräger., Z. Naturforsch. Teil A 32 (1977) 163.
132. H. H. Tippins., Phys. Rev. B 1 (1970) 126.
133. L. E. Iton, R. B. Beal, D. T. Hodul., J. Mol. Catal. A: Chem. 21 (1983) 151.
134. J. Patarin, M. H. Tullier, J. Durr, H. Kessler., Zeolites 12 (1992) 70.
135. G. Lehmann., Z. Phys. Chem. Neue Folge 72 (1970) 279.
136. G. Kortüm., Reflectance Spectroscopy, Springer, Berlin (1969).
137. R. A. Schoonheydt., in: F. Delannay (Ed.), Characterization of Catalysts, Marcel Dekker (1984) p. 125.
138. B. M. Weckhuysen, R. A. Schoonheydt., Catal. Today 49 (1999) 441.
139. P. Fejes, J. B. Nagy, J. Halasz, A. Oszko., Appl. Catal. A. 175 (1998) 89.
140. P. Marturano, A. Kogelbauer, R. Prins., J. Catal. 190 (2000) 460.
141. C. T. W. Chu, C. D. Chang., J. Phys. Chem. 89 (1985) 1569.

142. L. M. Kustov, V. B. Kazansky, P. Ratnasamy., Zeolites 7 (1987) 79.
143. R. Szostak, V. Nair, T. L. Thomas., J. Chem. Soc. Faraday Trans. I, 83 (1987) 487.
144. B. Hunger, J. Hoffmann, O. Heitzsch, M. Hunger., J. Therm. Anal. 36 (1990) 1379.
145. N.-Y. TopsØel, K. Pedersen, E. G. Derouane., J. Catal. 70 (1981) 41.
146. R. Stösser and G. Scholz, Appl. Magn. Reson. 12 (1997) 167.
147. A. Brückner, B. Kubias, B. Lücke., Catal. Today 32 (1996) 215.
148. G. Busca., Phys. Chem. Chem. Phys., 1 (1999) 723.
149.O. M. Busch, W. Brijoux, S. Thomson, F. Schüth, J. Catal. 222 (2004) 174.
150. R. Buzzoni, S. Bordiga, G. Ricchiardi, C. Lamberti, A. Zecchina, G. Bellussi., Langmuir 12 (1996) 930.
151. Hadjiivanov, K., Klissurski, D., Ramis, G., Busca, G., App.Catal. B. **7** (1996) 251.
152. K. Segawa, Y. Chen, J. E. Kubsh, W. N. Delgass, J. A. Dumesic, W. Keith Hall, J. Catal. 76 (1982) 112.
153. A. Davydov, Molecular Spectroscopy of oxide catalyst surfaces, John Wiley & Sons Ltd. Chichester, 2003, p. 124.
154. Javier Pérez-Ramírez, G. Mul, F. Kapteijn, J. A. Moulijn, A. R. Overweg, A. Domenech, A. Ribera, I. W. C. E. Arends., J. Catal. 207 (2002) 113.
155. Javier Pérez-Ramírez, F. Kapteijn, J. C. Groen, , A. A. Domenech, G. Mul, J. A. Moulijn., J. Catal. 214 (2002) 33.
156. H. Kosslick, G. Lischke, G. Walther, W. Storek, A. Martin and R. Fricke, Microporous Materials, 9 (1997) 13.
157. X. Xu, H. Xu, F. Kapteijn, J. A. Moulijn., Appl. Catal. B 53 (2004) 265.
158. R. T. Yang, T. J. Pinnavaia, W. Li, W. Zhang., J. Catal. 172 (1997) 488.
159. Javier Pérez-Ramírez, J. C. Groen, A. Brückner, M. Santhosh Kumar, U. Bentrup, M. N. Debbagh, L. A. Villaescusa., J. Catal. 232 (2005) 318.
160. Javier Pérez-Ramírez, F. Kapteijn, G. Mul, X. Xu, J. A. Moulijn., Catal. Today 76 (2002) 55.
161. M. Santhosh Kumar, Javier Pérez-Ramírez, M. N. Debbagh, M. Smarsly, A. Brückner., Appl. Catal. B, accepted.
162. M. Schwider, M. Santhosh Kumar, M. N. Debbagh, Javier Pérez-Ramírez, A. Brückner, W. Grünert., Micropor. Mesopor. Mater, to be submitted.
163. X.Gao, I. E. Wachs, J. Phys. Chem. B 104 (2000) 1261.
164. M. Schwidder, M. Santhosh Kumar, A. Brückner, W. Grünert., J. Chem. Soc., Chem. Comm. (2005) 805.
165. J. Tang, M. Myers, K. A. Bosnick, L. E. Brus, J. Phys. Chem. B 107 (2003) 7501.

166. A. Brückner, P. Rybarczyk, H. Kosslick, G.-U. Wolf and M. Baerns., Stud. Surf. Sci. Catal., 142B (2002) 1141.
167. R. Zysler, D. Fiorani, J. L. Dormann, A. M. Testa, J. Magn. Magn. Mater. 133 (1994) 71.
168. R. Berger, J.-C. Bissey, J. Liava, H. Daubric, C. Estournes, J. Magn. Magn. Mater. 234 (2001) 535.
169. T. R. Hughes, H. M. White, J. Phys. Chem. 71 (1967) 2192.
170. E. R. A. Matulewicz, F. R. J. M. Kerkhof, J. A. Moulijn, H. J. Reitsma, J. Colloid Interf. Sci. 77 (1980) 110.
171. P. A. Jacobs, C. F. Heylen, J. Catal. 34 (1974) 267.
172. E. Selli, I. Forni, Micropor. Mesopor. Mat. 31 (1999) 129.
173. J. Dedecek, D. Kaucky, B. Wichterlova., Micropor. Mesopor. Mater. 35-36 (2000) 483.
174. A. D. Cowan, R. Dümpelmann, N. W. Cant, J. Catal. 151 (1995) 356.
175. Y. Ukisu, S. Sato, G. Muramatu, K. Yoshida, Catal. Lett. 11 (1991) 177.
176. N. W. Hayes, W. Grünert, G. J. Hutchings, R. W. Joyner, E. S. Shpiro, J. Chem. Soc. Chem. Commun. 531 (1994).
177. K. A. Bethke, C. Li, M. C. Kung, B. Yang, H. H. Kung, Catal. Lett. 31 (1995) 287.
178. F. Radtke, R. A. Koeppel, E. G. Minardi, A. Baiker, J. Catal. 167 (1997) 127.
179. F. Poignant, J. Saussey, J.-C. Lavalley, G. Mabilon., J. Chem. Soc. Chem. Commun. 89 (1995).
180. Ursula Bentrup, Angelika Brückner, Manfred Richter and Rolf Fricke., Appl. Catal. B 32 (2001) 229.
181.G. Socrates, Infrared and Raman characteristic group frequencies, John Wiley & Sons Ltd. Chichester, 2001, p. 115 et sqq.
182. V. A. Shvets, V. B. Kazanski, J. Catal. 25 (1972) 123.
183. K. Hayashi, M. Hirano, S. Matsuishi, H. Hosono, J. Am. Chem. Soc. 124 (2002) 738.
184. M. Che, A.J. Tench, Adv. Catal. 31 (1982) 77.
185. E.V. Starokon, K.A. Dubkov, L.V. Pirutko, G.I. Panov, Top. Catal. 23 (2003) 137.
186. B. G. Fox, J. D. Lipscomb, in: C. C. Reddy, G. A. Hamilton, K. M. Madyastha (Eds.), Biological Oxidation Systems. Vol. 1, Academic Press, San Diego, CA, 1990, p. 367.
187. G. Berlier, A. Zecchina, G. Spoto, G. Ricchiardi, S. Bordiga, C. Lamberti., J. Catal. 215 (2003) 264.
188. Javier Pérez-Ramírez, F. Kapteijn, G. Mul, J. A.Mouljin., Catal. Commun.3 (2002) 19.
189. A. M. Volodin, V. I. Sobolev, G. M. Zhidomirov., Kinet. Catal. 39 (1998) 775.
190. P. Kubanek, B. Wichterlova, Z. Sobalik., J. Catal. 211 (2002) 109.

Acknowledgement

I am thankful to my PhD mentor Dr. HABIL. ANGELIKA BRÜCKNER for the opportunity to work with her, for her guidance and encouragement.
My sincere thanks to Prof. Dr. W. GRÜNERT and Prof. Dr. JAVIER PÉREZ-RAMÍREZ as well as to Dr. M. SCHWIDDER for providing the samples for the most part of the investigations carried out in this thesis, catalytic data and fruitful discussion.

I also thank Prof. Dr. R. STÖSSER for clarifying the doubts concerning the spectroscopy.

I am grateful to Dr. P. S. SAI PRASAD, Dr. HABIL. A. MARTIN und Prof. Dr. B. LÜCKE for encouraging me to do my Ph.D here in the Institut für Angwandte Chemie Berlin-Adlershof e.V.

I would like to thank my co-workers in the Institute for helping me during my course of study.
Dr. U. BENTRUP for her help with the FT-IR and helpful discussion.
Mr. U. MARX for his help with the EPR Experiments.
Mrs. UTE WOLF for her help with the FT-IR Experiments.
Mr. GERT-ULRICH WOLF for his help with the preparation of catalysts.
Dr. H. KOSSLICK for providing SBA-15 und MCM-41 materials.
Ms. CARLOTTA CORTELLI, Dr. EVGUENII KONDRATENKO, Dr. KALEVARU NARAYANA and Mr. R. KRÄHNERT for the help and Discussion.

I extend my thanks to Mr. LOTHAR MADER, Mrs. HEIDI FRENCH and Mrs. JUTTA KUBIAS for making my stay easier and enjoyable.
My special thanks go to Mrs. SMITHA PILLAI who helped me throughout my Ph.D with her constant support and encouragement.

Last but not least, I thank my parents and my sisters and their family, who encourage me always to do my work what I wish for. Their innumerable support and blessings always motivate me to go further into the pinnacle of success.

I dedicate this work to my PARENTS and GURUS

Versicherung

Hiermit versichere ich, dass ich die Arbeit selbständig und nur Verwendung der angegebenen Hilfsmittel angefertigt verfasst und habe

Berlin, den 12.08.2005 M. Santhosh Kumar

LEBENSLAUF

PERSÖNLICHE DATEN

- **Name:** Matam
- **Vorname:** Santhosh Kumar
- **Geburtsdatum:** 10.10.1975
- **Geburtsort:** Secunderabad, Indien
- **Nationalität:** Indien
- **Personenstand:** Ledig

AUSBILDUNG

- **1981-1986** **Primary School**
- **1986-1991** **High School**
- **1991-1993** **Intermediate (Pre University)**
- **1993-1996** **Bachelor of Science (B.Sc),** Graduation in Chemie und Biologie von Osmania University, Indien.
- **1997-1999** **Master of Science (M.Sc),** Post graduation in Angewandte Chemie von Kakatiya University, Warangal, Indien.
- **2000-2002** **Wissenschaftlicher Mitarbeiter,** Katalyse und Physikaliche Chemie Lehrstuhl, Indisches Institut für Chemische Technologie (IICT), Hyderabad, Indien
  Projekt**:** „Process development for the synthesis of pyrazinamide“
- **Seit 2002** **Doktorand,** Institut für Angewandte Chemie Berlin-Adlershof e.V, Deutschland
  Projekt**:** „Entwicklung neuer zeolithischen Redox-Katalysatorer für die selektive Reduktion von NO mit Ammoniak durch Aufklärung der Bezichungen zwischen Katalysatorstruktur und katalytischen Eigenschaften“.

LIST OF PUBLICATIONS

Patents

1. United States Patent number is 6,534,435, March 2003.

Articles in Scientific Journals

1. K.N. Rao, Rajesh Gopinath, **M. Santhosh Kumar,** I. Suryanarayana and P.S. Saiprasad, "Interaction-induced enhancement in the activity and selectivity of a titania-supported ammonium salt of a 12-molybdophospharic acid catalyst during ammoxidation of 2-methylpyrazine", ***J. Chem. Soc. Chem. Commun. (2001) 2088-2089***.

2. **M. Santhosh Kumar,** K.N. Rao, N. Lingaih, I. Suryanarayana and P.S. Saiprasad, "*In situ* synthesis by salt-surface interaction and the catalytic functionality of the ammonium salt of a 12-tungstophospharic acid", ***Green Chem. 4 (2002) 344-346***.

3. Javier Pérez-Ramírez, A. Brückner, **M. Santhosh Kumar,** F. Kapteijn, "Structure-activity relationships in N_2O conversion over FeMFI zeolites. Preparation of catalysts with a well-defined distribution of Fe species", ***Catalysis in Application. Page No. 308***, Published on 19th June 2003.

4. M. Schweidder, F. Heinrich, **M. Santhosh Kumar**, A. Brückner, W. Grünert, "Fe-ZSM-5-Catalysts fort he Selective Reduction of NO: Influence of Preparation Route on Structure and Catalytic Activity"–***Proceedings of the 14th International Zeolite Conference*** 25th April 2004, 2484.

5. Javier Pérez-Ramírez, **M. Santhosh Kumar** and A. Brückner, "Reduction of N_2O with CO over FeMFI zeolites: influence of the preparation method on the iron species and catalytic behavior" ***J. Catal. 223 (2004) 13-27.***

6. **M. Santhosh Kumar,** M. Schwider, W. Grünert and A. Brückner, "On the nature of different iron sites and their catalytic role in Fe-ZSM-5 $DeNO_x$ catalysts: new insights by a combined EPR and UV/VIS spectroscopic approach", ***J. Catal. 227 (2004) 384-397.***

7. M. Schwider, **M. Santhosh Kumar,** A. Brückner and W. Grünert, "Active sites for NO reduction over Fe-ZSM-5 catalysts", ***J. Chem. Soc. Chem. Commun. (2005) 805-807.***

8. M. Schwider, **M. Santhosh Kumar,** K. Klementiev, M. M. Pohl, A. Brückner and W. Grünert, "Selective reduction of NO with Fe-ZSM-5 of low Fe content I. Relations between active site structure and catalytic performance", ***J. Catal. 231 (2005) 328-344.***

9. Javier Pérez-Ramírez, J. C. Groen, A. Brückner, **M. Santhosh Kumar,** U. Bentrup, M. N. Debbagh and L. A. Villaescusa, "Evolution of isomorphously substituted iron zeolites during activation: comparison of Fe-beta and Fe-ZSM-5", ***J. Catal. 232 (2005) 318-334.***

10. **M. Santhosh Kumar,** Javier Pérez-Ramírez, M. N. Debbagh, B. Smarsly and A. Brückner**,** "Evidence of the vital role of the pore network on various catalytic conversions of N_2O over Fe-silicalite and Fe-SBA-15 with the same iron constitution" ***Appl. Catal. B: Environmental 62 (2005) 244-254.***

11. **M. Santhosh Kumar,** M. Schwider, W. Grünert and A. Brückner, "Selective reduction of NO with Fe-ZSM-5 of low Fe content: Part II: Assessing the function of different Fe sites by spectroscopic in situ studies", ***J. Catal, to be submitted***

12. M. Schwider, **M. Santhosh Kumar,** N. N. Debha, Javier Pérez-Ramírez, A. Brückner and W. Grünert, "The role of Bronsted acidity in the selective reduction of NO over Fe-ZSM-5 catalysts" ***Micropor. Mesopor. Mater, to be submitted***

Conferences*

1. Elucidating the structure of Fe^{+3} sites in Fe-ZSM-5 $DeNO_x$ catalysts by in-situ EPR and in-situ UV/Vis spectroscopy
   M. Santhosh Kumar, M. Schwidder, W. Grünert and A. Brückner-XXXVI. Jahrestreffen Deutscher Katalytiker 19th-21st March 2003 at Weimar-Germany.

2. Verschiedene wege zur Darstellung von Fe-ZSM-5 katalysatoren für die selective katalytische reduction (SCR) von NO mit NH_3 und iso-butan und Charakterisierung mittels Photoelektronen- und XAFS-Spektroskopie
   M. Schwidder, F. Heinrich, **M. Santhosh Kumar**, A. Brückner, W. Grünert-XXXVI. Jahrestreffen Deutscher Katalytiker 19th-21st March 2003 at Weimar-Germany.

3. Elucidating the structure of Fe^{+3} sites in Fe-ZSM-5 $DeNO_x$ catalysts by in-situ UV-Vis-DRS and in-situ EPR spectroscopy
   M. Santhosh Kumar, M. Schweidder, W. Grünert, U. Bentrup and A. Brückner-Presented at ACA - Status Seminar-2002, Berlin on 6th May 2003.

4. Structure and behavior of active sites in Fe-ZSM-5 $DeNO_x$ catalysts: New insights by spectroscopic in situ-studies
   M. Santhosh Kumar, M. Schwidder, W. Grünert and A. Brückner-18th NAM (North American catalysis society Meeting) 1st –6th June 2003 at Cancun-Mexico

5. Javier Pérez-Ramírez, A. Brückner, **M. Santhosh Kumar,** F. Kapteijn International Symposium on Applied Catalysis at University of Glasgow 16th July 2003. This was a joint meeting of RSC and the Institution of Chemical Engineers.

6. Multitechnique characterization of Fe-ZSM-5 catalysts for NO_x abatement: On the way to the identification of the active iron sites
   M. Santhosh Kumar, A. Brückner, M. Schweidder, K.V. Klementiev, W. Grünert - EUROPA CAT-VI, August 31st to 4th September 2003 at Innsbruck-Austria.

7. Structure and function of active iron sites in Fe-ZSM-5 catalysts during selective catalytic reduction (SCR) of NO: New Insights by Spectroscopic *In-situ* Studies
   M. Santhosh Kumar, M. Schwidder, W. Grünert, U. Bentrup and A. Brückner,
   Presented at Indo-German Catalysis Workshop, Berlin on 26th September 2003 on the occasion of Asian Pacific Weeks, Berlin 2003.

*Presented by the author underlined

8. Behavior of iron sites in Fe-ZSM-5 during N_2O decomposition studied by in-situ UV-Vis-DRS and in-situ EPR

   M. Santhosh Kumar, Javier Perez-Ramirez and Angelika Brückner, Presented at the Embassy of India, Berlin on 16th September 2003 on the occasion of Asian Pacific Weeks, Berlin 2003 (Germany).

9. Fe-ZSM-5 catalysts for the selective catalytic reduction of NO_x: Which iron does which job?

   M. Schweidder, **M. Santhosh Kumar**, U. Bentrup, A. Brückner, K.V. Klementiev, W. Grünert–16th Deutsche Zeolith-Tagung 3rd-5th March 2004 at Dresden-Germany

10. Structure and function of iron sites in FeMFI catalysts during N_2O decomposition studied by in-situ EPR and in-situ UV/Vis spectroscopy

    M. Santhosh Kumar, Javier Perez-Ramirez and Angelika Brückner-XXXVII. Jahrestreffen Deutscher Katalytiker 17th-19th March 2004 at Weimar-Germany.

11. Fe-ZSM-5 catalysts for the selective catalytic reduction of nitric oxide: New way to highly active materials

    M. Schweidder, **M. Santhosh Kumar**, A. Brückner, K.V. Klementiev, W. Grünert - XXXVII. Jahrestreffen Deutscher Katalytiker 17th-19th March 2004 at Weimar-Germany

12. Struktue-Wirkungs-Beziehungen in Fe-ZSM-5-Katalysatoren für die selektive Reduction von NO mit NH_3 bzw. Isobutan

    M. Schweidder, **M. Santhosh Kumar**, U. Bentrup, A. Brückner, K.V. Klementiev, W. Grünert -XXXVII. Jahrestreffen Deutscher Katalytiker 17th-19th March 2004 at Weimar-Germany

13. Fe-ZSM-5 catalysts for the selective catalytic reduction of NO: Influence of preparation route on structure and catalytic activity

    M. Schweidder, F. Heinrich, **M. Santhosh Kumar**, A. Brückner, W. Grünert – 14th International Zeolite Conference 25th-30th April 2004 at Cape Town-South Africa

14. Active sites for the selective catalytic reduction of NO with NH_3 or isobutane over Fe-ZSM-5: A new view onto a controversial question

    M. Schweidder, **M. Santhosh Kumar**, U. Bentrup, A. Brückner, K.V. Klementiev, W. Grünert-13th International Conference On Catalysis 11th-16th July 2004 at Paris-France

15. Structure and behavior of iron species in Fe-ZSM-5 zeolites in the selective catalytic reduction of NO by NH_3 using in-situ EPR and in-situ UV-Vis-DRS

    M. Santhosh Kumar, M. Schweidder, W. Grünert A. Brückner - Post 13th ICC conference summer school on "In situ and Operando spectroscopy for catalysts" 18th-21st July 2004 at Caen-France

16. Active sites in Fe-ZSM-5 catalysts: Structure-Activity Correlations for Selective NO Reduction

    M. Schwidder, K. Klementiev, **M. Santhosh Kumar**, A. Brückner and W. Grünert Deutsche Zeolith Tagung 2nd-4th March 2005 at Gießen-Germany

17. Monitoring different iron sites in Fe-ZSM-5 during selective catalytic reduction (SCR) of NO

    M. Santhosh Kumar, M. Schwidder, W. Grünert and A. Brückner-XXXVIII. Jahrestreffen Deutscher Katalytiker 16th-18th March 2005 at Weimar-Germany

18. Fe-ZSM-5 Catalysts with Tuneable High Activities in NO and N_2O Abatement Reactions: Reactivities, Structure and Identification of Active Sites

    M. Schweidder, **M. Santhosh Kumar**, A. Brückner, J. Pérez-Ramírez, N. Debbagh, K. V. Klementiev, and W. Grünert- International Congress of Environmental Catalysis 5TH –8TH June 2005 at Heidelberg-Germany

19. Design of iron zeolite catalysts for N_2O abatement in tail-gases of fluidised bed combustors

    M.N.B. Debbagh, C.S.M.deLecea, A.Brückner, **M. Santhosh Kumar** and J. Pérez-Ramírez International Congress of Environmental Catalysis 5TH–8TH June 2005 at Heidelberg-Germany